

QUANTUM COMPUTATION IN QUDIT SPACE AND APPLICATIONS IN OPEN QUANTUM DYNAMICS

by

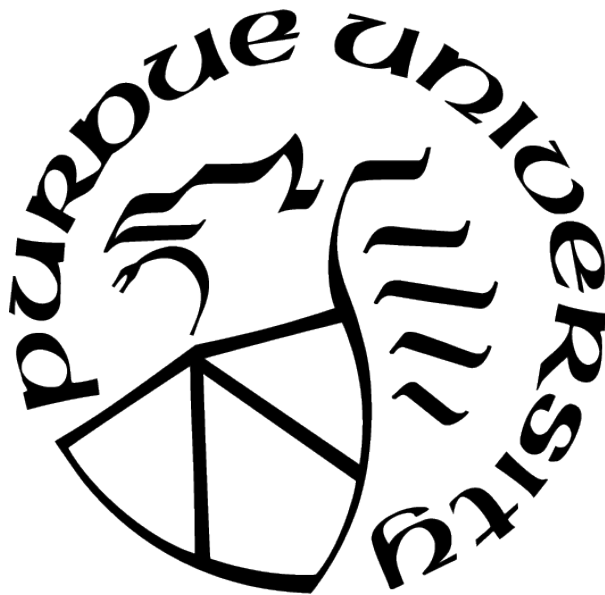
Yuchen Wang

A Dissertation

Submitted to the Faculty of Purdue University

In Partial Fulfillment of the Requirements for the degree of

Doctor of Philosophy



Department of Physics and Astronomy

West Lafayette, Indiana

May 2023

**THE PURDUE UNIVERSITY GRADUATE SCHOOL
STATEMENT OF COMMITTEE APPROVAL**

Dr. Sabre Kais, Chair

Department of Chemistry

Dr. Andrew M. Weiner

School of Electrical and Computer Engineering

Dr. Yong P. Chen

Department of Physics and Astronomy

Dr. Yuli Lyanda-Geller

Department of Physics and Astronomy

Approved by:

Dr. Gabor A. Csathy

To My Parents

ACKNOWLEDGMENTS

First and foremost, I would like to express my sincere gratitude to my advisor Prof. Sabre Kais for the continuous support of my Ph.D study and research, for his patience, motivation, enthusiasm, and immense knowledge. His passion in quantum computing gives me the enthusiasm to dive in the research of this field. He is always supportive when I am in need of help.

Also, I would like to thank the rest of my thesis committee: Prof. Andrew M. Weiner, Prof. Yong P. Chen, and Prof. Yuli Lyanda-Geller, for their encouragement, insightful comments, and inspiring questions.

Last but not least, I'd like to thank our collaborators of the NSF CCI: Prof. Eitan Geva's group from University of Michigan, Ann Arbor and Prof. Victor S. Batista's group from Yale University for their contributions to the Open quantum dynamics project. I'd also like to thank all the colleagues and collaborators for helping me develop this thesis. I'd like to give special thanks to Dr. Zixuan (Andrew) Hu for the helpful discussion that improved my thesis.

TABLE OF CONTENTS

LIST OF TABLES	8
LIST OF FIGURES	9
ABSTRACT	11
1 INTRODUCTION	13
1.1 Quantum computation in qudit space	13
1.2 Open quantum dynamics	16
2 QUDITS AND HIGH-DIMENSIONAL QUANTUM COMPUTING	22
2.1 Quantum gates for qudits	23
2.1.1 Criteria for universal qudit gates	23
Universality	23
Examples of universal gate sets	24
2.1.2 Examples of qudit gates	29
Qudit versions $\pi/8$ gate	30
Qudit SWAP gate	35
Simplified qubit Toffoli gate with a qudit	38
Qudit multi-level controlled gate	41
2.1.3 Geometrically quantifying qudit-gate efficiency	42
2.2 Quantum algorithms using qudits	46
2.2.1 Qudit oracle-decision algorithm	47
Parity determining algorithm	47
Qudit Deutsch-Jozsa algorithm	49
Qudit generalization of the Bernstein-Vazirani algorithm	51
2.2.2 Qudit algorithms for the hidden Abelian subgroup problems.	54
Quantum Fourier Transform with qudits	54
Phase-estimation algorithm with qudits	56
2.2.3 Quantum search algorithm with qudits	59

2.3	Alternative models of quantum computing with qudits	62
2.3.1	Measurement-based qudit computing	63
2.3.2	Adiabatic qudit computing	63
2.3.3	Topological quantum computing with qudits	64
2.4	Implementations of qudits and algorithms	65
2.4.1	Time and frequency bin of a photon	66
2.4.2	Ion trap	68
2.4.3	Nuclear magnetic resonance	71
2.4.4	Molecular magnets	72
2.5	Summary and future outlook of qudit system	74
2.5.1	Summary of the advantages of qudit systems compared to qubit systems	74
2.5.2	Future outlook of qudit system	75
3	QUANTUM PHASE ESTIMATION WITH TIME-FREQUENCY QUDITS IN A SINGLE PHOTON	77
3.1	Theory	77
3.2	Experimental results	79
3.3	Discussion	85
4	STATISTICAL APPROACH TO QUANTUM PHASE ESTIMATION	91
4.1	Phase Estimation Algorithms	91
4.2	Statistical Approach to PEA	95
4.3	Statistical PEA Simulation	97
4.3.1	Qiskit Simulation	98
4.3.2	Full Spectral Decomposition	100
4.3.3	Scaling to Higher Dimensions	102
4.4	Discussion	103
4.5	Conclusion	104
5	QUANTUM SIMULATION OF THE RADICAL PAIR DYNAMICS OF THE AVIAN COMPASS	109

5.1	The quantum algorithm	109
5.2	The Radical Pair Mechanism Theory and Dynamics	112
5.3	Complexity analysis	117
5.4	Conclusion	118
6	SIMULATING OPEN QUANTUM SYSTEM DYNAMICS ON NISQ COMPUTERS WITH GENERALIZED QUANTUM MASTER EQUATIONS	120
6.1	GQME-based propagators	120
6.2	A GQME-based quantum algorithm for simulating open quantum system dynamics	124
6.3	A demonstrative application to the spin-boson model	126
6.4	Reduced-dimensionality GQME-based	131
6.5	Concluding Remarks	134
7	SUMMARY	137
A	APPENDIX FOR CHAPTER 4	139
A.1	Quality of Eigenphase-Eigenstate retrieval	139
A.2	Details for the IBM Q SPEA calculations	140
A.3	Full H_2O Matrix	145
B	APPENDIX FOR CHAPTER 4	146
B.1	Quantum Simulation Details	146
C	APPENDIX FOR CHAPTER 6	149
C.1	Quantum circuit examples	149
	REFERENCES	155

LIST OF TABLES

2.1	Normalized photon counts and comparison of the true phase ϕ and the experimentally estimated phase $\hat{\phi}$	67
3.1	Normalized photon counts and comparison of true phase and experimentally estimated phase.	87
4.1	IBM Q Qiskit QASM simulator results.	106
4.2	Statistics for 120 successful trials of complete spectral decomposition of U_{H_2O} matrix.	107
4.3	Scalability results	108
5.1	Parameter values used in the calculation.	113
6.1	Spin-boson model and simulation parameters.	127

LIST OF FIGURES

1.1	Open quantum system dynamics and applications.	17
1.2	A comparison of the workflows for simulating the dynamics of a closed quantum system vs. an open quantum system.	21
2.1	The schematic circuit of $C_m(R_d)$ with $C_2(R_d)$ and $C_2(P_d(p, q))$	28
2.2	Two proposals of qudit SWAP gate.	36
2.3	Qudit SWAP circuits with the $G XOR$ and the K_d gates.	37
2.4	Qudit SWAP gate and the decomposing $C\tilde{X}$ gate.	37
2.5	Decomposing qubit Toffoli gate with the universal qubit gates.	39
2.6	The Simplified Toffoli gate.	39
2.7	d -valued Quantum Multiplexer.	42
2.8	Schematic view of the quantum circuit for the parity determining algorithm. . .	49
2.9	The Deutsch-Jozsa circuit in qudit system.	51
2.10	Quantum Fourier transform in qudit system.	56
2.11	The circuit for the first stage of the PEA and the schematic circuit for the whole stage of PEA.	58
2.12	Circuit illustration for Grover iteration and schematic circuit illustration of the qudit quantum search algorithm.	60
2.13	Illustration of a qudit multipod linkage.	61
2.14	Electronic level structure of the trapped ion.	71
3.1	Schematic for a general qubit-based PEA and schematic for a single-qudit-based PEA.	77
3.2	(a) Experimental setup. (b) Implementation of controlled-phase gate.	80
3.3	Experimental results for implementing (a) \hat{U}_1 , and (b) \hat{U}_2	83
3.4	The probability of the control qutrit collapsing to bin 0(blue), 1(red), 2(yellow). .	86
4.1	The traditional PEA using n control d_c -dimensional qudits in the control register. .	92
4.2	The iterative PEA.	93
4.3	Plot of $\mathcal{P}_0(\Delta\theta)$ from $\Delta\theta \in [-.5, .5)$ for various d_c	94
4.4	Diagram of variational classical-quantum system.	96
4.5	Full spectrum decomposition results.	101

5.1	The basic scheme of the radical pair mechanism.	111
5.2	The comparison of the singlet and triplet yields depends on the angle	115
5.3	The comparison of the singlet and triplet yields depends on the time	116
6.1	The electronic population difference calculated by the QASM quantum simulator.	129
6.2	The electronic population difference calculated by the IBM quantum computers.	130
6.3	The population-only-GQME-based quantum-computer-simulated result.	134
A.2.1	Gate representation of the unitary operators applied in the simulation.	142
A.2.2	Illustration of the 4-level control ($d_c = 4$) SPEA circuit implemented using Qiskit.	143
B.1.1	An example of a portion of the quantum gate sequence of a Kraus operator.	148
C.1.1	Heat map illustrations of the dilated 8×8 unitary matrix.	150
C.1.2	Probability distribution of the donor state and the acceptor state.	152
C.1.3	Transpiled quantum circuit of the dilated \mathcal{U}_{G_3} matrix.	153
C.1.4	Transpiled quantum circuit of the dilated \mathcal{U}_{G_4} matrix	154

ABSTRACT

Qudit, a multi-level computational unit for quantum computing, provides a larger state space for information processing, and thus can reduce the circuit complexity, simplify the experimental setup. We promote the qudit-based quantum computing by providing an overview that covers a variety of qudit topics ranging from gate universality, circuit building, algorithm design, to physical realization methods. Among all the important qudit algorithms, we perform the first experimental realization of a qudit-based phase estimation algorithm (PEA) on a photonic platform, utilizing the high dimensionality in time and frequency degrees of freedom (DoFs) in a single photon. In our scheme the controlled-unitary gates can be realized in a deterministic fashion, as the control and target registers are now represented by two DoFs in a single photon. Next we improve the PEA by introducing a new statistical and variational approach to the PEA that we called SPEA. The SPEA can determine any unknown eigenstate-eigenphase pair from a given unitary matrix by treating the probabilistic output of an Iterative PEA (IPEA)-like circuit as an eigenstate-eigenphase proximity metric, using this metric to estimate the proximity of the input state and input phase to the nearest eigenstate-eigenphase pair and approaching this pair via a variational process on the input state and phase. The SPEA can search over the entire computational space as well as some specified given range efficiently and thus outperforms the original PEA.

The simulation of open quantum dynamics has attracted wide interests recently with a variety of quantum algorithms developed and demonstrated. The second half of the thesis focus on the simulation of the open quantum dynamics which is a useful application for quantum computer based on qudit as well as qubit. We perform the first quantum simulations of the radical pair mechanism (RPM) in the avian compass with a Sz.-Nagy dilation theorem-based quantum algorithm to demonstrate the generality of the quantum algorithm and to open new opportunities for studying the avian compass with quantum computing devices. Next we apply the same quantum algorithm to simulate open quantum dynamics based on the Generalized Quantum Master Equation (GQME). This approach overcomes the limitations of the Lindblad equation by providing a rigorous derivation of the equations of motion for any subset of elements of the reduced density matrix. We validate our quantum algorithm as

applied to the spin-boson benchmark model by analyzing the impact of the quantum circuit depth on the accuracy of the results when the subset is limited to the diagonal elements of the reduced density matrix. Our findings demonstrate that our approach yields reliable results on noisy intermediate-scale quantum (NISQ) computers.

1. INTRODUCTION

1.1 Quantum computation in qudit space

Quantum computation has received enormous attention in recent years with rapid progress in both theoretical and experimental fronts[1]–[4]. The development of quantum algorithms used for quantum computation has been stimulated by the greater availability of more capable quantum devices[5]–[11]. Qudit technology, with a qudit being a quantum version of d -ary digits for $d > 2$ [12], is emerging as an alternative to qubit for quantum computation and quantum information science. Due to its multi-level nature, qudit provides a larger state space to store and process information and the ability to do multiple control operations simultaneously [13]. These features play an important role in the reduction of the circuit complexity, the simplification of the experimental setup and the enhancement of the algorithm efficiency [13]–[16]. The advantage of the qudit not only applies to the circuit model for quantum computers but also applies to adiabatic quantum computing devices [17], [18], topological quantum systems [19]–[21] and more. The qudit-based quantum computing system can be implemented on various physical platforms such as photonic systems [13], [22], continuous spin systems [23], [24], ion trap [25], nuclear magnetic resonance [26], [27] and molecular magnets [28].

Although the qudit system’s advantages in various applications and potentials for future development are substantial, this system receives less attention than the conventional qubit-based quantum computing, and a comprehensive review of the qudit-based models and technologies is needed. Chapter 2 provides an overview of qudit-based quantum computing [29]. It covers a variety of topics ranging from circuit building [30]–[34], algorithm designs [24], [27], [35]–[39], to experimental methods [13], [22]–[28]. In this part, high-dimensional generalizations of many widely used quantum gates are presented and the universality of the qudit gates is shown. Qudit versions of three major classes of quantum algorithms—algorithms for the oracles decision problems (e.g., the Deutsch-Jozsa algorithm [35]), algorithms for the hidden non-abelian subgroup problems (e.g. the phase-estimation algorithms (PEAs) [37]) and the quantum search algorithm (e.g. Grover’s algorithm [39])—are discussed and the comparison of the qudit designs versus the qubit designs is analyzed. Finally, it introduces various

physical platforms that can implement qudit computation and compare their performances with their qubit counterparts.

Chapter 3 presents the quantum phase estimation with time-frequency qudits in a single photon [13]. The phase estimation algorithm (PEA) is a key subroutine of several important algorithms such as the Shor’s factorization algorithm[40] and the Harrow-Hassidim-Lloyd (HHL) algorithm for solving linear systems of equations[41], [42]. PEA has also been developed to find the ground-state energy of a molecular Hamiltonian[10], [43]–[45], and experimentally demonstrated on various physical platforms[11], [46]–[48]. Currently most platforms designed for quantum computation are based on quantum bits, or qubits, represented by quantum states in a two-dimensional Hilbert space. The scalability of quantum computation requires representing high-dimensional quantum states with multiple interacting qubits and realizing high-dimensional quantum gates with sequences of one-qubit and two-qubit elementary gates. Due to experimental constraints and environmental noise, both the number of interacting qubits (width) and the length of the gate sequence (depth) limit the capability of quantum computing hardware.

As an alternative to qubits, qudits, represented by quantum states in a d -dimensional (with d greater than 2) Hilbert space, has been proposed. Using qudits as the building block can potentially reduce both the width and the depth of quantum circuits, and therefore may offer unique advantages over the conventional qubit systems. Indeed, several benefits of qudits, including higher information coding capacity, stronger non-locality, and enhanced security, have been proposed[49]–[53]. Various techniques have demonstrated the required hardware to generate and process qudits by utilizing different degrees of freedom (DoFs) in photons, including orbital angular momentum[54], time-bin[55], frequency-bin[56]–[58], and hybrid time-frequency bin encoding[59], [60]. Performing quantum simulation and computation with qudits have also been proposed[61], [62], but the implementation of a functional quantum algorithm (such as PEA) has not yet been realized on any qudit-based platform. In this chapter, we experimentally realize a proof-of-principle qudit-based PEA on a photonic platform by encoding two qutrits in a single photon, where the frequency DoF carries one qutrit as the control register, and the time DoF carries another qutrit as the target register. By working with two DoFs in a photon, the controlled-unitary operation required by the

PEA is realized within a *single* photon, thus circumventing the undesirable, probabilistic photon-photon interaction [59], [60], [63], [64]. Our qutrit-based implementation is tested on diagonal 3×3 unitary matrices. Eigenphases (i.e. phases associated with the eigenvalues) representable by one ternary digit (given by a single control qutrit) are retrieved with 98% fidelity. For arbitrary eigenphases, we fit their respective photon statistics to theoretical distributions, and minimize the mean squared error. The retrieved phases are all within 7.1% error. In the final section, we will discuss the possibility of increasing the dimension and complexity of our future system, and show the exploitation of qudits can provide certain advantage in this Noisy Intermediate-Scale Quantum (NISQ) era.

Chapter 4 presents a statistical approach to quantum phase estimation [65]. Efficient spectral decomposition of large matrices is a key component to many optimization and machine learning algorithms, with applications ranging from factoring and searching algorithms to computational chemistry [9]. On classical computers, spectral decomposition scales super-linearly with the system dimension [66], making it intractable for large problems. Due to the utility of spectral decomposition and its classical limitations, quantum approaches to spectral decomposition and eigenvalue estimation have been pursued [67]. One significant approach is the quantum phase estimation algorithm (PEA) [68] – a means of determining unknown eigenphases of a unitary matrix – which is a key subroutine in a number of quantum algorithms including Shor’s factoring algorithm [69], quantum principal component analysis [70], the generalized Grover’s search algorithm [71], and quantum simulations [10], [72], [73]. Near-term quantum systems operate in the noisy intermediate-scale quantum (NISQ) regime [74], facing restrictions on both circuit depth and breadth due to decoherence and gate infidelity. Consequently, interest in the traditional PEA [68] and quantum principal component analysis [70] has been channeled toward developments in the *iterative* PEA (IPEA) [75] – a method which estimates an unknown phase over multiple circuit iterations – allowing for significant reduction in both qubit usage (circuit breadth) and controlled-gate operations (circuit depth). The IPEA has been demonstrated on photonic systems [48]. On the other hand, variational quantum algorithms (VQA) – which use a classical computer to control and optimize the parameters applied in a quantum circuit – have been developed for a variety of

problems as they leverage the speedup of quantum algorithm with lower-depth circuits [76], [77].

Here, we introduce a quantum-classical hybrid algorithm combining the PEA with the VQA – which we call the *Statistical* PEA (SPEA) – and show preliminary simulation results on the IBM Q platform with the Qiskit package [78] as well as simulations on a local computer. The method is able to determine any unknown eigenstate-eigenphase pair from a unitary matrix by utilizing hardware intended for the IPEA. Further, the SPEA can be applied repeatedly to obtain a full spectral decomposition. The SPEA may be compared to other variational quantum eigensolvers [79]–[81], the primary difference being other variational eigensolvers work directly on a (Hermitian) matrix encoded as a quantum state using specially designed quantum circuits. The SPEA assumes access to a gate representation of the unitary exponentiation of the state – or assumes simultaneous availability of several copies of the quantum state to approximate the quantum gate à la [70]. In return, the SPEA requires a polynomially-reduced number of (classical) optimization parameters – as it optimizes for a single eigenstate, rather than diagonalize the entire matrix simultaneously – and directly delivers eigenstate-eigenphase pairs (whereas other approaches may allow on-demand generation of eigenstates, but require tomography if knowledge of the state is needed). The SPEA is also able to search for eigenphases within specified ranges, allowing those with some prior knowledge of their system to search for particular solutions, whether ground state (near minimum eigenphase), principle (near-maximal eigenphase), or any other region of interest.

1.2 Open quantum dynamics

This section introduce the topic of the second half of the thesis: the simulations of open quantum dynamics that are important applications for quantum computer based on qudit as well as qubit. Simulations of open quantum systems have become essential for studying the dynamics of quantum systems in the condensed phase, allowing for the inclusion of dissipative effects from the environment which are critical for accurate simulations. These powerful computational tools have enabled a wide range of studies, from chemical and

physical processes to excited state lifetimes, spectral diffusion and line-broadening, across multiple fields of research, including physical chemistry, molecular physics, condensed-phase physics, nanoscience, molecular electronics, quantum optics, nonequilibrium statistical mechanics, spectroscopy and quantum information science. [82]–[111] Examples of open quantum system dynamics include energy and charge transfer, dephasing, vibrational relaxation, nonadiabatic dynamics and photochemistry (see Fig. 1.1). By harnessing the power of open quantum system simulations, we can bridge the gap between theory and experiment, providing insight into various complex phenomena in a variety of light-induced physical and chemical processes, including photoinduced processes such as energy and charge transfer, vibronic relaxation, dephasing, and nonadiabatic dynamics. [9], [96], [97], [102], [112]–[129].

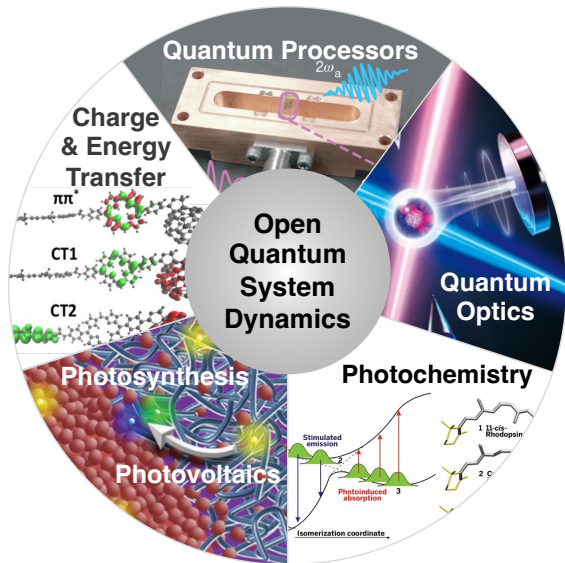


Figure 1.1. The simulation of open quantum system dynamics is central to many science and engineering disciplines (a few examples are showcased in the figure).

Recent advances in quantum computing have enabled the development of numerous algorithms for electronic structure calculations, [77], [81], [130], [131] and simulations of quantum dynamics of closed quantum systems [132]–[135]. However, relatively few studies have explored the simulation of open quantum system dynamics [136]–[142]. These studies have been mostly based on Lindblad-type quantum master equations (QMEs) which ensure complete positivity and conservation of probability but rely on the Markov and Born approximations

in the system-bath weak coupling limit [111]. With the aim of developing a more general approach, here we introduce a quantum algorithm based on the Generalized Quantum Master Equation (GQME), which corresponds to the formally exact equation of motion (EoM) for an open quantum system.

A major challenge facing the quantum simulation of open quantum system dynamics is the fact that the time evolution operators are non-unitary whereas quantum gates are unitary. To this end, we have previously developed a quantum algorithm for open quantum dynamics based on the Sz.-Nagy unitary dilation theorem, which converts non-unitary operators into unitary operators in an extended Hilbert space. This algorithm was originally applied to simulating a Markovian two-level model on IBM quantum computers.[143] Later, the same method was applied to simulating the non-Markovian Jaynes-Cummings model on IBM quantum computers.[144] In a recent work, the same Lindblad-QME-based quantum algorithm was applied to simulate the dynamics of the Fenna-Matthews-Olson complex, which includes five quantum states and seven elementary physical processes.[145] Thus far, this quantum algorithm has been used to simulate the dynamics of open quantum systems described by the operator sum representation or Lindblad-type QMEs.

Chapter 5 provides an examples of open quantum dynamics simulation: the Radical Pair Dynamics of the Avian Compass [142]. This Lindblad-QME-based dynamics is simulated with the quantum algorithm based on the Sz.-Nagy unitary dilation theorem. The radical pair mechanism (RPM) is a theory proposed to explain the magneto-reception and navigation abilities of certain bird species [146]–[148]. Many animals possess extraordinary abilities to sense the direction by perceiving the geomagnetic field. This is probably the result of natural selection over a very long time of evolution, since the ability to sense the direction is crucial for certain animals to find their habitats, such as migratory birds that change habitats from season to season.

In brief, the RPM involves two spatially separated electrons, which are correlated with each other and affected by the external weak magnetic field and internal nuclear spin couplings. The basic scheme of the RPM includes three stages: 1) the photons with certain energies activate a certain type of molecules located in the bird’s eyes, enabling an electron transfer reaction and generating a radical pair in the singlet state; 2) the state of the rad-

ical pair converts between the singlet state and the triplet state under the influence of the external magnetic field (the geomagnetic field) and the internal magnetic field (the hyperfine coupling effects); 3) the radical pairs in different states will generate different chemical products which can induce a detectable signal for birds to recognize the direction [149]. The RPM is a promising hypothesis that can explain the three unusual properties of the avian compass: 1. the inclination compass: the functional mode of the avian magnetic compass is based on the inclination of the field lines instead of their polarity [150]–[153]; 2. the light dependence: light with an energy above a certain threshold is needed for the RPM to work [154]–[160]; 3. the narrow range of responsive magnetic field intensities: both higher and lower magnetic fields will disable birds’ ability of navigation [161]. To understand the RP mechanism, E. M. Gauger *et. al.* proposed a way to model the dynamics of the RPM system with a Lindblad master equation by adding two “shelving states” for the singlet yield and triple yield [162]. In the following, we treat the same Lindblad formulation of the RPM dynamics with our general quantum algorithm for open quantum dynamics and simulate the RPM dynamics on the IBM QASM quantum simulator. To our best knowledge, this is the first ever demonstration of any quantum algorithm applied to simulating the RPM dynamics. This chapter not only shows the generality of the quantum algorithm, but also opens new potential ways to study the avian compass with quantum computing devices.

It is worth noticing that the Lindblad QME used in Ref. [142], [145] relies on several restrictive approximations, including Markovian dynamics, and the ensemble of Lindbladian trajectories method in Ref. [144], while capable of describing non-Markovian dynamics, involves user selection of *ad-hoc* system-bath parameters, therefore limiting the range of applications. Furthermore, while the operator sum representation of open quantum system dynamics is general, it requires knowledge of the Kraus operators, which to the best of our knowledge are only known in closed form for systems whose dynamics can be described by Lindblad-type QMEs. Therefore, in the next chapter, Chapter 6 we would like to Extend the range of quantum simulation of open quantum systems and therefore calls for formulating the dynamics within a less restrictive theoretical framework [163]. The GQME formalism introduced by Nakajima [164] and Zwanzig [165] represents such a general framework since the GQME corresponds to the formally exact EoM of the open quantum system, as opposed

to the Lindblad-type QMEs which correspond to approximate EoMs of the open quantum system. Using the GQME

A comparison of the workflows for simulating the dynamics of a closed quantum system governed by the quantum Liouville equation vs. an open quantum system governed by the GQME is shown in Fig. 1.2. The derivation of the GQME involves projecting out the bath degrees of freedom (DOF) to obtain the EoM of the system’s reduced density matrix, or a subset of its elements. Within this EoM, which is referred to as the GQME, the memory kernel superoperator, $\mathcal{K}(\tau)$, accounts for the main impact of the bath on the system’s dynamics. Thus, the GQME replaces the Liouville equation as the formally exact EoM of the system when we transition from a closed quantum system to an open quantum system, with the memory kernel playing a similar role in the open system to that of the Hamiltonian or Liouvillian in the closed system.

In chapter 6, we develop a GQME-based quantum algorithm for simulating the dynamics of an open quantum system. To this end, we develop a protocol for obtaining the non-unitary time evolution superoperator, or propagator, from the memory kernel. Then the Sz.-Nagy unitary dilation theorem is used to convert the GQME-based non-unitary propagator into a unitary superoperator in an extended Hilbert space. Given this dilated and now unitary time evolution superoperator and the initial state of the system, we can evolve the dynamics for any open quantum system on quantum computers.

Given the fact that the GQME is the exact EoM of the open quantum system, this quantum algorithm greatly extends the range of possible systems that can be simulated on a quantum computer, including complex non-Markovian photosynthetic and photovoltaic systems[102], [166], molecular electronics[122], linear and nonlinear spectroscopy[167], systems with inter-system crossing[168], and conical intersections[169]. Thus, this GQME-based quantum algorithm provides an essentially universal protocol for simulating open quantum system dynamics on quantum computing platforms. Given a powerful enough quantum computer, this algorithm opens the door for simulating open quantum system dynamics of large and complex molecular systems, which are currently beyond the reach of classical computers.

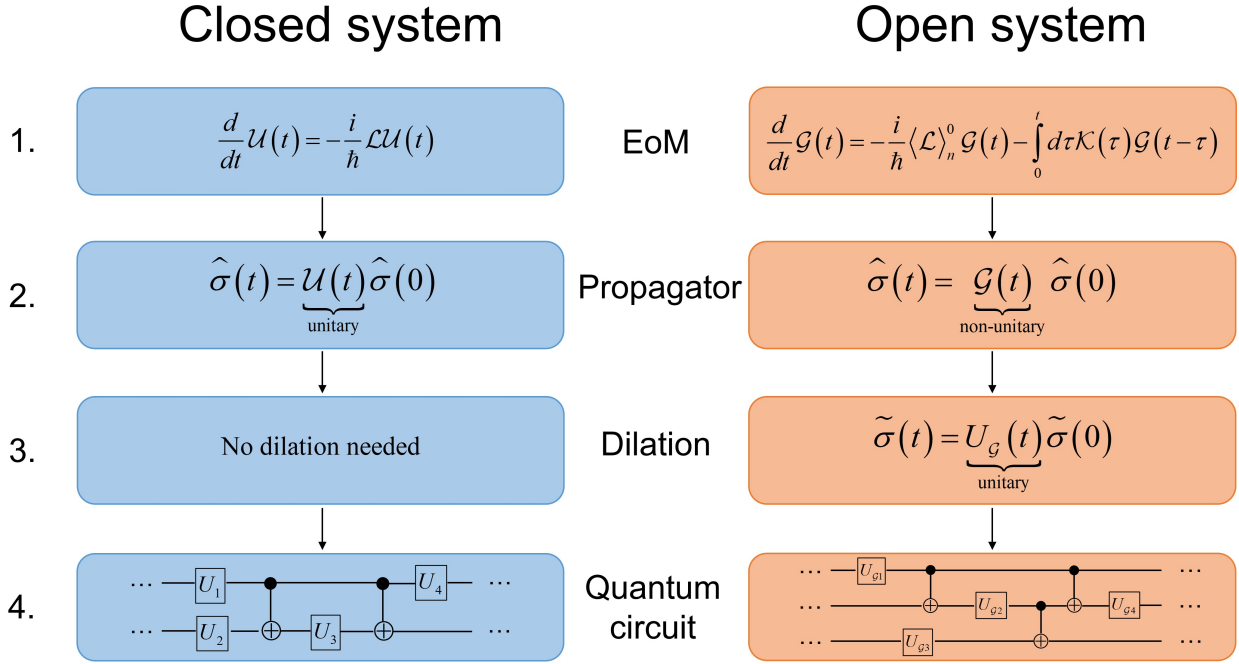


Figure 1.2. A comparison of the workflows for simulating the dynamics of a closed quantum system governed by the quantum Liouville equation vs. an open quantum system governed by the GQME. 1. The EoM is established; 2. the time evolution superoperator is generated from the EoM; 3. A unitary dilation is required in order to convert the GQME-based non-unitary time evolution superoperator into a unitary superoperator in an extended Hilbert space; 4. Translation of the unitary matrix into a quantum gate sequence.

2. QUDITS AND HIGH-DIMENSIONAL QUANTUM COMPUTING

The contents of this chapter are based on and modified from the article [29] Wang, Yuchen, Hu, Z., Sanders, B. C., & Kais, S. (2020). Qudits and high-dimensional quantum computing. Frontiers in Physics, 8, 479., Copyright (2020) by Wang, Hu, Sanders and Kais. This is an open-access article distributed under the terms of the Creative Commons Attribution License (CC BY). Published by Frontiers Media S.A.

This chapter gives a review of the Qudits and high-dimensional quantum computing and it is organized as follows. Definitions and properties of a qudit and related qudit gates are given in §2.1. The generalization of the universal gate set to qudit systems and several proposed sets are provided in §2.1.1. Then §2.1.2 lists various examples of qudit gates and discusses the difference and possible improvement of these gates over their qubit counterparts. A discussion of the gate efficiency of synthesizing an arbitrary unitary U using geometric method is given in §2.1.3. The next section, §2.2, provides an introduction to qudit algorithms: a single-qudit algorithm that finds the parity of a permutation in §2.2.1, the Deutsch-Josza algorithm in §2.2.1, the Bernstein-Vazirani algorithm in §2.2.1, the quantum Fourier transform in §2.2.2, the PEA in §2.2.2 and the quantum search algorithm in §2.2.3. §2.3 is a section focused on the qudit quantum computing models other than the circuit model, which includes the measurement-based model in §2.3.1, the adiabatic quantum computing in §2.3.2 and the topological quantum computing in §2.3.3. In §2.4, we provide various realizations of the qudit algorithms on physical platforms and discuss their applications. We discuss possible improvements in computational speed-up, resource saving and implementations on physical platforms. A qudit with a larger state space than a qubit can utilize the full potential of physical systems such as photon in §2.4.1, ion trap in §2.4.2, nuclear magnetic resonance in §2.4.3 and molecular magnet in §2.4.4. Finally, we give a summary of the qudit systems advantages and provide our perspective for the future developments and applications of the qudit in §2.5.

2.1 Quantum gates for qudits

A *qudit* is a quantum version of d -ary digits whose state can be described by a vector in the d dimensional Hilbert space \mathcal{H}_d [12]. The space is spanned by a set of orthonormal basis vectors $\{|0\rangle, |1\rangle, |2\rangle, \dots, |d-1\rangle\}$. The state of a qudit has the general form

$$|\alpha\rangle = \alpha_0 |0\rangle + \alpha_1 |1\rangle + \alpha_2 |2\rangle + \dots + \alpha_{d-1} |d-1\rangle = \begin{pmatrix} \alpha_0 \\ \alpha_1 \\ \alpha_2 \\ \vdots \\ \alpha_{d-1} \end{pmatrix} \in \mathbb{C}^d \quad (2.1)$$

where $|\alpha_0|^2 + |\alpha_1|^2 + |\alpha_2|^2 + \dots + |\alpha_{d-1}|^2 = 1$. Qudit can replace qubit as the basic computational element for quantum algorithms. The state of a qudit is transformed by qudit gates.

This section gives a review of various qudit gates and their applications. §2.1.1 provides criteria for the qudit universality and introduces several fundamental qudit gate sets. §2.1.2 presents examples of qudit gates and illustrates their advantages compared to qubit gates. In the last section, §2.1.3, a quantitative discussion of the circuit efficiency is included to give a boundary of the number of elementary gates needed for decomposing an arbitrary unitary matrix.

2.1.1 Criteria for universal qudit gates

This subsection describes the universal gates for qudit-based quantum computing and information processing. We elaborate on the criteria for universality in §2.1.1 and give examples in §2.1.1.

Universality

In quantum simulation and computation, a set of matrices $U_k \in U(d^n)$ is called the universal quantum gate set if the product of its elements can be used to approximate any

arbitrary unitary transformation U of the Hilbert space $\mathcal{H}_d^{\otimes n}$ with acceptable error measured in some appropriate norm [170]. This idea of *universality* not only applies to the qubit systems [171], but can also be extended to the qudit logic [31], [172]–[176]. Several discussions of standards and proposals for a universal qudit gate set exist. Vlasov shows that the combination of two noncommuting single qudit gates and a two-qudit gate are enough to simulate any unitary $U \in U(d^n)$ with arbitrary precision [170]. Qudit gates can themselves be reduced to, and thus simulated by, sequences of lower-dimensional qudit gates [177], [178] Brylinski and Brylinski prove a set of sufficient and necessary conditions for exact qudit universality which needs some random single qudit gates complemented by one two-qudit gate that has entangled qudits [12]. Exact universality implies that any unitary gate and any quantum process can be simulated with zero error. Neither of these methods is constructive and includes a method for physical implementation. A physically workable procedure is given by Muthukrishnan and Stroud using single- and two-qudit gates to decompose an arbitrary unitary gate that operates on N qudits [179]. They use the spectral decomposition of unitary transformations and involve a gate library with a group of continuous parameter gates. Brennen et al. identify criteria for exact quantum computation in qudit that relies on the QR decomposition of unitary transformations [180]. They generate a library of gates with a fixed set of single qudit operations and "one controlled phase" gate with single parameter as the components of the universal set. Implementing the concept of a coupling graph, they proved that by connecting the nodes (equivalently logical basis states) they can show the possibility of universal computation.

Examples of universal gate sets

An explicit and physically realizable universal set comprising one-qudit general rotation gates and two-qudit controlled extensions of rotation gates is explained in this section [14].

We first define

$$U_d(\boldsymbol{\alpha}) : \sum_{l=0}^{d-1} \alpha_l |l\rangle \mapsto |d-1\rangle, \quad \boldsymbol{\alpha} := (\alpha_0, \alpha_1, \dots, \alpha_{d-1}). \quad (2.2)$$

as a transformation in the d -dimensional space that maps any given qudit state to $|d-1\rangle$. Complex parameters of U_d may not be unique and have been addressed with probabilistic quantum

search algorithm [179]. Here in this scheme, U_d can be deterministically decomposed into $d - 1$ unitary transformations such that

$$U_d = X_d^{(d-1)}(a_{d-1}, b_{d-1}) \cdots X_d^{(1)}(a_1, b_1), \quad a_l := \alpha_l, \quad b_l := \sqrt{\sum_{i=0}^{l-1} \alpha_i^2} \quad (2.3)$$

with

$$X_d^{(l)}(x, y) = \begin{pmatrix} \mathbb{1}_{l-1} & & & \\ & \frac{x}{\sqrt{|x|^2+|y|^2}} & \frac{-y}{\sqrt{|x|^2+|y|^2}} & \\ & \frac{y^*}{\sqrt{|x|^2+|y|^2}} & \frac{x^*}{\sqrt{|x|^2+|y|^2}} & \\ & & & \mathbb{1}_{d-l-1} \end{pmatrix}. \quad (2.4)$$

The d -dimensional phase gate is

$$Z_d(\theta) := \sum_{l=0}^{d-1} e^{i(1-\text{sgn}(d-1-l))\theta} |l\rangle \langle l|, \quad (2.5)$$

which changes $|d - 1\rangle$ by a phase θ and ignores the other states, and sgn represents the sign function.

Each primitive gate (such as $X_d^{(l)}$ or Z_d) has two free complex parameters to be controlled (x, y in the $X_d^{(l)}$ gate and θ in the Z_d gate). Let R_d represents either $X_d^{(l)}$ or Z_d , then the controlled-qudit gate is

$$C_2[R_d] := \begin{pmatrix} \mathbb{1}_{d^2-d} & \\ & R_d \end{pmatrix}, \quad (2.6)$$

which is a $d^2 \times d^2$ matrix that acts on two qudits. R_d acts on d substates $|d - 1\rangle |0\rangle, \dots, |d - 1\rangle |d - 1\rangle$, and the identity operation $\mathbb{1}_{d^2-d}$ acts on the remaining substates.

Now we work on an $N = d^n$ dimensional unitary gate $U \in SU(d^n)$ operating on the n -qudit state. The sufficiency of the gates $X_d^{(l)}$, Z_d and $C_2[R_d]$ to construct an arbitrary unitary transformation of $SU(d^n)$ is proved in three steps. The first step is the eigen-decomposition

of U . By the representation theory, the unitary matrix U with N eigenvalues $\{\lambda_s\}$ and eigenstates $|E_s\rangle$ can be rewritten as

$$U = \sum_{j=1}^N e^{i\lambda_j} |E_j\rangle \langle E_j| = \prod_{j=1}^N \Upsilon_j \quad (2.7)$$

with eigenoperators

$$\Upsilon_j = \sum_{s=1}^N e^{i(1-|\text{sgn}(j-s)|)\lambda_s} |E_s\rangle \langle E_s|. \quad (2.8)$$

Then the eigenoperators can be synthesized with two basic transformations as [179]

$$\Upsilon_j = U_{j,N}^{-1} Z_{j,N} U_{j,N}. \quad (2.9)$$

Here $U_{j,N}$ and $Z_{j,N}$ are the N -dimensional analogues of U_d and Z_d such that $U_{j,N}$ is applied to the j th eigenstate to produce $|N-1\rangle$ and $Z_{j,N}$ modifies the phase of $|N-1\rangle$ by the j th eigenphase λ_j , while ignoring all the other computation states. According to Eq. (2.3), $U_{j,N}$ can be decomposed with primitive gates $X_{j,N}^{(l)}(x, y)$. Thus, $X_{j,N}(x, y)$ and $Z_{j,N}$ are sufficient to decompose U .

The second step is decomposing $U_{j,N}$ and $Z_{j,N}$. In other words, $U_{j,N}$ and $Z_{j,N}$ need to be decomposed in terms of multi-qudit-controlled gates. For convenience denote $C_m[R_d]$ as

$$C_m[R_d] = \begin{pmatrix} \mathbb{1}_{d^{m-d}} & \\ & R_d \end{pmatrix}, \quad (2.10)$$

which acts on the d^m -dimensional computational basis of m -qudit space. It is proved in the appendix of Ref. [14] that each $U_{j,N}$ can be decomposed into some combinations of $C_m[R_d]$ and $C_m[P_d(p, q)]$ where $P_d(p, q)$ is the permutation of $|p\rangle$ and $|q\rangle$ state. The third step is using the two-qudit gates $C_2[R_d]$ and $C_2[P_d(p, q)]$ to complete the decomposition of $C_m[R_d]$. Fig. 2.1 shows a possible decomposition for $d > 2$. There are $r = \lceil (m-2)/(d-2) \rceil$ auxiliary qudits in the circuits ($\lceil x \rceil$ denotes the smallest integer greater than x). The last box contains

$R_d = Z_d$ or $X_d^{(l)}$. $C_m[R_d]$ is implemented with these gates combined. All of the three steps together prove that the qudit gates set

$$\Gamma_d := \{X_d^{(l)}, Z_d, C_2[R_d]\} \quad (2.11)$$

is universal for the quantum computation using qudit systems.

One advantage of the qudit model (compared to the qubit model) is a reduction of the number of qudits required to span the state space. To explain this, we need at least $n_1 = \log_2 N$ qubits to represent an N -dimensional system in qubits while in qudits we need $n_2 = \log_d N$ qudits. The qudit system has a reduction factor $k = n_1/n_2 = \log_2 d$. According to Muthukrishnan and Stroud's method in Ref. [179] a binary equivalent of their construction requires a number of qubit gates in the scale of $O(n_1^2 N^2)$. By analogy, the scale of the required qudit gates using the same construction is $O(n_2^2 N^2)$. So the qudit method has a $(\log_2 d)^2$ scaling advantage over the qubit case. Furthermore, in this reviewed method, for an arbitrary unitary $U \in SU(N)$, from eq. (2.7) and (2.8) N eigenoperators is needed and each can be decomposed with three rotations shown in eq. (2.9). Deriving from the appendix of Ref. [14], $U_{j,N}$ can be decomposed with less than $3d^{n-1}$ multiple controlled operations. Finally, as Fig. 2.1 has shown, $C_m[R_d]$ needs m number of $C_2[R_d]$ and $C_2[P_d(p, q)]$. U_d can be composed with $d - 1$ numbers of $X_d^{(l)}$ as in eq.(2.3). Therefore the total number of primitive operations L in this decomposition method is

$$L \leq 2N \times 3d^{n-1} \times n \times (d - 1) + N \times n \leq 6nd^{2n} + nd^n. \quad (2.12)$$

It is clear that there is an extra factor of n reduction in the gate requirement as the number scale of this method is $O(nN^2)$. The other advantage is these primitive qudit gates can be easily implemented with fewer free parameters [14].

For qudit quantum computing, depending on the implementation platform, other universal quantum gate sets can be considered. For example, in a recent proposal for topological quantum computing with metaplectic anyons, Cui and Wang prove a universal gates set for qutrit and *qupit* systems, for a qupit being a qudit with p dimensions and p is an prime num-

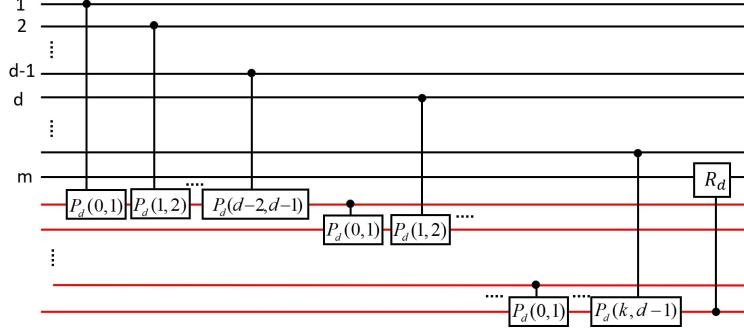


Figure 2.1. The schematic circuit of $C_m[R_d]$ with $C_2[R_d]$ and $C_2[P_d(p, q)]$. The horizontal lines represent qudits. The auxiliary qudits initialized to $|0\rangle$ is denoted by the red lines and the black lines denoting m controlling qudits. The two-qudit controlled gates is shown as the verticle lines. $P_d(p, q)$ is the permutation of $|p\rangle$ and $|q\rangle$ state, and R_d is either $X_d^{(l)}$ or Z_d .

ber larger than 3 [19]. The proposed universal set is a qudit analogy of the qubit universal set and it consists several generalized qudit gates from the universal qubit set.

The generalized Hadamard gate for qudits H_d is

$$H_d |j\rangle = \frac{1}{\sqrt{d}} \sum_{i=0}^{d-1} \omega^{ij} |i\rangle, j \in \{0, 1, 2, \dots, d-1\}, \quad (2.13)$$

where

$$\omega := e^{2\pi i/d}. \quad (2.14)$$

The SUM_d gate serves as a natural generalization of the CNOT gate

$$\text{SUM}_d |i, j\rangle = |i, i + j(\text{mod } d)\rangle, i, j \in \{0, 1, 2, \dots, d-1\}. \quad (2.15)$$

The Pauli σ_z , with the $\pi/8$ gate as its 4th root, can be generalized to $Q[i]$ gates for qudits,

$$Q[i]_d |j\rangle = \omega^{\delta_{ij}} |j\rangle, \quad (2.16)$$

with ω defined by Eq. (2.14) and the related $P[i]$ gates are

$$P[i]_d |j\rangle = (-\omega^2)^{\delta_{ij}} |j\rangle, \quad i, j \in \{0, 1, 2, \dots, d-1\}. \quad (2.17)$$

In general $Q[i]_p$ is always a power of $P[i]_p$ if p is an odd prime.

The proposed gate set for the qutrit system is the sum gate SUM_3 , the Hadamard gate H_3 and any gate from the set $\{P[0]_3, P[1]_3, P[2]_3\}$. As an analogue of the standard universal set for qubit $\{\text{CNOT}, H, T = \pi/8\text{-gate}\}$, the qutrit set generate the qutrit Clifford group whereas the qubit set generate the qubit Clifford group (the definition of the Clifford group can be found in §2.1.2). Whereas the rigorous proof can be found in Ref. [19], the proving process follows the idea introduced in Ref. [12] that the gate SUM_3 is imprimitive, and the Hadamard H_3 and any gate from $\{P[0]_3, P[1]_3, P[2]_3\}$ generates a dense subgroup of $SU(3)$. Similarly, the proposed gate set for the qupit system is the sum gate SUM_p , the Hadamard gate H_p and the gates $Q[i]_p$ for $i \in [p-1]$. The proof is analogous to that of the qutrit set. The Hadamard H_p and the $Q[i]$ gates are combined to form a dense subgroup of $SU(p)$ and SUM_p is shown to be imprimitive. Implementing Theorem 1.3 in Ref. [12], the set is a universal gate set. These universal gate sets for the qudit systems, with fewer numbers of gates in each set compare to that in the previous examples, have the potential to perform qudit quantum algorithms on the topological quantum computer.

2.1.2 Examples of qudit gates

In this section we introduce the qudit versions of many important quantum gates and discuss some of the gates' advantages compared to their qubit counterparts. The gates discussed are the qudit versions of the $\pi/8$ gate in §2.1.2, the SWAP gate in §2.1.2 and the multi-level controlled gate in §2.1.2. in §2.1.2, we also introduce how to simplify the qubit Toffoli gate by replacing one of the qubit to qudit. This gives ideas about improving the qubit circuits and gates by introducing qudits to the system.

Qudit versions $\pi/8$ gate

The qubit $\pi/8$ gate T has an important role in quantum computing and information processing. This gate has a wide range of applications because it is closely related to the Clifford group but does not belong to the group. From the Gottesman-Knill theorem [181] it is shown that the Clifford gates and Pauli measurements only do not guarantee universal quantum computation(UQC). The $\pi/8$ gate, which is non-Clifford and from the third level of the Clifford hierarchy, is the essential gate to obtaining UQC [182]. This gate can be generalized to a d dimensional qudit system, where, throughout the process, d is assumed to be a prime number greater than 2 [30].

To define the Clifford group for a d -dimensional qudit space, we first define the Pauli Z gate and Pauli X gate. The Pauli Z gate and Pauli X gate are generalized to d dimension in the matrix forms [23], [183]–[185]

$$X_d = \begin{pmatrix} 0 & 0 & \cdots & 0 & 1 \\ 1 & 0 & \cdots & 0 & 0 \\ 0 & 1 & \cdots & 0 & 0 \\ \vdots & \vdots & \ddots & \vdots & \vdots \\ 0 & 0 & \cdots & 1 & 0 \end{pmatrix}, Z_d = \begin{pmatrix} 1 & 0 & 0 & \cdots & 0 \\ 0 & \omega & 0 & \cdots & 0 \\ 0 & 0 & \omega^2 & \cdots & 0 \\ \vdots & \vdots & \vdots & \ddots & 0 \\ 0 & 0 & 0 & \cdots & \omega^{d-1} \end{pmatrix} \quad (2.18)$$

for ω the d^{th} root of unity (2.14). The function of the Z gate is adding different phase factors to each basis states and that of the X gate is shifting the basis state to the next following state. Using basis states the two gates are

$$Z_d |j\rangle := \omega^j |j\rangle \quad X_d |j\rangle := |j+1\rangle, \quad j \in \{0, 1, 2, \dots, d-1\}. \quad (2.19)$$

In general, we define the displacement operators as products of the Pauli operators,

$$D_{(x|z)} = \tau^{xz} X_d^x Z_d^z, \quad \tau := e^{(d+1)\pi i/d}, \quad (2.20)$$

where $(x|z)$ correspond to the x and y in the exponent of τ , X and Z . This leads to the definition of the Weyl-Heisenberg group (or the generalized Pauli group) for a single qudit as [23], [183]–[185]

$$\mathcal{G} = \{\tau^c D_{\vec{\chi}} | \vec{\chi} \in \mathbb{Z}_d^2, c \in \mathbb{Z}_d\} \quad (\mathbb{Z}_d = \{0, 1, \dots, d-1\}), \quad (2.21)$$

where $\vec{\chi}$ is a two-vector with elements from \mathbb{Z}_d . With these preliminary concepts defined in Eqs. (2.18) through (2.21), we now define the Clifford group as the following: the set of the operators that maps the Weyl-Heisenberg group onto itself under conjugation is called the *Clifford group* [185], [186],

$$\mathcal{C} = \{C \in U(d) | C\mathcal{G}C^\dagger = \mathcal{G}\}. \quad (2.22)$$

A recursively defined set of gates, the so-called Clifford hierarchy, was introduced by Gottesman and Chuang as

$$\mathcal{C}_{k+1} = \{U | UC_1U^\dagger \subseteq \mathcal{C}_k\}, \quad (2.23)$$

for \mathcal{C}_1 the Pauli group [187]. The sets $\mathcal{C}_{k \geq 3}$ do not form groups, although the diagonal subsets of \mathcal{C}_3 , which is our focus here, do form a group.

The following derivations follow those in Ref. [30]. The explicit formula for building a Clifford unitary gate with

$$F = \begin{pmatrix} \alpha & \beta \\ \gamma & \delta \end{pmatrix} \in \text{SL}(2, \mathbb{Z}_d), \quad \vec{\chi} = \begin{pmatrix} x \\ z \end{pmatrix} \in \mathbb{Z}_d^2 \quad (2.24)$$

is

$$C_{(F|\vec{\chi})} = D_{(x|z)} V_F, \quad (2.25)$$

$$V_F = \begin{cases} \frac{1}{\sqrt{d}} \sum_{j,k=0}^{d-1} \tau^{\beta^{-1}(\alpha k^2 - 2jk + \delta j^2)} |j\rangle \langle k|, & \beta \neq 0 \\ \sum_{k=0}^{d-1} \tau^{\alpha \gamma k^2} |\alpha k\rangle \langle k|, & \beta = 0. \end{cases} \quad (2.26)$$

The special case $\beta = 0$ is particularly relevant to the later derivation, and

$$\begin{aligned} \det \left(\sum_{k=0}^{d-1} \tau^{\alpha\gamma k^2} |k\rangle \langle k| \right) &= \tau^{\frac{\alpha\gamma}{6}(2d-1)(d-1)d}, \\ &= \begin{cases} \tau^{2\alpha\gamma}, & d = 3, \\ 1, & \forall d > 3, \end{cases} \end{aligned} \quad (2.27)$$

can be shown. In the $d = 3$ case, we use

$$C \left(\left(\begin{bmatrix} 1 & 0 \\ \gamma & 1 \end{bmatrix} \middle| \begin{bmatrix} x \\ z \end{bmatrix} \right) \right) \in SU(p) \quad \forall p > 3 \quad (2.28)$$

and

$$\det \left(C \left(\left(\begin{bmatrix} 1 & 0 \\ \gamma & 1 \end{bmatrix} \middle| \begin{bmatrix} x \\ z \end{bmatrix} \right) \right) \right) = \tau^{2\gamma} \quad \text{for } p = 3. \quad (2.29)$$

With all the mathematical definitions at hand, we are ready to give an explicit form of the qudit $\pi/8$ gate. We choose the qudit gate U_v to be diagonal in the computational basis and claim that, for $d > 3$, U_v has the form

$$U_v = U(v_0, v_1, \dots) = \sum_{k=0}^{d-1} \omega^{v_k} |k\rangle \langle k| \quad (v_k \in \mathbb{Z}_d). \quad (2.30)$$

A straightforward application of Eqs. (2.20) and (2.30) yields

$$U_v D_{(x|z)} U_v^\dagger = D_{(x|z)} \sum_k \omega^{v_{k+1} - v_k} |k\rangle \langle k|. \quad (2.31)$$

As U_v is to be a member of \mathcal{C}_3 , the right hand side of Eq. (2.31) must be a Clifford gate. We ignore the trivial case $U_v D_{(0|z)} U_v^\dagger = D_{(0|z)}$ and focus on the case $U_v D_{(1|0)} U_v^\dagger$ in order to derive an explicit expression for U_v .

We define $\gamma, z, \epsilon \in \mathbb{Z}_d$ such that

$$U_v D_{(1|0)} U_v^\dagger = \omega^\epsilon C \left(\left[\begin{array}{cc} 1 & 0 \\ \gamma & 1 \end{array} \right] \middle| \left[\begin{array}{c} 1 \\ z \end{array} \right] \right) \quad (2.32)$$

From Eqs. (2.26) and (2.31) we see that the right-hand side of Eq. (2.32) is the most general form, and we note that $U \in SU(d)$ implies $\omega^\gamma U \in SU(d)$. We rewrite the left-hand side of Eq. (2.32) using Eq. (2.31) and right-hand side using Eq. (2.26) and obtain

$$D_{(1|0)} \sum_k \omega^{v_{k+1}-v_k} |k\rangle \langle k| = \omega^\epsilon D_{(1|z)} \sum_{k=0}^{d-1} \tau^{\gamma k^2} |k\rangle \langle k|. \quad (2.33)$$

After cancelling common factors of $D_{(1|0)}$, an identity between two diagonal matrices remains such that

$$\omega^{v_{k+1}-v_k} = \omega^\epsilon \tau^z \omega^{kz} \tau^{\gamma k^2} \quad (\forall k \in \mathbb{Z}_d), \quad (2.34)$$

or, equivalently, using Eq. (2.20),

$$v_{k+1} - v_k = \epsilon + 2^{-1}z + kz + 2^{-1}\gamma k^2. \quad (2.35)$$

From here, we derive the recursive relation

$$v_{k+1} = v_k + k(2^{-1}\gamma k + z) + 2^{-1}z + \epsilon. \quad (2.36)$$

We solve for the v_k with a boundary condition $v_0 = 0$,

$$v_k = \frac{1}{12}k\{\gamma + k[6z + (2k - 3)\gamma]\} + k\epsilon, \quad (2.37)$$

where all factors are evaluated modulo d . For example, with $d = 5$, the fifth root of unity (2.14) is $\omega = e^{2\pi i/5}$ and choosing $z = 1, \gamma = 4$ and $\epsilon = 0$, we obtain

$$v = (v_0, v_1, v_2, v_3, v_4) = (0, 3, 4, 2, 1) \quad (2.38)$$

so that

$$U_v = \begin{pmatrix} \omega^0 & 0 & 0 & 0 & 0 \\ 0 & \omega^{-2} & 0 & 0 & 0 \\ 0 & 0 & \omega^{-1} & 0 & 0 \\ 0 & 0 & 0 & \omega^2 & 0 \\ 0 & 0 & 0 & 0 & \omega^1 \end{pmatrix} \quad (2.39)$$

The diagonal elements of U_v are powers of ω that sum to zero modulo d and, consequently, $\det(U_v) = 1$.

For the $d = 3$ case, because of Eq. (2.27) extra work is needed for solving a matrix equation similar to Eq. (2.32). We first introduce a global phase factor $e^{i\phi}$ such that

$$\det \left(e^{i\phi} \sum_{k=0}^{d-1} \tau^{\gamma k^2} |k\rangle \langle k| \right) = 1 \implies \phi = 4\pi\gamma/9. \quad (2.40)$$

The ninth root of unity (2.14) is $\omega = e^{2\pi i/9}$ and, from Eq. (2.29) we derive that

$$\det \left(\omega^{2\gamma C} \left(\left[\begin{array}{c|c} 1 & 0 \\ \gamma & 1 \end{array} \right] \left[\begin{array}{c} 1 \\ z \end{array} \right] \right) \right) = 1. \quad (2.41)$$

The qutrit version of $U_{\pi/8}$ has a more general form than in Eq. (2.30); i.e.

$$U_v = U(v_0, v_1, \dots) = \sum_{k=0}^2 \omega^{v_k} |k\rangle \langle k|, \quad v_k \in \mathbb{Z}_9. \quad (2.42)$$

Then the general solution is

$$v = (0, 6z + 2\gamma + 3\epsilon, 6z + \gamma + 6\epsilon) \pmod{9}. \quad (2.43)$$

For example, choosing $z = 1, \gamma = 2$ and $\epsilon = 0$,

$$U_v = \begin{pmatrix} \omega^0 & 0 & 0 \\ 0 & \omega^1 & 0 \\ 0 & 0 & \omega^{-1} \end{pmatrix}. \quad (2.44)$$

The $\pi/8$ gate, with its close relation to the Clifford group, has many applications and utilities in teleportation-based UQC [187], transversal implementation [188], [189], learning an unknown gate [190], or securing assisted quantum computation [191]. The generalized qudit version of the $\pi/8$ gate, U_v , is shown to be identical to the maximally robust qudit gates for qudit fault-tolerant UQC discussed in reference [192].

This gate also plays an important role in the magic-state distillation (MSD) protocols for general qudit systems, which was first established for qutrits [193] and then extended to all prime-dimensional qudits [194].

Qudit SWAP gate

A SWAP gate is used to exchange the states of two qudit such that:

$$\text{SWAP}|\phi\rangle|\psi\rangle = |\psi\rangle|\phi\rangle \quad (2.45)$$

Various methods to achieve the SWAP gate use different variants of qudit controlled gates [195]–[201] as shown in Fig.2.2. The most used component of the SWAP gate is a controlled-shift gate CX_d that perform the following operation:

$$CX_d|x\rangle|y\rangle = |x\rangle|x+y\rangle \quad (2.46)$$

with a modulo d addition. Its inverse operation is

$$CX_d^\dagger|x\rangle|y\rangle = |x\rangle|y-x\rangle \quad (2.47)$$

In some approaches, the operation K_d is required to complete the circuits, where

$$K_d |x\rangle = |d - x\rangle = |-x\rangle, \quad (2.48)$$

which outputs the modulo d complement of the input. These circuits are more complex and less intuitive than the qubit SWAP gate [198] because they are not Hermitian, i.e., $CX_d \neq CX_d^\dagger$.

One way to create a Hermitian version of the qudit CNOT uses the GXOR gate

$$GXOR |x\rangle |y\rangle = |x\rangle |x - y\rangle. \quad (2.49)$$

However, this SWAP gate needs to be corrected with an K_d [201] as shown in Fig. 2.3. A partial SWAP gate S_p [31] works on a hybrid system where $|i\rangle$ is a qudit of dimension d_c and $|j\rangle$ is a qudit of dimension d_t

$$S_p |i\rangle \otimes |j\rangle = \begin{cases} |j\rangle \otimes |i\rangle & \text{for } i, j \in \mathbb{Z}_{d_p} \\ |i\rangle \otimes |j\rangle & \text{otherwise} \end{cases} \quad (2.50)$$

where $d_p \leq d_{\min} = \min(d_c, d_t)$

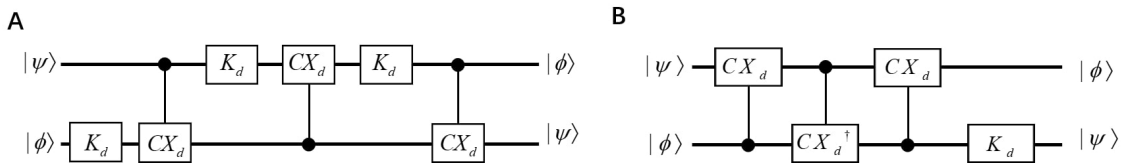


Figure 2.2. (A) is the qudit SWAP circuit using CX_d and K_d gates [198], [199]. (B) is the qudit SWAP circuits with the CX_d , the CX_d^\dagger and the K_d gates

In the rest of this section, we present a Hermitian generalization of the qudit CNOT gate with a symmetry configuration and a qudit SWAP circuit with a single type of qudit gate as shown in Fig. 2.4 A [32]. Compared with all the previously proposed SWAP gate for qudit,

this method is easier to implement since there is only one type of gate $C\tilde{X}$ needed. To begin with, we define a gate $C\tilde{X}$ acting on d -level qudits $|x\rangle$ and $|y\rangle$ such that

$$C\tilde{X} |x\rangle |y\rangle = |x\rangle |-x - y\rangle, \quad (2.51)$$

where $|-x - y\rangle$ represents a state $|i = -x - y\rangle$ in the range $i \in \{0, \dots, d-1\} \bmod d$. Notice that, for $d = 2$, the $C\tilde{X}$ gate is equivalent to the CNOT gate. The SWAP gate for qudit can be built using three $C\tilde{X}$ gates.

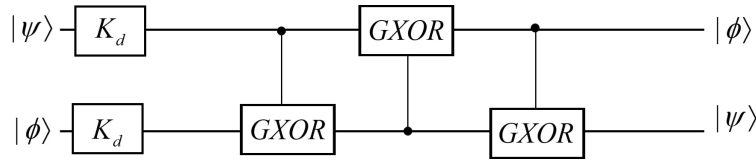


Figure 2.3. Qudit SWAP circuits with the $GXOR$ and the K_d gates [200], [201].

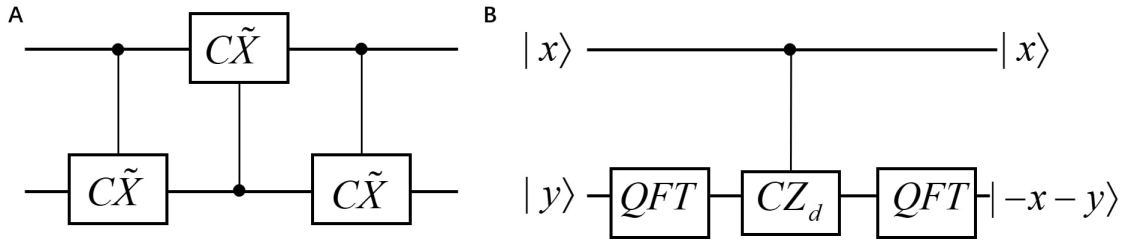


Figure 2.4. (A) is the qudit SWAP gate with the $C\tilde{X}$ gate. (B) is the decomposing $C\tilde{X}$ gate. The QFT represents the quantum Fourier transform while CZ_d is the selective phase shift gate.

$C\tilde{X}$ is generated with three steps: a qudit generalization of the CZ gate as CZ_d sandwiched by two quantum Fourier transform operations (QFT). The circuit illustration for the sequence of these gates is shown in Fig. 2.4 B. The QFT transforms the $|x\rangle$ into a uniform superposition

$$QFT |x\rangle = \frac{1}{\sqrt{d}} \sum_{k=0}^{d-1} e^{i2\pi xk/d} |k\rangle. \quad (2.52)$$

The CZ_d gate adds a phase to the target qudit depending on the state of the control qudit. Its effect on the input qudits is

$$CZ_d |x\rangle |y\rangle = e^{i2\pi xy/d} |x\rangle |y\rangle. \quad (2.53)$$

The inverse QFT undoes the Fourier transform process and the inverse of CZ_d is

$$CZ_d^\dagger |x\rangle |y\rangle = e^{-i2\pi xy/d} |x\rangle |y\rangle. \quad (2.54)$$

The full evolution of the $C\tilde{X}$ is

$$|x\rangle |y\rangle \xrightarrow{QFT_2} \frac{1}{\sqrt{d}} \sum_{k=0}^{d-1} e^{i\frac{2\pi ky}{d}} |x\rangle |k\rangle \quad (2.55)$$

$$\xrightarrow{CZ_d} \frac{1}{\sqrt{d}} \sum_{k=0}^{d-1} e^{i\frac{2\pi ky}{d}} e^{i\frac{2\pi xk}{d}} |x\rangle |k\rangle = \frac{1}{\sqrt{d}} \sum_{k=0}^{d-1} e^{i\frac{2\pi k(x+y)}{d}} |x\rangle |k\rangle \quad (2.56)$$

$$\xrightarrow{QFT_2} \frac{1}{d} \sum_{l=0}^{d-1} \sum_{k=0}^{d-1} e^{i\frac{2\pi k(x+y)}{d}} e^{i\frac{2\pi kl}{d}} |x\rangle |l\rangle = |x\rangle |-x-y\rangle. \quad (2.57)$$

It is easy to show that $C\tilde{X}$ is its own inverse and then $C\tilde{X} = C\tilde{X}^\dagger$. For the proposed SWAP gate, both the QFT and CZ_d operations are realizable on a multilevel quantum systems. For example, there are implementations of them for multilevel atoms [179], [202]. The resulting SWAP gate provides a way to connect systems limited to the nearest-neighbour interactions. This gate provides a useful tool in the design and analysis of complex qudit circuits.

Simplified qubit Toffoli gate with a qudit

The Toffoli gate is well known for its application to universal reversible classical computation. In the field of quantum computing, the Toffoli gate plays a central role in quantum error correction [203], fault tolerance [204] and offers a simple universal quantum gate set combined with one qubit Hadamard gates [205]. The simplest known qubit Toffoli gate, shown in Fig. 2.5, requires at least 5 two-qubit gates [206]. However, if the target qubit has a third level, i.e., a qutrit, the whole circuit can be achieved with three two-qubit gates [33].

A new qutrit gate X_a is introduced to the circuit that does the following: $X_a |0\rangle = |2\rangle$ and $X_a |2\rangle = |0\rangle$ with $X_a |1\rangle = |1\rangle$. The simplified circuit is shown in Fig. 2.6. The two controlled gates are the CNOT gate and a control- Z gate, which is achieved with a CNOT gate between two Hadamard gates. The Hadamard gate here operating on the qutrit is generalized from the normal Hadamard gate operating on a qubit—it only works with the $|0\rangle$ and $|1\rangle$, such that $H |0\rangle = 1/\sqrt{2}[|0\rangle+|1\rangle]$, $H |1\rangle = 1/\sqrt{2}[|0\rangle - |1\rangle]$ and $H |2\rangle = |2\rangle$. Comparing the circuit in Fig. 2.6 to that in Fig. 2.5, it is clear that the total number of gates is significantly reduced.

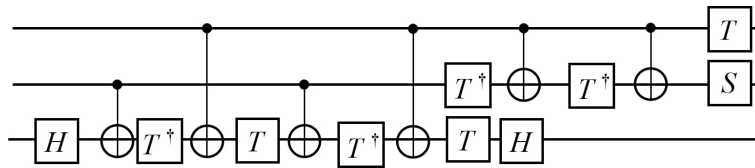


Figure 2.5. Decomposing qubit Toffoli gate with the universal qubit gates. H is the Hadamard gate, T is the $\pi/8$ gate and S is the phase gate.

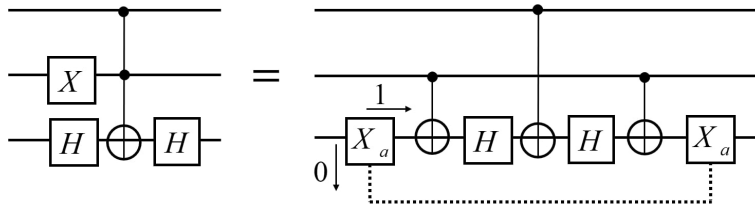


Figure 2.6. The Simplified Toffoli gate. The first two lines represent two control qubits and the third line represents a target qutrit that has three accessible levels. The initial and final quantum states of the quantum information carrier are encoded in the $|0\rangle$ and $|1\rangle$. The H is the generalized Hadamard gate such that $H |0\rangle = 1/\sqrt{2}[|0\rangle+|1\rangle]$, $H |1\rangle = 1/\sqrt{2}[|0\rangle - |1\rangle]$ and $H |2\rangle = |2\rangle$. X_a gate is a qutrit gate such that $X_a |0\rangle = |2\rangle$ and $X_a |2\rangle = |0\rangle$ with $X_a |1\rangle = |1\rangle$. With the control being qubit, the target being qutrit, the two qutrit gate in this case is a hybrid gate.

This method can be generalized to n -qubit-controlled Toffoli gates by utilizing a single $(n + 1)$ -level target carrier and using only $2n - 1$ two-qubit gates [33]. In other words, the target carrier needs an extra level for each extra control qubit. Compare to the best known

realization previously that requires $12n - 11$ two-qubit gates [206], this method offers a significant resource reduction. Furthermore, these schemes can be extended to more general quantum circuits such as the multi-qudit-controlled-unitary gate C^nU .

The previous method turns the target qubit into a qudit; another method simplifies the Toffoli gate by using only qudits and treating the first two levels of the qudit as qubit levels and other levels as auxiliary levels. The reduction in the complexity of Toffoli gate is accomplished by utilizing the topological relations between the dimensionality of the qudits, where higher qudit levels serve as the ancillas [34].

Suppose we have a system of n qudits denoted as Q_i , $i \in \{1, \dots, n\}$ and each qudit has dimension $d_i \geq 2$. Qudits are initialized into pure or mix states on the first two levels, i.e., the qubit states, and zero population for the other levels, i.e., the auxiliary states. This scheme assumes the ability to perform single-qubit operations. We can apply the desirable unitary operation on the qubit states and leave the auxiliary states unchanged. We also assume that we have the ability to manipulate the auxiliary levels by a generalized inverting gate X_m

$$X_m |0\rangle = |m\rangle, X_m |m\rangle = |0\rangle, X_m |y\rangle = |y\rangle, \text{ for } y \neq m, 0. \quad (2.58)$$

At the same time, the two-qubit CZ gates are applied according to certain topological connections between qudits. We introduce a set E of ordered pairs (i, j) , such that $i, j \in \{1, \dots, n\}$, $i < j$ to obtain this topology and the CZ gate is defined as

$$CZ |11\rangle_{Q_i, Q_j} = -|11\rangle_{Q_i, Q_j} \quad CZ |xy\rangle_{Q_i, Q_j} = |xy\rangle_{Q_i, Q_j} \text{ for } xy \neq 1, \quad (2.59)$$

with $x \in \{0, \dots, d_i - 1\}$ and $y \in \{0, \dots, d_j - 1\}$.

The set E describes an n -vertex-connected graph. Let $\tilde{E} \subseteq E$ defines an n -vertex connected *tree* (acyclic graph). The main result is: the n -qubit Toffoli gate can be achieved with less number of operations if

$$d_i \geq k_i + 1, \quad (2.60)$$

where d_i is the dimension of a qudit and the number k_i is the qudit's connections to other qudits within \tilde{E} . With this condition fulfilled, the n -qubit Toffoli gate can be realized by

$2n - 3$ two-qudit CZ gates. The detailed realization of the n -qubit Toffoli gate by the properties and special operations of the tree in topology can be found in Ref. [34]. The advantage of this scheme is the scalability and the ability to implement it for the multi-qubit controlled unitary gate C^nU .

These C^nU gates are a crucial component in the PEA which has many important applications such as the quantum simulation [207] and Shor’s factoring algorithm [208]. This idea of combining qudits of different dimensions or hybrid qudit gates can also be applied to other qudit gates such as the SWAP and SUM gates as shown in Refs. [31], [209]. Thus, introducing qudits into qubit systems to create a hybrid qudit system offers the potential of improvement to quantum computation.

Qudit multi-level controlled gate

For a qubit controlled gate, the control qubit has only two states so it is a “do-or-don’t” gate. Qudits, on the other hand, have multiple accessible states and thus a qudit-controlled gate can perform a more complicated operation [210]. The *Muthukrishnan-Stroud gate* (MS gate) for a qudit applies the specified operation on the target qudit only if the control qudit is in a selected one of the d states, and leaves the target unchanged if the control qudit is in any other $d - 1$ states. Hence, the MS gate is essentially a ”do-or-don’t” gate generalized to qudits and does not fully utilize the d states on the control qudit [179].

To fully utilize the d states on the control qudit, people have developed the quantum multiplexer to perform the controlled U operations in a qudit system as shown in Fig. 2.7, where the MS gate and shifting gates are combined to apply different operations to the target depending on different states on the control states [211]. Here we discuss the *multi-value-controlled gate* (*MVCG*) for qudits, which applies a unique operation to the target qudit for each unique state of the control qudit [13].

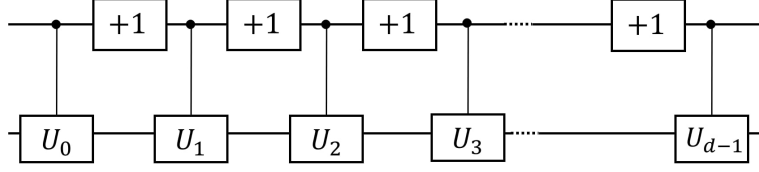


Figure 2.7. d -valued Quantum Multiplexer for the second qudit and its realization in terms of Muthukrishnan-Stroud gates (the control U operation that only act on one specific control state). The gate labeled $+1$ is the shifting gate that increases the state value of the control qudit by $1 \pmod{d}$. Depending on the value of the top control qudit, one of U_i is applied to the second qudit, for $i \in \{0, 1, \dots, d-1\}$.

For a d -dimensional qudit system, a two-qudit multi-value-controlled gate is represented by a $d^2 \times d^2$ matrix

$$MVCG = \begin{pmatrix} U_0 & 0 & 0 & \cdots & 0 \\ 0 & U_1 & 0 & \cdots & 0 \\ 0 & 0 & U_2 & \cdots & 0 \\ \vdots & \vdots & \vdots & \ddots & \vdots \\ 0 & 0 & 0 & \cdots & U_{d-1} \end{pmatrix}, \quad (2.61)$$

where each U_i ($i = 0, 1, \dots, d-1$) is a unique unitary single-qudit operation. The U_i operation is applied to the target qudit when the control qudit is in $|i\rangle$ state. In the later sections, §2.2.2 and §2.2.2 the controlled gates are $MVCG$ and improve the efficiency of the qudit algorithm. $MVCG$ can be built in many physical systems and one example in a photonic system is introduced in §2.4.1.

2.1.3 Geometrically quantifying qudit-gate efficiency

In a quantum computer, each qudit can remain coherent for a limited amount of time (decoherence time). After this time, the quantum information is lost due to the outside perturbations and noises. In the computation process, quantum gates take certain amount of time to alter the states of the qudits. The decoherence time of a qudit state limits the number of quantum gates in the circuit. Therefore, we need to design more efficient algorithms and circuits. A method exists to do a general systematic evaluation of the circuit

efficiency with the mathematical techniques of Riemannian geometry [212]. By reforming the quantum circuits designing problems as a geometric problem, we are able to develop new quantum algorithms or to exploring and evaluating the full potential of the quantum computers. This evaluation is able to generalized to qutrit systems, where the least amount of the gates required to synthesize any unitary operation is given [15].

To begin with, we assume that the operations done by the quantum circuit can be described by a unitary evolution U derived from the time-dependent Schrödinger equation $dU/dt = -iHU$ with the boundary condition $t_f, U(t_f) = U$. The complexity of realizing U can be characterized by a cost function $F[H(t)]$ on the Hamiltonian control $H(t)$. This allow us to define a Riemannian geometry on the space of unitary operations [213]. Finding the minimal geodesics of this Riemannian geometry is equivalent to finding the optimal control function $H(t)$ of synthesizing the desired U .

Now we transform the problem of calculating a lower bound to the gate number to finding the minimal geodesic distance between the identity operation I and U . Instead of Pauli matrices for the qubit representation of the Hamiltonian, the qutrit version of Hamiltonian is expanded in terms of the Gell-Mann matrices. Here we give an explicit form of the Gell-Mann matrices representation in d -dimension [16] which is used for qutrit (where $d = 3$) as well as other qudit systems in the later part of the section. Let e_{jk} denote the $d \times d$ matrix with a 1 in the (j, k) elements and 0s elsewhere, a basis can be described as

$$u_{jk}^d = e_{jk} + e_{kj}, \quad 1 \leq j < k \leq d, \quad (2.62)$$

$$u_{jk}^d = i(e_{jk} - e_{kj}), \quad 1 \leq k < j \leq d, \quad (2.63)$$

$$u_{jj}^d = \text{diag}(1, \dots, 1, -j, 0_{d-2j}), j \in [d-1]. \quad (2.64)$$

Here, diag represents the diagonal matrix, 0_{d-2j} denotes the zeros of length $d - 2j$. u_{jk}^d are traceless and Hermitian and together with the identity matrix $\mathbb{1}_d$ serve as the basis of the vector space of $d \times d$ Hermitian matrix. These generalized Gell-Mann matrices can be used to generate the group representation of $SU(d)$ while the other representations can be achieved

by transform these matrices uniformly. To derive the bases of $SU(d^n)$, we first define $x_l = u_{jk}^d$ with $l = jd + k, l \in [d^2]$ and

$$X_l^s = I^{\otimes s-1} \otimes x_l \otimes I^{\otimes d-s} \quad (2.65)$$

acts on the s -th qudit with x_l and leaves the other qudits unchanged. The bases of $SU(d^n)$ is constructed by $\{Y_t^{P_t}\}, t \in [n], P_t = \{i_1, \dots, i_t\}$ with all possible $1 < i_1 < \dots < i_k < n$, where

$$Y_t^{P_t} = \prod_{k=1}^t X_{j_k}^{i_k}. \quad (2.66)$$

Y_t^P denotes all operators with generalized Gell-Mann matrices x_{j_1}, \dots, x_{j_k} acting on t qudits at sites $P = \{i_1, \dots, i_k\}$, respectively, and rest with identity. It is easy to prove that with the generalized Gell-Mann matrices representations, 1-body and 2-body interactions can generate all 3-body interactions.

Now the Hamiltonian in terms of the Gell-Mann matrices (with the notation σ) can be written as

$$H = \sum_{\sigma} h_{\sigma} \sigma + \sum''_{\sigma} h_{\sigma} \sigma. \quad (2.67)$$

All coefficients h_{σ} are real and, in $\sum_{\sigma} h_{\sigma} \sigma$, σ goes over all possible one- and two-body interactions whereas, in $\sum''_{\sigma} h_{\sigma} \sigma$, σ goes over everything else. The cost function is

$$F(H) := \sqrt{\sum_{\sigma} h_{\sigma}^2 \sigma + p^2 \sum''_{\sigma} h_{\sigma}^2 \sigma}, \quad (2.68)$$

where p is a penalty cost by applying many-body terms. Now that the control cost is well defined, it is natural to form the distance in the space $SU(3^n)$ of n -qudit unitary operators with unit determinant. We can treat the function $F(H)$ as the norm related to a Riemannian metric with a metric tensor g as:

$$g = \begin{cases} 0, & \sigma \neq \tau \\ 1, & \sigma = \tau \text{ and } \sigma \text{ is one or two body} \\ p^2, & \sigma = \tau \text{ and } \sigma \text{ is three or more body} \end{cases}. \quad (2.69)$$

The distance $d(I, U)$ between I and U which is the minimum curve connecting I and U equals to the minimal length solution to the geodesic equation

$$\left\langle \frac{dH}{dt}, K \right\rangle = i \langle H, [H, K] \rangle, \quad (2.70)$$

where \langle, \rangle denotes the inner product on the tangent space $SU(3^n)$ defined by the metric components (2.69), and $[,]$ denotes the matrix commutator and K is an arbitrary operator in $SU(3^n)$.

All lemmas backing up the final theorem have been proven in detail [15], but the reasoning behind can be summarized in four parts. First let p be the three- and more-body items penalty. With large enough p , the distance $d(I, U)$ is guarantee to have a supremum that does not depend on p . Secondly, we have

$$\|U - U_P\| \leq 3^n d([U])/p, \quad (2.71)$$

where $\|\bullet\|$ is the operator norm and U_P the corresponding unitary operator generated by the one- and two-body items projected Hamiltonian $H_P(t)$. Thirdly, given an n -qutrit unitary operator U generated by $H(t)$ with the condition $\|H(t)\| \leq c$ in a time interval $[0, \Delta]$, then

$$\|U - \exp(-i\bar{H})\Delta\| \leq 2(e^{c\Delta} - 1 - c\Delta) = O(c^2\Delta^2), \quad (2.72)$$

where \bar{H} is the mean Hamiltonian. Lastly, for H as an n -qutrit one- and two-body Hamiltonian, a unitary operator U_A exists that satisfies

$$\|e^{iH\Delta} - U_A\| \leq c_2 n^2 \Delta^3 \quad (2.73)$$

and can be generated with at most $c_1 n^2/\Delta$ one- and two-qutrit gates, and constants c_1 and c_2 .

All these lemmas combined gives the final theorem for the qutrit system: for a unitary operator U in $SU(3^n)$, $O(n^k d(I, U)^3)$ one- and two-qutrit gates is the lower bound to synthesize a unitary U_A with the condition $\|U - U_A\| \leq c$, given a constant c . It is worth mentioning

that for any groups of unitaries U , which is labeled by the number of qudits n , the final theorem shows a quantum circuit exists with a polynomial of $d(I, U)$ number of gates such that it can approximate U to arbitrary accuracy. Alternatively, a polynomial-sized quantum circuit exists if and only if the distance $d(I, U)$ itself is scaling polynomially with n .

With appropriate modification, the Riemannian geometry method can be used to ascertain the circuit-complexity bound for a qudit system [16]. In this scheme, the unitary matrix $U \in SU(d^n)$ is represented by the generalized Gell-Mann matrices as defined in the earlier part of the section. The main theorem in the qudit case of the Ref. [16] is “for any small constant ε , each unitary $U_A \in SU(d^n)$ can be synthesized using $O(\varepsilon^{-2})$ one- and two-qudit gates, with error $\|U - U_A\| \leq \varepsilon$.” To break up the constant ε to an explicit form, we have $\varepsilon^{-2} = N^2 d^4 n^2$, where d is the dimension of the qudit, n is the number of qudits and N is the number of the intervals that $d(I, U)$ divides into, such that a small $\delta = d(I, U)/N \leq \varepsilon$. The qudit case shows the explicit relation between the non-local quantum gate cost and the approximation error for synthesizing quantum qudit operations. In summary, for the quantum circuit model, one can decide a lower bound for the number of gates needed to synthesize U by finding the shortest geodesic curve linking I and U . This provides a good reference for the design of the quantum circuit using qudits.

2.2 Quantum algorithms using qudits

A qudit, with its multi-dimensional nature, is able to store and process a larger amount of information than a qubit. Some of the algorithms described in this section can be treated as direct generalizations of their qubit counterparts and some utilize the multi-dimensional nature of the qudit at the key subroutine of the process. This section introduces examples of the well-known quantum algorithms based on qudits and divides them into two groups: algorithms for the oracle-decision problems in §2.2.1 and algorithms for the hidden Abelian subgroup problems in §2.2.2. Finally, §2.2.3 discusses how the qudit gates can improve the efficiency of the quantum search algorithm and reduce the difficulty in its physical set-up.

2.2.1 Qudit oracle-decision algorithm

In this subsection we explore the qudit generalizations of the efficient algorithms for solving the oracle decision problems, which are quite important historically and used to demonstrate the classical-quantum complexity separation [214], [215]. The oracle decision problems is to locate the contents we want from one of the two mutually disjoint sets that is given. We start in §2.2.1 with a discussion about a single-qudit algorithm that determines the parity of a permutation. In §2.2.1, the Deutsch-Jozsa algorithm in qudit system is discussed and its unique extension, the Bernstein-Vazirani algorithm is provided in §2.2.1.

Parity determining algorithm

In this section we review a single qudit algorithm which provides a two to one speedup than the classical counterpart. This algorithm can also be generalized to work on an arbitrary d -dimensional qudit which solves the same problem of a larger computational space [27]. In quantum computing, superposition, entanglement and discord are three important parts for the power of quantum algorithms and yet the full picture behind this power is not completely clear [216].

Recent research shows that we can have a speedup in a fault tolerant quantum computation mode using the quantum contextuality [217]. The contextual nature can be explained as “a particular outcome of a measurement cannot reveal the pre-existing definite value of some underlying hidden variable” [218], [219]. In other words, the results of measurements can depend on how we made the measurement, or what combination of measurements we chose to do. For the qudit algorithm discussed below, a contextual system without any quantum entanglement is shown to solve a problem faster than the classical methods [27]. Because this qudit algorithm uses a single qudit throughout the process without utilizing any correlation of quantum or classical nature, it acts as a perfect example to study the sources of the quantum speed-up other than the quantum correlation.

The algorithm solves a black-box problems that maps d inputs to d outputs after a permutation. Consider the case of three objects where six possible permutations can be divided into two groups: *even* permutation that is a cyclic change of the elements and *odd*

permutation that is an interchange between two elements. If we define a function $f(x)$ that represents the permutation on the set $x \in \{-1, 0, 1\}$, the problems become determining the parity of the bijection $f : -1, 0, 1 \rightarrow -1, 0, 1$. We use Cauchy's two-line notation to define three possible even functions f_k , namely,

$$f_1 := \begin{pmatrix} 1 & 0 & -1 \\ 1 & 0 & -1 \end{pmatrix}, f_2 := \begin{pmatrix} 1 & 0 & -1 \\ 0 & -1 & 1 \end{pmatrix}, f_3 := \begin{pmatrix} 1 & 0 & -1 \\ -1 & 1 & 0 \end{pmatrix}, \quad (2.74)$$

and the remaining three odd function are

$$f_4 := \begin{pmatrix} 1 & 0 & -1 \\ -1 & 0 & 1 \end{pmatrix}, f_5 := \begin{pmatrix} 1 & 0 & -1 \\ 0 & 1 & -1 \end{pmatrix}, f_6 := \begin{pmatrix} 1 & 0 & -1 \\ 1 & -1 & 0 \end{pmatrix}. \quad (2.75)$$

The circuit for the single qutrit algorithm in a space spanned by $\{|1\rangle, |0\rangle, |-1\rangle\}$ is shown in Fig. 2.8, where the operation U_{f_k} applies f_k to the state: $U_{f_k}(|1\rangle + |0\rangle + |-1\rangle) = |f_k(1)\rangle + |f_k(0)\rangle + |f_k(-1)\rangle$, and FT is the single-qutrit Fourier transform

$$FT = \frac{1}{\sqrt{3}} \begin{pmatrix} \omega & 1 & \omega^{-1} \\ 1 & 1 & 1 \\ \omega^{-1} & 1 & \omega \end{pmatrix} \quad (2.76)$$

using ω as the cube root of unity (2.14). The process starts with state $|1\rangle$ undergoing FT and becoming $|\psi_1\rangle$ as $FT|1\rangle = |\psi_1\rangle = \omega|1\rangle + |0\rangle + \omega^{-1}|-1\rangle$. Then we obtain $|\psi_k\rangle$ by applying U_{f_k} to $|\psi_1\rangle$. It is easy to show that

$$|\psi_1\rangle = \omega^{-1}|\psi_2\rangle = \omega|\psi_3\rangle \quad (2.77)$$

and, similarly,

$$|\psi_4\rangle = \omega^{-1}|\psi_5\rangle = \omega|\psi_6\rangle. \quad (2.78)$$

Hence, application of U_{f_k} on $|\psi_1\rangle$ gives $|\psi_1\rangle$ (up to a phase factor) for an even permutation and $|\psi_4\rangle = FT|-1\rangle$ for an odd permutation. Thus, applying inverse Fourier transform FT^{-1}

at the end, we measure $|1\rangle$ for even f_k and $|-1\rangle$ for odd f_k . We are able to determine the parity of f_k by a single application of f_k on a single qutrit.

Generalizing to a d -dimensional qudit system,

$$|\psi_k\rangle := \frac{1}{\sqrt{d}} \sum_{k=1}^d \omega^{(k-1)(k-1)} |k\rangle. \quad (2.79)$$

In this scenario, a positive cyclic permutation maps $|\psi_2\rangle$ onto itself whereas negative permutations give $|\psi_d\rangle$. We then measure the results after applying an inverse Fourier transform to solve for the parity of the permutation. This algorithm has been implemented on the NMR system for both the qutrit [26] and ququart [27] cases. It is also realized on a linear optic system [220]. Although the model problem has no significant applications and the speedup in the higher dimensional cases is not exponential, this proposed algorithm provides an elegant yet simple example for quantum computation without entanglement.

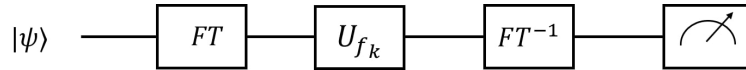


Figure 2.8. Schematic view of the quantum circuit for the parity determining algorithm. FT is the Fourier transform and U_{f_k} is the gate that does one of the two permutations and the last box represents the measurement.

Qudit Deutsch-Jozsa algorithm

Deutsch algorithm (with its origin in [214] and improved in [209]) is one of the simplest examples to show the speed advantage of quantum computation. Deutsch-Jozsa algorithm is n -qubits generalization of the Deutsch algorithm. Deutsch-Jozsa algorithm can determine if a function $f(x)$ is *constant*, with constant output, or *balanced*, that gives equal instances of both outputs [206]. The process itself consists of only one evaluation of the function $f(x)$. In this algorithm, Alice sends Bob N qubits in the query register and one in the answer register where Bob applies the function to the query register qubits and stores the results in the answer register. Alice can measure the qubits in the query register to determine whether Bob's function is constant or balanced. This algorithm makes use of the superposition

property of the qubit and reduces the minimum number of the function call from $2^n/2 + 1$ classically to only 1 with quantum algorithm. This gives another example of the advantages of quantum algorithms.

The Deutsch-Jozsa algorithm can be performed in the qudit system with a similar setup. Furthermore, with the qudit system, Deutsch-Jozsa algorithm can also find the closed expression of an affine function accurate to a constant term [221]. The *constant* and *balanced* function in the n dimensional qudit case have the following definition: “An r -qudit multi-valued function of the form

$$f : \{0, 1, \dots, n - 1\}^r \rightarrow \{0, 1, \dots, n - 1\} \quad (2.80)$$

is *constant* when $f(x) = f(y) \forall x, y \in \{0, 1, \dots, n - 1\}^r$ and is *balanced* when an equal number of the n^r domain values, namely n^{r-1} , is mapped to each of the n elements in the co-domain” [221].

It can be shown that all of the affine functions of r qudits

$$f(x_1, \dots, x_r) := A_0 \oplus A_1 x_1 \oplus \dots \oplus A_r x_r, \quad A_0, \dots, A_r \in \mathbb{Z}_n, \quad (2.81)$$

can be categorized to either constant or balanced functions [221]. If all the coefficients $A_{i \neq 0} = 0$ then the function is constant. For affine function with non-zero coefficient $A_{i \neq 0}$, every element in its domain $\{0, 1, \dots, n - 1\}^r$ is reducible modulo n to a unique element $m \in \{0, 1, \dots, n - 1\}$. As $f(p) = f(q)$ if $p \equiv q \pmod{n}$, each of the elements in the codomain $\{0, 1, \dots, n - 1\}$ is mapped to n^{r-1} different elements in the domain. To finish the proof of the n -nary Deutsch-Jozsa algorithm, another trivial lemma is needed: Primitive n^{th} roots of unity satisfy $\sum_{k=0}^{n-1} \omega^{\alpha k} = 0$ for nonzero integers α .

The circuit of the Deutsch-Jozsa algorithm in qudits is shown in Fig. 2.9. This algorithm of r qudits can both distinguish whether a function U_f is balanced or constant and verify a closed expression for an affine function in U_f within a constant term which is a universal phase factor of the x -register and thus is lost during the measurement. The other coefficients

of the affine function A_1, \dots, A_r are determined by measuring the state of the x -register at the output, $|A_1, \dots, A_r\rangle$.

A detailed derivation of the circuit has been shown [221], but the reasoning is an analogy to the qubit version of the Deutsch-Jozsa algorithm. If the function U_f is constant, the final state after the measurement is $|0\rangle^{\otimes r} |n-1\rangle$ as for $j \neq 0$ every states in the x -register have null amplitudes. Therefore, if every x -register qudit yields $|0\rangle$, it is a constant function; otherwise the function is balanced.

The Deutsch-Jozsa algorithm in the qudit system shares the same idea while enabling more applications such as determining the closed form of an affine function. Although this algorithm is mainly of theoretical interest, the n -nary version of it may have applications in image processing. It has the potential to distinguish between maps of texture in a Marquand chart since the images of which are encoded by affine functions [35]. This algorithm can also be modified to set up a secure quantum key-distribution protocol [35]. Other proposed Deutsch-Jozsa algorithms exist such as a method that makes use of the artificially allocated “subsystems” as qudits [222] and a generalized algorithm on the virtual spin representation [223].

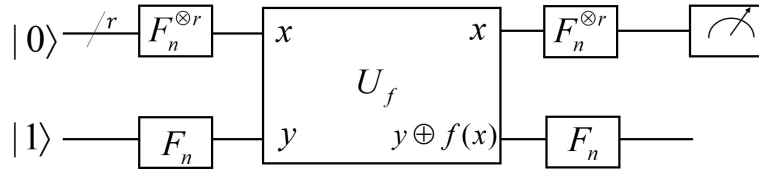


Figure 2.9. The Deutsch-Jozsa circuit in qudit system. The F_n are the qudit Hadamard gates achieved with quantum Fourier transform.

Qudit generalization of the Bernstein-Vazirani algorithm

in §2.2.1 we have discussed an application of a qudit Deutsch-Jozsa algorithm (DJA): verify a closed expression of an affine function. This application is closely related to the Bernstein-Vazirani algorithm discussed in this section. Given an input string and a function that calculates the bit-wise inner-product of the input string with an unknown string, the

Bernstein-Vazirani algorithm determines the unknown string [224]. This algorithm can be treated as an extension of the Deutsch-Jozsa algorithm.

The qudit generalization of the Bernstein–Vazirani algorithm can determine a number string of integers modulo d encoded in the oracle function [36], [225]. First we introduce a positive integer d and consider the problem in modulo d throughout. Given an N -component natural number string

$$g(a) := (g(a_1), g(a_2), g(a_3), \dots, g(a_N)), g(a_j) \in \{0, 1, \dots, d-1\}, \quad (2.82)$$

we define

$$f(x) := g(a) \cdot x \pmod{d} = g(a_1)x_1 + g(a_2)x_2 + \dots + g(a_N)x_N \pmod{d}, \quad (2.83)$$

for

$$x = (x_1, x_2, \dots, x_N) \in \{0, 1, \dots, d-1\}^N. \quad (2.84)$$

The oracle in the algorithm applies $f(x)$ to the input string x and computes the result, namely, the number string $g(a)$ encoded in the function $f(x)$.

The input state x is chosen to be $|\psi_0\rangle = |0\rangle \otimes^N |d-1\rangle$, where $|0\rangle \otimes^N$ means initialization of the N control-qudits into their $|0\rangle$ states and $|d-1\rangle$ means the target qudit is in its $d-1$ state. Quantum Fourier transforms of the pertinent input states are

$$|0\rangle \xrightarrow{QFT} \sum_{y=0}^{d-1} \frac{|y\rangle}{\sqrt{d}} \quad (2.85)$$

and

$$|d-1\rangle \xrightarrow{QFT} \sum_{y=0}^{d-1} \frac{1}{\sqrt{d}} \omega^{d-y} |y\rangle,$$

for ω a root of unity (2.14). The component-wise Fourier transform of a string encoded in the state $|x_1 x_2 \dots x_N\rangle$ is

$$|x_1 x_2 \dots x_N\rangle \xrightarrow{QFT} \sum_{z \in K} \frac{\omega^{x \cdot z} |z\rangle}{\sqrt{d^N}}, \quad (2.86)$$

where

$$K = \{0, 1, \dots, d-1\}^N, \quad z := (z_1, z_2, \dots, z_N). \quad (2.87)$$

We denote the Fourier transform of the $|d-1\rangle$ state as $|\phi\rangle$ and the input state after the Fourier transform is

$$|\psi_1\rangle = \sum_{x \in K} \frac{|x\rangle}{\sqrt{d^N}} |\phi\rangle \quad (2.88)$$

Now we introduce the oracle as the $O_{f(x)}$ gate such that

$$|x\rangle |j\rangle \xrightarrow{O_{f(x)}} |x\rangle |(f(x) + j) \bmod d\rangle, \quad (2.89)$$

where

$$f(x) = g(a) \cdot x \bmod d. \quad (2.90)$$

By applying the $O_{f(x)}$ gate to $|\psi_1\rangle$ and following the formula by phase kick-back, we obtain the output state

$$O_{f(x)} |\psi_1\rangle = |\psi_2\rangle = \sum_{x \in K} \frac{\omega^{f(x)} |x\rangle}{\sqrt{d^N}} |\phi\rangle. \quad (2.91)$$

Finally, obtain the $|\psi_3\rangle$ which is the state after inverse Fourier transform of the first N qudits of $|\psi_2\rangle$. By measuring the first N quantum state of $|\psi_3\rangle$ we can obtain the natural number string we want that is offset up to a constant

$$g(a_1), g(a_2), g(a_3), \dots, g(a_N) \quad (2.92)$$

using a single query of the oracle function.

The Bernstein-Vazirani algorithm clearly demonstrates the power of quantum computing. It outperforms the best classical algorithm in terms of speed by a factor of N [225]. The qudit generalizations of the Bernstein-Vazirani algorithm helps us comprehend the potential of the qudit systems.

2.2.2 Qudit algorithms for the hidden Abelian subgroup problems.

Many of the widely used quantum algorithms such as the discrete Fourier transform, the phase estimation and the factoring fit into the framework of the hidden subgroup problem (HSP). In this section, we review the qudit generalization of these algorithms. The qudit Fourier transform is discussed in §2.2.2 and its application, the PEA is reviewed in §2.2.2. A direct application of these algorithms, Shor's factoring algorithm performed with qutrits and in metaplectic quantum architectures is also introduced §2.2.2.

Quantum Fourier Transform with qudits

The quantum Fourier transform algorithm (QFT) is realizable on a qubit system [206]. QFT, as the heart of many quantum algorithms, can also be performed in a qudit system [202], [226]. In an N -dimensional system represented with n d -dimensional qudits, the QFT, $F(d, N)$, where $N = d^n$, transforms the computational basis

$$\{|0\rangle, |1\rangle, \dots, |N-1\rangle\} \quad (2.93)$$

into a new basis set [37]

$$F(d, N) |j\rangle = \frac{1}{\sqrt{N}} \sum_{k=0}^{N-1} e^{2\pi i j k / N} |k\rangle. \quad (2.94)$$

For convenience, we write an integer j in a base- d form. If $j > 1$ then

$$j = j_1 j_2 \cdots j_n = j_1 d^{n-1} + j_2 d^{n-2} + \cdots + j_n d^0 \quad (2.95)$$

and, if $j < 1$, then

$$j = 0.j_1 j_2 \cdots j_n = j_1 d^{-1} + j_2 d^{-2} + \cdots + j_n d^{-n}. \quad (2.96)$$

The QFT acting on a state $|j\rangle$ can be derived and rewritten in a product form as

$$\begin{aligned}
|j\rangle = |j_1 j_2 \cdots j_n\rangle &\mapsto \frac{1}{d^{n/2}} \sum_{k=0}^{d^n-1} e^{2\pi i j k / d^n} |k\rangle \\
&= \frac{1}{d^{n/2}} \sum_{k_1=0}^{d-1} \cdots \sum_{k_n=0}^{d-1} e^{2\pi i j (\sum_{l=1}^n k_l d^{-l})} |k_1 k_2 \cdots k_n\rangle \\
&= \frac{1}{d^{n/2}} \sum_{k_1=0}^{d-1} \cdots \sum_{k_n=0}^{d-1} \bigotimes_{l=1}^n e^{2\pi i j k_l d^{-l}} |k_l\rangle \\
&= \frac{1}{d^{n/2}} \bigotimes_{l=1}^n \left[\sum_{k_l=0}^{d-1} e^{2\pi i j k_l d^{-l}} |k_l\rangle \right].
\end{aligned}$$

This process can be realized with the quantum circuit shown in Fig. 2.10, and the fully expanded expression of the product form is shown on the right side of the figure. The generalized Hadamard gate H^d in the figure is defined as $H^d := F(d, d)$ which effects the transform

$$H^d |j_n\rangle = |0\rangle + e^{2\pi i 0 \cdot j_n} |1\rangle + \cdots + e^{2(d-1)\pi i 0 \cdot j_n} |d-1\rangle. \quad (2.97)$$

The matrix representation of H^d is

$$\begin{pmatrix}
1 & 1 & \cdots & 1 \\
1 & e^{2\pi i 0 \cdot 1} & \cdots & e^{2\pi i 0 \cdot (d-1)} \\
\vdots & \vdots & \ddots & \vdots \\
1 & e^{2(d-1)\pi i 0 \cdot 1} & \cdots & e^{2(d-1)\pi i 0 \cdot (d-1)}
\end{pmatrix}. \quad (2.98)$$

In the circuit the R_k^d gate is a phase gate that has the expression

$$R_k^d = \begin{pmatrix}
1 & 0 & \cdots & 0 \\
0 & e^{2\pi i / d^k} & \cdots & 0 \\
\vdots & \vdots & \ddots & \vdots \\
0 & 0 & \cdots & e^{2\pi i (d-1) / d^k}
\end{pmatrix}. \quad (2.99)$$

The black dots in the circuit are multi-value-controlled gates that apply R_k^d to the target qudit j times for a control qudit in state $|j\rangle$. In order to complete the Fourier transform

and ensure the correct sequence of $j_1 j_2 \cdots j_n$, a series of SWAP gates are applied at the end, which are not explicitly drawn in Fig. 2.10.

The QFT developed in qudit system offers a crucial subroutine for many quantum algorithm using qudits. Qudit QFT offers superior approximations where the magnitude of the error decreases exponentially with d and the smaller error bounds are smaller [226], which outperforms the binary case [227].

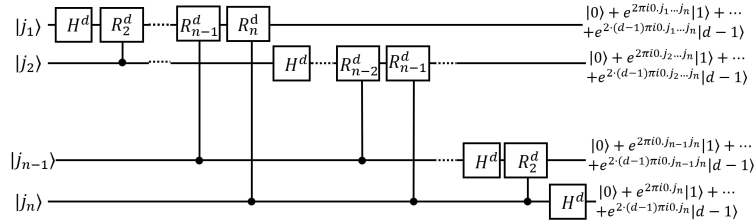


Figure 2.10. Quantum Fourier transform in qudit system. H^d is the d -dimensional Hadamard gate and the expression of the R^d gate is shown in Eq. (2.99). Resultant states are shown to the right.

Phase-estimation algorithm with qudits

With the qudit quantum Fourier transform, we are able to generalize the PEA to qudit circuits [37]. Similar to the PEA using qubit, the PEA in the qudit system is composed by two registers of qudits. The first register contains t qudits and t depends on the accuracy we want for the estimation. We assume that we can perform a unitary operation U to an arbitrary number of times using qudit gates and generate its eigenvector $|u\rangle$ and store it using the second register's qudits [38]. We want to calculate the eigenvalue of $|u\rangle$ where $U|u\rangle = e^{2\pi i r} |u\rangle$ by estimating the phase factor r .

The following derivations follow those in Ref. [37]. For convenience, we rewrite the rational number r as

$$r = R/d^t = \sum_{l=1}^t \bar{R}_l/d^l = 0.\bar{R}_1\bar{R}_2 \cdots \bar{R}_t. \quad (2.100)$$

As shown in Fig. 2.11 A, each qudit in the first register passes through the generalized Hadamard gate $H \equiv F(d, d)$. For the l^{th} qudit of the first register, we have

$$F(d, d) |0\rangle_l = \frac{1}{\sqrt{d}} \sum_{k_l=0}^{d-1} |k_l\rangle. \quad (2.101)$$

Then the l^{th} qudit is used to control the operation $U^{d^{t-l}}$ on the target qudits of the state $|u\rangle$ in the second register, which gives

$$CU^{d^{t-l}} |k\rangle \otimes |u\rangle = |k\rangle (U^{d^{t-l}})^k |u\rangle = e^{2\pi i k d^{t-l} r} |k\rangle \otimes |u\rangle. \quad (2.102)$$

Note that the function of the controlled operation $CU^{d^{t-l}}$ can be considered as a 'quantum multiplexer' [174], [211], [228]. After executing all the controlled operations on the qudits, the qudit system state turns out to be

$$\left(\prod_{l=1}^t \frac{1}{\sqrt{d}} \sum_{k_l=0}^{d-1} e^{2\pi i k_l d^{t-l} r} |k_l\rangle \right) \otimes |u\rangle. \quad (2.103)$$

Therefore, through a process called the "phase kick-back", the state of the first register receives the phase factor and becomes

$$|\text{Register 1}\rangle = \frac{1}{d^{t/2}} \sum_{k=0}^{d^t-1} e^{2\pi i r k} |k\rangle. \quad (2.104)$$

The eigenvalue r which is represented by the state $|R\rangle$ can be derived by applying the inverse QFT to the qudits in the first register:

$$F^{-1}(d, d^t) |\text{Register 1}\rangle = |R\rangle. \quad (2.105)$$

The whole process of PEA is shown in Fig. 2.11 B. To obtain the phase $r = R/d^t$ exactly, we can measure the state of the first register in the computational basis.

The PEA in qudit system provides a significant improvement in the number of the required qudits and the error rate decreases exponentially as the qudit dimension increases [229]. A long list of PEA applications includes Shor's factorization algorithm [208], simulation of

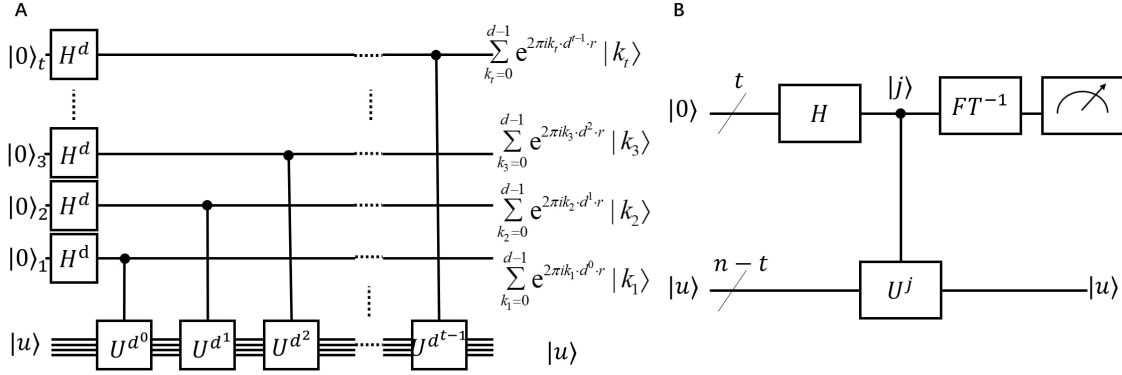


Figure 2.11. A The circuit for the first stage of the PEA. The qudits in the second register whose states represent $|u\rangle$ are undergoing the U operations and the generated phase factors are kicking back to the qudits in the first register, giving the results to the right. **B** The schematic circuit for the whole stage of PEA. After the first stage of the PEA, inverse Fourier transform(FT^{-1}) is applied to the qudits in the first register and the phase factors can be obtained by measuring the states of the first register qudits.

quantum systems [230], solving linear equations [41], [231], and quantum counting [232]. To give some examples, a quantum simulator utilizing the PEA algorithm has been used to calculate the molecular ground-state energies [207] and to obtain the energy spectra of molecular systems [67], [233]–[236]. Recently, a method to solve the linear system using a qudit version of the PEA has been proposed [237]. The qudit version of the PEA opens the possibility to realize all those applications that have the potential to out-perform their qubit counterparts.

Shor’s quantum algorithm for prime factorization gives an important example of super-polynomial speed-up offered by a quantum algorithm over the currently-available classical algorithms for the same purpose [40]. The order-finding algorithm at the core of the factoring algorithm is a direct application of the PEA. With the previous discussion on the qudit versions of the quantum Fourier transform and phase estimation, we have the foundation to generalize Shor’s factoring algorithm to the higher dimensional qudit system. Several proposals for performing Shor’s algorithm on the qudit system, such as the adiabatic quantum algorithm of two qudits for factorization [17], exist. This method makes use of a time-

dependent effective Hamiltonian in the form of a sequence of rotation operators that are selected according to the qudit’s transitions between its neighboring levels.

Another proposal carries out a computational resource analysis on two quantum ternary platforms [38]. One is the “generic” platform that uses magic state distillation for universality [194]. The other, known as a metaplectic topological quantum computer (MTQC), is a non-Abelian anyonic platform, where anyonic braiding and interferometric measurement is used to achieved the universality with a relatively low cost [19], [20]. The article discusses two different logical solutions for Shor’s period-finding function on each of the two platforms: one that encodes the integers with the binary subspace of the ternary state space and optimizes the known binary arithmetic circuits; the other encodes the integer directly in the ternary space using the arithmetic circuits stemming in Ref [21]. Significant advantages for the MTQC platform are found compared to the others. In particular the MTQC platform can factorize an n -bit number with $n + 7$ logical qutrits with the price of a larger circuit-depth. To sum up the comparison, the MTQC provides significant flexibility at the period finding algorithm for the ternary quantum computers.

2.2.3 Quantum search algorithm with qudits

The quantum search algorithm, also known as Grover’s algorithm, is one of the most important quantum algorithms that illustrates the advantage of quantum computing. Grover’s algorithm is able to outperform the classical search algorithm for a large database. The size of the computational space in an n -qubit system is a Hilbert space of 2^n dimensions.

Since there is a practical limit for the number of working qubits, the working Hilbert space can be expanded by increasing the dimension of each carrier of information, i.e., using qudits and qudit gates. Several schemes of Grover’s quantum search with qudits have been proposed, such as one that uses the discrete Fourier transform as an alternative to the Hadamard gate [238] or another d -dimensional transformation [239] for the construction of the reflection-about-average operator (also known as the diffusion operator). In this section, an instruction on setting up Grover’s algorithm in the qudit system is reviewed as well as a proposal of a new way to build a quantum gate F that can generate an equal-weight

superposition state from a single qudit state [39]. With the new gate F , it is easier to realize Grover's algorithm in a physical system and improve the overall efficiency of the circuit.

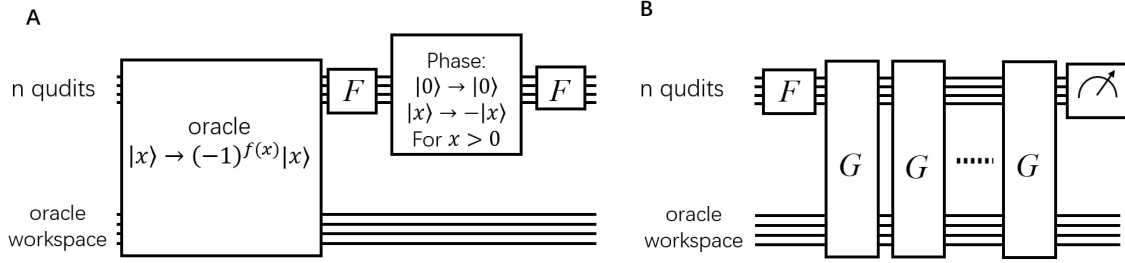


Figure 2.12. (A) Circuit illustration for Grover iteration, G , in a qudit system. The F gate is the proposed qudit gate that transforms the single-qudit state $|0_k\rangle$ into an equal weight superposition state. (B) Schematic circuit illustration of the qudit quantum search algorithm.

Grover's algorithm solves the unstructured search problem by applying Grover's oracle iteratively as shown in Fig. 2.12 B. To construct the oracle, we build qudit gates to perform the oracle function $f(x)$ that acts differently on the search target s as compared to all the others. The logic behind the algorithm is to amplify the amplitude of the marked state $|s\rangle$ with the oracle function, while attenuating the amplitudes of all the other states. The marked state is amplified enough to be located in $O(\sqrt{N})$ steps for an N dimensional search space. In each step Grover's oracle is executed one time. This oracle can be broken into two parts: (1) *Oracle query*. The oracle shifts the phase of the marked state $|s\rangle$ and leaving others unchanged by doing

$$\mathbf{R}_s(\phi_s) = \mathbf{1} + (e^{i\phi_s} - 1) |s\rangle \langle s|. \quad (2.106)$$

(2) *Reflection-about-average*. This operation is a reflection about a vector $|a\rangle$ with a phase ϕ_a :

$$\mathbf{R}_a(\phi_a) = \mathbf{1} + (e^{i\phi_a} - 1) |a\rangle \langle a|. \quad (2.107)$$

It is constructed by applying the generalized Hadamard gate H , applying phase shift to $|0\rangle$ state and then applying H again. It is straightforward to show that

$$H^{\otimes n} \mathbf{R}_0(\phi_a) H^{\otimes n} = \mathbf{R}_a(\phi_a).$$

The two steps combined form Grover's operator \mathbf{G} , which is one execute of Grover's iteration. This process of Grover's iteration \mathbf{G} is shown in Fig.2.12 A.

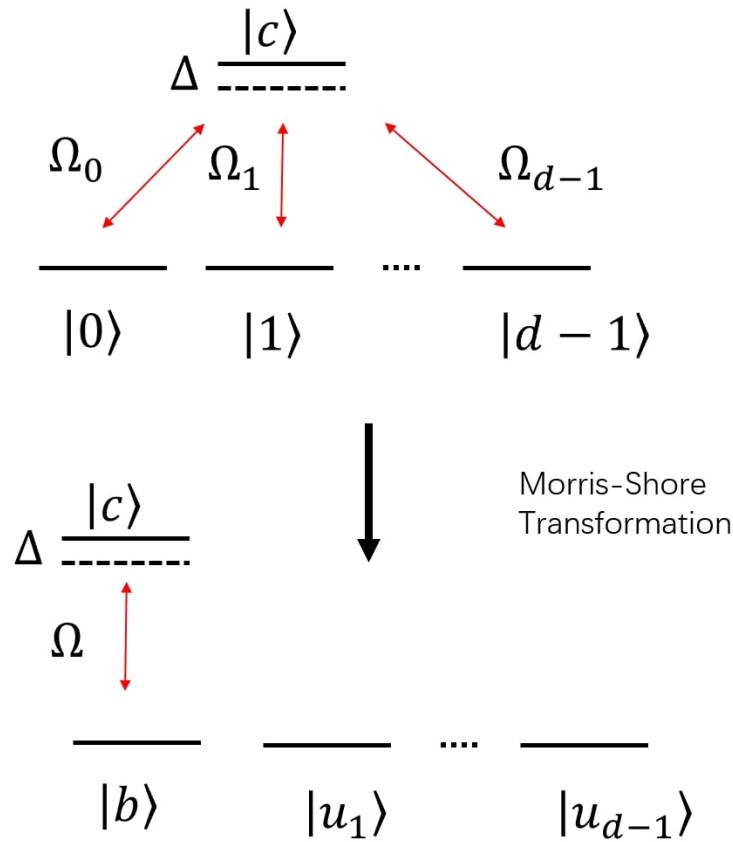


Figure 2.13. Illustration of a qudit multipod linkage: the top is in the original basis and the bottom is in the Morris-Shore basis. Δ is a common detuning between a common (ancilla) state and other qudit states, Ω_k represents the single-photon Rabi frequencies. State $|b\rangle$ is a superposition of the qudit states weighted by the couplings Ω_k ; $|u_n\rangle$ are the states that are not in the dynamics.

Building Grover's operator in a qudit system can be simplified both algorithmically and physically. The most important improvement can be achieved by replacing the Hadamard

gate H with F which drives the single-qudit state $|0_k\rangle$ into an equal weight superposition state,

$$F|0_k\rangle = \sum_{q=0}^{d-1} \xi_q |q_k\rangle, \quad (2.108)$$

with $|\xi_q| = d^{-1/2}$, in all qudits ($k \in \{1, 2, \dots, n\}$). The F function can be realized by a single physical interaction in a multipod system easily. The multipod system consists of d degenerate quantum states $|0\rangle, |1\rangle, \dots, |d-1\rangle$. A common (ancilla) state $|c\rangle$ couples these states to each other by two-photon Raman processes, as illustrated in Fig. 2.13. The root-mean-square (rms) Rabi frequency as the coupling factor of the two states is

$$\Omega(t) = \sqrt{\sum_{k=0}^{d-1} |\Omega_k(t)|^2}. \quad (2.109)$$

Then from the two-state solution, we can calculate the dynamics of the multipod [240].

This method of building F minimizes the number and the duration of algorithmic steps and thus is fast to implement and, in addition, it also provides better protection against detrimental effects such as decoherence or imperfections. Due to its conceptual simplicity, this method has applications in numerous physical systems. Thus, it is one of the most natural and simplest realizations of Grover's algorithm in qudits.

2.3 Alternative models of quantum computing with qudits

The gate-based description of quantum computing is useful to establish principles of quantum computing with qudits, similar to the case for qubits. There are various approaches to quantum computing besides the gate-based model, such as the measurement-based [241], adiabatic quantum computing [242], [243] and topological quantum computing [244]. Qudit versions of these approaches are barely explored to date, and we summarize the current status of these studies below.

2.3.1 Measurement-based qudit computing

Measurement-based quantum computing was introduced as an alternative approach to quantum computing whereby a highly entangled state, such as a cluster state [245] or its graph-state generalization [246], is prepared and then computation is performed by sequential single-qubit measurements in bases that are determined by a constant number of previous measurement outcomes [241], [247]. Measurement-based quantum computing is appealing in settings where preparing a highly entangled many-qubit graph state is feasible, such as parallelized controlled-phase operations [241] or cooling to the ground-state of a special Hamiltonian [247].

Measurement-based qudit quantum computing is unexplored to date. Preparatory work on generalizing graph states, implicitly including the cluster-state special case, to qudit graph states has been reported [248]. Regarding implement, qudit-based approaches have only been reported for the error-correction aspect of measurement-based qubit quantum computing [249]. In this approach, the cluster state is envisioned as comprising qudits, with the high-dimensional nature of qudits serving to encode qubits for error correction. They propose continuous-variable realizations of a qudit cluster state in a continuous-variable setting [249].

2.3.2 Adiabatic qudit computing

Adiabatic quantum computing approaches quantum computing by encoding the solution of a computational problem as the ground-state of a Hamiltonian whose description is readily obtained; the solution is obtained by preparing the ground state of a Hamiltonian whose ground-state is efficiently constructed and then evolving slowly, according to the adiabatic condition, into a close approximation of the ground state of the Hamiltonian specifying the problem [242]. The advantage of adiabatic quantum computing is evident in its natural correspondence to quantizing satisfiability problems [242], and current efforts to exploit adiabatic quantum computing focus on quantum annealing, which is a quantum generalization of the simulated annealing metaheuristic used for non-quantum global optimization problems [250]–[252].

Quantum annealing is an important branch of quantum computing, particularly at the commercial level exemplified by D-Wave’s early and continuing work in this domain. As D-Wave researchers themselves point out, realistic solid-state devices treated as qubits are not actually two-level systems and higher-dimensional representations of the dynamics must be considered to model and simulate realistic solid-state quantum annealers. The effect of states outside the qubit space, namely the treatment of solid-state quantum annealing as qudit dynamics, has been studied carefully with conditions established for soundness of qubit approximations [18].

In fact the qudit nature of so-called superconducting qubits, i.e., the higher-dimensional aspects of the objects serving as qubits, is not just a negative feature manifesting as leakage error; remarkable two-qubit gate performance is achieved by exploiting adiabatic evolution involving avoided crossings with higher levels [253], [254] with this exploitation for fast, high-fidelity quantum gates extendable to three-qubit gates and beyond by exploiting intermediate qudit dynamics and avoided level crossings [255], [256]. Another suggestion for exploiting qudit dynamics concerns using a degenerate two-level system with the additional freedom perhaps improving the energy gap and thus increasing success probability [257].

A dearth of studies have taken place to date into qudit-based adiabatic quantum computing. The one proposal thus far concerns a quantum adiabatic algorithm for factorization on two qudits [17]. Specifically, they consider two qudits of possibly different dimensions, thus necessitating a hybrid two-qudit gate [31]. They propose a time-dependent effective Hamiltonian to realize this two-qudit gate and its realization as radio-frequency magnetic field pulses. For this model, they simulate factorization of each of the numbers 35, 21, and 15 for two quadrupole nuclei with spins $3/2$ and 1, respectively, corresponding to qudit dimensions of 4 and 3, respectively.

2.3.3 Topological quantum computing with qudits

Topological quantum computing offers advantages over other forms of quantum computing by reducing quantum error correction overheads by exploiting topological protection.

Some work has been done on topological quantum computing with qudits by proposing quantum computing with parafermions [258], [259].

Majorana fermions are expected to exhibit non-abelian statistics, which makes these exotic particles, or their quasiparticle analogue, sought after for anyonic quantum computing [260]. Majorana fermions can be generalized to \mathbb{Z}_d parafermions, which also exhibit non-abelian statistics and reduce to standard Majorana fermions for $d = 2$. One advantage of $d > 2$ is that parafermion braiding is an entangling operation. Importantly, encoding a qudit of dimension d in the four-parafermion fusion space enables all single-qudit Clifford gates to be generated modulo phase terms [258].

Clifford gates do not provide a universal set of gates for quantum computing. A non-Clifford gate can be achieved for parafermions encoded into parafermion zero modes by exploiting the Aharonov-Casher effect, physically implemented by move a half-fluxon around the parafermionic zero modes. Combining this non-Clifford gate with the Clifford gates achieved by parafermion braiding yields a universal gate set of non-abelian quantum computing with qudits [259].

2.4 Implementations of qudits and algorithms

The qubit circuit and qubit algorithm have been implemented on various physical systems such as defects in solids [261]–[263], quantum dots [264], [265], photons [266], [267], superconducting systems [268], [269], trapped ions [270], [271], magnetic [272]–[275] and non-magnetic molecules [276], [277]. For each physical representation of the qubit, only two levels of states are used to store and process quantum information. However, many quantum properties of these physical systems have more than two levels, such as the frequency of the photon [13], energy levels of the trapped ions [25], spin states of the nuclear magnetic resonance systems [26] and the spin state of the molecular magnetic magnets [278]. Therefore, these systems have the potential to represent qudit systems. In this section, we briefly review several physical platforms that have been used to implement qudit gates or qudit algorithms.

Although most of the systems have three or four levels available for computation, they are extensible to higher level systems and scalable to multi-qudit interactions. These pio-

neer implementations of qudit systems show the potential of future realization of the more powerful qudit quantum computers that have real-life applications.

2.4.1 Time and frequency bin of a photon

Photonic system is a good candidate for quantum computing because photons rarely interact with other particles and thus have a comparatively long decoherence time. In addition, photon has many quantum properties such as the orbital angular momentum [54], [279], frequency-bin [280]–[283] and time-bin [55], [284] that can be used to represent a qudit. Each of these properties provides an extra degrees of freedom for the manipulation and computation. Each degree of freedom usually has dimensions greater than two and thus can be used as a unique qudit. The experimental realization of arbitrary multidimensional multiphotonic transformations has been proposed with the help of ancilla state, which is achievable via the introduction of a new quantum nondemolition measurement and the exploitation of a genuine high-dimensional interferometer [22]. Experimental entanglement of high-dimensional qudits, where multiple high-purity frequency modes of the photons are in a superposition coherently, is also developed and demonstrated [280].

Here we review a single photon system that has demonstrated a proof-of-principle qutrit PEA [13]. In a photonic system, there is no deterministic way to interact two photons and thus it is hard to build a reliable controlled gate for the photonic qudits. The following photonic system bypasses this difficulty via using the two degrees of freedom on a single photon—i.e., the time-bin and frequency-bin to be the two qutrits. The frequency degree of freedom carries one qutrit as the control register and the time degree of freedom carries another qutrit as the target register. The experimental apparatus consists of the well-established techniques and fiber-optic components: continuous-wave(CW) laser source, phase modulator(PM), pulse shaper(PS), intensity modulator(IM) and chirped fiber Bragg grating(CFBG). The device is divided into three parts [13]: 1. A state preparation part that comprises a PM followed by a PS and a IM that encodes the initial state to qudits; 2. a controlled-gate part that is built with a PM sandwiched by two CFBGs to perform the control- U operation; and 3. an inverse Fourier transformation comprising a PM and then

a PS to extract the phase information. Note that the controlled-gate part can perform a multi-value-controlled gate that applies different operations based on the three unique states of the control qutrit. In the PEA procedure, eigenphases can be retrieved with 98% fidelity. In addition to having long coherence lifetime, the photonic system also has a unique advantage over other common quantum devices i.e., the ability to process and measure thousands of photons simultaneously. This allows us to generate statistical patterns quickly and infer the phase accurately whereas the normal PEA has to use additional qudits on the control register to increase accuracy.

Table 2.1. Normalized photon counts and comparison of the true phase ϕ and the experimentally estimated phase $\hat{\phi}$ for each eigenstate of \hat{U}_1 (Eq. 2.110) and \hat{U}_2 (Eq. 2.111) [13].

\hat{U}_1			
Eigenstate	$ 0\rangle_t$	$ 1\rangle_t$	$ 2\rangle_t$
E_0	$.9948 \pm .0004$	$.0101 \pm .0004$	$.0122 \pm .0005$
E_1	$.0023 \pm .0002$	$.9805 \pm .0009$	$.0120 \pm .0005$
E_2	$.0029 \pm .0002$	$.0094 \pm .0004$	$.9758 \pm .0010$
True Phase, ϕ	0	$2\pi/3$	$4\pi/3$
Est. Phase, $\hat{\phi}$	1.972π	$.612\pi$	1.394π
Error, $\frac{ \phi-\hat{\phi} }{2\pi}$	1.4%	2.7%	3.0%
\hat{U}_2			
Eigenstate	$ 0\rangle_t$	$ 1\rangle_t$	$ 2\rangle_t$
E_0	$.878 \pm .002$	$.316 \pm .003$	$.143 \pm .002$
E_1	$.032 \pm .001$	$.530 \pm .003$	$.318 \pm .003$
E_2	$.090 \pm .002$	$.154 \pm .002$	$.539 \pm .003$
True Phase, ϕ	0	$.3511\pi$	1.045π
Est. Phase, $\hat{\phi}$	1.859π	$.377\pi$	1.045π
Error, $\frac{ \phi-\hat{\phi} }{2\pi}$	7.1%	1.3%	0.0%

Here we provide an example for the statistical inference of the phase based on numerical data generated by the photonic PEA experiment just described. The two unitary operations used in the experimental setup are

$$\hat{U}_1 = \text{diag}(1, \omega, \omega^2), \quad (2.110)$$

with ω being the cube root of unity (2.14), and

$$\hat{U}_2 = \text{diag}\left(1, e^{i0.351\pi}, e^{i1.045\pi}\right). \quad (2.111)$$

In the experiment, photonic qutrits are sent through the control and target registers and the state of the control register qutrits is measured and counted to obtain the phase information.

Given the eigenphase ϕ of an eigenstate of the target register, the probability for the qutrit output state to fall into $|n\rangle$, where $n \in \{0, 1, 2\}$, is

$$C(n, \phi) = \frac{1}{9} \left| 1 + e^{i(\phi - \frac{n2\pi}{3})} + e^{i2(\phi - \frac{n2\pi}{3})} \right|^2. \quad (2.112)$$

Now let E_0 , E_1 , and E_2 be the counts of the photons that fell into $|0\rangle_f$, $|1\rangle_f$, and $|2\rangle_f$. The estimated phase, denoted $\tilde{\phi}$, is the phase that has the smallest the mean-square error between the measured and theoretical results:

$$\min_{\tilde{\phi}} \sum_{n=0}^2 (E_n - C(n, \tilde{\phi}))^2 \quad (2.113)$$

The estimated phases for \hat{U}_1 (2.110) and \hat{U}_2 (2.111) are shown in Table 2.1 [13]. The first experiment with U_1 estimates the phase of a eigenvector and gives the eigenvalue. The second experiment with U_2 estimates the phase of a state with an arbitrary value (not a fraction of π), but, by repeating the experiment, the eigenvalue can be estimated from the statistical distribution of the results.

2.4.2 Ion trap

Intrinsic spin, an exclusively quantum property, has an inherently finite discrete state space which is a perfect choice for representing qubit or qudit. When a charged particle has spin, it possess a magnetic momentum and is controllable by external electromagnetic pulses. This concept leads to the idea of ion trap where a set of charged ions are confined by electromagnetic field. The hyperfine (nuclear spin) state of an atom, and lowest level vibrational modes (phonons) of the trapped atoms serves as good representations of the

qudits. The individual state of an atom is manipulated with laser pulse and the ions interact with each other via a shared phonon state.

The set-up of an ion trap qutrit system reviewed here can perform arbitrary single qutrit gates and a control-not gate [25]. These two kinds of gates form a universal set and thus can be combined to perform various quantum algorithms such as those discussed in §2.2. The electronic levels of an ion are shown in Fig. 2.14. The energy levels $|0\rangle, |1\rangle, |2\rangle$ are used to store the quantum information of a qutrit. The transition between the levels are driven by the classical fields $\Omega_{03}, \Omega_{13}, \Omega_{04}$ and Ω_{24} of the Raman transitions through independent channels linked to orthogonal polarizations. We first develop a system acting as a single qutrit gate that can manipulate the energy levels of the ion via Raman transitions driven by the classical fields. The following expressions follow those in Ref. [25]. For single qutrit gates, where the center-of-mass motion is excluded, we can include the spatial dependence of the Raman fields as phase factors Δ and assuming the conditions

$$\Delta \gg \Omega_{04}, \Omega_{03}, \Omega_{31}, \Omega_{42}, \quad (2.114)$$

the effective Hamiltonian describing the ion in this system is

$$\frac{H}{\hbar} = -\frac{|\Omega_{31}|^2}{\Delta} |1\rangle \langle 1| - \frac{|\Omega_{42}|^2}{\Delta} |2\rangle \langle 2| - \frac{|\Omega_{30}|^2 + |\Omega_{40}|^2}{\Delta} |0\rangle \langle 0| - \quad (2.115)$$

$$- \left[\frac{\Omega_{31}\Omega_{30}^*}{\Delta} |0\rangle \langle 1| + \frac{\Omega_{42}\Omega_{40}^*}{\Delta} |0\rangle \langle 2| + \text{hc} \right]. \quad (2.116)$$

Knowing the Hamiltonian we are able to derive the evolution operator in the restricted three-dimensional space spanned by $\{|2\rangle, |1\rangle, |0\rangle\}$ as the following

$$U(\varphi) = \begin{pmatrix} 1 + |g|^2 C(\varphi) & gg'^* C(\varphi) & -ig \sin \varphi \\ gg^* C(\varphi) & 1 + |g|^2 C(\varphi) & -ig \sin \varphi \\ -ig^* \sin \varphi & -ig'^* \sin \varphi & \cos \varphi \end{pmatrix}, \quad (2.117)$$

where $\varphi = \Omega t$ represents interaction time and

$$C(\varphi) = \cos \varphi - 1, \quad \Omega^2 = |\kappa|^2 + |\kappa|^2. \quad (2.118)$$

The notation g and g represents

$$g := \kappa/\Omega, \quad g = \kappa/\Omega, \quad \kappa := \Omega_{42}^* \Omega_{40}/\Delta, \quad \kappa = \Omega_{31}^* \Omega_{30}/\Delta. \quad (2.119)$$

This evolution operator can perform all kinds of the required coherent operations that are acting on any two of the logical states. It operates on the system and works essentially as a single qutrit gate. All kinds of transitions can be realized by manipulating the κ and κ coupling. Therefore with the proper manipulation of the parameters κ and κ we are able to perform any arbitrary one-qutrit gate as desired.

Single qutrit gate alone is not sufficient to form a universal computational set, as we need a conditional two-qutrit gate or a two-qutrit controlled-gate to achieve universality. To define the conditional two-qutrit gate we need an auxiliary level $|0\rangle$ as shown in Fig. 2.14. The conditional two-qutrit gate is achievable via the center-of-mass (CM) motion of ions inside the trap. The ion CM coupled to the electronic transition $|0\rangle \rightarrow |q\rangle$ is described by the Hamiltonian

$$H_{n,q} = \frac{\Omega_q \eta}{2} [|q\rangle_n \langle 0| a e^{-i\delta t - i\phi} + a^\dagger |0\rangle_n \langle q| e^{i\delta t + i\phi}]. \quad (2.120)$$

Here a is the annihilation operator and a^\dagger is the creation operator of the CM phonons. Ω_q is the effective Rabi frequency after adiabatic elimination of upper excited levels and ϕ is the laser phase, and δ is the detuning. The Lamb-Dicke parameter is

$$\eta := \sqrt{\hbar k_\theta^2 / (2M\nu_x)}. \quad (2.121)$$

This Hamiltonian governs the coherent interaction between qutrits and collective CM motion. With appropriate selection of effective interaction time and laser polarizations, the CM motion coupled to electronic transitions is coherently manipulated [25].

To complete the universal quantum computation requirements, we need to develop a measurement scheme. In this scheme, von Neumann measurements distinguishing three directions $|0\rangle$, $|1\rangle$, $|2\rangle$ are made possible via the resonant interactions from $|1\rangle$ and $|2\rangle$ to states $|3\rangle$ and $|4\rangle$, respectively. The single and two-qutrit controlled gate are combined to perform various qutrit algorithms such as the quantum Fourier transform. Other variations

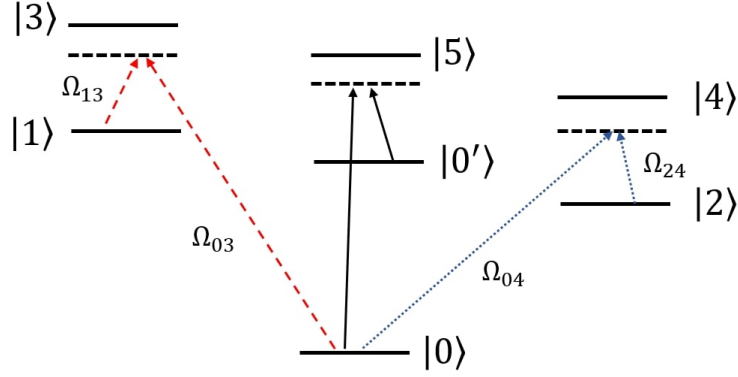


Figure 2.14. Electronic level structure of the trapped ion. The carrier of the quantum information is the qutrit states $|0\rangle$, $|1\rangle$, and $|2\rangle$. $|0'\rangle$ is an auxiliary level used for the conditional two-qutrit gate.

of the ion-trap qutrit quantum computer designs use trapped ions in the presence of a magnetic field gradient [285]. The qutrit ion-trap computer provides a significant increase of the available Hilbert space while demanding only the same amount of physical resources.

2.4.3 Nuclear magnetic resonance

Nuclear magnetic resonance (NMR) is an essential tool in chemistry and involves manipulating and detecting molecules' nuclear spin states using radio-frequency electromagnetic waves [286]. Some technologies of this field are sophisticated enough to control and observe thousands of nuclei in an experiment. The NMR has the potential to scale up quantum computer to thousands of qudits [287].

In this section we review the implementation of a single-qudit algorithm that can determine the parity of a permutation on an NMR system [26]. The algorithm itself is the parity determining algorithm explained in §2.2.1. The molecule in this NMR setup is embedded in a liquid crystalline environment and the strong magnetic field is used to adjust the anisotropic molecular orientation. This added a finite quadrupolar coupling term to the Hamiltonian which is as follows

$$H = -\omega_0 I_z + \Lambda(3I_z^2 - I^2), \quad (2.122)$$

where $\Lambda = e^2qQS/4$ is the effective value of the quadrupolar coupling [26]. The Fourier transformation is implemented by a sequence of three transition-selective pulses. A series of combinations of 180° pulses, both transition-selective and non-selective, is used to implement the permutations.

Final states of the system can be derived from a single projective measurement. Pseudopure spin states act as approximation of effect of the system on an ensemble NMR quantum computer since it is impossible to do the true projective measurements [288]. The fidelity measurement of the experiment is given as

$$F := \frac{\text{tr}(\rho_{\text{th}}^\dagger \rho_{\text{expt}})}{\sqrt{\text{tr}(\rho_{\text{th}}^\dagger \rho_{\text{th}})} \sqrt{\text{tr}(\rho_{\text{expt}}^\dagger \rho_{\text{expt}})}} \quad (2.123)$$

is used, where ρ_{th} and ρ_{expt} are, respectively, theoretically expected and experimentally obtained density matrices. Fidelities obtained for these proposed operations are 0.92 and above.

Another set-up of the same algorithm treats a single ququart [27]. The algorithm implementation is achieved using a spin- $\frac{3}{2}$ nuclei, which is commonly selected for NMR-QIP applications. In their NMR systems the four energy levels needed is made via the Zeeman splitting using a strong static magnetic field. All of the two implementations of the single-qudit algorithm show that the NMR system provides a way to realize a reliable and efficient qudit system for the quantum computing.

2.4.4 Molecular magnets

Molecular quantum magnets, also called the single-molecule magnets (SMM), provides another physical representation of qudits [278]. They have phenomenal magnetic characteristics and can be manipulated via chemical means. This enables the alternation of the ligand field of the spin carriers and the interaction between the SMM with the other units. As pointed out in one of the proposals, the nuclear spin states of the molecules, which have a long life-time, are used to store the quantum information. This information is read out by

the electronic states. In the mean time, the robustness of the molecule allows it to conserve its molecular, electronic and magnetic characteristics at high temperatures [289].

As one of the SMMs, the single molecule TbPc₂ complex reviewed in this section possesses all necessary properties such as long lifetime and robustness. These properties are integrated as important components of a serious quantum mechanical devices, for examples, resonator [290], molecular spin valve [291] and transistor [237], [292]. TbPc₂ gains its SMM properties from the strong spin-orbit coupling of lanthanide ions and the ligand field [293]. Magnetic properties of TbPc₂ are governed by the Hamiltonian:

$$\mathcal{H} = \mathcal{H}_{\text{lf}} + g_J \mu_0 \mu_B J \cdot H + A_{\text{hf}} I \cdot J + (I_z^2 - \frac{1}{3}(I+1)I), \quad (2.124)$$

where \mathcal{H}_{lf} is the ligand field Hamiltonian(lf), and $g_J \mu_0 \mu_B J \cdot H$ represents the Zeeman energy. $A_{\text{hf}} I \cdot J$ accounts for hyperfine interactions(hf) and $(I_z^2 - \frac{1}{3}(I+1)I)$ is the quadrupole term. A sweeping magnetic field associated with $m_I = \pm 1/2$ and $\pm 3/2$ can cause quantum tunnelling of magnetisation, which preserves nuclear spin while changing electronic magnetic moment. This field enables nuclear-spin measurement by suspending the TbPc₂ molecule on carbon nanotubes (CNT) and between gold junctions.

This measurement uses the technique of electro-migration. Initialisation and manipulation of the four spin states of TbPc₂ can be obtained from QTM transitions driven by external ramping magnetic field. The transitions between the $|+1/2\rangle \leftrightarrow |-1/2\rangle$ states and $|+3/2\rangle \leftrightarrow |-3/2\rangle$ is achieved via applying appropriate resonate frequencies ν_{12} and ν_{23} . Relaxation and coherence times are important aspects to be analyzed for the TbPc₂ system, and this process is accomplished by imaging the initialized nuclear spin trajectory in real-time.

Statistical analysis of the nuclear spin coherence time makes use of the spin-lattice relaxation times by fitting the data for an exponential form ($y = \exp(-t/T_1)$) and yields $T_1 \approx 17$ s for $m_I = \pm 1/2$ and $T_1 \approx 34$ s for $m_I = \pm 3/2$ with fidelities of $F(m_I = \pm 1/2) \approx 93\%$ and $F(m_I = \pm 3/2) \approx 87\%$ accordingly [278]. The TbPc₂ SMM can be used to execute Grover's algorithm, where the alternation of the m_I state contained in the TbPc₂ molecular qubit are treated by resonance frequencies [28], [294].

2.5 Summary and future outlook of qudit system

2.5.1 Summary of the advantages of qudit systems compared to qubit systems

Throughout the article we discuss and review many aspects of the qudit systems such as qudit gates, qudit algorithms, alternative computation models and implementations. Most gates and algorithms based on qudits have some advantages over those for qubits, such as shorter computational time, lower requirement of resources, higher availability, and the ability to solve more complex problems. The qudit system, with its high-dimensional nature, can provide more degrees of freedom and larger computational space. This section summarizes the advantages of the qudit system compared to the qubit system.

Qudit gates have the advantage of a larger working Hilbert space which reduces the number of qudits needed to represent an arbitrary unitary matrix. In our discussion of universality in §2.1.1, the qudit method proposed by Muthukrishnan and Stroud's has a $(\log_2 d)^2$ scaling advantage over the qubit case. Furthermore, Luo and Wang show that with their proposed universal computation scheme [14], there is an extra factor of n reduction in the gate requirement, where n is the number of qudits. By introducing qudits to the construction of some well-known gates such as the Toffoli gate, the elementary gate required are reduced from $12n - 11$ gates in the qubit case to $2n - 1$ gates by introducing a single $(n + 1)$ -level target carrier [33] and to $2n - 3$ gates by utilizing the topological properties [34]. In our discussion of the geometrically quantified qudit-gate efficiency in §2.1.3, the qubit system needs $O(n^6 d(I, U)^3)$ one- and two-qubit gates to synthesize a unitary [213] while in the qutrit case the lower bound is $O(n^k d(I, U)^3)$ where k is an integer that depends on the accuracy of the approximation and can be smaller than 6 [15].

For many of the physical systems such as photons [266], [267], super conducting systems [268], [269], trapped ions [270], [271], magnetic [272]–[275] and non-magnetic molecules [276], [277] there are usually more than two available physical states available for the applications. The qudit system has a higher efficiency utilizing those extra states than the qubit system. Also using the photonic system, we can perform the multi-level controlled gate (§2.1.2) which can perform multiple control operations at and same time and largely reduce the number of controlled gates requirement [13].

Other than computation, the qudit also has advantages in quantum communication as it possesses a higher noise resilience than the qubit [295]. The qudit system has a higher quantum bit error rate (QBER), which is a measure of resistance to the environmental noise or eavesdropping attacks, compared to the qubit system. The higher noise tolerance of the qudits helps to increase the secret key rate as it can be shown that the secret key rate increases as the Hilbert space dimensions increase at the same noise level [296]. Notice that in practical situation, the qudit system performed on each particular physical apparatus has varied amount of advantages than the qubit and there might be cases in which the high-dimensional states have a higher transmission distance [295]. This higher noise resilience of qudits is more advantageous if the qudits are entangled. The entanglement becomes more robust by increasing the dimension of the qudits while fixing their numbers. In other words, as the noise sources act locally on every system, increasing the dimension d will reduce the number of systems and thus reduce the effect of noise resulting in the robustness increase [297]. The increasing noise level tolerance as the qudit dimension increases can be shown on an photonic OAM system as an example of its implementation [298].

In summary the qudit system possesses advantages in the circuit design, physical implementation and has the potential to outperform the qubit system in various applications.

2.5.2 Future outlook of qudit system

This review article introduces the basics of the high-dimensional qudit systems and provides details about qudit gates, qudit algorithms and implementations on various physical systems. The article serves as a summary of recent developments of qudit quantum computing and an introduction for newcomers to the field of qudit quantum computing. Furthermore we show the advantages and the potential for qudit systems to outperform qubit counterparts. Of course these advantages can come with challenges such as possibly harder-to-implement universal gates, benchmarking [299]–[301], characterization of qudit gate [302], [303] and error correction connected with the complexity of the Clifford hierarchy for qudits [186].

Compared to qubit systems, qudit systems currently have received less attention in both theoretical and experimental studies. However, qudit quantum computing is becoming in-

creasingly important as many topics and problems in this field are ripe for exploration. Extending from qubits to qudits ushes in some mathematical challenges, with these mathematical problems elegant and perhaps giving new insights into quantum computing in their own right. Connections between quantum resources such as entanglement, quantum algorithms and their improvements, scaling up qudit systems both to higher dimension and to more particles, benchmarking and error correction, and the bridging between qudits and continuous-variable quantum computing [184] are examples of the fantastic research directions in this field of high-dimensional quantum computing.

3. QUANTUM PHASE ESTIMATION WITH TIME-FREQUENCY QUDITS IN A SINGLE PHOTON

The contents of this chapter are based on and modified from the article [13] Lu, H. H., Hu, Z., Alshaykh, M. S., Moore, A. J., Wang, Yuchen, Imany, P., ... & Kais, S. (2020). Quantum phase estimation with time-frequency qudits in a single photon. *Advanced Quantum Technologies*, 3(2), 1900074, Copyright (2019) by John Wiley & Sons, Inc.

This chapter presents the quantum phase estimation with time-frequency qudits in a single photon [13]. It is organized in three sections, theory, experimental results and discussion.

3.1 Theory

Suppose $|\psi\rangle$ is an eigenstate of a unitary operator \hat{U} with the unknown eigenvalue $e^{i\phi}$, the phase estimation algorithm can evaluate the phase (ϕ) with polynomial resource (in terms of the number of qudits and gates needed)[206]. The PEA procedure is illustrated in Figure 3.1(a) with a target register to represent $|\psi\rangle$ and a control register to hold the information on ϕ which is then extracted by an inverse quantum Fourier transform (QFT)[206]. The dimension of the target register has to match that of $|\psi\rangle$ to fully represent the quantum

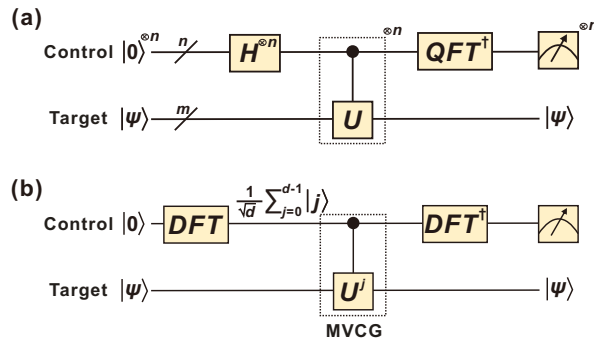


Figure 3.1. (a) Schematic for a general qubit-based PEA using n -qubit control and m -qubit target states. $H^{\otimes n}$ is a set of Hadamard gates acting on n qubits in parallel. U is an unitary operator operating on the target state. n control- U gates, one for each control rail, are present. QFT^\dagger is the inverse quantum Fourier transform on the n -qubit control register. (b) Schematic for a single-qudit-based PEA. d -point discrete Fourier transform (DFT) is a Hadamard gate generalized to d -dimensional state (See Eq. (3.1)). A multi-value-controlled-gate (MVCG) applies \hat{U}^j to the target when the control is in the $|j\rangle$ state.

state, while the dimension of the control register determines the precision of the evaluation of ϕ . In particular, if we use n d -dimensional qudits for the control register then we can evaluate ϕ with the precision $2\pi/d^n$. A Hilbert space of dimension $N = 2^m = d^n$ can be represented either by m qubits ($d = 2$) or n qudits ($d > 2$), therefore using a qudit based PEA allows us to achieve the same precision or represent the same $|\psi\rangle$ with fewer number of qudits – more precisely $m = n \log_2(d)$ implies a $\log_2(d)$ reduction of the circuit width (number of qudits) required. Using qudits may also reduce the circuit depth by reducing the number of controlled gates used to realize the controlled- \hat{U} operation. The quantum circuit for a qudit based PEA[37] generalizes the two-value controlled- \hat{U} gate for the qubit case to a multi-value-controlled-gate (MVCG) that applies \hat{U}^j to the target register when the control register is in the $|j\rangle$ state ($j = 0, 1, \dots, d-1$). The functionalities of the n two-qubit controlled gates utilized in the conventional qubit-based PEA circuit[206] can be realized with a single MVCG having 2^n controlled values, thus reducing the depth of our PEA circuit.

Figure 3.1(b) shows the schematic of a qudit-based PEA. The DFT gate here is a d -point discrete Fourier transform (DFT) defined as $DFT^{(d)} |j\rangle = \frac{1}{\sqrt{d}} \sum_{k=0}^{d-1} e^{2\pi i(jk/d)} |k\rangle$. The DFT gate can be understood as a qudit generalization of the Hadamard gate to dimensions beyond $d = 2$ [57], [304]. When operating on a single qudit, both the Hadamard gates and the QFT in Figure 3.1(a) are reduced to a single DFT gate. We would like to emphasize that, in this work we use the “DFT” to denote a *single*, high-dimensional gate capable of applying the discrete Fourier transform to a single qudit state, while the “QFT” denotes the standard quantum algorithm of applying the discrete Fourier transform to a multi-qubit state. Different from the DFT, the QFT often requires a sequence of single-qubit and two-qubit gates to implement. The MVCG then applies \hat{U}^j on the target state conditional on the control state $|j\rangle$ (i.e., $|j\rangle |\psi\rangle \rightarrow |j\rangle \hat{U}^j |\psi\rangle$). Finally, the phase kickback mechanism in the PEA[206] allows us to evaluate the ϕ by applying an inverse DFT on the control register, and performing measurements in the computational basis. The quantum circuit can deterministically evaluate the eigenphase ϕ for each eigenstate of \hat{U} , insofar as ϕ can be written exactly with the given precision. If the input state is in superposition of eigenstates instead, performing measurements on the control register will yield probabilistic results, and one can obtain the correct statistics of ϕ .

As a proof-of-concept implementation, here we limit our dimension to $d = 3$ (qutrit) for both the control and target registers, capable of retrieving the eigenphase of a given three-dimensional unitary with $2\pi/3$ precision. We introduce the three-point DFT gate in its matrix form,

$$DFT^{(3)} = \frac{1}{\sqrt{3}} \begin{pmatrix} 1 & 1 & 1 \\ 1 & e^{2\pi i/3} & e^{4\pi i/3} \\ 1 & e^{4\pi i/3} & e^{2\pi i/3} \end{pmatrix}. \quad (3.1)$$

And the unitary (\hat{U}_1) of interest in our first demonstration is simply a Pauli-Z gate generalized to the qutrit space:

$$\hat{U}_1 = \begin{pmatrix} 1 & 0 & 0 \\ 0 & e^{2\pi i/3} & 0 \\ 0 & 0 & e^{4\pi i/3} \end{pmatrix} \quad (3.2)$$

where the eigenphases 0 , $2\pi/3$, and $4\pi/3$ can be exactly represented with a single ternary digit expansion.

3.2 Experimental results

In this experiment, we leverage the well-established techniques and fiber-optic components developed for optical communication and wavelength division multiplexing to create and manipulate high dimensional quantum states for PEA implementation. Figure 3.2(a) provides a schematic of the setup, which can be decomposed into three stages: state preparation, high-dimensional controlled operation, and measurement on the control qudit.

To prepare an equi-amplitude superposition of frequency qutrit as the control register, we send a continuous-wave (CW) laser source operating in the C-band through a phase modulator (PM1) driven at 18 GHz, which creates a total number of ~ 10 frequency bins with a spacing of 18 GHz. Subsequently, a pulse shaper (PS1) is programmed to filter out all but three equi-amplitude frequency bins, now with a frequency spacing (Δf) of 54 GHz. Note that since the controlled gate in our proposed setup is a one-photon operation, the

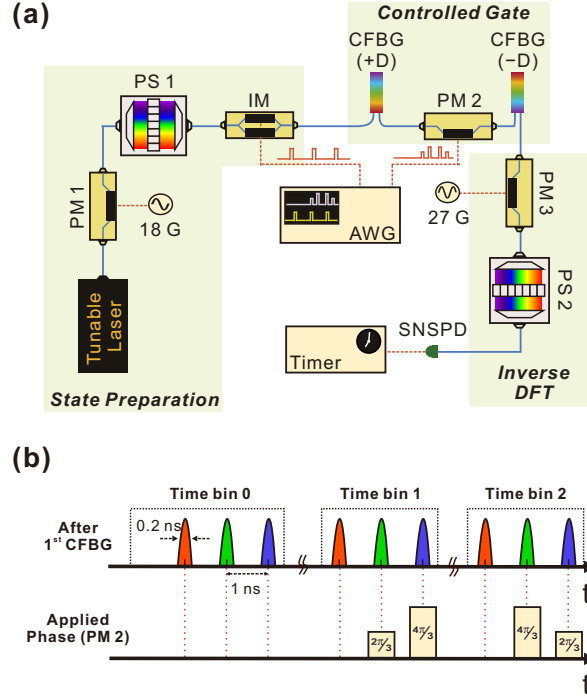


Figure 3.2. (a) Experimental setup. (b) Implementation of controlled-phase gate. See text for details. (PM/IM: Electro-optic phase/intensity modulator; PS: Fourier-transform pulse shaper; CFBG: Chirped fiber bragg grating; SNSPD: Superconducting nanowire single-photon detector; AWG: Arbitrary waveform generator. Both radio-frequency oscillators (18 and 27 GHz) are synchronized to the 10 MHz reference clock of the AWG.)

input photon number statistics have no impact on the operation, thus coherent states can be used instead of true single photons as the input.

To prepare the target qutrit state, we employ an intensity modulator (IM) driven by an arbitrary waveform generator (AWG), and carve out three narrow time bins each with a 6 ns spacing, a 24 ns repetition period, and a full width at half maximum of ~ 0.2 ns which broadens the frequency-bin line-width to 2.2 GHz. As our unitary matrix of interest (Eq 3.2) is diagonal, the target qutrit eigenstates are single time bins. Thus, we choose to treat each time bin as an independent eigenstate. Each experimental trial can be thought of as three separate measurements made in quick (6 ns) succession. Considering only one of the

time bins (eigenstates) at a time, the state after the state preparation stage can be written as:

$$|\psi\rangle_{in} \propto \sum_{j=0}^2 |j\rangle_f \otimes |\tau\rangle_t \quad (3.3)$$

where $\tau = \{0, 1, 2\}$ denotes which time bin is chosen to operate. The controlled gate itself consists of a phase modulator (PM2) sandwiched between two chirped fiber Bragg grating (CFBG). The first CFBG has a dispersion of 2 ns/nm imparting a frequency-dependent delay which splits each time bin into 3 daughter time bins, each of which corresponds to one frequency mode [red, green and blue pulses in Figure 3.2(b)]. The spacing between daughter time bins (Δt) is 0.9 ns, which is larger than the time-bin coherence time (~ 0.2 ns) and its product with the frequency-bin spacing (54 GHz) exceeds the Fourier transform limit (i.e., $\Delta f \Delta t > 1$), allowing independent manipulation of the time and frequency DoFs. Using the AWG, we program the phase modulator to apply the unitary U^j defined in Eq. (3.2) to time-bin states conditional on the frequency-bin state $|j\rangle_f$. The second CFBG with an opposite dispersion of -2 ns/nm cancels the first dispersion module and recombines the three daughter time bins back into a single indistinguishable time bin. After the application of MVCG, we can obtain an output state

$$|\psi\rangle_{out} \propto \sum_{j=0}^2 e^{\frac{i2\pi j\tau}{3}} |j\rangle_f \otimes |\tau\rangle_t \quad (3.4)$$

Note that the phases applied to the time-bin state are now attached to the control register, a process called “phase kickback.”

An ideal three-point inverse DFT gate performs the following transformation:

$$\frac{1}{\sqrt{3}} \sum_{j=0}^2 e^{\frac{i2\pi j\tau}{3}} |j\rangle_f \xrightarrow{DFT^{-1}} |\tau\rangle_f \quad (3.5)$$

and thus applying inverse DFT on the control state allows us to read out the phase based on the detection pattern in the logical basis. Detection in output state $|\tau\rangle_f$ indicates the retrieved phase $\tilde{\phi}$ equals to $2\pi\tau/3$ ($2\pi \times 0.\tau_3$ in ternary expression). Recently a near-deterministic, three-dimensional DFT for frequency-encoded qutrit has been demonstrated

with near-unity fidelity, utilizing a quantum frequency processor circuit[305] consisting of two electro-optic phase modulators and one pulse shaper. Due to equipment availability, we elect to implement a simpler, probabilistic ¹ version of inverse DFT using a single phase modulator (PM3), capable of performing the equivalent functions in a multi-shot fashion. The control state, consisting of three frequency bins with 54 GHz spacing, is phase modulated by a 27 GHz sine waves to create frequency sidebands. We fine-tune the modulation index to 1.843 rad such that each frequency bin projects onto the central bin $|1\rangle_f$ with equal probability. We utilize another pulse shaper (PS2) as a bandpass filter to pick out this overlapped bin, and then route to a superconducting nanowire single-photon detector (SNSPD) for measurement. Since the output now consists of projections from all three frequency bins, the measured counts will reflect the relative phases due to interference.

Given a control register in the state $\propto \sum_{j=0}^2 |j\rangle_f$ (LHS of Eq. (3.5) when $\tau = 0$) as the input of the PM3, after frequency mixing we have maximum photon counts in the overlapped bin due to constructive interference. The other two orthogonal states will instead experience destructive interference and thus contribute no photon counts. This operation is equivalent to the transformation described in Eq. (3.5) for $\tau = 0$, namely the projection onto $|0\rangle_f$. We can also tune the delays between the input photons and the electrical drive on PM3, such that the other two transformations (Eq. (3.5) for $\tau = 1, 2$) can be achieved. Different delay settings can be achieved by introducing an additional pulse shaper prior to frequency mixing, or a radio-frequency phase shifter to impart the required delay. Here we choose to lump this function into PS1 in the state preparation stage to reduce the insertion loss and the complexity of the system. To avoid any confusion, for the rest of the paper we name the three delay settings required to realize the equivalent inverse DFT functions simply as “projection onto $|0\rangle_f$, $|1\rangle_f$ and $|2\rangle_f$ ”, respectively.

Under each delay setting, we measure the photon counts in three time bins recorded over 1 second. We note that these time bins are widely spaced and do not interfere, hence, this measurement can be considered as three independent measurements of each eigenstate in

¹↑A single phase modulator will necessarily scatter input photons out of the computational space, thus make the gate probabilistic. See [57], [58], [306] for detailed discussions.

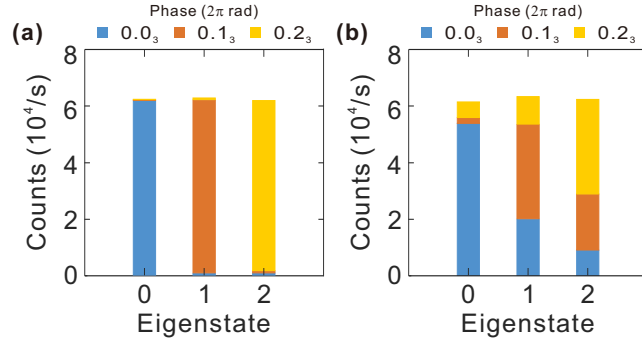


Figure 3.3. Experimental results for implementing (a) \hat{U}_1 (Eq. 3.2), and (b) \hat{U}_2 (Eq 3.7). Color of the bars corresponds to number of photon counts registered after inverse DFT projection onto $|0\rangle_f$ (blue), $|1\rangle_f$ (red), and $|2\rangle_f$ (yellow). Photon counts are recorded over 1 second.

series. As shown in Eq. 3.4, the phase attached to the control register after the MVCG matches the inverse DFT transformation described in Eq. 3.5, thus we have

$$\sum_{j=0}^2 e^{\frac{i2\pi j\tau}{3}} |j\rangle_f \otimes |\tau\rangle_t \xrightarrow{DFT^{-1} \otimes I} |\tau\rangle_f \otimes |\tau\rangle_t \quad (3.6)$$

which shows for time-bin $|\tau\rangle_t$ as the input target, ideally we will only obtain photon counts after projecting the control register onto $|\tau\rangle_f$. Figure 3.3(a) shows the experimental results for estimating the eigenphase of \hat{U}_1 . For each target eigenstate, we stack three color-coded vertical bars in a single slot to represent the registered counts for different frequency projections. The total number of counts remain stable across three successive measurements, and most of the counts for eigenstate $|\tau\rangle_t$ are recorded after projection onto $|\tau\rangle_f$. The results match our prediction, as all three eigenphases for \hat{U}_1 can be represented with exactly one ternary digit, and thus the phase can be retrieved deterministically. The fidelity of this measurement, here defined as the ratio of photon counts registered at the correct output to the total number of received photons, is $98 \pm 1\%$.

For the second part of the experiment, we reprogram our MVCG operation by applying a different temporal phase mask imparted by the AWG to implement another unitary \hat{U}_2 :

$$\hat{U}_2 = \begin{pmatrix} 1 & 0 & 0 \\ 0 & e^{i0.351\pi} & 0 \\ 0 & 0 & e^{i1.045\pi} \end{pmatrix}. \quad (3.7)$$

Note that two of the eigenphases are no longer integer multiples of $2\pi/3$, or namely, the phase attached onto the control frequency bins (after phase kickback mechanism) does not match the inverse DFT to transform into a single logical state. Figure 3.3(b) shows the measured counts for all eigenstates under different inverse DFT settings. For the first eigenstate, its corresponding phase is 0 and hence most of the counts are still registered in $|0\rangle_f$. The other two eigenstates, as discussed above, possess phases which cannot be accurately retrieved given a single ternary digit precision, and thus the counts are distributed over different projections. Following the conventional PEA approach, we report the retrieved phase ($\tilde{\phi}$)

based on the projection with the highest number of counts. For eigenphases ϕ equal to 0.351π and 1.045π , the corresponding $\tilde{\phi}$ are $2\pi/3$ and $4\pi/3$, respectively. In the following section, we will discuss whether more information can be extracted from the counts distribution shown in Figure 3.3, given (i) the input state is already prepared in the eigenstate, and (ii) an ample amount of counts are registered for further analysis.

3.3 Discussion

When the input target register of a PEA circuit is an eigenstate with a corresponding eigenphase ϕ , the probability for the qutrit output control state to collapse to $|n\rangle$, where $n = \{0, 1, 2\}$, is

$$C(n, \phi) = \frac{1}{9} \left| 1 + e^{i(\phi - \frac{n2\pi}{3})} + e^{i2(\phi - \frac{n2\pi}{3})} \right|^2. \quad (3.8)$$

All three $C(n, \phi)$, for $n = \{0, 1, 2\}$, are plotted in Figure 3.4. Observe that for each ϕ , the ordered set $\{C(0, \phi), C(1, \phi), C(2, \phi)\}$ is unique. Now let E_0 , E_1 , and E_2 be the measured, normalized ($\sum E_n = 1$) photon counts projected, respectively, onto $|0\rangle_f$, $|1\rangle_f$, and $|2\rangle_f$. The phase we estimate from our measurement, denoted $\tilde{\phi}$, is the phase which minimizes the mean squared error between the measured and theoretical probabilities:

$$\min_{\tilde{\phi}} \sum_{n=0}^2 (E_n - C(n, \tilde{\phi}))^2 \quad (3.9)$$

The estimated phases for \hat{U}_1 (Eq. 3.2) and \hat{U}_2 (Eq. 3.7) are shown in Table 3.1. The results for \hat{U}_2 are plotted in Figure 3.4 alongside the three $C(n, \phi)$ curves of Eq. 3.8. The largest error in $\tilde{\phi}$ is 7.1%, and the error is less than 3% in all other cases. Our photonic system's ability to execute large number of trials enables this statistical approach to phase estimation. Agreement between estimated and true phase can be used to quantify error in the experimental setup; however, because the statistical approach requires an eigenstate input, it should not be viewed as a standalone method for determining an unknown phase. To obtain a more precise phase estimate, where the input need not be an eigenstate and the

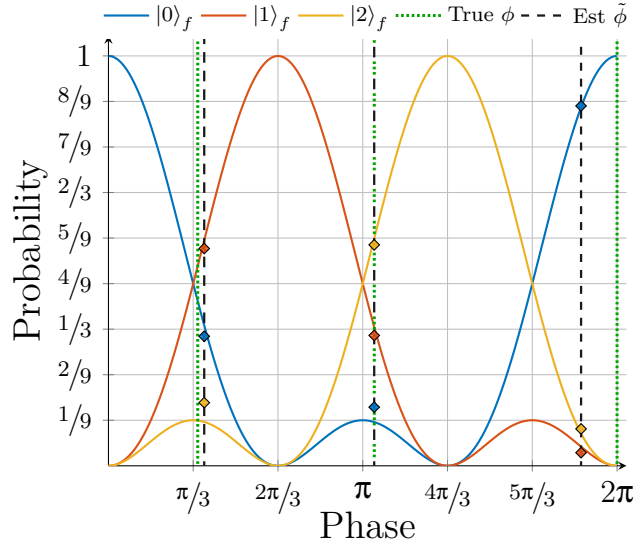


Figure 3.4. The three curves represent the probability of the control qutrit collapsing to bin $|n\rangle_f$ for $n = \{0(\text{blue}), 1(\text{red}), 2(\text{yellow})\}$ for any eigenphase corresponding to the eigenstate input of a PEA circuit. The normalized experimental photon counts for all three eigenstates of \hat{U}_2 are fitted to – and plotted at – the estimated phase ($\tilde{\phi}$) which minimizes mean squared error (Eq 3.9). $\tilde{\phi}$ is denoted by the position of the markers and the black dashed line; the location of the true phase (ϕ) for each eigenstate is noted with a green dashed line. The curves are described by Eq 3.8; the plotted values can be found in Table 3.1.

phase is not restricted to a value representable by a single ternary digit, an iterative PEA, explained below, must be implemented.

The next steps for our qudit-based PEA are (i) implementing arbitrary unitaries (i.e. non-diagonal) in addition to increasing the qudit dimension ($d > 3$); and (ii) increasing the digits of precision for evaluating the phase. For Step (i) we choose to work with frequency and time DoF in photons, since we can take advantage of their inherent high dimensionality to encode more quantum information in a single qudit. For example, our group has recently demonstrated a two-photon four-party GHZ state by encoding two 32 dimensional qudits in each photon.[59] In addition, the recipe of constructing high-dimensional quantum gate, though still relatively limited, has been proposed and experimentally realized on both time-bin and frequency-bin platforms. Scalable processing of time-bin qudits has been proposed using a cascade of electro-optic phase modulator and coded fiber Bragg grating pairs.[307]

Table 3.1. Normalized photon counts and comparison of true phase ϕ and experimentally estimated phase $\tilde{\phi}$ for each eigenstate of \hat{U}_1 (Eq. 3.2) and \hat{U}_2 (Eq. 3.7). Photon counts normalized from results in Figure 3.3.

\hat{U}_1			
Eigenstate	$ 0\rangle_t$	$ 1\rangle_t$	$ 2\rangle_t$
E_0	$.9948 \pm .0004$	$.0101 \pm .0004$	$.0122 \pm .0005$
E_1	$.0023 \pm .0002$	$.9805 \pm .0009$	$.0120 \pm .0005$
E_2	$.0029 \pm .0002$	$.0094 \pm .0004$	$.9758 \pm .0010$
True Phase, ϕ	0	$2\pi/3$	$4\pi/3$
Est. Phase, $\tilde{\phi}$	1.972π	$.612\pi$	1.394π
Error, $\frac{ \phi-\tilde{\phi} }{2\pi}$	1.4%	2.7%	3.0%
\hat{U}_2			
Eigenstate	$ 0\rangle_t$	$ 1\rangle_t$	$ 2\rangle_t$
E_0	$.878 \pm .002$	$.316 \pm .003$	$.143 \pm .002$
E_1	$.032 \pm .001$	$.530 \pm .003$	$.318 \pm .003$
E_2	$.090 \pm .002$	$.154 \pm .002$	$.539 \pm .003$
True Phase, ϕ	0	$.3511\pi$	1.045π
Est. Phase, $\tilde{\phi}$	1.859π	$.377\pi$	1.045π
Error, $\frac{ \phi-\tilde{\phi} }{2\pi}$	7.1%	1.3%	0.0%

Quantum state tomography of time-bin ququarts ($d = 4$) has also been realized with cascaded Mach-Zehnder interferometers fabricated on planar light-wave circuit.[308] And finally, our group has been involved in the design and construction of a quantum frequency processor[305], [309] consisting of a series of phase modulators and pulse shapers, found capable of implementing qudit transformations with favorable component requirements. Though eventually to implement a general MVCG operation still demands careful design and perhaps exploitation of other DoFs to realize the controlled operation, the basic formula is ready to be explored.

For Step (ii), our current setup uses a single control qudit to estimate the phase with $2\pi/d$ precision (in this experiment, $d = 3$). To achieve higher precision phase estimation we can either increase the number of control qudits or implement an iterative PEA.[75] The iterative PEA is the more viable approach for photonic systems, as it avoids the difficulty in manipulating and interacting multiple photon qudits. Using only one d -dimensional qudit as the control register, the iterative PEA can evaluate the phase with $2\pi/d^n$ precision by running n iterations of a modified single-qudit PEA algorithm. Here each iteration requires a modified MVCG and an additional quantum gate. For the k^{th} iteration out of all n iterations, the \hat{U} gate becomes \hat{U}^x , where $x = d^{(n-k)}$, and therefore the modified MVCG applies $(\hat{U}^x)^j$ to the target qudit when the control qudit is $|j\rangle$. As our current approach applies \hat{U}^j directly (i.e. not cascading \hat{U} j times), implementing the MVCG with $(\hat{U}^x)^j$ is no more challenging than the MVCG with \hat{U}^j . For the additional quantum gate, on the k^{th} iteration the control qudit undergoes an R_z -rotation of the angle $\theta = -\sum_{i=1}^{k-1} \frac{\phi_i}{d^{k-i}}$ where each ϕ_i is the phase determined by the i^{th} iteration prior to the k^{th} iteration. Our successful implementation of the controlled gate in this paper demonstrates all the capability needed for implementing the arbitrary (diagonal) R_z -rotation. We note the two operations needed to achieve a standard iterative PEA can also be used to implement a Bayesian phase estimation approach known as rejection filtering phase estimation (RFPE)[48]. RFPE is robust to noise and promises a speed up over standard iterative PEAs by gaining information about multiple bits (for us, dits) of the phase at a time. For the standard (non-Bayesian) PEA, qudits provide a $\log_2(d)$ reduction in the number of iterations needed to estimate a given phase with success rate identical to the qubit case. As with qubit systems, an arbitrarily-high success rate can be

achieved via multiple trials for some (or all) iterations. As our photonic system provides photon statistics easily, a low-error iterative PEA or RFPE is a natural next step. Using an iterative PEA avoids cumbersome multi-photon gates for the control qudit; however, we note that multiple target qudits may be needed to accommodate a unitary \hat{U} of a high dimension M . To be precise, the number of target qudits m must be $\geq \log_d(M)$, thus \hat{U} becomes a multi-photon gate when $\log_d(M) > 1$. Our ability to implement a high-dimensional \hat{U} scales polynomially with the qudit dimension d and exponentially with the number of target qudits m .

Combining Step (i) and (ii), we provide the outlook for a potential high-dimensional single-photon PEA system capable of implementing any arbitrary (non-diagonal) unitary U . Extending to higher dimensions, we prefer frequency as the target register as we have developed a more concrete recipe to construct high-dimensional gates with favorable resource requirement [309]. The state preparation will be similar to that of Fig. 3.2, in which the number of frequency bins should match the dimension of U . The dimension of the control (time) qudit d , on the other hand, can be significantly smaller and arbitrarily chosen as the desired precision of the phase retrieval can be achieved with the introduction of iterative PEA. As described in the previous paragraph, each iteration provides an additional d -digit of precision in phase estimation. To implement the MVCG for the k^{th} iteration out of all n iterations, we could introduce a Mach-Zehnder-based switch to route d time bins to d different optical paths, in each of which we place a quantum frequency processor programmed to apply a high-dimensional frequency operation $(\hat{U}^x)^j$ to the target qudit for the j^{th} path (i.e., when the control qudit is $|j\rangle_t$). The additional R_z -rotation on the control qudits required for the iterative PEA amounts to an overall phase shift at each path, and can be absorbed in the quantum frequency processor design as well. Finally, we can recombine all paths and utilize a cascaded interferometer tree [55] to realize the d -dimensional DFT gate for projective measurement.

In conclusion, this work has successfully demonstrated the first implementation of the PEA on a qudit-based photonic platform. This experiment utilized the high dimensionality of the time and frequency DoFs on a single photon to realize the 2-qudit MVCG gate, circumventing the inherently probabilistic photon-photon interactions. Although limited to a

proof-of-principle model with arbitrary-phase diagonal unitaries, this work is a first physical demonstration of a qudit-based PEA. Future improvements to our PEA include higher-dimensional qudits ($d > 3$), arbitrary (non-diagonal) unitaries, and statistical estimation of the phase via large ensemble measurements.

4. STATISTICAL APPROACH TO QUANTUM PHASE ESTIMATION

The contents of this chapter are based on and modified from the article [65] Moore, A. J., Wang, Yuchen, Hu, Z., Kais, S., & Weiner, A. M. (2021). Statistical approach to quantum phase estimation. New Journal of Physics, 23(11), 113027., Copyright (2021) by The Author(s). Original content from this work may be used under the terms of the Creative Commons Attribution 4.0 licence. Published by IOP Publishing Ltd on behalf of the Institute of Physics and Deutsche Physikalische Gesellschaft.

This chapter presents a statistical approach to quantum phase estimation. It is organized as follows: §4.1 reviews the traditional and iterative PEA and introduces a statistical metric \mathcal{C} for quantifying the proximity of any given input-state to its closest eigenstate. §4.2 describes the Statistical PEA and discusses the connections between the \mathcal{C} factor and the quality (in terms of proximity) of the derived eigenstate-eigenphase pairs (with the derivation details in A.1). §4.2 also outlines the optimization process for obtaining the eigenstate-eigenphase pairs. Simulation results on different platforms are reported and discussed in §4.3; methodology details are provided in A.2 and A.3. Scaling for larger systems is considered in §4.4. We conclude with a discussion on the performance of the SPEA and propose future directions and applications of the method in §4.5.

4.1 Phase Estimation Algorithms

Traditional PEA implementations, diagrammed in Figure 4.1, take any given unitary \hat{U} and any given eigenstate $|\nu\rangle$ of \hat{U} and return the corresponding eigenphase θ where

$$\hat{U} |\nu\rangle = e^{i2\pi\theta} |\nu\rangle. \tag{4.1}$$

The (approximate) eigenphase $\tilde{\theta} \in [0, 1)$ (equivalently, $\in [-.5, .5)$) may be directly measured on the control qubits (or qudits, when the control is d_c -dimensional) of the PEA. The target register is typically unmeasured during the process. For an arbitrary target register input $|\Phi\rangle$, the probability of the circuit representing a particular eigenstate $|\nu_k\rangle$ and the associated eigenphase θ_k is $|\langle \nu_k | \Phi \rangle|^2$. If $|\Phi\rangle$ is not itself an eigenstate, the eigenphase retrieved varies

each time the PEA circuit is run. The prototypical PEA thus approximates a particular θ in a single trial.

The traditional PEA requires large quantum circuits which are often unreliable in the NISQ regime. To overcome hardware constraints, the iterative PEA (IPEA) was developed. The IPEA significantly reduces circuit depth requirements by approximating a particular θ one qubit (or d_c -level qudit) at a time, starting from the least significant qubit (qudit). The IPEA requires a rotation gate – a linear phase across the control register – to “subtract” off eigenphase information determined in previous iterations. (I.e. if the quantum circuit’s state before $R_z(\theta_R)$ is $\sum_q \alpha_q |q\rangle |\Phi_q\rangle$, then after the rotation gate the quantum circuit’s state is $\sum_q \alpha_q e^{-iq2\pi\theta_R} |q\rangle |\Phi_q\rangle$.) The iterative PEA, as the name suggests, requires a number of iterations equal to the number of bits (dits) of precision desired from the eigenphase. Additionally, the input to the target register of an IPEA must either be an eigenstate (and identically prepared each iteration) or the previous iteration’s output must propagate forward and serve as the next iteration’s input.

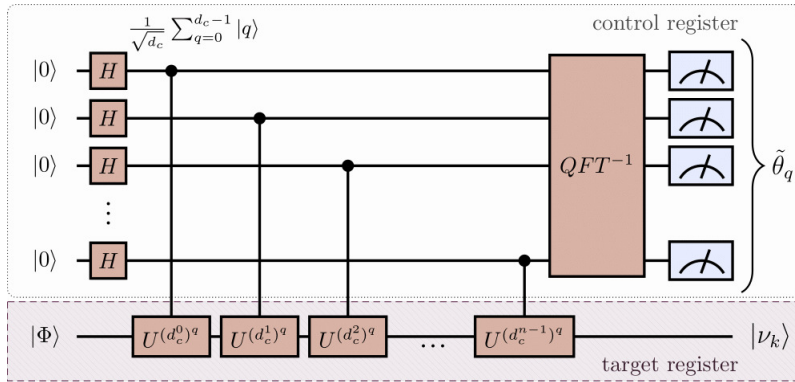


Figure 4.1. The traditional PEA using n control d_c -dimensional qudits in the control register. The quantum gates are colored in brown and the measurement gates in blue. The target register is highlighted in purple with dashed outline and control register in grey with dotted outline. Note that in the $d_c > 2$ case, the H “Hadamard” gate acts as a discrete quantum Fourier transform (QFT) gate. Additionally, in the $d_c > 2$ case the control gates acts as MVCGs, applying the gate to the q^{th} power when the control qudit is in state $|q\rangle$. The circuit will estimate the phase $\tilde{\theta}_k$ of eigenstate $|\nu_k\rangle$ to precision $d_c^{-(n)}$. The estimate of eigenphase θ_k is returned with probability $|\langle \Phi | \nu_k \rangle|^2$.

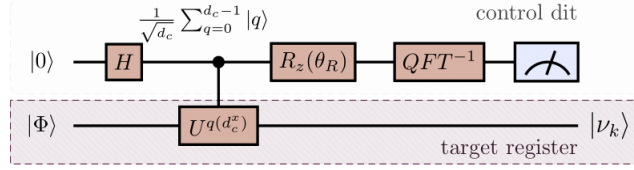


Figure 4.2. The iterative PEA. See Fig. 4.1 for color-conventions and notes on the MVCG. To retrieve n dits of the eigenphase (i.e. phase precision $\pm 1/d_c^n$), run the circuit with $x = n - 1$ and $\theta_R = 0$; the measured control state is the n^{th} base- d_c dit of the unknown phase. Proceed to run the circuit for $x = n - 2$ and set θ_R according to the previous control results; the measured control state is the $(n - 1)^{\text{th}}$ dit. Continue the process iteratively until $x = 0$ and the entire phase is recovered. Note that the iterative method is diagrammed for a single qudit control, but may be realized with any number of control qudits, similar to the traditional PEA

An IPEA circuit is diagrammed in Figure 4.2. In the general case, the control qudit may be high-dimensional (d_c -level). In this case, the Hadamard gates represent a d_c -dimensional quantum Fourier transform gate and the control- \hat{U} gate is a multi-level control gate (MLCG) [13]: when the control state is $|q\rangle$, a \hat{U}^q gate is applied to the target register. Consider the IPEA in its “last” iteration’s settings ($x = 0$ in Figure 4.2). When the target register is an eigenstate $|\Phi\rangle = |\nu\rangle$ and the rotation gate is used to subtract off phase $2\pi\theta_R = 2\pi\theta$, the control dits deterministically collapse to state $|0\rangle$. When either the target input is not an eigenstate and/or θ_R is not the corresponding eigenphase, the control dits will collapse to $|0\rangle$ with non-unity probability.

Indeed, for eigenstate input $|\nu\rangle$ with a d_c -level control, the final state of the control qudit before measurement is

$$|\Psi_C\rangle = \frac{1}{d_c} \sum_{q=0}^{d_c-1} \sum_{n=0}^{d_c-1} e^{2\pi i n(\theta - \theta_R - \frac{q}{d_c})} |q\rangle \quad (4.2)$$

where θ is the eigenphase of $|\nu\rangle$ and $-\theta_R$ ($\theta_R \in [0, 1)$) is the rotation applied by the rotation gate. The probability of measuring the system in output bin $|0\rangle$ is

$$\begin{aligned} \mathcal{P}_\theta(-\theta_R) &= |\langle 0 | \Psi_C \rangle|^2 = \frac{1}{d_c^2} \left| \sum_{n=0}^{d_c-1} e^{2\pi i n(\theta - \theta_R)} \right|^2 \\ &= \mathcal{P}_0(\theta - \theta_R). \end{aligned} \quad (4.3)$$

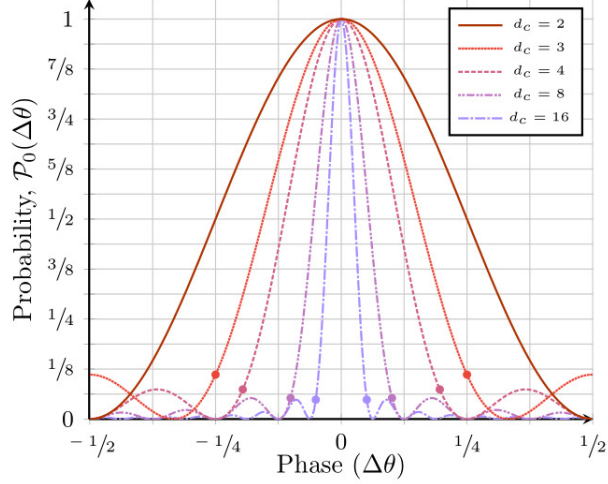


Figure 4.3. Plot of $\mathcal{P}_0(\Delta\theta)$ (Equation 4.3) from $\Delta\theta \in [-.5, .5)$ for various d_c . Note that \mathcal{P}_0 has infinite domain with period 1. Probability of the (d_c -level) control register of an iterative PEA collapsing to $|0\rangle$ as a function of difference between the eigenphase θ and the applied rotation θ_R , $\Delta\theta \equiv \theta - \theta_R$ for an eigenstate input. Note that when the applied rotation matches the eigenphase ($\Delta\theta = 0$), the control collapses to $|0\rangle$ deterministically. Denote the region around $\Delta\theta = 0$ (from dot to dot) as the central lobe of $\mathcal{P}_0(\Delta\theta)$, and the small lobes with local maxima outside of it as the sidelobes. See that the higher the system's dimensionality, the narrower the probability curve's central lobe and the lower local maxima in the sidelobes. Note that $d_c = 2$ has no sidelobes (the probability is monotonic on either side of the central lobe). Also note $\mathcal{P}(\Delta\theta) = 0$ for $\Delta\theta = d_c^{-1}$ and the width of the central lobe is therefore $\Delta\theta_{\text{FWFM}} = 2d_c^{-1}$.

$\mathcal{P}_\theta(-\theta_R)$ goes to one as θ_R approaches θ , as shown in Figure 4.3. In the most general case, where the target register is an arbitrary (non-eigenstate) input state $|\Phi\rangle$ and the rotation gate subtracts off phase $2\pi\theta_R$, the probability that the control qudits will collapse to $|0\rangle$ is

$$\begin{aligned}
\mathcal{C}(|\Phi\rangle, \theta_R) &= \sum_{k=0}^{d_t-1} |\langle \nu_k | \Phi \rangle|^2 \mathcal{P}_{\theta_k}(-\theta_R) \\
&= \frac{1}{d_c^2} \sum_{k=0}^{d_t-1} |\langle \nu_k | \Phi \rangle|^2 \left| \sum_{n=0}^{d_c-1} e^{2\pi i n(\theta_k - \theta_R)} \right|^2.
\end{aligned} \tag{4.4}$$

Where \hat{U} is d_t -by- d_t -dimensional and the target register is d_t -dimensional. Appreciate that $\mathcal{C}(|\Phi\rangle, \theta_R) = 1$ if and only if $|\Phi\rangle$ is an eigenstate and θ_R is its corresponding eigenphase.

4.2 Statistical Approach to PEA

The non-deterministic nature of the IPEA (in the non-eigenstate case) disqualifies the circuit from use as an eigenphase estimator in the standard approach. The SPEA instead considers the probabilistic outputs of the IPEA (and PEA) as valuable information which – when coupled with a classical controller as in Figure 4.4 – allows quantum PEA-like hardware to be used in a variational approach to determine any unknown eigenphase-eigenstate pair. The quantum hardware required is that of a traditional PEA with single-bit precision ($n = 1$) and the rotation gate standard to the IPEA (i.e. an iterative PEA with x set to 0). The classical controller determines $|\Phi\rangle$ and θ_R which are used in the PEA-type circuit. Multiple trials of the quantum circuit are run to approximate the probability $\tilde{\mathcal{C}} \approx \mathcal{C}(|\Phi\rangle, \theta_R)$ (of Equation 4.4). Note that the PEA-like circuit need only detect two measurement outcomes: $|0\rangle$ and $\text{not}(|0\rangle)$, further reducing hardware requirements compared to typical high-dimensional PEAs. Treating the estimate $-1 \cdot \tilde{\mathcal{C}}(|\Phi\rangle, \theta_R)$ as a cost function in an optimization process (making $\tilde{\mathcal{C}}$ the negative cost function), the classical controller adjusts $|\Phi\rangle$ and θ_R , until the quantum circuit near-deterministically returns $|0\rangle$ as the output state. When $\tilde{\mathcal{C}}(|\Phi\rangle^*, \theta_R^*) \approx 1$, the classical controller has found the (approximate) eigenstate $|\Phi\rangle^*$ and the associated eigenphase θ_R^* .

The quality of the eigenstate $|\Phi\rangle^*$ and eigenphase θ_R^* retrieval can be quantified by $\mathcal{C}^* = \mathcal{C}(|\Phi\rangle^*, \theta_R^*)$. \mathcal{C}^* can both (1) determine the maximum distance from the eigenphase θ_R to the nearest eigenphase θ_k and (2) find the fidelity of $|\Phi\rangle^*$ to actual eigenstate(s). Derivations of both are provided in A.1.

The (negative) cost function \mathcal{C} acts as a metric for quality of eigenvalue-eigenstate retrieval as shown in A.1; by finding $|\Phi\rangle$ and θ_R which maximize this metric, we arrive at good estimates for an eigenstate ($|\Phi\rangle$) and eigenphase (θ_R) pair. Following is the classical algorithm used to maximize \mathcal{C} , which is similar to a gradient search algorithm:

- (1) The classical controller chooses a $|\Phi\rangle$ at random
- (2) The classical controller constructs an orthogonal basis $\{|B_m\rangle\}$ including $|\Phi\rangle$

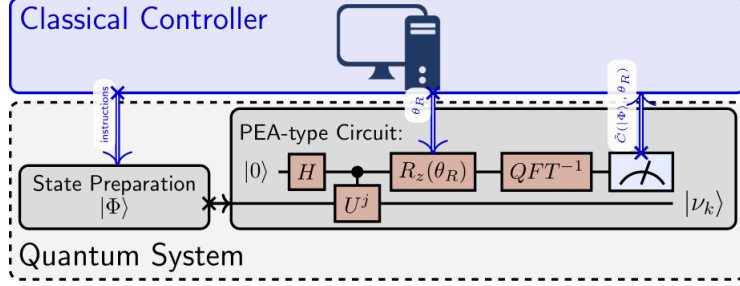


Figure 4.4. Diagram of variational classical-quantum system. Classical processes are indicated by double blue lines and quantum processes by single black lines. Quantum gates are shown in brown and measurement gates in blue. The (potentially high-dimensional) PEA-type circuit is simplified from the typical iterative PEA in that U need not be raised to high orders (d_c^x) corresponding to desired eigenphase precision and the measurement gate need only distinguish between the $|0\rangle$ -state and the not($|0\rangle$)-state. The (negative) cost function (estimate) $\tilde{\mathcal{C}}$ is returned after a predetermined number of trials of the quantum circuit, approximating a probability. The classical controller optimizes $|\Phi\rangle$ and θ_R based on the (negative) cost function returned by the quantum circuit. Process continues until $\tilde{\mathcal{C}}(|\Phi\rangle, \theta_R) = 1$ or improvement in $\tilde{\mathcal{C}}(|\Phi\rangle, \theta_R)$ ceases.

- (3) • (Standard Method: viable when the quantum circuit can measure output bins $|0\rangle$ and not($|0\rangle$))

The quantum circuit evaluates $\tilde{\mathcal{C}}(|\Phi\rangle, \theta_R)$ over a range of θ_R and returns the maximum value \mathcal{C}^*

- (Alternative Method: viable when the quantum circuit can measure all d_c output bins: $|0\rangle$ through $|d_c - 1\rangle$.)

The quantum circuit evaluates $\tilde{\mathcal{C}}(|\Phi\rangle, 0)$ and uses this result to approximate the eigenphase θ^* . The quantum circuit then evaluates $\tilde{\mathcal{C}}(|\Phi\rangle, \theta_R = \theta^*)$ and returns \mathcal{C}^* .

- (4) For all $m = 0$ to $2d_t - 1$, we set $a=1$ and the following occurs:

- if $m \geq d_t$ then $z = \sqrt{-1}$. Otherwise $z = 1$.
- the classical controller generates the new state:

$$|\Phi\rangle = \frac{|A\rangle}{\sqrt{\langle A|A\rangle}} \quad (4.5)$$

where $|A\rangle = |\Phi\rangle + z \cdot a \cdot (1 - \mathcal{C}^*) |B_{m \bmod d_t}\rangle$.

- $|\Phi\rangle$ is fed to the quantum circuit, the maximum value returned is \mathcal{C}^*
- if $\mathcal{C}^* > \mathcal{C}$, then $|\Phi\rangle = |\Phi\rangle$ and $\mathcal{C}^* = \mathcal{C}$. Otherwise $|\Phi\rangle$ and \mathcal{C}^* are unchanged.

(5) If $|\Phi\rangle$ was not updated during step 4, set $a = a/2$ and repeat step 4.

(6) If \mathcal{C}^* is greater than the stopping condition or the maximum run-time has been exceeded, the classical controller concludes and returns $|\Phi\rangle$, \mathcal{C}^* , and θ_R^* . Otherwise the process continues from step 2.

A few observations on the optimization process may be made. For each iteration, at least $2d_t$ distinct input states are used. For each of these input states a set of $\{\theta_R\}$ is applied (when using the ‘standard approach’ in step 3). Initially, the $\{\theta_R\}$ range from 0 to 1 with coarse resolution; as the optimization proceeds, $\{\theta_R\}$ will become fine and include phases from a limited region. Notably, we can choose to run the optimization process limiting $\{\theta_R\}$ to a narrow range of space from the outset. In this way, we may choose to look only for ground state (small θ), principle (large θ), or any other particular solutions to Equation 4.1. In addition, we may eliminate known eigenstates or directions not of interest by excluding them from $\{|B_m\rangle\}$ (step 2) each iteration. In this fashion, the SPEA may be used to determine a complete (or partial) spectral decomposition of \hat{U} . Finally, we note while the hardware conventional to a PEA is utilized, this system is superior to the original PEA, as it determines both the eigenstate and the eigenphase, given no prior knowledge.

4.3 Statistical PEA Simulation

We test the proposed algorithm on the IBM Q platform and on a local computer. In both cases, a classical computer is used to simulate the \mathcal{C} parameter (of Equation 4.4) delivered by a quantum circuit. These simulations of a quantum system are ideal: neither the IBM Q nor the local computer simulations include any noise terms. I.e. all quantum gates are assumed to operate with perfect fidelity. The IBM Q trials study the convergence of the optimization algorithm to any single eigenstate on 2- and 4-dimensional systems. The local computer simulations run a *full* spectral decomposition on a 16-dimensional system with

various control levels d_c . The local computer simulations also consider the convergence of the optimization algorithm to any single eigenstate for various control levels d_c on systems ranging from 8 to 512-dimensional, to provide some indication of the method’s scalability.

Both simulations apply the variational algorithm as defined in Section 4.2, with one primary difference: the local computer simulations follows the primary method of step 3 whereas the IBM Q simulations follow the alternative method. The IBM Q simulation runs one measurement with $R_z(\theta_R = 0)$ and applies the eigenphase estimation methodology introduced in the Discussion of [13] – under the (inaccurate first, but increasingly accurate) assumption that the input state is an eigenstate – to obtain a phase estimate θ^* . Then, the measurement is run with $R_z(\theta_R = -\theta^*)$ to obtain the metric \mathcal{C} used for the optimization. By contrast, the local computer’s simulations follow the primary method, picking a representative sample of input phases to apply to the R_z gate and selecting the largest \mathcal{C} that arises. The local computer’s simulations therefore require more runs of the quantum circuit per trial, but only require two control-qudit detectors: one for the $|0\rangle$ state and one for the not($|0\rangle$), whereas the IBM Q methodology needs one detector for each control level ($|0\rangle, |1\rangle, \dots, |d_c - 1\rangle$). The alternative approach (or some hybrid approach) is generally preferable if the hardware is available for d_c detectors.

4.3.1 Qiskit Simulation

On the IBM Q experience platform, we developed our quantum algorithms with Qiskit, the python-based programming package provided by IBM Q which offers all the facilities to design, simulate and execute quantum algorithms on IBM’s quantum computers [78]. In this section we present the simulation results of the SPEA on the Qiskit quantum simulator.

Three sets of simulations are run on the IBM Q, one with 2-dimensional operator U_1 and the other two with 4-dimensional operators U_2 and U_3 , the matrix forms of which are shown in A.2. U_1 and U_2 are operators directly built with the default gates offered by the IBM Q and U_3 is a unitary exponentiation based on the Hamiltonian of the hydrogen molecule generated with Bravyi-Kitaev transformation[310]. The second quantization Hamiltonian of a hydrogen molecule with a bond length 0.74Å is calculated by the *STO – 3G* minimal basis

using PySCF [311] and the transformation is done by OpenFermion[312]. We encode the matrix into the “Operator” class provided by Qiskit[78]. In the simulations of each unitary operation U_i where $i = 1, 2, 3$, we start with the input states that are good approximations of one of the operator’s eigenstates and then move to input states which are nearly equal-distance from every eigenstate. We quantify the distance of the input state $|\Phi\rangle$ to its nearest eigenstate $|\nu\rangle$ by taking the absolute inner product $|\langle\Phi|\nu\rangle|$ as reported in Table 4.1. In each simulation we run the same input state 20 times and set the maximum iteration number to be 50 (to save the resources) and the stopping condition, which is the difference between the \mathcal{C} factor and 1, to be 10^{-4} . The stopping condition is set so that when it is met we will have a reasonably good approximation of the eigenstate. We then calculate the average number of iterations and standard deviation of the number of iterations required to exceed the stopping condition. Most trials reach the stopping condition before exceeding the iteration limit and give a good approximation of one of the eigenstate-eigenphase pair, as indicated by the low mean phase error reported. The results are shown in Table 4.1.

For each operator U_1, U_2, U_3 , input states which are initially close to an eigenstate (input states with a large absolute inner product) have lower required iteration number than those which are initially far from all eigenstates (low absolute inner product). Appreciate that the eigenstate converged to is non-deterministic, as the optimizer itself is non-deterministic due to randomness added by the random orthogonal basis in step 2. In other words, added randomness may converge the input state to an eigenstate other than the closest eigenstate. The mean phase error recorded in Table 4.1 is calculated by taking the absolute value of the difference between the eigenphase of the converged input state and the true eigenphase of the eigenstate that the input state converged to. As the input state can converge to different eigenstates in the simulation, we report the absolute phase error rather than the error percentage. No correlation between the phase error and the absolute inner product is apparent, indicating the quality of the final eigenphase-eigenstate pair is agnostic to the proximity of the initial input state to any eigenstate. Variations in mean phase error are likely a function of which particular eigenphase-eigenstate pair was converged to. During the simulation of U_3 with an input state of equal weight combination of all the eigenstates – i.e. the hardest input state to converge to an eigenstate – there are few cases that the iteration

limit is reached and the simulation did not reach the stopping condition. This can usually be fixed by increasing the iteration limit.

In summary, these results indicate that the SPEA method is capable of delivering high-quality estimates of eigenphase-eigenstate pairs with no prior knowledge of the operator’s eigenstates, in the case of both arbitrary (U_1, U_2) and physically relevant (U_3) operators. The quality of the estimates is not influenced by prior system knowledge; however, the resources required to deliver an eigenstate-eigenphase pair may be reduced with prior knowledge.

4.3.2 Full Spectral Decomposition

The statistical approach differs from some other variational approaches [79] in that it does not diagonalize the input state matrix, but solves for only one eigenphase-eigenstate pair. This allows for significant reduction in the number of parameters (and iterations) needed to perform the optimization. However, as shown below, a complete spectral decomposition is realizable. As a representative case, we consider the 16-by-16 Hamiltonian \mathcal{H}_{H_2O} for the water molecule H_2O with the H-O-H angle at 104.5° and the bond length at 1.0 a.u. given in A.3 [236]. The Hamiltonian is converted to a unitary exponentiation, $U_{H_2O} = e^{i\mathcal{H}_{H_2O}}$, and the matrix’s spectral decomposition is simulated with the statistical variational algorithm (SPEA) on a local computer.

The simulation is run for various control levels d_c until 120 successful spectral decompositions are achieved. Each of the 16 eigenphases are retrieved in a random order. The optimization runs until $\mathcal{C}^* \geq C_{goal}$. If the optimizer is unable to reach C_{goal} , the process for that eigenphase will conclude so long as $\mathcal{C}^* \geq C_{req}$. If C_{req} is not met, the entire spectral decomposition is abandoned and the trial is classified as failed. Generally, C_{goal} is achieved for the first 10 eigenvalues and the latter 2 to 6 eigenvalues must settle at a lower value (due to small cumulative errors). Results are recorded in Table 4.2 and plotted in Figure 4.5.

To determine the fidelity of the spectral decomposition, the retrieved eigenphase-eigenstate pairs, $(\theta_k, |\nu_k\rangle)$ were used to create the matrix,

$$U_{retrieved} = \sum_k e^{i2\pi\theta_k} |\nu_k\rangle \langle \nu_k|. \tag{4.6}$$

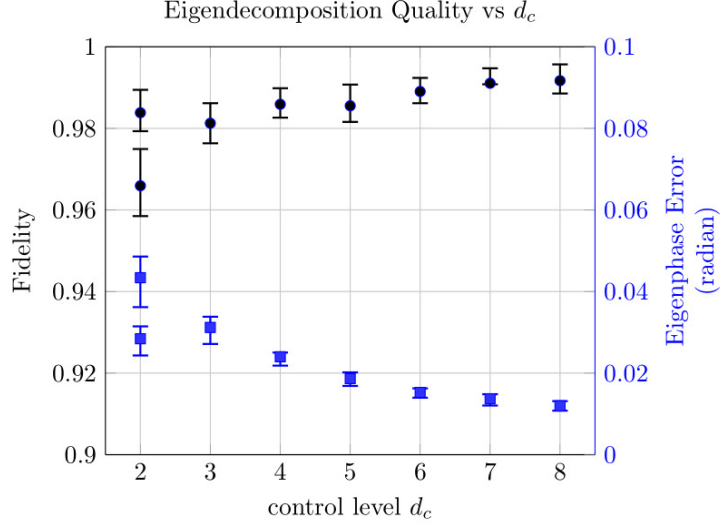


Figure 4.5. (Left axis; black; circles) mean fidelity achieved for optimization simulation at control level d_c , with error bars from the 25th to 75th percentile. (Right axis; blue; squares) mean phase error (per phase) for optimization simulation at control level d_c , with error bars from the 25th to 75th percentile.

Letting $M = U_{H_2O}^\dagger U_{retrieved}$, the fidelity is defined as

$$\text{fidelity} = \frac{\text{Tr}(MM^\dagger) + |\text{Tr}(M)|^2}{n \cdot (n + 1)} \quad (4.7)$$

following the average fidelity definition of [313] where n is matrix dimension (i.e. $n = 16$). The reported phase error is the average absolute phase error over all 16 phases,

$$\text{phase error} = \frac{\sum_k |2\pi\theta_k - 2\pi\theta_{k,true}|}{n}. \quad (4.8)$$

Note that the $d_c = 2$ was run for two different sets of C_{goal} and C_{req} . Increasing these values increased the optimization failure rate, but also improved decomposition fidelity and reduced the average eigenphase error. The high failure rate suggests superior results will be achieved by increasing d_c , the number of control levels, over increasing \mathcal{C}^* (analogous to C_{goal}), when possible. This is expected, as increasing d_c leads to a narrower cost function. Overall, these results indicate both the viability of the SPEA for full and partial eigenphase

recovery and provides an example of a quantum algorithm which benefits from working with high-dimensional quantum states, i.e. qudits.

4.3.3 Scaling to Higher Dimensions

The classical controller is a modified gradient descent algorithm and in this work has not been optimized for scaling to very high-dimensional systems. Here the controller serves to demonstrate that the function \mathcal{C} – the output of the quantum circuit – is usable as a (negative) cost function for any classical optimizer. Nevertheless, we consider randomly generated systems from 8 to 512 dimensions under control levels $d_c = 2, 3, 4, 8$ to briefly observe how the SPEA may scale.

The classical controller was set to run with no value for the stopping condition. Instead, the value of \mathcal{C}^* over the course of a single optimization was recorded for iterations 5, 20, 100, and 500 for randomly generated system U and a randomly selected starting state. One iteration of this process is considered one trial. Over all trials, the average values of $1 - \mathcal{C}^*$ are reported in Table 4.3. Each control level $d_c = 2, 3, 4,$ and 8 uses the same set of random systems and starting points. Different trials may drive the optimizer to different eigenstates, due to inherent randomness in the controller. After iteration 500, the absolute difference between the final estimated eigenphase and the true eigenphase is recorded. This average final absolute phase error is reported.

Under an ideal optimization, \mathcal{C}^* will approach 1 as rapidly as possible. It should be noted (see A.1) that \mathcal{C}^* should not be directly compared across different values of d_c . The higher the value of d_c the lower \mathcal{C}^* will be for a given estimated eigenstate-eigenphase pair. See that, for a given d_u , the final phase error decreases as d_c increases, whether or not \mathcal{C}^* increases. Regardless, see that for $d_u \leq 64$, higher values of d_c may cause a lower initial value for \mathcal{C}^* , but generally achieves a lower \mathcal{C}^* near the end of the optimization process. The final \mathcal{C}^* values for all d_c for a given d_u are within an order of magnitude in all cases. All tested dimensions are able to achieve a final \mathcal{C}^* better than 0.997. These results suggest the system is capable of scaling favorably to high-dimensional systems. The Discussion section addresses improvements to the classical controller for realizing this scalability.

4.4 Discussion

Section 4.3 demonstrates that \mathcal{C} of Equation 4.4 can be used effectively as a cost function to determine an eigenphase-eigenstate pair of an arbitrary unitary system despite the simplistic nature of the control algorithm (outlined in Section 4.2). No prior system knowledge is required for successful convergence. The process was reported here for fundamental unitary gates, unitary systems relevant to computational chemistry, and entirely arbitrary choices of U . For large U , concern over the coherence time of the operations which need to take place can be reduced by systems which decompose U into a set of smaller gates whose operations may take place concurrently [77], [314], [315]. Given the controlled-nature of the PEA, a similar advantage may not be available to the SPEA, or its implementation may be more complex. However, the SPEA only requires a single control gate – differentiating it from the traditional PEA which has a number of operations scaling with $1/p$ where p is the desired eigenphase precision – allowing the SPEA to be more competitive with other circuit-depth sensitive variational approaches.

Other advantages common to variational algorithms can be applied to the SPEA – notably the SPEA classical controller need not know the complete $\mathcal{O}(2d)$ parameters defining the input quantum state, only a (potentially) smaller number of parameters necessary to prepare the state, avoiding the N-representability problem. Like a more select number of variational solvers, the SPEA offers self-verification of its results (the proximity of \mathcal{C} to one)[315]. The SPEA is not designed around systems which are representable with a polynomial number of terms[77], [315]; the SPEA may be more suitable for non-representable systems than other variational approaches.

As \mathcal{C} is the expectation value of a quantum circuit’s output, the algorithm as outlined in this work asks for an increasingly large number of runs of the quantum circuit in order to estimate \mathcal{C} with sufficient accuracy as \mathcal{C} approaches one. Such requirements can be mitigated with a more sophisticated classical controller, which may employ more efficient sampling techniques (such as a Metropolis–Hastings algorithm) or make better use of the information available from \mathcal{C} (e.g. driving $\mathcal{C}(|\psi\rangle, \theta) \rightarrow 1$ is closely related to forcing $\mathcal{C}(|\psi\rangle, \theta + \frac{1}{dc}) \rightarrow 0$). The issue can also be ameliorated by substituting the control- U for control- U^k (for $k > 1$)

as \mathcal{C} approaches one, decreasing \mathcal{C} for a given estimated eigenphase-eigenstate pair and thus allowing it to be estimated with fewer calls to the quantum circuit. The quality of the eigenstate-eigenphase retrieval may be more accurately defined by using U^k or (rather than following A.1) by fitting the distribution of $\mathcal{C}(|\psi\rangle, \theta + x)$ over x to the ideal distribution of $\mathcal{P}_\theta(x)$.

4.5 Conclusion

In this work, we have proposed a novel statistical variational approach (SPEA) to the quantum phase estimation algorithm (PEA). From the probabilistic output of a PEA circuit using non-eigen input states, we have defined a statistical metric \mathcal{C} indicating the proximity of any given input state to the nearest eigenstate and develop an optimization process that can variationally retrieve all the eigenstate-eigenphase pairs of a given unitary operator. The SPEA takes advantage of the hardware intended for the Iterative PEA and therefore requires no novel quantum hardware development. The main disadvantage of the SPEA is the non-deterministic nature of the measurements requires running the quantum circuit repeatedly for each measurement setting. However, in the near-term era, repeated runs of a quantum circuit per measurement is already the norm, due to noise and imperfect gate fidelity. One of the main advantages of the SPEA compared to the PEA and IPEA is the ability to systematically find both the eigenstates and associated eigenphases, rather than just the eigenphases.

The simulations on the IBM Q platform with Qiskit proves the feasibility of applying the SPEA on standard quantum computation platforms. On the local computer, the full spectral decomposition of the operator generated from the water molecule Hamiltonian demonstrates the viability of the SPEA for applications in quantum chemistry. The ability to retrieve eigenstates and efficiency (in terms of low iterations requirement) of this method shows the improvement to the original PEA methods and offers the clear potential to work with larger physical and chemical systems. Further, SPEA is demonstrated to work with arbitrary U and does not require that the U be expanded into a sum of simpler operations. As compared

to variational approaches that search only for the ground state, the SPEA is able to search for any eigenstate with no modifications to the quantum circuit.

Future work includes improving the optimization process with a more sophisticated algorithm for the classical controller. In addition to improving efficiency and failure rate, this may also improve the accuracy of the eigenphase-eigenstate retrieval as well as the fidelity of the full spectral decomposition. The efficiency and the viability of our methods enable us to simulate more complex systems in quantum chemistry. Future work also includes implementing this method on real computational systems provided by the IBM Q and also on a photonic platform with high-dimensional control qudit capabilities.

Table 4.1. IBM Q Qiskit QASM simulator results. Three unitary operators are simulated on the IBM Q platform. The SPEA is run 20 times starting from each input state. The distance from the input state to the nearest eigenstate is quantified by the absolute inner product of the two vectors (inner product 1 being identical and smaller values indicating greater difference). The table records the mean and standard deviation (S.D.) of the number of iterations needed to reach the stopping condition ($1 - \tilde{C} = 10^{-4}$). The average absolute phase error is reported in radians. For each U_i the input states range from good approximations of one of the operator's eigenstates to input states which are nearly equal-distance from every eigenstate. See that the iteration mean tends to increase with decreasing inner product but the ultimate phase error is generally agnostic to the input state difference.

Unitary	Input State	Abs. Inner	Iteration		Phase Error
		Product	Mean	S.D.	Mean
U_1	(0.1951, 0.9808)	0.98	6.20	2.82	$1.099 \cdot 10^{-2}$
	(0.3827,0.9239)	0.92	8.15	3.41	$1.005 \cdot 10^{-2}$
	(0.7071,0.7071)	0.71	8.90	3.34	$1.005 \cdot 10^{-2}$
U_2	(0 , 0, 0.7432, 0.6690)	0.99	5.85	8.14	$2.083 \cdot 10^{-2}$
	(0 , 0,0.6690, 0.7432)	0.99	6.7	10.42	$2.168 \cdot 10^{-2}$
	(0,0,1,0)	0.71	17.7	6.06	$1.663 \cdot 10^{-2}$
	(1,0,0,0)	0.71	23.05	11.22	$2.167 \cdot 10^{-2}$
	(0.7071, 0 , 0.7071, 0)	0.50	21.3	10.71	$2.262 \cdot 10^{-2}$
U_3	(-0.1379, 0 , 0 , 0.9904)	0.99	1.15	0.36	$1.885 \cdot 10^{-2}$
	(0 , 0.7807, 0.6247, 0)	0.99	1.1	0.3	$1.508 \cdot 10^{-2}$
	(0,1,0,0)	0.71	4.35	4.17	$1.414 \cdot 10^{-2}$
	(0.7071, 0 ,0 , 0.7071)	0.62	4.15	1.01	$1.570 \cdot 10^{-2}$
	(0.5774, 0.5774, 0 , 0.5774)	0.51	21.5	11.06	$2.199 \cdot 10^{-2}$

Table 4.2. Statistics for 120 successful trials of complete spectral decomposition of U_{H_2O} matrix. C_{goal} is the \tilde{C} value the optimizer attempts to reach, and generally does reach for at least the first 10 (of 16) eigen-estimates. C_{req} is the \tilde{C} value the optimizer is required to reach for all eigen-estimates, else the trial is abandoned. For successful trials, the mean Fidelity and standard deviation are reported, as well as the mean eigenphase error (in radians). Note that $d_c = 2$ was run on two different C_{goal}, C_{req} levels for comparison.

d_c	C_{goal}	C_{req}	Trials	Fails	Fidelity		Phase Error	
					Mean	S.D.	Mean	S.D.
2	0.999	0.95	120	77	0.984	$7.29 \cdot 10^{-3}$	$2.84 \cdot 10^{-2}$	$10.7 \cdot 10^{-2}$
2	0.995	0.9	120	13	0.966	$10.68 \cdot 10^{-3}$	$4.34 \cdot 10^{-2}$	$17.3 \cdot 10^{-2}$
3	0.995	0.9	120	17	0.981	$6.62 \cdot 10^{-3}$	$3.12 \cdot 10^{-2}$	$9.14 \cdot 10^{-2}$
4	0.995	0.9	120	32	0.986	$5.32 \cdot 10^{-3}$	$2.40 \cdot 10^{-2}$	$7.36 \cdot 10^{-2}$
5	0.995	0.9	120	30	0.986	$7.10 \cdot 10^{-3}$	$1.86 \cdot 10^{-2}$	$4.98 \cdot 10^{-2}$
6	0.995	0.9	120	26	0.989	$4.80 \cdot 10^{-3}$	$1.53 \cdot 10^{-2}$	$3.80 \cdot 10^{-2}$
7	0.995	0.9	120	60	0.991	$7.05 \cdot 10^{-3}$	$1.37 \cdot 10^{-2}$	$3.65 \cdot 10^{-2}$
8	0.995	0.9	120	132	0.992	$6.13 \cdot 10^{-3}$	$1.20 \cdot 10^{-2}$	$3.54 \cdot 10^{-2}$

Table 4.3. For d_u -by- d_u dimensional randomly generated unitary systems U , the quantity $1 - \mathcal{C}^*$ is averaged over multiple trials at for SPEA systmes with varying control levels d_c . Quantity $1 - \mathcal{C}^*$ is reported at iterations 5, 20, 100, 500 over the course of an optimization run with no stopping conditions. After iteration 500, the mean absolute phase error is reported in radians.

d_u	d_c	Trials	Average $1 - \mathcal{C}^*$				Mean Final Phase Error
			5	20	100	500	
8	2	100	$3.84 \cdot 10^{-2}$	$8.39 \cdot 10^{-3}$	$0.69 \cdot 10^{-4}$	$3.43 \cdot 10^{-5}$	$0.04 \cdot 10^{-2}$
	3		$4.36 \cdot 10^{-2}$	$6.63 \cdot 10^{-3}$	$0.38 \cdot 10^{-4}$	$1.63 \cdot 10^{-5}$	$0.02 \cdot 10^{-2}$
	4		$4.71 \cdot 10^{-2}$	$3.97 \cdot 10^{-3}$	$0.23 \cdot 10^{-4}$	$1.01 \cdot 10^{-5}$	$0.01 \cdot 10^{-2}$
	8		$6.37 \cdot 10^{-2}$	$2.84 \cdot 10^{-3}$	$0.17 \cdot 10^{-4}$	$0.48 \cdot 10^{-5}$	$0.005 \cdot 10^{-2}$
16	2	100	$4.16 \cdot 10^{-2}$	$8.04 \cdot 10^{-3}$	$1.29 \cdot 10^{-4}$	$11.76 \cdot 10^{-5}$	$0.33 \cdot 10^{-2}$
	3		$6.38 \cdot 10^{-2}$	$7.45 \cdot 10^{-3}$	$0.67 \cdot 10^{-4}$	$3.24 \cdot 10^{-5}$	$0.04 \cdot 10^{-2}$
	4		$8.93 \cdot 10^{-2}$	$6.51 \cdot 10^{-3}$	$0.48 \cdot 10^{-4}$	$1.73 \cdot 10^{-5}$	$0.02 \cdot 10^{-2}$
	8		$14.95 \cdot 10^{-2}$	$6.93 \cdot 10^{-3}$	$0.17 \cdot 10^{-4}$	$0.82 \cdot 10^{-5}$	$0.01 \cdot 10^{-2}$
32	2	100	$5.03 \cdot 10^{-2}$	$9.11 \cdot 10^{-3}$	$1.48 \cdot 10^{-4}$	$12.79 \cdot 10^{-5}$	$0.54 \cdot 10^{-2}$
	3		$11.12 \cdot 10^{-2}$	$10.46 \cdot 10^{-3}$	$1.4 \cdot 10^{-4}$	$18.31 \cdot 10^{-5}$	$0.45 \cdot 10^{-2}$
	4		$18.44 \cdot 10^{-2}$	$12.17 \cdot 10^{-3}$	$1.16 \cdot 10^{-4}$	$10.86 \cdot 10^{-5}$	$0.17 \cdot 10^{-2}$
	8		$31.71 \cdot 10^{-2}$	$22.15 \cdot 10^{-3}$	$0.95 \cdot 10^{-4}$	$2.34 \cdot 10^{-5}$	$0.01 \cdot 10^{-2}$
64	2	100	$8.74 \cdot 10^{-2}$	$10.48 \cdot 10^{-3}$	$1.79 \cdot 10^{-4}$	$27.74 \cdot 10^{-5}$	$1.12 \cdot 10^{-2}$
	3		$23.27 \cdot 10^{-2}$	$25.76 \cdot 10^{-3}$	$2.27 \cdot 10^{-4}$	$20.49 \cdot 10^{-5}$	$0.50 \cdot 10^{-2}$
	4		$33.65 \cdot 10^{-2}$	$96.27 \cdot 10^{-3}$	$2.32 \cdot 10^{-4}$	$38.2 \cdot 10^{-5}$	$0.63 \cdot 10^{-2}$
	8		$49.44 \cdot 10^{-2}$	$154.09 \cdot 10^{-3}$	$1.54 \cdot 10^{-4}$	$5.97 \cdot 10^{-5}$	$0.04 \cdot 10^{-2}$
128	2	100	$16.45 \cdot 10^{-2}$	$24.17 \cdot 10^{-3}$	$2.26 \cdot 10^{-4}$	$34.45 \cdot 10^{-5}$	$1.12 \cdot 10^{-2}$
	3		$35.69 \cdot 10^{-2}$	$175.24 \cdot 10^{-3}$	$4.59 \cdot 10^{-4}$	$65.51 \cdot 10^{-5}$	$0.98 \cdot 10^{-2}$
	4		$44.98 \cdot 10^{-2}$	$135.54 \cdot 10^{-3}$	$4.68 \cdot 10^{-4}$	$54.59 \cdot 10^{-5}$	$0.78 \cdot 10^{-2}$
	8		$58.69 \cdot 10^{-2}$	$137.72 \cdot 10^{-3}$	$4.78 \cdot 10^{-4}$	$59.57 \cdot 10^{-5}$	$0.41 \cdot 10^{-2}$
256	2	100	$25.29 \cdot 10^{-2}$	$156.88 \cdot 10^{-3}$	$5.37 \cdot 10^{-4}$	$60.39 \cdot 10^{-5}$	$0.68 \cdot 10^{-2}$
	3		$43.44 \cdot 10^{-2}$	$124.12 \cdot 10^{-3}$	$9.71 \cdot 10^{-4}$	$110.67 \cdot 10^{-5}$	$0.64 \cdot 10^{-2}$
	4		$51.71 \cdot 10^{-2}$	$193.64 \cdot 10^{-3}$	$11.82 \cdot 10^{-4}$	$136.93 \cdot 10^{-5}$	$0.59 \cdot 10^{-2}$
	8		$65.86 \cdot 10^{-2}$	$400.17 \cdot 10^{-3}$	$20.37 \cdot 10^{-4}$	$119.06 \cdot 10^{-5}$	$0.48 \cdot 10^{-2}$
512	2	26	$32.12 \cdot 10^{-2}$	$146.61 \cdot 10^{-3}$	$19.61 \cdot 10^{-4}$	$117.08 \cdot 10^{-5}$	$0.44 \cdot 10^{-2}$
	3		$49.53 \cdot 10^{-2}$	$288.44 \cdot 10^{-3}$	$22.36 \cdot 10^{-4}$	$227.46 \cdot 10^{-5}$	$0.44 \cdot 10^{-2}$
	4		$58.17 \cdot 10^{-2}$	$398.08 \cdot 10^{-3}$	$51.21 \cdot 10^{-4}$	$239.06 \cdot 10^{-5}$	$0.37 \cdot 10^{-2}$
	8		$73.14 \cdot 10^{-2}$	$411.68 \cdot 10^{-3}$	$26.01 \cdot 10^{-4}$	$173.41 \cdot 10^{-5}$	$0.28 \cdot 10^{-2}$

5. QUANTUM SIMULATION OF THE RADICAL PAIR DYNAMICS OF THE AVIAN COMPASS

The contents of this chapter are based on and modified from the article [142] Zhang, Y., Hu, Z., Wang, Yuchen, & Kais, S. (2022). Quantum Simulation of the Radical Pair Dynamics of the Avian Compass. The Journal of Physical Chemistry Letters, 14, 832-837., Copyright (2023) by American Chemical Society

In this Chapter, we apply the general quantum algorithm to simulating the radical pair mechanism in the avian compass and further demonstrate its generality. We introduce the Sz.-Nagy dilation theorem-based quantum algorithm in §5.1 and the basic scheme of the RPM is discussed in §5.2. We perform a complexity analysis to our quantum simulations in §5.3 and provide our conclusion remarks in §5.4. An example of the quantum circuit for our simulation is given in B.1.

5.1 The quantum algorithm

The general quantum algorithm for open quantum dynamics has different versions that can evolve the Kraus representation [316], the Lindblad master equation [317], and the generalized quantum master equation [163]. In this work we use the version for the Lindblad master equation [317].

We first review how the generalized quantum algorithm converts the non-unitary matrix that encodes the open quantum dynamics into a unitary evaluation based on the Sz.-Nagy unitary dilation procedure [316], [317]. We assume the initial density matrix that describes the physical system is composed of a set of unique pure quantum states $|\phi_i\rangle$ that are weighted by their corresponding probabilities p_i :

$$\rho = \sum_i p_i |\phi_i\rangle \langle \phi_i|$$

we want to simulate the time evolution of $\rho(t)$ given the initial ρ and the Kraus operators M_k 's. This task can be achieved by preparing each input state $|\phi_i\rangle$ in a vector form v_i in a given basis and then building a quantum circuit that generates the quantum state:

$$|\phi_{ik}(t)\rangle = M_k v_i \xrightarrow{\text{unitary dilation}} U_{M_k}(v_i^T, 0, \dots, 0)^T. \quad (5.1)$$

The U_{M_k} is generated via the 1-dilation of M_k :

$$U_{M_k} = \begin{pmatrix} M_k & D_{M_k^\dagger} \\ D_{M_k} & -M_k^\dagger \end{pmatrix}, \quad (5.2)$$

where $D_{M_k} = \sqrt{I - M_k^\dagger M_k}$, $D_{M_k^\dagger} = \sqrt{I - M_k M_k^\dagger}$ [318]. After obtaining each $|\phi_{ik}(t)\rangle$, we can calculate the population of each basis state in the current basis from the diagonal vector:

$$\text{diag}(\rho(t)) = \sum_{ik} p_i \cdot \text{diag}(|\phi_{ik}(t)\rangle\langle\phi_{ik}(t)|), \quad (5.3)$$

where $\text{diag}(|\phi_{ik}(t)\rangle\langle\phi_{ik}(t)|)$ can be efficiently obtained by applying projection measurements on the first half subspace of $U_{M_k}(v_i^T, 0, \dots, 0)^T$.

For the dynamics of an open quantum system, the time evolution of the density matrix can be represented as:

$$\rho(s + \delta s) = \sum_k M_{sk} \rho(s) M_{sk}^\dagger \quad (5.4)$$

where $\rho(s)$ is the density matrix at time step s , and δs is considered as the discrete time step, during which the Kraus operators M_{sk} are assumed to be constant. The formula eq.(5.4)

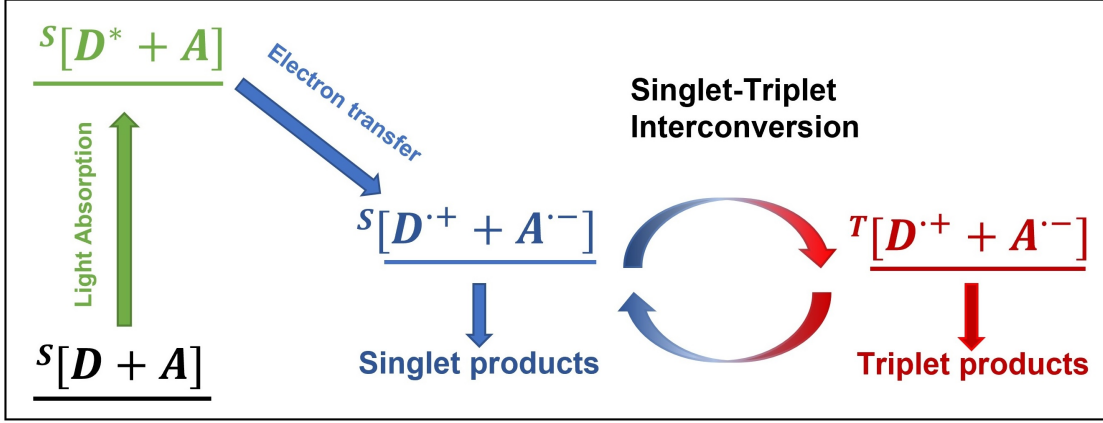


Figure 5.1. The basic scheme of the radical pair mechanism. After absorbing light, donor (D) and acceptor (A) molecules form radical pairs in its singlet state. Then, under the influence of the magnetic fields, the states of the radical pair interconvert between the singlet states and triplet states. Finally, the singlet and triplet radical pairs end up with different products.

can be used iteratively until reaching the time of interest. Explicitly, the dynamics of the density matrix is described as:

$$\rho(1) = \rho(1\delta t) = \sum_k M_{0k} \rho(0) M_{0k}^\dagger \quad (5.5)$$

$$\rho(2) = \rho(2\delta t) = \sum_k M_{1k} \rho(1) M_{1k}^\dagger = \sum_k \sum_j M_{1k} M_{0j} \rho(0) M_{0j}^\dagger M_{1k}^\dagger \quad (5.6)$$

$$\rho(3) = \rho(3\delta t) = \sum_k M_{2k} \rho(2) M_{2k}^\dagger = \sum_k \sum_j \sum_i M_{2k} M_{1j} M_{0i} \rho(0) M_{0i}^\dagger M_{1j}^\dagger M_{2k}^\dagger \quad (5.7)$$

...

Here without losing any generality, the Kraus operators M_{sk} are indexed by the time step s , which allows each time step to have a different set of Kraus operators. However, the RPM dynamical model used in this work is a Markovian process described by the Lindblad master equation, therefore all the time steps have the same set of Kraus operators M_k where the time step index s has been removed.

5.2 The Radical Pair Mechanism Theory and Dynamics

The basic scheme of the RPM is shown in Fig. 5.1. To simplify the fields, we assume that only the electron near the donor interacts with the nucleus, and the electron away from the donor is not affected by the anisotropic hyperfine coupling [162]. Therefore, the Hamiltonian of the system is

$$H = \gamma[\hat{I} \cdot \mathbf{A} \cdot \hat{S}_1 + \mathbf{B} \cdot (\hat{S}_1 + \hat{S}_2)] \quad (5.8)$$

where \mathbf{A} is the anisotropic hyperfine tensor coupling the nucleus and one of two spatially separated electrons, and $\mathbf{A} = \text{diag}\{A_x, A_y, A_z\}$ with $A_x = A_y = A_z/2$; $\mathbf{B} = B_0(\cos \varphi \sin \theta, \sin \varphi \sin \theta, \cos \theta)$, and B_0 is the magnitude of the geomagnetic field; φ is the angle between the x-axis of the radical pair and the external magnetic field; θ is the angle between the z-axis of the radical pair and the external magnetic field; $\gamma = \frac{1}{2}\mu_0 g$, and μ_0 is the Bohr magneton and $g = 2$ is the electron-spin g -factor.

To model the dynamics of the system with a quantum master equation formulation, two ‘‘shelving states’’ were added to the 8-dimensional Hilbert space of the three spins (two electron spins and one nuclear spin) [162]. We employ operators as shown in Eq.(5.9) to represent the spin-selective relaxation into the singlet shelf $|S\rangle$ from the electron singlet state, or the triplet shelf $|T\rangle$ from the electron triplet state. The final populations of $|S\rangle$ and $|T\rangle$ give the singlet and triplet yields.

With the usual definition of singlet $|s\rangle$ and triplet states $|t_i\rangle$ in the electronic subspace, while $|\uparrow\rangle$ and $|\downarrow\rangle$ describing the states of the nuclear spin, we define the following decay operators:

$$\begin{aligned} P_1 &= P_{S,\uparrow} = |S\rangle\langle s, \uparrow|, P_2 = P_{T_0,\uparrow} = |T\rangle\langle t_0, \uparrow| \\ P_3 &= P_{T_+,\uparrow} = |T\rangle\langle t_+, \uparrow|, P_4 = P_{T_-, \uparrow} = |T\rangle\langle t_-, \uparrow| \\ P_5 &= P_{S,\downarrow} = |S\rangle\langle s, \downarrow|, P_6 = P_{T_0,\downarrow} = |T\rangle\langle t_0, \downarrow| \\ P_7 &= P_{T_+,\downarrow} = |T\rangle\langle t_+, \downarrow|, P_8 = P_{T_-, \downarrow} = |T\rangle\langle t_-, \downarrow| \end{aligned} \quad (5.9)$$

This gives a standard Lindblad master equation:

$$\dot{\rho} = -\frac{i}{\hbar}[H, \rho] + k_d \sum_{i=1}^8 [P_i \rho P_i^\dagger - \frac{1}{2}(P_i^\dagger P_i \rho + \rho P_i^\dagger P_i)], \quad (5.10)$$

Table 5.1. Parameter values used in the calculation.

Parameter Details		
Symbol	Description	Values
A_x	Anisotropic hyperfine tensor	$1 \times 10^{-4} T$
B_0	Magnitude of the geomagnetic field	$5 \times 10^{-5} T$
γ	Half of the product of the Bohr magneton and electron-spin g -factor	$9.27 \times 10^{-24} J/T$
\hbar	Reduced Planck constant	$1.05457 \times 10^{-32} J \cdot s$
φ	Angle between x -axis of the radical pair and the magnetic field	0
k_d	Decay Rate of the singlet and triplet states	$1 \times 10^4 s^{-1}$

where k_d is the decay rate of the singlet and triplet states. Note the decay rate k_d is independent of the radical pair states, so we have assigned the same decay rate k_d to all eight projectors.

Now to apply the general quantum algorithm to the RPM dynamics, we first consider the non-unitary part on the right side of Eq. (5.10) which can be rewritten as:

$$\frac{\delta\rho(t)}{\delta t} = \mathcal{L}(\rho) = k_d \sum_{i=1}^8 [P_i \rho P_i^\dagger - \frac{1}{2} \{P_i^\dagger P_i, \rho\}] \quad (5.11)$$

Given a very small δt , Eq. (5.11) becomes:

$$\rho(t + \delta t) - \rho(t) = k_d \delta t \sum_{i=1}^8 [P_i \rho(t) P_i^\dagger - \frac{1}{2} \{P_i^\dagger P_i, \rho(t)\}] + \mathcal{O}(\delta t^2). \quad (5.12)$$

Now assuming $M_0 = \sqrt{\mathbf{I} - \frac{1}{2} k_d \delta t \sum_{k=1}^8 P_k^\dagger P_k}$ and $M_k = \sqrt{k_d \delta t} P_k$ for $k > 0$, and ignoring the second order of δt as $\delta t \rightarrow 0$, Eq. ((5.12)) can be rewritten as:

$$\rho(t + \delta t) = M_0 \rho(t) M_0^\dagger + \sum_{k=1}^8 M_k \rho(t) M_k^\dagger \quad (5.13)$$

Eq.(5.13) is in the same form of Eq.(5.4), thus knowing the initial state $\rho(0)$ we can evolve the density matrix to a certain time with the iterative procedure described in Eq.(5.5) to Eq.(5.7).

In the meantime,

$$\begin{aligned} \sum_{k=0}^8 M_k^\dagger M_k &= M_0^\dagger M_0 + \sum_{k=1}^8 M_k^\dagger M_k \\ &= \mathbf{I} - k_d \delta t \sum_{k=1}^8 P_k^\dagger P_k + \mathcal{O}(\delta t^2) + k_d \delta t \sum_{k=1}^8 P_k^\dagger P_k \\ &= \mathbf{I} + \mathcal{O}(\delta t^2) \end{aligned} \quad (5.14)$$

When $\delta t \rightarrow 0$, according to the above equation, we have:

$$M_0 = \sqrt{\mathbf{I} - k_d \delta t \sum_{k=1}^8 P_k^\dagger P_k} \quad (5.15)$$

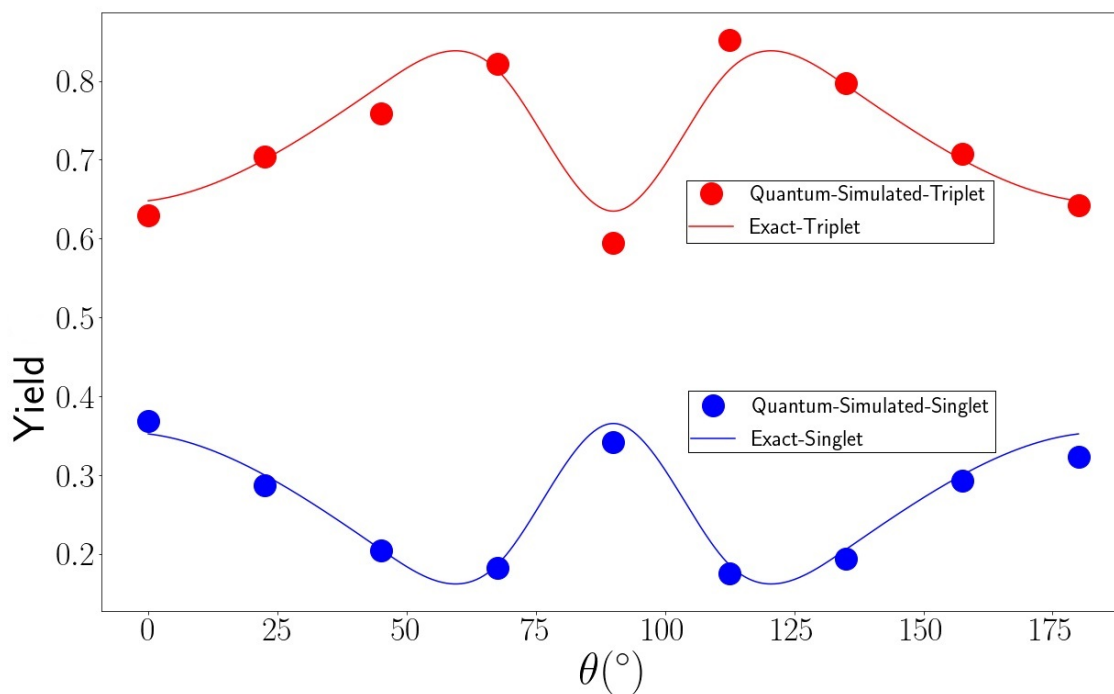


Figure 5.2. The comparison of the singlet (in blue) and triplet (in red) yields between the results obtained from exact calculation and the quantum simulation of the RPM dynamics. The exact curves are generated from the cubic interpolation of the exact calculation of the yields at each data points. The dots represent the results simulated by the general quantum algorithm as implemented on the IBM QASM simulator. The parameters used are shown in Table 5.1. The yields are calculated around $7.5 \times 10^{-4} s$ after the system has already reached the steady-state. The y-axis is the final singlet/triplet yields – i.e. the populations of singlet/triplet shelf state; and the x-axis is the angle between z-axis of the radical pair and the magnetic field.

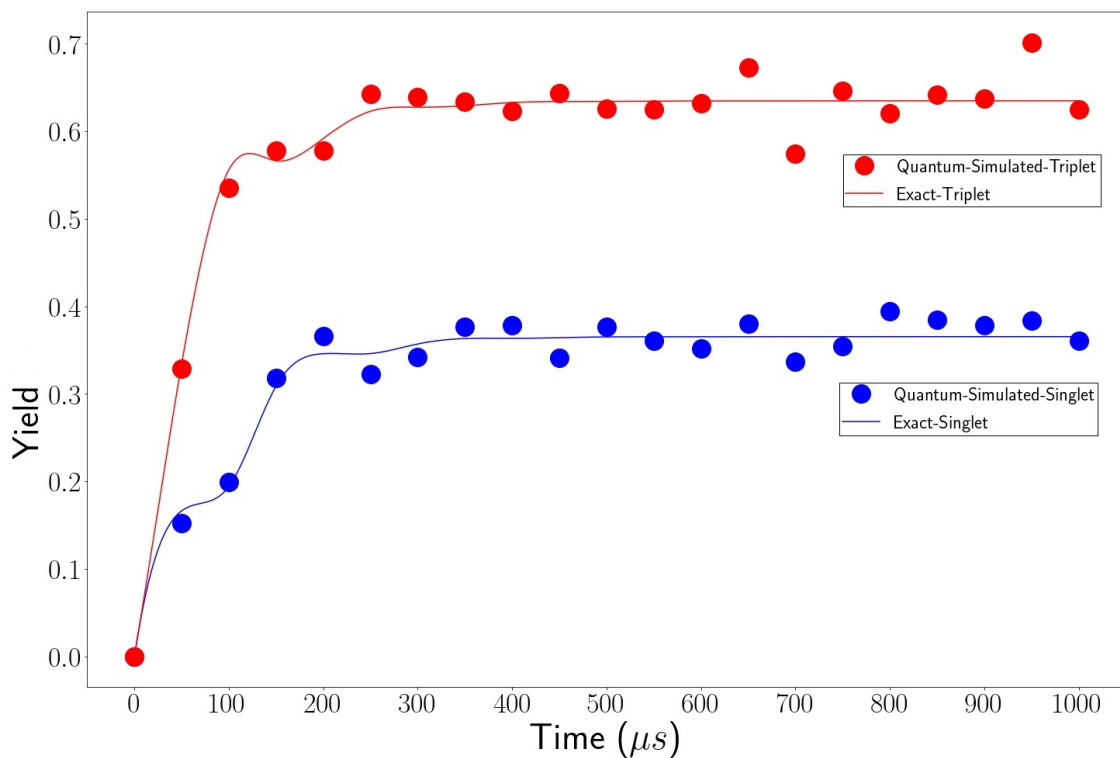


Figure 5.3. The comparison of the dynamics of the singlet(in blue) and triplet(in red) yields between the exact and quantum simulated results. The exact curves are generated from the cubic interpolation of the exact calculation of the yields at each data points. The dots represent the results simulated by the general quantum algorithm as implemented on the IBM QASM simulator. After about $2 \times 10^{-4}s$, both yields reach steady-state. The y-axis is the final singlet/triplet yields – i.e. the populations of singlet/triplet shelf state; and the x-axis is the time.

With Eq. (5.15), we can formulate the Kraus operators to satisfy the condition $\sum_k M_k^\dagger M_k = \mathbf{I}$. Thus, we have defined all the 9 Kraus operators M_k required to describe the RPM dynamics.

There is one additional term containing the Hamiltonian, $-\frac{i}{\hbar}[H, \rho]$, in Eq. (5.10) as compared with Eq. (5.11). This “oscillating part” of the dynamics is unitary and thus can be easily realized by multiplying each Kraus operator by a unitary matrix obtained through the diagonalization of the Hamiltonian [317].

With the parameters in Table 5.1, we simulated the RPM dynamics by iteratively applying Eq. (5.13) on the IBM QASM quantum simulator and then used the output results to calculate the singlet and triplet yields. Also, we assume the initial state of the two electron spins is $\frac{1}{\sqrt{2}}(|\uparrow\downarrow\rangle - |\downarrow\uparrow\rangle)$, and the initial state of the nuclear spin is $\frac{1}{\sqrt{2}}(|\uparrow\rangle - |\downarrow\rangle)$. In our simulation, the time interval δt is set as $0.5/k_d = 5 \times 10^{-5} s$. We then apply the procedure shown in Eq.(5.5), Eq.(5.6) and Eq.(5.7). As mentioned above, the populations of $|S\rangle$ and $|T\rangle$ is the singlet and triplet yields respectively, after the system reaches the steady state. The populations are calculated by the procedure explained in Eq. (5.3), where the diagonal elements of the density matrix are obtained by projection measurements into the computational subspace.

The results are compared with those obtained from classical methods in Fig. 5.2, where the quantum algorithm results are highly consistent with the classical method results. Fig. 5.3 shows the dynamical evolution of the singlet and triplet yields (when $\theta = \frac{\pi}{2}$) as simulated by the general quantum algorithm on the IBM quantum simulator. After $2 \times 10^{-4} s$, the yields almost reach steady-state, which is consistent with the chosen decay rate of $k_d = 1 \times 10^4 s^{-1}$.

5.3 Complexity analysis

One factor that contributes to the complexity of the quantum algorithm is the system’s size. For a density matrix of the size $n \times n$, the cost to realize the unitary dilation of a most general $n \times n$ Kraus operator M_k is $\mathcal{O}(n^2)$ [316], [317]. However, in our calculation of the dynamics of the RPM, the Kraus operators each represents a single elementary physical process and thus the M_k matrices are often sparse with few non-zero elements. This means

the practical complexity scaling of implementing each M_k matrix on a quantum circuit can be greatly reduced to $\mathcal{O}(\log^2 n)$. Taking into account the total K number of M_k matrices to be simulated on the quantum circuit, the total complexity scaling is $\mathcal{O}(K \log^2 n)$ for our given system. It is worth noting that the K is determined on a case-by-case basis by the dynamical model and different M_k matrices can be evolved in parallel, therefore the scaling in K is a “soft” scaling that does not contribute to either the depth or the width of each individual quantum circuit [316], [317]. Another contributing factor to the quantum algorithm’s complexity is the number of time steps. In the most general case, as can be seen from Eq.(5.5) to Eq.(5.7), taking s steps requires K^s matrices to be evolved, which is an exponential scaling in the number of time steps. However, fortunately the actual number of matrix terms to be simulated can be greatly reduced once again due to the sparsity of the M_k matrices. As mentioned above, the Kraus operators represent elementary physical processes and thus the M_k matrices are often sparse with very few non-zero elements: this means that most matrix product terms in e.g. Eq.(5.7) are zero matrices or matrices with negligible norms. The actual number of matrix products we need to evaluate is determined on a case-by-case basis. In the current simulation, in theory the total number of terms in n -th iteration will be 9^n with nine Kraus operators $\{M_k|k = 0, 1, 2, \dots, 8\}$. However, since the product of each pair of the the decay operators $\{P_k|k = 1, 2, 3, \dots, 8\}$ is 0, the product of each pair of the Kraus operator $\{M_k|k = 1, 2, 3, \dots, 8\}$ is 0. Therefore, there will be only 8 more terms when adding one more iteration. Thus, there will be $8 \times n + 1$ terms in n -th iteration, reducing the terms significantly. More simulation details are in the Supplementary Information.

5.4 Conclusion

Based on the calculations and results, we can conclude that the general quantum algorithm based on the Sz.-Nagy dilation can accurately simulate the RPM dynamics described by the Lindblad master equation. As discussed above, the RPM is an important theory that can explain the magneto-reception process of the avian compass. The RPM also acts as an ideal model to help explaining the isotope effects in xenon anaesthesia and lithium treatment

of hyperactivity, magnetic field effects on the circadian clock, as well as hypomagnetic field effects on neurogenesis and microtubule assembly [319], [320]. Our simulation of the RPM model with the quantum algorithm not only demonstrates the generality of the algorithm but also helps bridging the gap between applying tools of quantum-information science to the investigation of new areas of quantum biology.

6. SIMULATING OPEN QUANTUM SYSTEM DYNAMICS ON NISQ COMPUTERS WITH GENERALIZED QUANTUM MASTER EQUATIONS

The contents of this chapter are based on and modified from the article [163] Wang, Yuchen; Mulvihill, E.; Hu, Z.; Lyu, N.; Shivpuje, S.; Liu, Y.; Soley, M. B.; Geva, E.; Batista, V. S.; Kais, S. Simulation of open quantum system dynamics based on the generalized quantum master equation on quantum computing devices. arXiv:2209.04956, Copyright (2022) by the authors.

In this chapter we develop a GQME-based quantum algorithm for simulating the dynamics of an open quantum system [163]. We provide details for calculating the GQME-based non-unitary propagator for the reduced density matrix of the open quantum system in §6.1 and describe using the Sz.-Nagy’s unitary dilation procedure to convert the non-unitary quantum open system propagator in §6.2. The quantum simulation results for the spin-boson benchmark model is provides in §6.3 and the results for the reduced-dimensionality GQME-based simulaion is in §6.4. The concluding remarks with a future outlook is in §6.5. We include further details concerning the quantum algorithm, including the dilation process, circuit transpiling, QASM simulations, and simulations running on the IBM quantum computers in C.1.

6.1 GQME-based propagators

In this section, we outline our approach for calculating the GQME-based non-unitary propagator for the reduced density matrix of the open quantum system (see Eq. (6.9)). The analogous procedure for calculating the non-unitary propagator for a subset of the reduced density matrix elements is outlined in Sec. 6.4.

Previously developed quantum algorithms for open system dynamics involved mapping Lindblad operators to Kraus operators before using the Sz.-Nagy dilation theorem to reach a unitary quantum algorithm[143]–[145]. While useful for many systems, these methods are either Markovian[143], [145] or involve user selection of *ad-hoc* system-bath parameters[144], therefore limiting the range of applications. In this paper, we introduce a method based on the GQME, a formally exact EoM for the dynamics of an open quantum system. Instead

of casting the non-unitary propagator in terms of Kraus operators and dilating them, this method uses the GQME to obtain the system’s time evolution superoperator, or propagator, $\mathcal{G}(t)$, and perform the dilation on it to obtain a unitary quantum algorithm. This subsection describes the first step in the workflow outlined in Fig. 1.2, namely obtaining the time evolution superoperator of an open quantum system starting from its formally exact EoM in GQME form.

For the sake of concreteness, we will focus on molecular systems with an overall Hamiltonian of the following commonly encountered form:

$$\hat{H} = \sum_{j=1}^{N_e} \hat{H}_j |j\rangle\langle j| + \sum_{\substack{j,k=1 \\ k \neq j}}^{N_e} \hat{V}_{jk} |j\rangle\langle k| \quad (6.1)$$

and an overall system initial state of the following commonly assumed single-product form:

$$\hat{\rho}(0) = \hat{\rho}_n(0) \otimes \hat{\sigma}(0) \quad . \quad (6.2)$$

It should be noted that the GQME approach is not limited to this form of Hamiltonian and initial state and that the choice to focus on them is solely motivated by clarity of presentation and the wide range of applications based on an Hamiltonian and an initial state of this form. The system and bath in this case correspond to the electronic and nuclear DOF, respectively. In Eqs. (6.1) and (6.2), $\hat{H}_j = \hat{\mathbf{P}}^2/2 + V_j(\hat{\mathbf{R}})$ is the nuclear Hamiltonian when the system is in the diabatic electronic state $|j\rangle$, with the index j running over the N_e electronic states; $\hat{\mathbf{R}} = (\hat{R}_1, \dots, \hat{R}_{N_n})$ and $\hat{\mathbf{P}} = (\hat{P}_1, \dots, \hat{P}_{N_n})$ are the mass-weighted position and momentum operators of the $N_n \gg 1$ nuclear DOF, respectively; $\{\hat{V}_{jk} | j \neq k\}$ are the coupling terms between electronic states (which can be either nuclear operators or constants); and $\hat{\rho}_n(0)$ and $\hat{\sigma}(0)$ are the reduced density operators that describe the initial states of the nuclear (bath) and electronic (system) DOF, respectively. Throughout this paper, boldfaced variables, e.g., \mathbf{A} , indicate vector quantities; a hat over a variable, e.g., \hat{B} , indicates an operator quantity; and calligraphic font, e.g., \mathcal{L} , indicates a superoperator.

Using projection operator techniques, one can then derive the following formally exact EoM, or GQME, for the reduced electronic density operator, $\hat{\sigma}(t)$ [101]–[103], [105]:

$$\frac{d}{dt}\hat{\sigma}(t) = -\frac{i}{\hbar}\langle\mathcal{L}\rangle_n^0\hat{\sigma}(t) - \int_0^t d\tau \mathcal{K}(\tau)\hat{\sigma}(t-\tau) . \quad (6.3)$$

The open quantum system dynamics of the reduced electronic density matrix described by this GQME is generated by the two terms on the R.H.S. of Eq. (6.3). The first term is given in terms of the projected overall system Liouvillian $\langle\mathcal{L}\rangle_n^0 \equiv \text{Tr}_n\{\hat{\rho}_n(0)\mathcal{L}\}$ (where $\mathcal{L}(\cdot) = [\hat{H}, \cdot]$ is the overall system Liouvillian and $\text{Tr}_n\{\cdot\}$ is the partial trace over the nuclear (bath) Hilbert space), which is represented by a $N_e^2 \times N_e^2$ time-independent matrix. The second term is given in terms of the memory kernel $\mathcal{K}(\tau)$, which is represented by a $N_e^2 \times N_e^2$ time-dependent matrix.

The GQME formalism provides a general framework for deriving the exact EoM for any quantity of interest. The derivation begins with the Nakajima-Zwanzig equation [164], [165], which describes the dynamics of a projected state $\mathcal{P}\hat{\rho}(t)$, where \mathcal{P} is a projection superoperator and $\hat{\rho}(t)$ is the density operator of the overall system:

$$\begin{aligned} \frac{d}{dt}\mathcal{P}\hat{\rho}(t) = & -\frac{i}{\hbar}\mathcal{P}\mathcal{L}\mathcal{P}\hat{\rho}(t) - \frac{1}{\hbar^2}\int_0^t d\tau\mathcal{P}\mathcal{L}e^{-i\mathcal{Q}\mathcal{L}\tau/\hbar}\mathcal{Q}\mathcal{L}\mathcal{P}\hat{\rho}(t-\tau) \\ & -\frac{i}{\hbar}\mathcal{P}\mathcal{L}e^{-i\mathcal{Q}\mathcal{L}t/\hbar}\mathcal{Q}\hat{\rho}(0). \end{aligned} \quad (6.4)$$

Here, \mathcal{L} is the overall system-bath Liouvillian and $\mathcal{Q} = 1 - \mathcal{P}$ is the complimentary projection superoperator to \mathcal{P} . Importantly, the only requirements are that \mathcal{L} is Hermitian and \mathcal{P} satisfies $\mathcal{P}^2 = \mathcal{P}$. Otherwise, there is complete flexibility in the choice of \mathcal{L} and \mathcal{P} , with each choice leading to a different GQME for a different quantity of interest [105].

Following Ref. [101] we focus an overall system-bath Hamiltonian of the form of Eq. (6.1) and the following choice of projection operator which gives rise to the GQME for the system reduced density matrix, $\hat{\sigma}(t)$:

$$\mathcal{P}(\hat{A}) = \hat{\rho}_n(0) \otimes \text{Tr}_n\{\hat{A}\}. \quad (6.5)$$

Plugging Eq. (6.5) into Eq. (6.4) and tracing over the nuclear (bath) Hilbert space leads to the GQME in Eq. (6.3). The memory kernel in Eq. (6.3) is given by

$$\mathcal{K}(\tau) = \frac{1}{\hbar^2} \text{Tr}_n \left\{ \mathcal{L} e^{-i\mathcal{Q}\mathcal{L}\tau/\hbar} \mathcal{Q}\mathcal{L}\hat{\rho}_n(0) \right\}, \quad (6.6)$$

and can be obtained by solving the following Volterra equation [101]:

$$\mathcal{K}(\tau) = i\dot{\mathcal{F}}(\tau) - \frac{1}{\hbar} \mathcal{F}(\tau) \langle \mathcal{L} \rangle_n^0 + i \int_0^\tau d\tau' \mathcal{F}(\tau - \tau') \mathcal{K}(\tau'). \quad (6.7)$$

Here, $\mathcal{F}(\tau)$ and $\dot{\mathcal{F}}(\tau)$ are the so-called projection-free inputs (PFIs), which are given by

$$\begin{aligned} \mathcal{F}(\tau) &= \frac{1}{\hbar} \text{Tr}_n \left\{ \mathcal{L} e^{-i\mathcal{L}\tau/\hbar} \hat{\rho}_n(0) \right\}, \\ \dot{\mathcal{F}}(\tau) &= -\frac{i}{\hbar^2} \text{Tr}_n \left\{ \mathcal{L} e^{-i\mathcal{L}\tau/\hbar} \mathcal{L} \hat{\rho}_n(0) \right\}. \end{aligned} \quad (6.8)$$

The memory kernels for the spin-boson model used in this paper were adopted from Ref. [321], where they were obtained from quantum-mechanically exact PFIs calculated via the tensor-train thermo-field dynamics (TT-TFD) method.

The quantum open system's *non-unitary* time evolution superoperator, or propagator, $\mathcal{G}(t)$, is defined by:

$$\hat{\sigma}(t) = \mathcal{G}(t) \hat{\sigma}(0) . \quad (6.9)$$

Substituting Eq. (6.9) into Eq. (6.3) and noting that the GQME should be satisfied for an arbitrary choice of $\hat{\sigma}(0)$, it is straightforward to show that $\mathcal{G}(t)$ satisfies the same GQME as $\hat{\sigma}(t)$:

$$\frac{d}{dt} \mathcal{G}(t) = -\frac{i}{\hbar} \langle \mathcal{L} \rangle_n^0 \mathcal{G}(t) - \int_0^t d\tau \mathcal{K}(\tau) \mathcal{G}(t - \tau) . \quad (6.10)$$

Thus, given the projected Liouvillian and memory kernels ($\langle \mathcal{L} \rangle_n^0$ and $\mathcal{K}(\tau)$, respectively), $\mathcal{G}(t)$ can be obtained by solving Eq. (6.10) numerically, which in this work was accomplished via a Runge–Kutta fourth-order (RK4) algorithm [102]. This superoperator, $\mathcal{G}(t)$, serves a role similar to that of the Kraus operators in the operator sum representation and can also

be dilated to a unitary form which can be implemented on a quantum computer. Importantly, while the Kraus operators are only known in closed form for the Markovian Lindblad equation, the non-unitary propagator $\mathcal{G}(t)$ can always be obtained from the formally exact GQME (see Eq. (6.10)).

6.2 A GQME-based quantum algorithm for simulating open quantum system dynamics

In this subsection, we describe the next step in the workflow outlined in Fig. 1.2, namely using the Sz.-Nagy's unitary dilation procedure [318] to convert the non-unitary quantum open system propagator $\mathcal{G}(t)$ [see Eqs. (6.9) and (6.10)] into a unitary propagator in an extended Hilbert space. It should be noted that the Sz.-Nagy unitary dilation procedure is one out of several methods that can convert non-unitary operators into unitary operators (e.g. block-encoding represents an alternative method [322], [323]).

The Sz.-Nagy's unitary dilation procedure starts out by calculating the operator norm of $\mathcal{G}(t)$ to determine if it is a *contraction*. For $\mathcal{G}(t)$ to be a contraction, the operator norm of $\mathcal{G}(t)$ needs to be less than or equal to 1, i.e., $\|\mathcal{G}(t)\|_O = \sup \frac{\|\mathcal{G}(t)v\|}{\|v\|} \leq 1$. In the case where the original $\mathcal{G}(t)$ is *not* a contraction, we introduce a normalization factor $n_c = \|\mathcal{G}(t)\|_O$ in order to define a contraction form of $\mathcal{G}(t)$, namely $\mathcal{G}'(t) = \mathcal{G}(t)/n_c$.

In the next step, we apply a 1-dilation procedure to $\mathcal{G}'(t)$ to obtain a unitary $\mathcal{U}_{\mathcal{G}'(t)}$ in an extended Hilbert space of double the dimension of the original system's Hilbert space:

$$\mathcal{U}_{\mathcal{G}'(t)} = \begin{pmatrix} \mathcal{G}'(t) & \mathcal{D}_{\mathcal{G}'^\dagger(t)} \\ \mathcal{D}_{\mathcal{G}'(t)} & -\mathcal{G}'^\dagger(t) \end{pmatrix}. \quad (6.11)$$

Here, $\mathcal{D}_{\mathcal{G}'(t)} = \sqrt{I - \mathcal{G}'^\dagger(t)\mathcal{G}'(t)}$ and $\mathcal{D}_{\mathcal{G}'^\dagger(t)} = \sqrt{I - \mathcal{G}'(t)\mathcal{G}'^\dagger(t)}$, where $\mathcal{D}_{\mathcal{G}'(t)}$ is the so-called defect superoperator of $\mathcal{G}'(t)$. The 1-dilation procedure generates a unitary superoperator $\mathcal{U}_{\mathcal{G}'(t)}$ that operates in the extended Hilbert space and replicates the effect of the contraction form of the original time evolution superoperator, $\mathcal{G}'(t)$, when the input and output vectors are both projected onto the original smaller Hilbert space.

In the original system's Hilbert space, the system reduced density operator $\hat{\sigma}(t)$ is represented by an $N_e \times N_e$ matrix:

$$\hat{\sigma}(t) \doteq \begin{pmatrix} \sigma_{11}(t) & \dots & \sigma_{1N_e}(t) \\ \vdots & \ddots & \vdots \\ \sigma_{N_e1}(t) & \dots & \sigma_{N_eN_e}(t) \end{pmatrix}. \quad (6.12)$$

Alternatively, the same system reduced density operator can also be represented by an N_e^2 -dimensional vector in Liouville space:

$$\hat{\sigma}(t) \doteq (\sigma_{11}(t), \dots, \sigma_{1N_e}(t), \dots, \sigma_{N_e1}(t), \dots, \sigma_{N_eN_e}(t))^T. \quad (6.13)$$

Since the GQME formalism is given in terms of superoperators, it is convenient to work in Liouville space, which we will do from this point on. We also define the norm of the vector representing $\hat{\sigma}(t)$ in Liouville space as the Frobenius norm: $\|\sigma(t)\|_F = \sqrt{\sum_{ij} |\sigma_{ij}|^2}$ and divide $\hat{\sigma}(t)$ by $\|\sigma(t)\|_F$ to normalize $\hat{\sigma}(t)$. [143]

Given the dilated unitary operator $\mathcal{U}_{\mathcal{G}'}(t)$ and the initial quantum input state $\hat{\sigma}(0)$, operating with the non-unitary $\mathcal{G}(t)$ on $\hat{\sigma}(0)$ has now been converted into a unitary transformation as follows:

$$\mathcal{G}'(t)\hat{\sigma}(0) \xrightarrow{\text{unitary dilation}} \mathcal{U}_{\mathcal{G}'}(t) \left(\hat{\sigma}(0)^T, 0, \dots, 0 \right)^T. \quad (6.14)$$

The 0s in the input vector on the R.H.S. are added to match the dimension of the input vector with that of $\mathcal{U}_{\mathcal{G}'}(t)$. The unitary process can then be simulated on a quantum circuit with unitary quantum gates. The electronic populations, $\{\sigma_{jj}(t) \equiv \langle j|\hat{\sigma}(t)|j\rangle | j = 1, \dots, N_e\}$ can be retrieved by taking the square roots of the probability of measuring each basis state $P_j(t) = |\sigma'_{jj}(t)|^2$ and multiplying by the n_c factor.

Finally, we perform a complexity analysis of the quantum algorithm. Given that $\mathcal{G}(t)$ in its most general form is represented by a matrix of N_e^4 non-zero elements, the defect superoperators $\mathcal{D}_{\mathcal{G}'}(t)$ as well as $-\mathcal{G}^\dagger(t)$ as shown in Eq. (6.11) all have N_e^4 non-zero elements. Generally speaking, the number of the two-level unitaries necessary to decompose a unitary

gate is comparable to the number of non-zero elements in the lower-triangular part of the gate [177], [206]. Therefore, the gate complexity to simulate this specific $\mathcal{U}_{\mathcal{G}'}(t)$ is $O(N_e^4)$. If the two-level unitaries are further decomposed into 1-qubit and 2-qubit elementary gates commonly used to design conventional quantum circuits, they need to be transformed to the Gray code sequences and some multi-control gate sequences, adding another factor of complexity logarithmic in N_e^2 , and the total complexity becomes $O(N_e^4 \log^2 N_e^2)$ [206]. This means that the maximum total complexity of a GQME-based simulation of an open quantum system dynamics is comparable to classical methods [143]. However, as demonstrated in previous simulations of certain dynamical models, our quantum algorithm can take advantage of the case when the $\mathcal{G}(t)$ is a sparse matrix, and thus the gate complexity scaling for $\mathcal{G}(t)$ can be reduced to $O(\log^2 N_e^2)$ instead of $O(N_e^4)$ [143], [145].

6.3 A demonstrative application to the spin-boson model

In this subsection, we test the applicability of the quantum algorithm outlined in the previous sections on the spin-boson benchmark model. This model and its derivatives have a wide range of applicability to chemical and physical systems, including electron, proton, energy, and charge transfer processes; polaron formation and dynamics in condensed phase environments; vibrational relaxation, impurity relaxation in solids, spin-lattice relaxation, and qubit decoherence [96], [97], [324], [325]. It should also be noted that quantum-mechanically exact memory kernels for this model are available [321], [326], [327].

The spin-boson Hamiltonian has the form of Eq. (6.1) with $N_e = 2$ and $\{\hat{H}_j, \hat{V}_{jk}\}$ given by:

$$\begin{aligned}\hat{H}_0 &\equiv \hat{H}_D = \epsilon + \sum_{k=1}^{N_n} \frac{\hat{P}_k^2}{2} + \frac{1}{2} \omega_k^2 \hat{R}_k^2 - c_k \hat{R}_k, \\ \hat{H}_1 &\equiv \hat{H}_A = -\epsilon + \sum_{k=1}^{N_n} \frac{\hat{P}_k^2}{2} + \frac{1}{2} \omega_k^2 \hat{R}_k^2 + c_k \hat{R}_k, \\ \hat{V}_{01} &\equiv \hat{V}_{DA} = \hat{V}_{10} \equiv \hat{V}_{AD} = \Gamma.\end{aligned}\tag{6.15}$$

Here, the two electronic states are designated as the donor and acceptor ($|D\rangle$ and $|A\rangle$, respectively), 2ϵ is the shift in equilibrium energy between the donor (D) and acceptor (A)

Table 6.1. Spin-boson model and simulation parameters.

Model #	Model Parameters					Numerical Parameters		
	ϵ	Γ	β	ξ	ω_c	ω_{\max}	N_n	Δt
1	1.0Γ	1.0	$5.0 \Gamma^{-1}$	0.1	1.0Γ	5Γ	60	$1.50083 \times 10^{-3} \Gamma^{-1}$
2	1.0Γ	1.0	$5.0 \Gamma^{-1}$	0.1	2.0Γ	10Γ	60	$1.50083 \times 10^{-3} \Gamma^{-1}$
3	1.0Γ	1.0	$5.0 \Gamma^{-1}$	0.4	2.0Γ	10Γ	60	$1.50083 \times 10^{-3} \Gamma^{-1}$
4	0.0Γ	1.0	$5.0 \Gamma^{-1}$	0.2	2.5Γ	12Γ	60	$4.50249 \times 10^{-3} \Gamma^{-1}$

states, and Γ is a positive constant describing the electronic coupling between the donor and acceptor states. Since Γ is a constant, this system is assumed to satisfy the Condon approximation.

The results shown below were obtained for the case where the nuclear modes' frequencies and coupling coefficients $\{\omega_k, c_k\}$ are sampled from an Ohmic spectral density with exponential cutoff:

$$J(\omega) = \frac{\pi}{2} \sum_{k=1}^{N_n} \frac{c_k^2}{\omega_k} \delta(\omega - \omega_k) \xrightarrow{N_n \rightarrow \infty} \frac{\pi \hbar}{2} \xi \omega e^{-\omega/\omega_c} . \quad (6.16)$$

Here, ξ is the Kondo parameter and ω_c is the cutoff frequency. The reader is referred to Appendix C of Ref. [101] for a description of the procedure used to obtain a discrete set of N_n nuclear mode frequencies $\{\omega_k\}$ and coupling coefficients $\{c_k\}$ from the spectral density in Eq. (6.16).

The initial state is assumed to be of the form of Eq. (6.2), with the initial electronic (system) reduced density operator given by

$$\hat{\sigma}(0) = |D\rangle\langle D| \quad (6.17)$$

and the initial nuclear (bath) reduced density operator given by

$$\hat{\rho}_n(0) = \frac{e^{-\beta(\hat{H}_D + \hat{H}_A)/2}}{\text{Tr}_n \left\{ e^{-\beta(\hat{H}_D + \hat{H}_A)/2} \right\}} . \quad (6.18)$$

Calculations were carried out for four different sets of parameter values (see Table 6.1). Models 1 and 2 correspond to systems with an energy bias between the donor and acceptor states ($\epsilon \neq 0$) and differ in their cutoff frequencies, with model 2 having a higher cutoff frequency. Model 3 corresponds to a biased system with the same parameters as model 2 except for a larger Kondo parameter. Model 4 corresponds to a symmetric system with zero energy bias between the donor and acceptor states ($\epsilon = 0$). The results reported in this paper were obtained with a time step of $\Delta t = 1.50083 \times 10^{-3} \Gamma^{-1}$ for models 1-3 and a time step of $\Delta t = 4.50249 \times 10^{-3} \Gamma^{-1}$ for model 4.

Starting with the quantum-mechanically exact memory kernels (adopted from Ref. [321]), the time evolution superoperator for the electronic reduced density matrix $\mathcal{G}(\tau)$ was generated for the four models given in Table 6.1 by solving the corresponding GQME, Eq. (6.10).

The GQME-based quantum algorithm for simulating the electronic dynamics within the spin-boson model was implemented on the IBM quantum platforms via the Qiskit package [78]. The quantum implementation involved the translation of $\mathcal{G}'(t)$ into $\mathcal{U}_{\mathcal{G}'}(t)$ at each time step, followed by the construction of a quantum circuit based on $\mathcal{U}_{\mathcal{G}'}(t)$, and lastly the use of the quantum circuit to simulate the time evolution of the reduced electronic density matrix. To build the circuit, we dilated the 4×4 $\mathcal{G}'(t)$ into a unitary 8×8 $\mathcal{U}_{\mathcal{G}'}(t)$ by using a 1-dilation procedure [see Eq. (6.11)]. The unitary $\mathcal{U}_{\mathcal{G}'}(t)$ was then transpiled into a 3-qubit quantum circuit composed of three elementary quantum gates: R_Z , \sqrt{X} , and CX . Examples of $\mathcal{U}_{\mathcal{G}'}(t)$ and details of the elementary quantum gates and circuits are given in the supplementary information (SI). The initial electronic state is set to $(1, 0, 0, 0, 0, 0, 0, 0)^T$, where the last four 0s are the extra dimensions from the dilation procedure. The QASM simulator and the real quantum devices initialize the input state $(1, 0, 0, 0, 0, 0, 0, 0)^T$ and apply the unitary operation $\mathcal{U}_{\mathcal{G}'}(t)$ to the input state followed by projection measurements to retrieve the probability distribution of all the 8 basis states. Each circuit runs 2000 shots and the resulting probabilities $P_{000}(t)$ of measuring the state $|000\rangle$ and $P_{011}(t)$ of measuring $|011\rangle$ correspond to the diagonal elements of the modified density matrix $|\sigma'_{00}(t)|^2$ and $|\sigma'_{11}(t)|^2$. The populations of the donor state, $\sigma_{00}(t)$, and acceptor state, $\sigma_{11}(t)$, are retrieved as follows:

$$\sigma_{00}(t) = \sqrt{P_{000}(t)} \times n_c \text{ and } \sigma_{11}(t) = \sqrt{P_{011}(t)} \times n_c \text{ .} \quad (6.19)$$

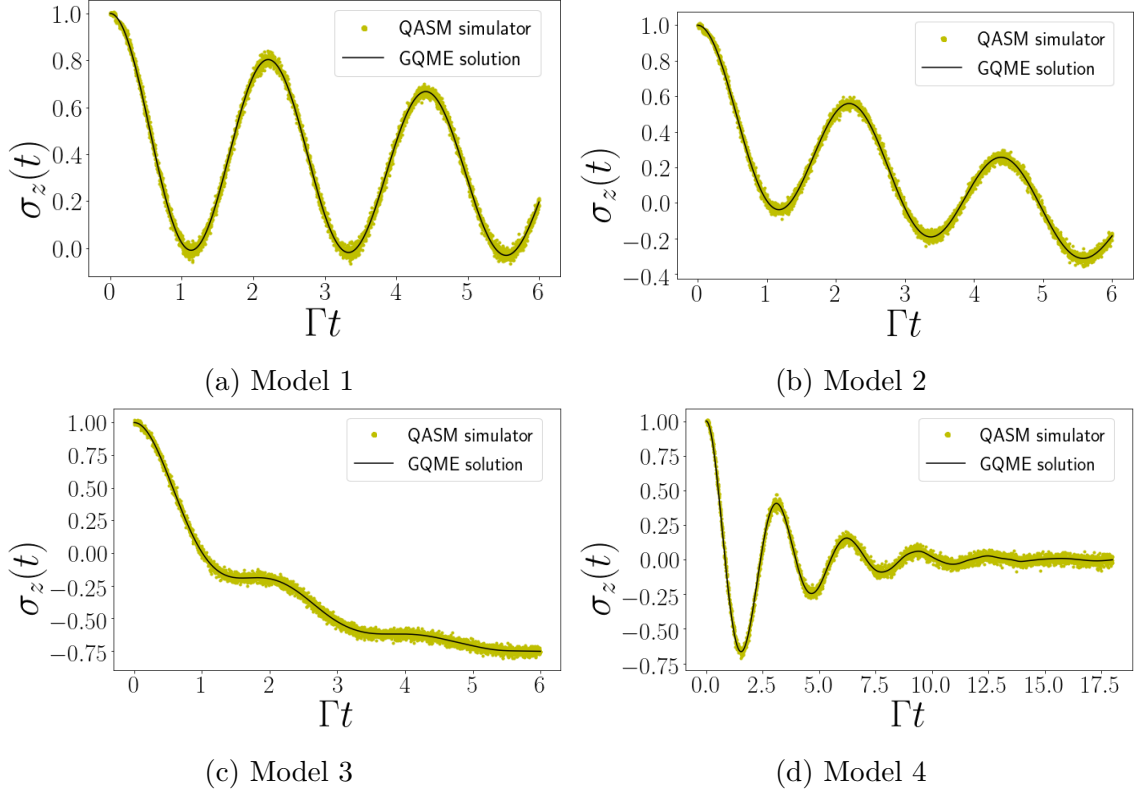


Figure 6.1. The spin-boson model simulated by the GQME-based quantum algorithm as implemented on the IBM QASM quantum simulator, showing the electronic population difference between the donor state and acceptor state $\sigma_z(t) = \sigma_{DD}(t) - \sigma_{AA}(t)$ as a function of time for (a) model 1, (b) model 2, (c) model 3, and (d) model 4 as given in Table 6.1, with units scaled to the electronic coupling, Γ . Each figure shows the comparison between the GQME-based exact results represented by the black curves and the QASM-based results represented by the yellow dots. The time step for both the exact and simulated results is $\Delta t = 1.50083 \times 10^{-3} \Gamma^{-1}$ for models 1-3 and $\Delta t = 4.50249 \times 10^{-3} \Gamma^{-1}$ for model 4. Each model is simulated for 4000 time steps. The number of projection measurements applied by the QASM simulator to obtain a single time step is 2000 shots.

In what follows, we report results in terms of the difference between the donor and acceptor populations, $\sigma_z(t) = \sigma_{00}(t) - \sigma_{11}(t)$.

The comparison between the exact results obtained by solving the GQME on a classical computer and results obtained by performing the quantum algorithm on the QASM simulator is shown in Fig. 6.1. The QASM simulator results are in excellent agreement with the exact results for all four models under consideration. The small amplitude oscillations of the

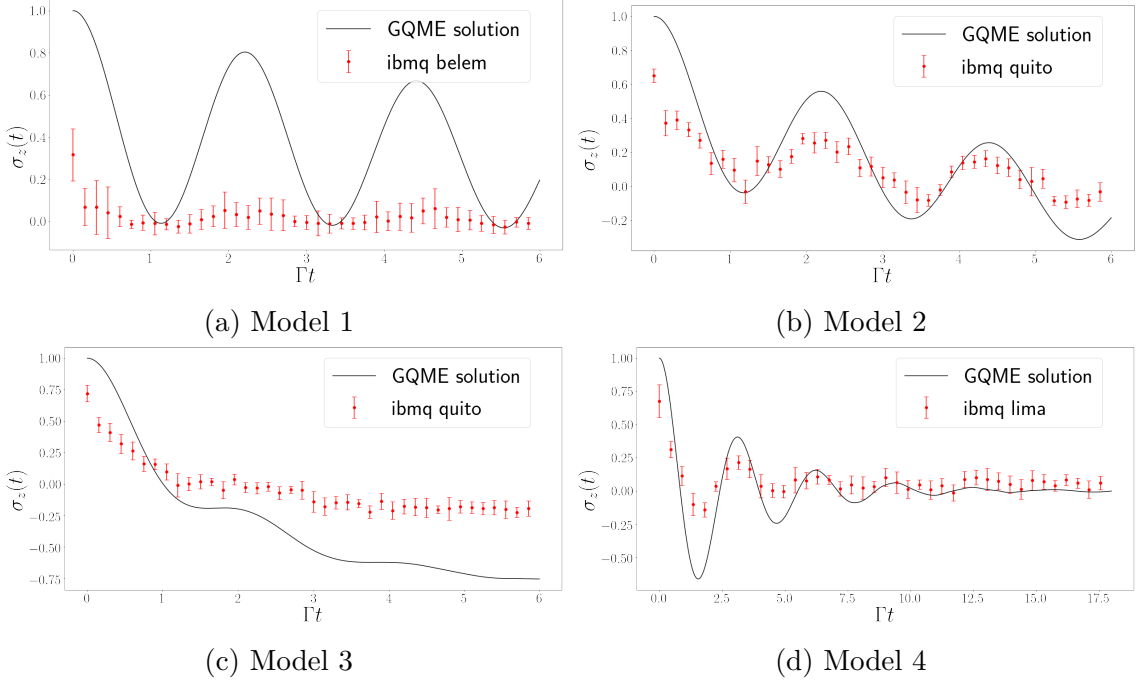


Figure 6.2. The spin-boson model simulated by the GQME quantum algorithm as implemented on the IBM quantum computers **ibmq belem**, **ibmq quito** and **ibmq lima**, showing the electronic population difference between the donor state and acceptor state $\sigma_z(t) = \sigma_{DD}(t) - \sigma_{AA}(t)$ as a function of time for (a) model 1 , (b) model 2 (c) model 3 and (d) model 4 as given in Table 6.1, with units scaled to the electronic coupling, Γ . Each figure shows the comparison between the GQME-based exact results represented by the black curves and quantum-computer-based results represented by the red dots with error bars. The time step for the real machine simulation is $\Delta t = 0.150083 \Gamma^{-1}$ for model 1,2 and 3 and $\Delta t = 0.450249 \Gamma^{-1}$ for model 4. The experiments of both models take 40 evenly-spaced time steps out of the 4000 time steps used in the QASM simulator runs and the error bars represent the standard deviations of the 10 separate runs on the **ibmq belem**, **ibmq quito** and **ibmq lima** for models 1 to 4. The number of projection measurements applied by all the devices to obtain a single time step is 2000 shots.

QASM-based results around the exact results can be traced back to the inherent uncertainty associated with projection measurements. These results validate the GQME-based quantum algorithm and demonstrate its ability to reproduce results obtained via the GQME-based classical algorithm.

To test the performance of the quantum algorithm on real quantum devices, we also performed the simulations on the quantum computers provided by IBM Quantum (IBM Q).

The simulations were performed for models 1 to 4 on **ibmq quito**, **ibmq belem** and **ibmq lima**. All devices are equipped with 5 qubits that have the same qubit connectivity and use IBM’s **Falcon r4T** processor with the same architecture. In each simulation of a given model, three qubits were used and 10 repeated experiments were performed. In a single experiment, 40 time steps are chosen at an equal spacing out of the 4000 time steps used in the QASM simulations, i.e., the time step in each experiment is 100 times greater than the time step used in the QASM simulations as listed in Table 6.1. The average CX gate error and readout error are $(1.191 \times 10^{-2}, 5.194 \times 10^{-2})$ for the **ibmq quito**, $(1.160 \times 10^{-2}, 2.590 \times 10^{-2})$ for the **ibmq belem** and $(1.032 \times 10^{-2}, 2.834 \times 10^{-2})$ for the **ibmq lima** as of the time of the experiments. The quantum circuits are the same in both the QASM simulations and the real machine simulations. The transpiled quantum gate counts for each of the $\mathcal{U}_{G'}(t)$ superoperators are 153 R_Z gates, 98 \sqrt{X} gates, and 41 CX gates. The transpiling process is done internally by the Qiskit package and examples of the quantum circuits can be found in the SI.

The comparison between the GQME-generated exact results and real machine simulations is given in Fig. 6.2. In the figure, the red dots are the average of the 10 experiments and the error bars represent standard derivations of the 10 experiments. While the results obtained on the IBM Q quantum computers reproduce some of the trends exhibited by the exact results, the agreement is qualitative at best. The lack of quantitative agreement can be traced back to the rather extensive circuit depth, which makes the calculation susceptible to noise. In the next section, we propose a way to lower the circuit depth and enhance the accuracy of the calculation on the IBM Q quantum computers by using reduced-dimensionality GQMEs.

6.4 Reduced-dimensionality GQME-based

Since the quantum algorithm on the QASM simulator was able to accurately reproduce the exact results, as shown in Fig. 6.1, we attribute the lack of quantitative agreement between the exact results and the results obtained via the IBM Q quantum computers, as seen in Fig. 6.2, to noise within the real quantum devices. If so, reducing the circuit depth would improve the accuracy. In this subsection, we validate this hypothesis by reducing the

dimensionality of the non-unitary propagator $\mathcal{G}(t)$, and thereby lowering the circuit depth to levels that allow for an accurate calculation on the NISQ quantum computers.

To this end, we take inspiration from reduced-dimensionality GQMEs, which correspond to EoMs for subsets of the open quantum system's reduced density matrix elements, rather than the full reduced density matrix.[105], [321] For example, for the spin-boson model described in Sec. 6.3, the memory kernel in the GQME for the full reduced density matrix, $\hat{\sigma}(t)$, is a 4×4 matrix, while the memory kernel in the GQME for only the two populations (the diagonal elements of the reduced density matrix, $\sigma_{00}(t)$ and $\sigma_{11}(t)$) is a 2×2 matrix. [105], [321] Below, we demonstrate how one can take advantage of this reduced dimensionality to lower the circuit depth and thereby improve the accuracy of the simulation on quantum machines.

For the spin-boson model under consideration in this paper, the electronic populations can be propagated using only the four corner elements of $\mathcal{G}(t)$, i.e.,

$$\begin{pmatrix} \sigma_{11}(t) \\ \sigma_{22}(t) \end{pmatrix} = \begin{pmatrix} \mathcal{G}_{11,11}(t) & \mathcal{G}_{11,22}(t) \\ \mathcal{G}_{22,11} & \mathcal{G}_{22,22}(t) \end{pmatrix} \begin{pmatrix} \sigma_{11}(0) \\ \sigma_{22}(0) \end{pmatrix}. \quad (6.20)$$

It should be noted that this equality only holds when the initial electronic state is of the form $\hat{\sigma}(0) = \sum_{j=1}^{N_e} \sigma_{jj}(0)|j\rangle\langle j|$, which is consistent with the initial state under consideration in this paper (see Eq. (6.17)). It should also be noted that Eq. (6.20) is still exact, in the sense that the time evolution of $\sigma_{11}(t)$ and $\sigma_{00}(t)$ as described by the equation is exactly the same time evolution as described by Eq. (6.9). Thus, the only price one pays for the reduced dimensionality is the loss of the ability to simulate the dynamics of the off-diagonal matrix elements $\sigma_{10}(t)$ and $\sigma_{01}(t)$. However, given that the primary goal is often to simulate the dynamics of electronic energy/charge transfer, the populations of the corresponding electronic states is all that one needs.

The 2×2 propagator in Eq. (6.20), which we will refer to as $\mathcal{G}^{\text{pop}}(t)$, can be dilated following a procedure similar to that we used to dilate the 4×4 propagator for the full density matrix, $\mathcal{G}(t)$. More specifically, $\mathcal{G}^{\text{pop}}(t)$ can be divided by a normalization factor

$n_c^{\text{pop}} = \|\mathcal{G}^{\text{pop}}(t)\|_{\mathcal{O}}$ to obtain its contraction form $\mathcal{G}^{\text{pop}'}(t) = \mathcal{G}^{\text{pop}}(t)/n_c^{\text{pop}}$. Applying a 1-dilation procedure to $\mathcal{G}^{\text{pop}'}(t)$, similar to that in Eq. (6.11), then leads to the following unitary propagator:

$$\mathcal{U}_{\mathcal{G}^{\text{pop}'}}(t) = \begin{pmatrix} \mathcal{G}^{\text{pop}'}(t) & \mathcal{D}_{\mathcal{G}^{\text{pop}'\dagger}}(t) \\ \mathcal{D}_{\mathcal{G}^{\text{pop}'}}(t) & -\mathcal{G}^{\text{pop}'\dagger}(t) \end{pmatrix}. \quad (6.21)$$

Notably, for the spin-boson model, while $\mathcal{U}_{\mathcal{G}'}(t)$ is an 8×8 time-dependent matrix, $\mathcal{U}_{\mathcal{G}^{\text{pop}'}}(t)$ is a 4×4 time-dependent matrix.

A comparison between the exact results and results obtained by performing the quantum algorithm based on Eq. (6.21) on IBM Q quantum machines is shown in Fig. 6.3. The results shown were obtained for models 1-4 on **ibmq belem**, **ibmq lima**, **ibm oslo** and **ibm nairobi**, respectively. Here, **ibm oslo** and **ibm nairobi** are each equipped with 7 qubits of the same qubit connectivity and both use IBM's **Falcon r5.11H** processor. The average CX gate error and readout error are $(1.038 \times 10^{-2}, 2.280 \times 10^{-2})$ for the **ibm nairobi** and $(8.537 \times 10^{-3}, 2.310 \times 10^{-2})$ for the **ibm oslo** as of the time of the experiments. The new simulations use the same time steps, experiment shots and follow the same procedures as that used to obtain the results in Fig. 6.2. The quantum circuits are re-transpiled to implement the reduced-dimensionality GQME-based quantum algorithm where only two qubits are used. The transpiled quantum gate counts for each of the $\mathcal{U}_{\mathcal{G}^{\text{pop}'}}(t)$ superoperators are 17 R_Z gates, 12 \sqrt{X} gates, and 2 CX gates. The transpiling processes are done internally by the Qiskit package.

The results in Fig. 6.3 confirm that the lack of quantitative agreement seen in Fig. 6.2 can be attributed to noise on the real quantum devices. More specifically, significantly more accurate results are obtained when the populations-only reduced dimensionality GQME-based propagators are used, which can be traced back to their ability to give rise to shallower quantum circuits. Thus, reduced dimensionality make it possible to accurately simulate the open quantum system dynamics on NISQ quantum computers.

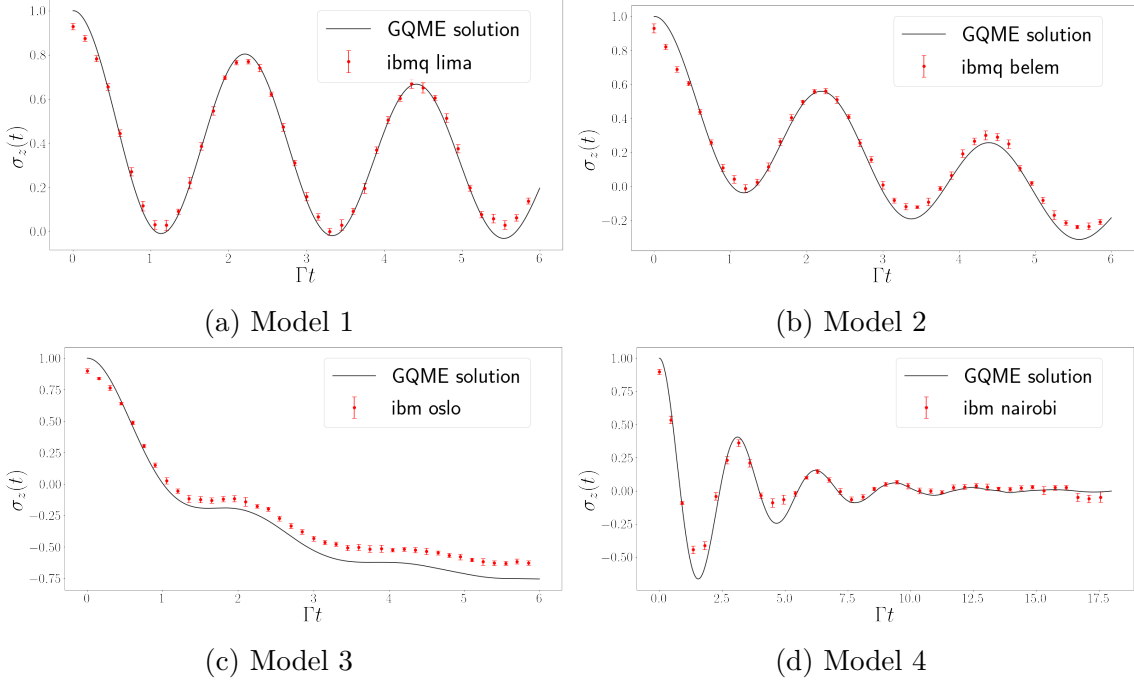


Figure 6.3. A comparison between the exact results for the spin-boson model and results obtained by performing the quantum algorithm based on Eq. (6.21) on the IBM Q quantum machines. The electronic population difference between the donor state and acceptor state, $\sigma_z(t) = \sigma_{DD}(t) - \sigma_{AA}(t)$, is plotted as a function of time for (a) model 1, (b) model 2, (c) model 3 and (d) model 4 as given in Table 6.1, with units scaled to the electronic coupling, Γ . Each panel shows the comparison between the exact results represented by the black curves and the population-only-GQME-based quantum-computer-simulated results represented by the red dots with error bars. The time step for the real machine simulation is $\Delta t = 0.150083 \Gamma^{-1}$ for model 1, 2 and 3 and $\Delta t = 0.450249 \Gamma^{-1}$ for model 4. The experiments of both models take 40 evenly-spaced time steps out of the 4000 time steps used in the QASM simulator runs and the error bars represent the standard deviations of the 10 separate runs on the **ibmq lima**, **ibmq belem**, **ibm oslo** and **ibm nairobi** for models 1-4, respectively. The number of projection measurements applied by all the devices to simulate a single time step is 2000 shots.

6.5 Concluding Remarks

The GQME-based quantum algorithm proposed herein substantially expands the range of open quantum systems that can be simulated on a quantum computer. In this paper, we demonstrated the applicability and versatility of the algorithm by using it to simulate

the dynamics of electronic populations within the benchmark spin-boson model on the IBM QASM quantum simulator and IBM quantum computers.

The results obtained via the noise-free QASM simulator were found to be highly accurate, with the only errors inherently associated with the quantum projection measurements and giving rise to very slight deviations from the exact results. However, while the implementation of the algorithm on the NISQ IBM Q quantum computers was found to reproduce some of the trends exhibited by the exact results, the agreement was qualitative at best. This lack of quantitative agreement was traced back to the rather extensive circuit depth, which made the calculation susceptible to noise. This issue was confirmed and fixed by implementing a populations-only reduced-dimensionality version of the quantum algorithm, which significantly shortened the circuit depth and as a result gave rise to quantitatively accurate results.

Further improvement can be achieved by reducing the circuit depth via optimizing the quantum circuit design. This can be achieved by optimizing the decomposition of unitary operations into elementary gate sequences [328]–[331]. One particularly interesting idea is to reduce the circuit depth by adding qubits.[332] To this end, it should be noted that we have only used 3 qubits out of the 5 currently available on the IBM quantum computers. Another way for improving accuracy is by active error correction using dynamical decoupling (DD) protocols, that employ pulses to suppress the system’s coupling with the environment.[333]–[337] Recent implementations of DD on IBM machines was found to improve the fidelity of the overall performance [338]–[340]. Yet another direction is to implement the circuit on high-dimensional qudit machines. Quantum computers based on three-dimensional circuit quantum electrodynamics (3D cQED) microwave cavities are particularly promising in this respect, as they feature unique quantum error correction schemes [341]–[343] and longer coherence times [344], [345] than standard superconducting quantum computers. Bosonic quantum computing algorithms have also been recently shown to significantly reduce the number of quantum gates required for the calculation of the Franck-Condon factors [346] and dynamics of rhodopsin near conical intersections [347]. Lossless 3D cQED systems have not yet been employed to simulate open quantum system dynamics. An adaptation of the algorithm presented here to bosonic quantum computing could therefore provide another

way to efficiently simulate open quantum system dynamics and demonstrate how qudit-based quantum architectures can reduce the computational cost and enhance the accuracy of quantum simulations.

7. SUMMARY

Qudit is a multi-level computational unit alternative to the conventional 2-level qubit. It provides a larger state space for information processing, and thus can reduce the circuit complexity, simplify the experimental setup. The first half of this thesis includes a review of the qudit quantum computing, presents an implementation of the qudit phase estimation algorithm on a photonic system and introduces a statistical and variational approach to the phase estimation algorithm. Chapter 2 is an overview of qudit-based quantum computing. It covers a variety of topics ranging from circuit building, algorithm design, to experimental methods. It first discusses the qudit gate universality and a variety of qudit gates and then presents the qudit version of several representative quantum algorithms. Finally it discusses various physical realizations for qudit computation such as the photonic platform, ion trap, and nuclear magnetic resonance. Chapter 3 presents the implementation of the qudit phase estimation algorithm on a photonic system. The Phase Estimation Algorithm (PEA) is an important quantum algorithm used independently or as a key subroutine in other quantum algorithms. This chapter reports the first experimental realization of a qudit-based PEA on a photonic platform, utilizing the high dimensionality in time and frequency degrees of freedom (DoFs) in a single photon. The controlled-unitary gates can be realized in a deterministic fashion, as the control and target registers are now represented by two DoFs in a single photon. A new statistical and variational approach to the phase estimation algorithm, or SPEA, is introduced in Chapter 4. The SPEA can determine any unknown eigenstate-eigenphase pair from a given unitary matrix utilizing a simplified version of the hardware intended for the Iterative PEA (IPEA). This is achieved by treating the probabilistic output of an IPEA-like circuit as an eigenstate-eigenphase proximity metric, using this metric to estimate the proximity of the input state and input phase to the nearest eigenstate-eigenphase pair and approaching this pair via a variational process on the input state and phase. This method may search over the entire computational space, or can efficiently search for eigenphases (eigenstates) within some specified range (directions), allowing those with some prior knowledge of their system to search for particular solutions.

The second half of the thesis focus on the simulation of the open quantum dynamics which is a useful application for quantum computer based on qudit as well as qubit. The simulation of open quantum dynamics on quantum circuits has attracted wide interests recently with a variety of quantum algorithms developed and demonstrated. In the Chapter 5, we apply a Sz.-Nagy dilation theorem-based quantum algorithm to simulating the dynamics of the radical pair mechanism(RPM) in the avian compass on the IBM QASM quantum simulator. This first quantum simulations of the RPM in the avian compass not only demonstrates the generality of the quantum algorithm, but also opens new opportunities for studying the avian compass with quantum computing devices. Chapter 6 presents a quantum algorithm based on the Generalized Quantum Master Equation (GQME) approach to simulate open quantum system dynamics on noisy intermediate-scale quantum (NISQ) computers. This approach overcomes the limitations of the Lindblad equation by providing a rigorous derivation of the equations of motion for any subset of elements of the reduced density matrix. The GQME generated non-unitary propagator is transformed into a unitary one in a higher-dimensional Hilbert space with the dilation-based algorithm, which can then be implemented on a quantum circuit. We validate our quantum algorithm as applied to the spin-boson benchmark model by analyzing the impact of the quantum circuit depth on the accuracy of the results when the subset is limited to the diagonal elements of the reduced density matrix. Our findings demonstrate that our approach yields reliable results on NISQ IBM computers.

A. APPENDIX FOR CHAPTER 4

A.1 Quality of Eigenphase-Eigenstate retrieval

Preliminary note: All phases $\theta \in [0, 1)$. The difference between two phases can be found via the function

$$d(\theta_a, \theta_b) \equiv \frac{\arg(e^{i2\pi(\theta_a - \theta_b)})}{2\pi} \quad (\text{A.1})$$

where $d(\theta_a, \theta_b) \in [-.5, .5)$. In short, as the phase wraps around the phase difference also wraps around. E.g. $d(\frac{1}{8}, \frac{3}{4}) = \frac{3}{8}$, not $\frac{-5}{8}$. And $d(\frac{3}{4}, \frac{1}{8}) = \frac{-3}{8}$, not $\frac{5}{8}$. Like usual differences, $d(\theta_a, \theta_b) = -d(\theta_b, \theta_a)$. Appreciate that – for \mathcal{P}_0 of Equation 4.3 – $\mathcal{P}_0(d(\theta_a, \theta_b)) = \mathcal{P}_0(\theta_a - \theta_b) \forall \theta_a, \theta_b$.

Here, we quantify the quality of the eigenstate $|\Phi\rangle^*$ and eigenphase θ_R^* using $\mathcal{C}^* = \mathcal{C}(|\Phi\rangle^*, \theta_R^*)$. When \mathcal{C}^* is greater than the largest (non-global) local maximum of \mathcal{P}_θ (of Equation 4.3), then θ_R^* must be within the primary lobe of \mathcal{P}_θ (examples shown in Figure 4.3). That is, when

$$\mathcal{C}^* > \max_{\zeta \in [\frac{1}{d_c}, 0.5]} \mathcal{P}_0(\zeta) \quad (\text{A.2})$$

we are within the primary lobe of \mathcal{P}_θ . Let θ_{k^*} be the eigenvalue closest to θ_R and define $\delta^* \equiv d(\theta_{k^*}, \theta_R)$. When Equation A.2 is true, then $\mathcal{P}_0(\delta^*) \geq \mathcal{P}_0(\theta_k - \theta_R) \forall k$ and

$$\begin{aligned} \mathcal{C}^* &= \sum_{k=0}^{d_t-1} |\langle \theta_k | \Phi \rangle|^2 \mathcal{P}_0(\theta_k - \theta_R) \leq \sum_{k=0}^{d_t-1} |\langle \theta_k | \Phi \rangle|^2 \mathcal{P}_0(\delta^*) \\ &= \mathcal{P}_0(\delta^*) \sum_{k=0}^{d_t-1} |\langle \theta_k | \Phi \rangle|^2 = \mathcal{P}_0(\delta^*) \\ \mathcal{C}^* &\leq \mathcal{P}_0(\delta^*) \end{aligned} \quad (\text{A.3})$$

As \mathcal{P}_0 is symmetric and monotonic within the primary lobe,

$$|\delta^*| \leq \mathcal{P}_0^{-1}(\mathcal{C}^*). \quad (\text{A.4})$$

Therefore the estimated eigenphase θ_R^* is within $\pm \mathcal{P}_0^{-1}(\mathcal{C}^*)$ of the nearest eigenphase (whenever Equation A.2 is met).

Now to quantify the eigenstate estimate. Define a Δ -eigenstate $|\nu_\Delta\rangle$ as any superposition of eigenstates where the corresponding eigenphases are within $\pm\Delta$ of θ_R^*

$$|\nu_\Delta\rangle = \sum_m \alpha_m |\nu_m\rangle, \quad (\text{A.5})$$

where $|d(\theta_m, \theta_R^*)| \leq \Delta \forall m$

(and where $\sum_m |\alpha_m|^2 = 1$). That is, $|\nu_\Delta\rangle$ is a superposition of eigenstates (indexed $\{m\}_\Delta$) that are *nearly* degenerate: the corresponding eigenphases are all within 2Δ of one another. Proceeding from Equation 4.4 (whenever Equation A.2 holds),

$$\begin{aligned} \mathcal{C}^* &= \mathcal{C}(|\Phi\rangle^*, \theta_R^*) = \sum_{k=0}^{d_t-1} |\langle \nu_k | \Phi \rangle|^2 \mathcal{P}_0(\theta_k - \theta_R^*) \\ &\leq \sum_{k \in \{m\}_\Delta} |\langle \nu_k | \Phi \rangle|^2 (1) + \sum_{k \notin \{m\}_\Delta} |\langle \nu_k | \Phi \rangle|^2 \mathcal{P}_0(\theta_k - \theta_R^*) \\ &\leq \sum_{k \in \{m\}_\Delta} |\langle \nu_k | \Phi \rangle|^2 + \sum_{k \notin \{m\}_\Delta} |\langle \nu_k | \Phi \rangle|^2 \mathcal{P}_0(\Delta). \end{aligned} \quad (\text{A.6})$$

Letting $\sum_{k \in \{m\}_\Delta} |\langle \nu_k | \Phi \rangle|^2 = f$,

$$\begin{aligned} \mathcal{C}^* &\leq f + (1 - f)\mathcal{P}_0(\Delta) \\ \therefore f &\geq \frac{\mathcal{C}^* - \mathcal{P}_0(\Delta)}{1 - \mathcal{P}_0(\Delta)} \end{aligned} \quad (\text{A.7})$$

The estimated eigenstate $|\Phi\rangle^*$ matches some Δ -eigenstate (as defined by Equation A.5) with fidelity f given by Equation A.7 (whenever Equation A.2 holds and $|\Delta| \in [0, \frac{1}{d_c}]$).

A.2 Details for the IBM Q SPEA calculations

On IBM Q we realize an SPEA with a four-dimensional control register by using two qubits (the top two rails) as controls. The target is either two- or four-dimensional, using the bottom one or two rails, respectively.

We list out the three operators in matrix form used in our simulations on the IBM Q accompanied by the eigenstates of each matrix as well as showing how we achieved these matrices with the Qiskit.

In the following we use the rotation- Z gate as defined by Qiskit [78]:

$$RZ(\theta) = \begin{pmatrix} e^{-i\theta/2} & 0 \\ 0 & e^{i\theta/2} \end{pmatrix} \quad (\text{A.8})$$

as well as the phase gate:

$$P(\theta) = \begin{pmatrix} 1 & 0 \\ 0 & e^{i\theta} \end{pmatrix} \quad (\text{A.9})$$

and the Hadamard gate:

$$H = \frac{1}{\sqrt{2}} \begin{pmatrix} 1 & 1 \\ 1 & -1 \end{pmatrix} \quad (\text{A.10})$$

The first operator U_1 is a single qubit rotation- Z gate with $\theta = \pi/2$,

$$U_1 = RZ(\pi/2) = \begin{pmatrix} e^{-i\pi/4} & 0 \\ 0 & e^{i\pi/4} \end{pmatrix} \text{ with eigenstates } v_1 = \begin{pmatrix} 0 \\ 1 \end{pmatrix}, v_2 = \begin{pmatrix} 1 \\ 0 \end{pmatrix} \quad (\text{A.11})$$

The second operator is a two qubit operation achieved by a phase gate $P(\theta = \pi/4)$ acting on the first qubit and a rotation- Z gate $RZ(\theta = \pi/2)$ sandwiched between two Hadamard gates H , acting on the second qubit. The matrix form is

$$U_2 = P(\pi/4) \otimes (H \cdot RZ(\pi/2) \cdot H) = \frac{1}{\sqrt{2}} \begin{pmatrix} 1 & -i & 0 & 0 \\ -i & 1 & 0 & 0 \\ 0 & 0 & e^{i\frac{\pi}{4}} & e^{-i\frac{\pi}{4}} \\ 0 & 0 & e^{-i\frac{\pi}{4}} & e^{i\frac{\pi}{4}} \end{pmatrix} \quad (\text{A.12})$$

with eigenstates

$$v_3 = \begin{pmatrix} 0 \\ 0 \\ 1 \\ 1 \end{pmatrix}, v_4 = \begin{pmatrix} 0 \\ 0 \\ 1 \\ -1 \end{pmatrix}, v_5 = \begin{pmatrix} 1 \\ 1 \\ 0 \\ 0 \end{pmatrix}, v_6 = \begin{pmatrix} 1 \\ -1 \\ 0 \\ 0 \end{pmatrix} \quad (\text{A.13})$$

The gate representations of the two operators can be found in Figure A.2.1.

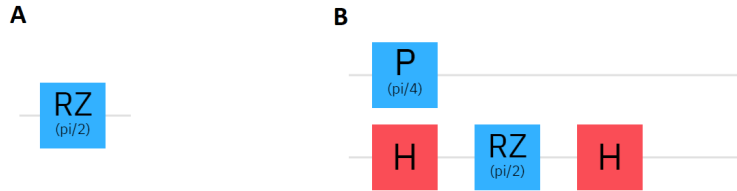


Figure A.2.1. Gate representation of the unitary operators applied in the simulation. **(A)** represents operator U_1 , a 2-dimensional operator applied to a single qubit. **(B)** represents operator U_2 , a 4-dimensional operator applied to two qubits. RZ is the rotation- Z gate, P is the phase gate and H is the Hadamard gate. When a control qubit is present the RZ gate and the P gate become controlled gates. The Hadamard gates will serve as their own inverse and therefore do not need to be implemented as controlled gates.

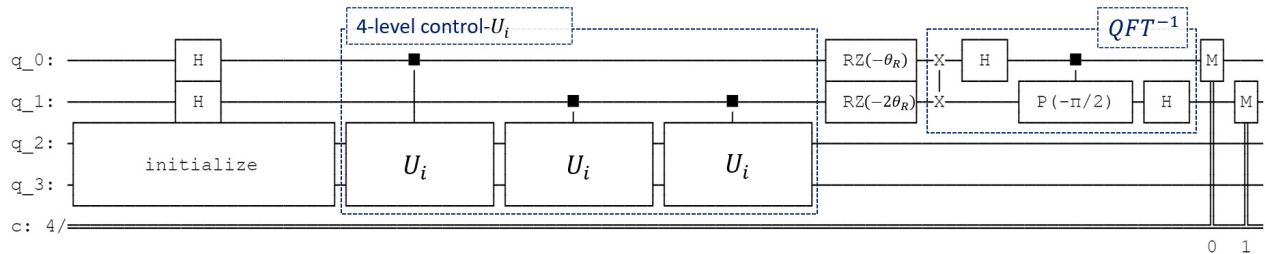


Figure A.2.2. Illustration of the 4-level control ($d_c = 4$) SPEA circuit implemented using Qiskit. H is the Hadamard gate, RZ is the rotation- Z gate, P is the phase gate, and M represents a measurement. The top two rails are the control qubits and realize a 4-dimensional control register. The bottom two rails represents the target register. The initialize block prepares the input state differently throughout the optimization process. U_i represents the unitary the SPEA is running. For $i = 2, 3$ we implement the circuit as diagrammed. For $i = 1$, the unitary is 2-dimensional and we use only a single target rail. The three control gates together realize a multi(4)-level control gate as described in the main text. The two RZ -gates together realize a realize four-level $R_z(-\theta_R)$ as described in the main text. The double line at the bottom represents the classical information retrieved from the measurement gates (a total of 2 bits).

For the third operators we start with the lowest energy Hamiltonian of the hydrogen molecule generated with Bravyi-Kitaev transformation in $STO - 3g$ basis,

$$H = \begin{pmatrix} 0.487049 & 0 & 0 & 0.180653 \\ 0 & -0.337700 & 0.180653 & 0 \\ 0. & 0.180653 & -0.337700 & 0 \\ 0.180653 & 0 & 0 & -1.117194 \end{pmatrix}. \quad (\text{A.14})$$

Then we take the exponential of the Hamiltonian to generate our unitary operator

$$U_3 = e^{iH} = \begin{pmatrix} 0.8686 + 0.4687i & 0 & 0 & 0.0499 + 0.1531i \\ 0 & 0.9282 - 0.3259i & 0.0595 + 0.1695i & 0 \\ 0 & 0.0595 + 0.1695i & 0.9282 - 0.3259i & 0 \\ 0.0499 + 0.1531i & 0 & 0 & 0.4256 - 0.8905i \end{pmatrix}. \quad (\text{A.15})$$

The exponential of the Hamiltonian is done with the `scipy.linalg.expm` in the `scipy` python package [348]. The eigenstates are

$$v_7 = \begin{pmatrix} -0.1105 \\ 0 \\ 0 \\ 0.9939 \end{pmatrix}, v_8 = \begin{pmatrix} 0 \\ 0.7071 \\ -0.7071 \\ 0 \end{pmatrix}, v_9 = \begin{pmatrix} 0 \\ 0.7071 \\ 0.7071 \\ 0 \end{pmatrix}, v_{10} = \begin{pmatrix} -0.9939 \\ 0 \\ 0 \\ 0.1105 \end{pmatrix} \quad (\text{A.16})$$

We design the phase estimation algorithms that work with up to two qubits in the control register and four qubits in total as shown in Figure A.2.2. Due to the restrictions in the qubit numbers, the simulations on the IBM Q are focused on the lower dimensional systems, i.e. one or two qubits in the target register. The rotation RZ gates are applied to each qubit in the control register after the controlled- U_i operations but before inverse Fourier transform. Every time the quantum algorithm is called to generate a new \mathcal{C} factor (following the “alternative method” in step 3 of Section 4.2), the algorithm runs twice: the first time the RZ gates are set to zero and the phase factor θ_R is calculated statistically; the second time the upper RZ gate applies phase $-\theta_R$ and the lower gate applies phase $-2\theta_R$, together acting as a $-\theta_R$ -rotation would on a $d_c = 4$ qudit system. The classical optimization process described in Section 4.2 is implemented using python. The basis set $\{|B_m\rangle\}$ is generated using the Gram-Schmidt methods with the input vector plus a set of linearly independent

vectors obtained from a randomly generated unitary matrix. As a deviation from how the algorithm is described in the main text, the search step a factor is set to 1/2 in step 4 and is doubled in step 5 (rather than halved) if \mathcal{C} -factor is not updated, up to seven times. The optimization concludes when the \mathcal{C} factor meets the stopping condition which means the input state is converged to an eigenstate, or when the maximum iteration time is exceeded.

A.3 Full H_2O Matrix

The Hamiltonian of the water molecule with the H-O-H angle at 104.5° and the bond length at 1.0 a.u. is calculated by $STO-3G$ minimal basis using PySCF [311] and chemistry package provided by the Qiskit[78]. The 16-by-16 Hamiltonian of the water molecule [236] used for the local computer’s spectral decomposition simulations is sparse with nonzero entries,

$$\begin{aligned}
 \mathcal{H}_{H_2O}(1, 1) &= 1.027 \cdot 10^{-15}, & \mathcal{H}_{H_2O}(2, 2) &= -2.594, \\
 \mathcal{H}_{H_2O}(3, 3) &= -2.654, & \mathcal{H}_{H_2O}(4, 4) &= -4.583, \\
 \mathcal{H}_{H_2O}(5, 5) &= -2.594, & \mathcal{H}_{H_2O}(6, 6) &= -4.427, \\
 \mathcal{H}_{H_2O}(7, 7) &= -4.529, & \mathcal{H}_{H_2O}(8, 8) &= -5.696, \\
 \mathcal{H}_{H_2O}(9, 9) &= -2.654, & \mathcal{H}_{H_2O}(10, 10) &= -4.529, \\
 \mathcal{H}_{H_2O}(11, 11) &= -4.428, & \mathcal{H}_{H_2O}(12, 12) &= -5.637, \\
 \mathcal{H}_{H_2O}(13, 13) &= -4.583, & \mathcal{H}_{H_2O}(14, 14) &= -5.696, \\
 \mathcal{H}_{H_2O}(15, 15) &= -5.637, & \mathcal{H}_{H_2O}(16, 16) &= -6.085, \\
 \mathcal{H}_{H_2O}(6, 11) &= \mathcal{H}_{H_2O}(11, 6) = 0.054, \\
 \mathcal{H}_{H_2O}(7, 10) &= \mathcal{H}_{H_2O}(10, 7) = 0.054.
 \end{aligned}
 \tag{A.17}$$

The exponential of the Hamiltonian is done with the MATLAB expm function.

B. APPENDIX FOR CHAPTER 4

B.1 Quantum Simulation Details

Here we give an example of the quantum circuit of the $M_1 = \sqrt{k_d \delta t} P_1$ at the first time step, $5 \times 10^{-5} s$ to evolve the states. After multiplied by the unitary matrix accounting for the coherent part as in Eq. (B.1), M_1 becomes a 10×10 sparse matrix shown in Eq. (B.2) and the non-zero values are shown in Eq. (B.3).

$$\dot{\rho} = -\frac{i}{\hbar}[H, \rho] + k_d \sum_{i=1}^8 [P_i \rho P_i^\dagger - \frac{1}{2}(P_i^\dagger P_i \rho + \rho P_i^\dagger P_i)], \quad (\text{B.1})$$

$$\begin{bmatrix} 0 & 0 & 0 & 0 & 0 & 0 & 0 & 0 & 0 & 0 \\ 0 & 0 & 0 & 0 & 0 & 0 & 0 & 0 & 0 & 0 \\ 0 & 0 & 0 & 0 & 0 & 0 & 0 & 0 & 0 & 0 \\ 0 & 0 & 0 & 0 & 0 & 0 & 0 & 0 & 0 & 0 \\ 0 & 0 & 0 & 0 & 0 & 0 & 0 & 0 & 0 & 0 \\ 0 & 0 & 0 & 0 & 0 & 0 & 0 & 0 & 0 & 0 \\ 0 & 0 & 0 & 0 & 0 & 0 & 0 & 0 & 0 & 0 \\ 0 & 0 & 0 & 0 & 0 & 0 & 0 & 0 & 0 & 0 \\ 0 & 0 & 0 & 0 & 0 & 0 & 0 & 0 & 0 & 0 \\ m_1 & m_2 & m_3 & m_4 & m_5 & m_6 & m_7 & m_8 & 0 & 0 \\ 0 & 0 & 0 & 0 & 0 & 0 & 0 & 0 & 0 & 0 \end{bmatrix} \quad (\text{B.2})$$

$$\begin{aligned}
m_1 &= -5.22 \times 10^{-2} - 4.05 \times 10^{-1}i \\
m_2 &= -6.53 \times 10^{-4} + 1.23 \times 10^{-2}i \\
m_3 &= -2.93 \times 10^{-1} + 3.80 \times 10^{-3}i \\
m_4 &= -1.70 \times 10^{-2} + 1.38 \times 10^{-4}i \\
m_5 &= 2.93 \times 10^{-1} + 3.78 \times 10^{-3}i \\
m_6 &= -7.39 \times 10^{-1} - 2.62 \times 10^{-3}i \\
m_7 &= -5.22 \times 10^{-3} + 4.05 \times 10^{-1}i \\
m_8 &= 5.63 \times 10^{-4} + 5.37 \times 10^{-3}i
\end{aligned} \tag{B.3}$$

$$U_{M_k} = \begin{pmatrix} M_k & D_{M_k^\dagger} \\ D_{M_k} & -M_k^\dagger \end{pmatrix}, \tag{B.4}$$

After we apply the unitary dilation described in Eq. (B.4) on the M_1 , we obtain a 20×20 unitary matrix U_{M_1} . To simulate this operation on quantum simulator, we have to use 5 qubits to cover the 20 dimensions. Leveraging the Qiskit's transpile function (`qiskit.compliler.transpile`), we decomposed the resulted unitary operator U_{M_1} to 2097 gates where a portion of the circuit is shown below (Fig. B.1.1) using the basis gates: 'u3',

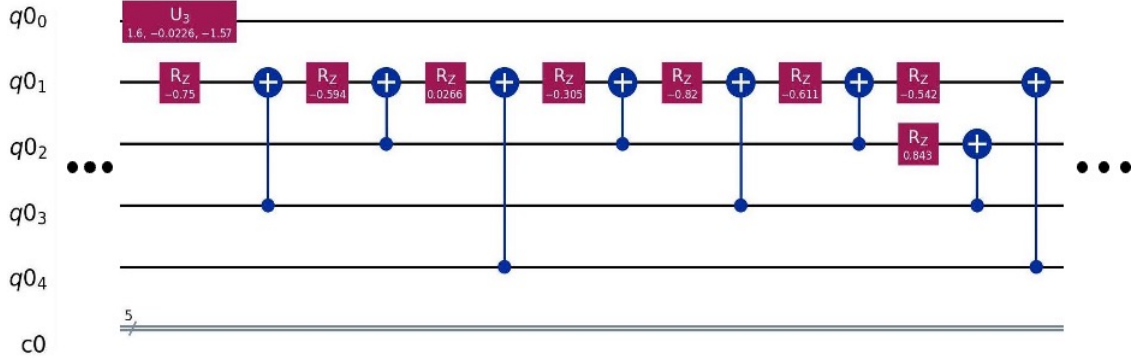


Figure B.1.1. An example of a portion of the quantum gate sequence of a Kraus operator. This is only a small portion of the circuit. The full circuit has 2097 gates and the details will be available from the authors on reasonable request.

‘cx’ and ‘rz’ as shown in Eq.(B.5) , on the backend of qasm_simulator. The details of the decomposition of all the quantum circuits used are available on reasonable request.

$$\begin{aligned}
 U_3(\theta, \phi, \lambda) &= \begin{pmatrix} \cos\left(\frac{\theta}{2}\right) & -e^{i\lambda} \sin\left(\frac{\theta}{2}\right) \\ e^{i\phi} \sin\left(\frac{\theta}{2}\right) & e^{i(\phi+\lambda)} \cos\left(\frac{\theta}{2}\right) \end{pmatrix} \\
 CX &= I \otimes |0\rangle\langle 0| + X \otimes |1\rangle\langle 1| = \begin{pmatrix} 1 & 0 & 0 & 0 \\ 0 & 0 & 0 & 1 \\ 0 & 0 & 1 & 0 \\ 0 & 1 & 0 & 0 \end{pmatrix} \\
 Rz(\theta) &= \begin{pmatrix} e^{-i\frac{\theta}{2}} & 0 \\ 0 & e^{i\frac{\theta}{2}} \end{pmatrix}
 \end{aligned} \tag{B.5}$$

C. APPENDIX FOR CHAPTER 6

C.1 Quantum circuit examples

In this section, we include further details concerning the quantum algorithm, including the dilation process, circuit transpiling, QASM simulations, and simulations running on the IBM quantum computers **ibmq quito** and **ibmq lima**. The normalized time evolution operator of the electronic reduced density operator $\mathcal{G}'(t) = \mathcal{G}(t)/n_c$ (where $\mathcal{G}(t)$ is generated from the GQME formalism) is dilated into a unitary operator $\mathcal{U}_{\mathcal{G}'(t)}$. We start with \mathcal{G}_3 , which corresponds to the $\mathcal{G}(t)$ of the 1500th time step from model 3, and \mathcal{G}_4 , which corresponds to the $\mathcal{G}(t)$ of the 1500th time step from model 4. The matrix of \mathcal{G}_3 and \mathcal{G}_4 are, respectively:

$$\mathcal{G}_3 = \begin{pmatrix} 0.38 - 3.76 \times 10^{-10}j & 0.04 + 2.90 \times 10^{-2}j & 0.04 - 2.90 \times 10^{-2}j & 0.06 - 1.88 \times 10^{-10}j \\ -0.13 + 7.04 \times 10^{-2}j & 0.28 - 2.63 \times 10^{-2}j & 0.02 + 2.37 \times 10^{-2}j & -0.15 - 3.06 \times 10^{-2}j \\ -0.13 - 7.04 \times 10^{-2}j & 0.02 - 2.37 \times 10^{-2}j & 0.28 + 2.63 \times 10^{-2}j & -0.15 + 3.06 \times 10^{-2}j \\ 0.62 + 3.77 \times 10^{-10}j & -0.04 - 2.90 \times 10^{-2}j & -0.04 + 2.90 \times 10^{-2}j & 0.94 + 1.87 \times 10^{-10}j \end{pmatrix}, \quad (\text{C.1})$$

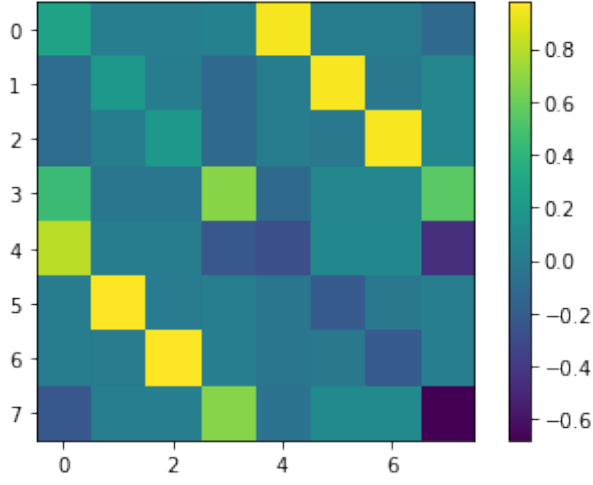
and

$$\mathcal{G}_4 = \begin{pmatrix} 0.54 + 4.7 \times 10^{-11}j & -1.7 \times 10^{-6} + 5.7 \times 10^{-2}j & -1.6 \times 10^{-6} - 5.6 \times 10^{-2}j & 0.46 + 7.1 \times 10^{-11}j \\ -0.46 + 5.7 \times 10^{-2}j & 3.6 \times 10^{-2} + 6.1 \times 10^{-5}j & -1.6 \times 10^{-2} - 5.7 \times 10^{-5}j & -0.46 - 5.7 \times 10^{-2}j \\ -0.46 - 5.7 \times 10^{-2}j & -1.6 \times 10^{-2} + 5.7 \times 10^{-5}j & 3.7 \times 10^{-2} - 6.1 \times 10^{-5}j & -0.46 + 5.7 \times 10^{-2}j \\ 0.54 - 4.7 \times 10^{-11}j & 1.6 \times 10^{-6} - 5.6 \times 10^{-2}j & 1.6 \times 10^{-6} + 5.6 \times 10^{-2}j & 0.54 - 7.1 \times 10^{-11}j \end{pmatrix}. \quad (\text{C.2})$$

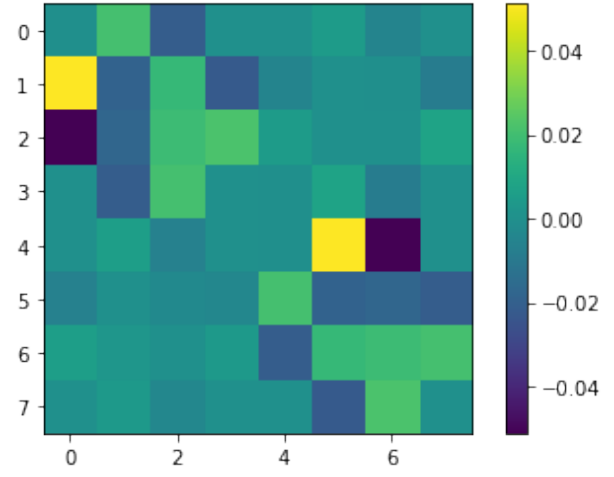
The normalization factors used for model 3 and model 4 are $n_{c3} = 1.376$ and $n_{c4} = 1.376$.

Following the 1-dilation process, the 4×4 $\mathcal{G}'(t)$ [derived from corresponding $\mathcal{G}(t)$ divided by the n_c factor] is converted into a unitary 8×8 $\mathcal{U}_{\mathcal{G}'(t)}$. We show $\mathcal{U}_{\mathcal{G}'_3}$ and $\mathcal{U}_{\mathcal{G}'_4}$ in the form of heat maps in Fig. C.1.1.

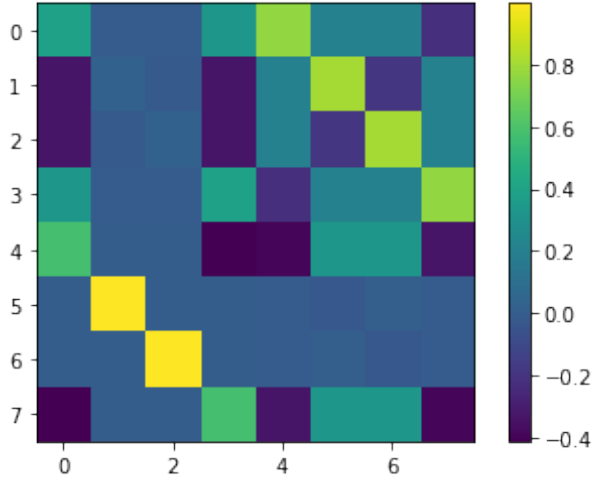
The unitary operation $\mathcal{U}_{\mathcal{G}'(t)}$ is transpiled into a 3-qubit quantum circuit composed of three elementary quantum gates: R_Z , \sqrt{X} , and CX , which have the matrix form:



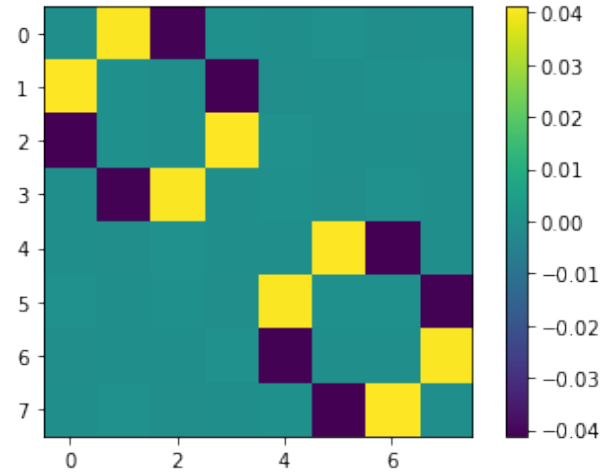
(a) $\mathcal{U}_{\mathcal{G}_3}$ real part



(b) $\mathcal{U}_{\mathcal{G}_3}$ imaginary part



(c) $\mathcal{U}_{\mathcal{G}_4}$ real part



(d) $\mathcal{U}_{\mathcal{G}_4}$ imaginary part

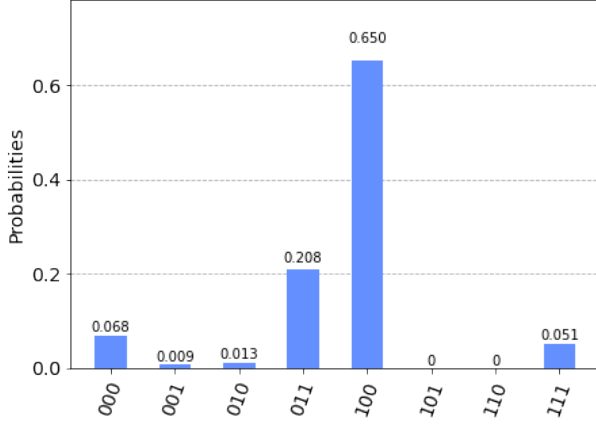
Figure C.1.1. Heat map illustrations of the dilated 8×8 unitary matrix $\mathcal{U}_{\mathcal{G}_3}$ and $\mathcal{U}_{\mathcal{G}_4}$ for the 1500th $\mathcal{G}(t)$ matrix, \mathcal{G}_3 at $t = 2.25\Gamma^{-1}$ for model 3 and \mathcal{G}_4 at $t = 6.75\Gamma^{-1}$ for model 4.

$$R_Z(\lambda) = \exp\left(-i\frac{\lambda}{2}Z\right) = \begin{pmatrix} e^{-i\frac{\lambda}{2}} & 0 \\ 0 & e^{i\frac{\lambda}{2}} \end{pmatrix} \quad (\text{C.3})$$

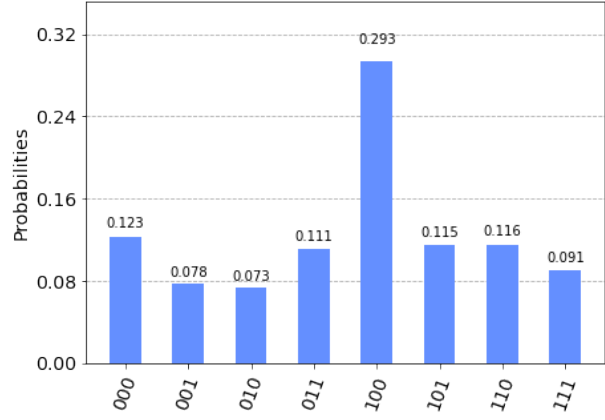
$$\sqrt{X} = \frac{1}{2} \begin{pmatrix} 1+i & 1-i \\ 1-i & 1+i \end{pmatrix} \quad (\text{C.4})$$

$$CX_{q_0, q_1} = I \otimes |0\rangle\langle 0| + X \otimes |1\rangle\langle 1| = \begin{pmatrix} 1 & 0 & 0 & 0 \\ 0 & 0 & 0 & 1 \\ 0 & 0 & 1 & 0 \\ 0 & 1 & 0 & 0 \end{pmatrix} \quad (\text{C.5})$$

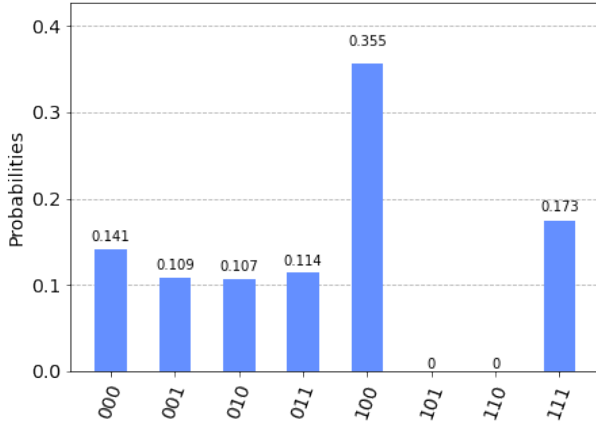
The full quantum circuits for $\mathcal{U}_{\mathcal{G}_3}$ and $\mathcal{U}_{\mathcal{G}_4}$ are shown in Fig. C.1.3 and C.1.4. The probability distribution of the projection measurement results of the two circuits are shown in Fig. C.1.2. Both the QASM simulator results and the real machine simulated results are recorded.



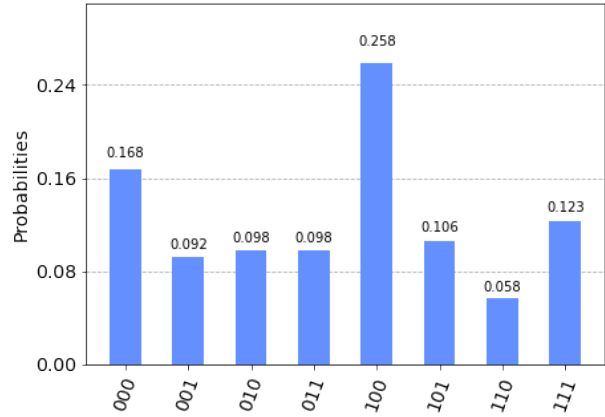
(a) QASM simulation of model 3



(b) **ibm quito** simulation of model 3



(c) QASM simulation of model 4



(d) **ibmq lima** simulation of model 3

Figure C.1.2. Probability distribution of the quantum state after the projection measurement applied to the circuit for $\mathcal{U}_{\mathcal{G}_3}$ and $\mathcal{U}_{\mathcal{G}_4}$ on the QASM and real quantum devices. The $|000\rangle$ state corresponds to the population squared of the donor state $\sigma_{DD}(t)$ and the $|100\rangle$ state corresponds to the population squared of the acceptor state $\sigma_{AA}(t)$. The last four states are ancilla states.

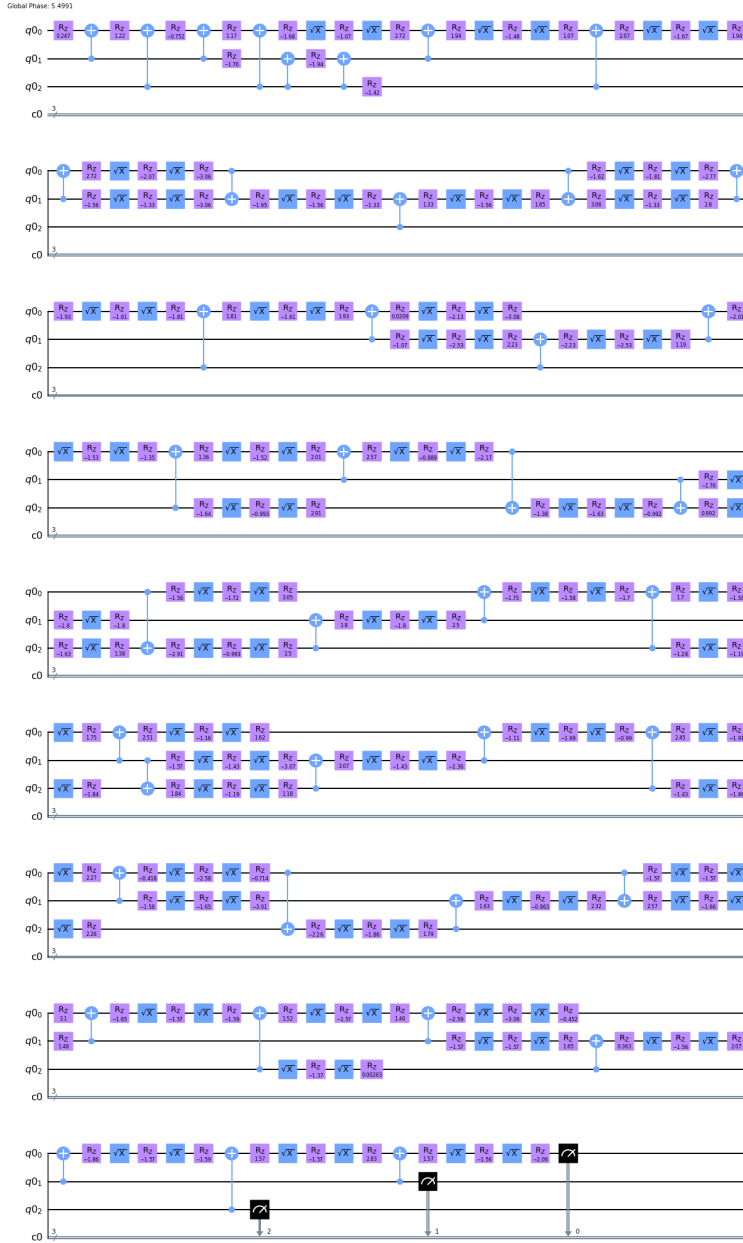


Figure C.1.3. Transpiled quantum circuit of the dilated \mathcal{U}_{G_3} matrix at 1500 time steps for model 3. Each horizontal black line denotes a qubit. The \sqrt{X} gate (blue square) is the square root of X gate; the R_z gate (magenta square) is the rotation Z gate. The two-qubit gates are the controlled-NOT gate, where the dot denotes the controlled qubit and \oplus denotes the target qubit. The black gates at the end of the circuit denote the projection measurements. The number of required R_z , \sqrt{X} , and CNOT gates are 153, 98, and 41, respectively.

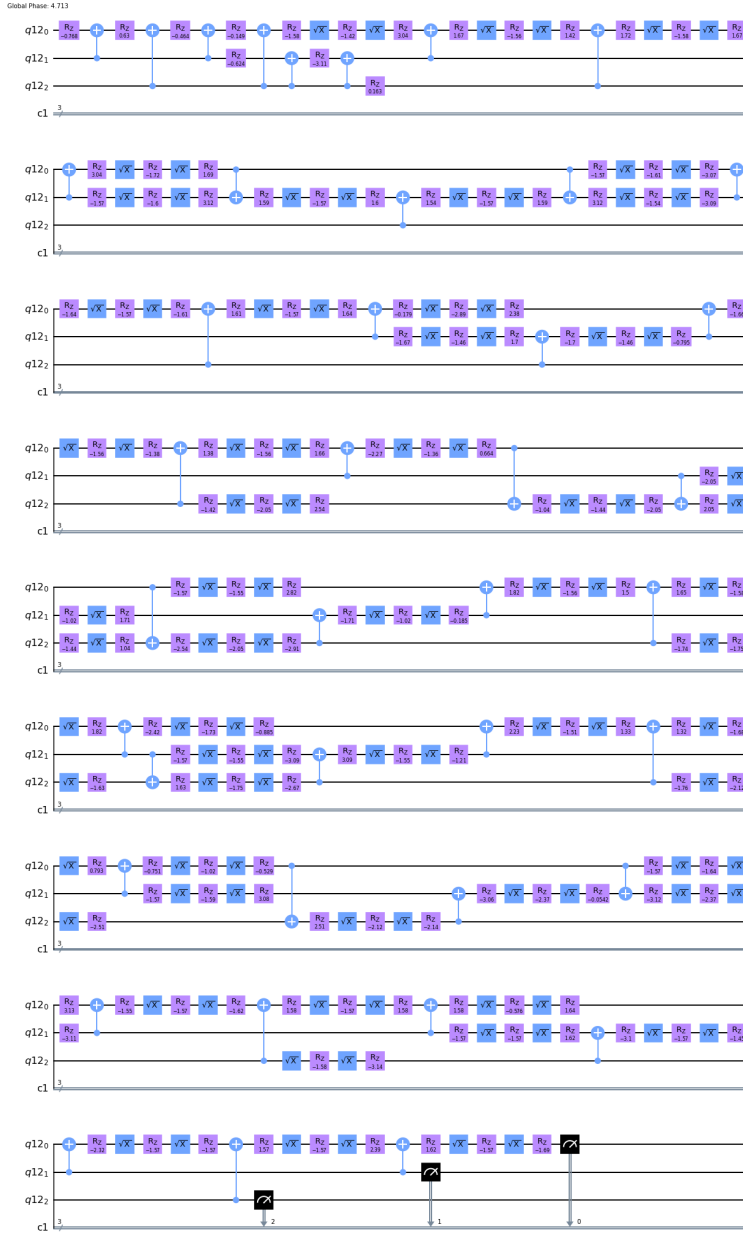


Figure C.1.4. Transpiled quantum circuit of the dilated $\mathcal{U}_{\mathcal{G}_4}$ matrix at 1500 time steps for model 4. Each horizontal black line denotes a qubit. The \sqrt{X} gate (blue square) is the square root of X gate; the R_z gate (magenta square) is the rotation Z gate. The two-qubit gates are the controlled-NOT gate, where the dot denotes the controlled qubit and \oplus denotes the target qubit. The black gates at the end of the circuit denote the projection measurements. The number of required R_z , \sqrt{X} , and CNOT gates are 153, 98, and 41, respectively.

REFERENCES

- [1] E. National Academies of Sciences and Medicine, *Quantum Computing: Progress and Prospects*, E. Grumblin and M. Horowitz, Eds. Washington, DC: The National Academies Press, 2019, ISBN: 978-0-309-47969-1. DOI: [10.17226/25196](https://doi.org/10.17226/25196). [Online]. Available: <https://www.nap.edu/catalog/25196/quantum-computing-progress-and-prospects>.
- [2] T. D. Ladd, F. Jelezko, R. Laflamme, Y. Nakamura, C. Monroe, and J. L. O’Brien, “Quantum computers,” *Nature*, vol. 464, no. 7285, pp. 45–53, 2010.
- [3] J. Preskill, “Quantum Computing in the NISQ era and beyond,” *Quantum*, vol. 2, p. 79, Aug. 2018, ISSN: 2521-327X. DOI: [10.22331/q-2018-08-06-79](https://doi.org/10.22331/q-2018-08-06-79). [Online]. Available: <https://doi.org/10.22331/q-2018-08-06-79>.
- [4] J. Biamonte, P. Wittek, N. Pancotti, P. Rebentrost, N. Wiebe, and S. Lloyd, “Quantum machine learning,” *Nature*, vol. 549, p. 195, 2017.
- [5] R. Blatt and C. F. Roos, “Quantum simulations with trapped ions,” *Nat. Phys.*, vol. 8, no. 4, p. 277, 2012.
- [6] H. Bernien, S. Schwartz, A. Keesling, *et al.*, “Probing many-body dynamics on a 51-atom quantum simulator,” *Nature*, vol. 551, no. 7682, p. 579, 2017.
- [7] E. F. Dumitrescu, A. J. McCaskey, G. Hagen, *et al.*, “Cloud quantum computing of an atomic nucleus,” *Phys. Rev. Lett.*, vol. 120, no. 21, p. 210 501, 2018.
- [8] C. Sparrow, E. Martín-López, N. Maraviglia, *et al.*, “Simulating the vibrational quantum dynamics of molecules using photonics,” *Nature*, vol. 557, no. 7707, p. 660, 2018.
- [9] S. Kais, K. Whaley, A. Dinner, and S. Rice, *Quantum Information and Computation for Chemistry* (Advances in Chemical Physics). Wiley, 2014, ISBN: 9781118742600. [Online]. Available: <https://books.google.com/books?id=dCXPAgAAQBAJ>.
- [10] H. Wang, S. Kais, A. Aspuru-Guzik, and M. R. Hoffmann, “Quantum algorithm for obtaining the energy spectrum of molecular systems,” *Physical Chemistry Chemical Physics*, vol. 10, no. 35, pp. 5388–5393, 2008.
- [11] P. J. J. O’Malley, R. Babbush, I. D. Kivlichan, *et al.*, “Scalable quantum simulation of molecular energies,” *Phys. Rev. X*, vol. 6, p. 031 007, 3 Jul. 2016. DOI: [10.1103/PhysRevX.6.031007](https://doi.org/10.1103/PhysRevX.6.031007). [Online]. Available: <https://link.aps.org/doi/10.1103/PhysRevX.6.031007>.
- [12] J.-L. Brylinski and R. Brylinski, “Universal quantum gates,” in *Mathematics of quantum computation*, Chapman and Hall/CRC, 2002, pp. 117–134.

- [13] H.-H. Lu, Z. Hu, M. S. Alshaykh, *et al.*, “Quantum phase estimation with time-frequency qudits in a single photon,” *Adv. Quantum Technol.*, vol. 0, no. 0, p. 1900074, 2019. DOI: [10.1002/qute.201900074](https://onlinelibrary.wiley.com/doi/pdf/10.1002/qute.201900074). eprint: <https://onlinelibrary.wiley.com/doi/pdf/10.1002/qute.201900074>. [Online]. Available: <https://onlinelibrary.wiley.com/doi/abs/10.1002/qute.201900074>.
- [14] M. Luo and X. Wang, “Universal quantum computation with qudits,” *Science China Physics, Mechanics & Astronomy*, vol. 57, no. 9, pp. 1712–1717, Sep. 2014, ISSN: 1869-1927. DOI: [10.1007/s11433-014-5551-9](https://doi.org/10.1007/s11433-014-5551-9). [Online]. Available: <https://doi.org/10.1007/s11433-014-5551-9>.
- [15] B. Li, Z.-H. Yu, and S.-M. Fei, “Geometry of quantum computation with qutrits,” *Sci. Rep.*, vol. 3, p. 2594, 2013.
- [16] M.-X. Luo, X.-B. Chen, Y.-X. Yang, and X. Wang, “Geometry of quantum computation with qudits,” *Sci. Rep.*, vol. 4, p. 4044, 2014.
- [17] V. E. Zobov and A. S. Ermilov, “Implementation of a quantum adiabatic algorithm for factorization on two qudits,” *J. Exp. Theor. Phys.*, vol. 114, pp. 923–932, Jul. 2012. DOI: [10.1134/S106377611205007X](https://doi.org/10.1134/S106377611205007X).
- [18] M. H. Amin, N. G. Dickson, and P. Smith, “Adiabatic quantum optimization with qudits,” *Quantum Inf. Process.*, vol. 12, pp. 1819–1829, 4 Apr. 2013. DOI: [10.1007/s11128-012-0480-x](https://doi.org/10.1007/s11128-012-0480-x).
- [19] S. X. Cui and Z. Wang, “Universal quantum computation with metaplectic anyons,” *J. Math. Phys.*, vol. 56, no. 3, p. 032202, 2015.
- [20] S. X. Cui, S.-M. Hong, and Z. Wang, “Universal quantum computation with weakly integral anyons,” *Quantum Information Processing*, vol. 14, no. 8, pp. 2687–2727, 2015.
- [21] A. Bocharov, S. X. Cui, M. Roetteler, and K. M. Svore, “Improved quantum ternary arithmetic,” *Quantum Info. Comput.*, vol. 16, no. 9–10, pp. 862–884, Jul. 2016, ISSN: 1533-7146.
- [22] X. Gao, M. Erhard, A. Zeilinger, and M. Krenn, “Computer-inspired concept for high-dimensional multipartite quantum gates,” *Phys. Rev. Lett.*, vol. 125, p. 050501, 5 Jul. 2020. DOI: [10.1103/PhysRevLett.125.050501](https://doi.org/10.1103/PhysRevLett.125.050501). [Online]. Available: <https://link.aps.org/doi/10.1103/PhysRevLett.125.050501>.
- [23] S. D. Bartlett, H. de Guise, and B. C. Sanders, “Quantum encodings in spin systems and harmonic oscillators,” *Phys. Rev. A*, vol. 65, p. 052316, 5 May 2002. DOI: [10.1103/PhysRevA.65.052316](https://doi.org/10.1103/PhysRevA.65.052316). [Online]. Available: <https://link.aps.org/doi/10.1103/PhysRevA.65.052316>.

- [24] M. R. A. Adcock, P. Høyer, and B. C. Sanders, “Quantum computation with coherent spin states and the close Hadamard problem,” *Quantum Inf. Process.*, vol. 15, no. 4, pp. 1361–1386, Jan. 2016. DOI: [10.1007/s11128-015-1229-0](https://doi.org/10.1007/s11128-015-1229-0).
- [25] A. B. Klimov, R. Guzmán, J. C. Retamal, and C. Saavedra, “Qutrit quantum computer with trapped ions,” *Phys. Rev. A*, vol. 67, p. 062313, 6 Jun. 2003. DOI: [10.1103/PhysRevA.67.062313](https://doi.org/10.1103/PhysRevA.67.062313). [Online]. Available: <https://link.aps.org/doi/10.1103/PhysRevA.67.062313>.
- [26] S. Dogra, Arvind, and K. Dorai, “Determining the parity of a permutation using an experimental nmr qutrit,” *Phys. Lett. A*, vol. 378, no. 46, pp. 3452–3456, 2014, ISSN: 0375-9601. DOI: <https://doi.org/10.1016/j.physleta.2014.10.003>. [Online]. Available: <http://www.sciencedirect.com/science/article/pii/S0375960114009955>.
- [27] Z. Gedik, I. A. Silva, B. Lie akmak, *et al.*, “Computational speed-up with a single qudit,” *Sci. Rep.*, vol. 5, 14671 EP -, Oct. 2015, Article. [Online]. Available: <https://doi.org/10.1038/srep14671>.
- [28] M. N. Leuenberger and D. Loss, “Quantum computing in molecular magnets,” *Nature*, vol. 410, no. 6830, p. 789, 2001.
- [29] Y. Wang, Z. Hu, B. C. Sanders, and S. Kais, “Qudits and high-dimensional quantum computing,” *Frontiers in Physics*, vol. 8, p. 479, 2020.
- [30] M. Howard and J. Vala, “Qudit versions of the qubit $\pi/8$ gate,” *Phys. Rev. A*, vol. 86, p. 022316, 2 Aug. 2012. DOI: [10.1103/PhysRevA.86.022316](https://doi.org/10.1103/PhysRevA.86.022316). [Online]. Available: <https://link.aps.org/doi/10.1103/PhysRevA.86.022316>.
- [31] J. Daboul, X. Wang, and B. C. Sanders, “Quantum gates on hybrid qudits,” *J. Phys. A.*, vol. 36, no. 10, pp. 2525–2536, Feb. 2003. DOI: [10.1088/0305-4470/36/10/312](https://doi.org/10.1088/0305-4470/36/10/312). [Online]. Available: <https://doi.org/10.1088/0305-4470/36/10/312>.
- [32] J. C. Garcia-Escartin and P. Chamorro-Posada, “A swap gate for qudits,” *Quantum Inf. Process.*, vol. 12, no. 12, pp. 3625–3631, Dec. 2013, ISSN: 1573-1332. DOI: [10.1007/s11128-013-0621-x](https://doi.org/10.1007/s11128-013-0621-x). [Online]. Available: <https://doi.org/10.1007/s11128-013-0621-x>.
- [33] T. C. Ralph, K. J. Resch, and A. Gilchrist, “Efficient Toffoli gates using qudits,” *Phys. Rev. A*, vol. 75, p. 022313, 2 Feb. 2007. DOI: [10.1103/PhysRevA.75.022313](https://doi.org/10.1103/PhysRevA.75.022313). [Online]. Available: <https://link.aps.org/doi/10.1103/PhysRevA.75.022313>.
- [34] E. O. Kiktenko, A. S. Nikolaeva, P. Xu, G. V. Shlyapnikov, and A. K. Fedorov, “Scalable quantum computing with qudits on a graph,” *Phys. Rev. A*, vol. 101, p. 022304, 2 Feb. 2020. DOI: [10.1103/PhysRevA.101.022304](https://doi.org/10.1103/PhysRevA.101.022304). [Online]. Available: <https://link.aps.org/doi/10.1103/PhysRevA.101.022304>.

- [35] D. M. Nguyen and S. Kim, “Quantum key distribution protocol based on modified generalization of Deutsch–Jozsa algorithm in d-level quantum system,” *Int. J. Theor. Phys.*, vol. 58, no. 1, pp. 71–82, Jan. 2019, ISSN: 1572-9575. DOI: [10.1007/s10773-018-3910-4](https://doi.org/10.1007/s10773-018-3910-4). [Online]. Available: <https://doi.org/10.1007/s10773-018-3910-4>.
- [36] K. Nagata, H. Geurdes, S. K. Patro, S. Heidari, A. Farouk, and T. Nakamura, “Generalization of the Bernstein–Vazirani algorithm beyond qubit systems,” *Quantum Stud.: Math. Found.*, vol. 7, pp. 17–21, 1 Mar. 2020. DOI: [10.1007/s40509-019-00196-4](https://doi.org/10.1007/s40509-019-00196-4). [Online]. Available: <https://doi.org/10.1007/s40509-019-00196-4>.
- [37] Y. Cao, S.-G. Peng, C. Zheng, and G.-L. Long, “Quantum fourier transform and phase estimation in qudit system,” *Communications in Theoretical Physics*, vol. 55, no. 5, pp. 790–794, May 2011. DOI: [10.1088/0253-6102/55/5/11](https://doi.org/10.1088/0253-6102/55/5/11). [Online]. Available: <https://doi.org/10.1088/0253-6102/55/5/11>.
- [38] A. Bocharov, M. Roetteler, and K. M. Svore, “Factoring with qutrits: Shor’s algorithm on ternary and metaplectic quantum architectures,” *Phys. Rev. A*, vol. 96, p. 012306, 1 Jul. 2017. DOI: [10.1103/PhysRevA.96.012306](https://doi.org/10.1103/PhysRevA.96.012306).
- [39] S. S. Ivanov, H. S. Tonchev, and N. V. Vitanov, “Time-efficient implementation of quantum search with qudits,” *Phys. Rev. A*, vol. 85, p. 062321, 6 Jun. 2012. DOI: [10.1103/PhysRevA.85.062321](https://doi.org/10.1103/PhysRevA.85.062321). [Online]. Available: <https://link.aps.org/doi/10.1103/PhysRevA.85.062321>.
- [40] P. W. Shor, “Polynomial-time algorithms for prime factorization and discrete logarithms on a quantum computer,” *SIAM review*, vol. 41, no. 2, pp. 303–332, 1999.
- [41] A. W. Harrow, A. Hassidim, and S. Lloyd, “Quantum algorithm for linear systems of equations,” *Phys. Rev. Lett.*, vol. 103, p. 150502, 15 Oct. 2009. DOI: [10.1103/PhysRevLett.103.150502](https://doi.org/10.1103/PhysRevLett.103.150502). [Online]. Available: <https://link.aps.org/doi/10.1103/PhysRevLett.103.150502>.
- [42] Y. Cao, A. Daskin, S. Frankel, and S. Kais, “Quantum circuit design for solving linear systems of equations,” *Molecular Physics*, vol. 110, no. 15-16, pp. 1675–1680, 2012. DOI: [10.1080/00268976.2012.668289](https://doi.org/10.1080/00268976.2012.668289).
- [43] A. Aspuru-Guzik, A. D. Dutoi, P. J. Love, and M. Head-Gordon, “Simulated quantum computation of molecular energies,” *Science*, vol. 309, no. 5741, pp. 1704–1707, 2005.
- [44] A. Daskin and S. Kais, “Decomposition of unitary matrices for finding quantum circuits: Application to molecular hamiltonians,” *The Journal of Chemical Physics*, vol. 134, no. 14, p. 144112, 2011. DOI: [10.1063/1.3575402](https://doi.org/10.1063/1.3575402).

- [45] A. Aspuru-Guzik and P. Walther, “Photonic quantum simulators,” *Nature Physics*, vol. 8, p. 285, 2012.
- [46] B. P. Lanyon, J. D. Whitfield, G. G. Gillett, *et al.*, “Towards quantum chemistry on a quantum computer,” *Nat. Chem.*, vol. 2, no. 2, p. 106, 2010.
- [47] X.-Q. Zhou, P. Kalasuwan, T. C. Ralph, and J. L. O’Brien, “Calculating unknown eigenvalues with a quantum algorithm,” *Nat. Photon.*, vol. 7, no. 3, p. 223, 2013.
- [48] S. Paesani, A. A. Gentile, R. Santagati, *et al.*, “Experimental bayesian quantum phase estimation on a silicon photonic chip,” *Phys. Rev. Lett.*, vol. 118, no. 10, p. 100503, 2017.
- [49] L. Sheridan and V. Scarani, “Security proof for quantum key distribution using qudit systems,” *Phys. Rev. A*, vol. 82, p. 030301, 3 Sep. 2010. DOI: [10.1103/PhysRevA.82.030301](https://doi.org/10.1103/PhysRevA.82.030301). [Online]. Available: <https://link.aps.org/doi/10.1103/PhysRevA.82.030301>.
- [50] L. Y. He, T.-J. Wang, and C. Wang, “Construction of high-dimensional universal quantum logic gates using a Λ system coupled with a whispering-gallery-mode microresonator,” *Opt. Express*, vol. 24, no. 14, pp. 15429–15445, Jul. 2016. DOI: [10.1364/OE.24.015429](https://doi.org/10.1364/OE.24.015429). [Online]. Available: <http://www.opticsexpress.org/abstract.cfm?URI=oe-24-14-15429>.
- [51] R.-B. Jin, R. Shimizu, M. Fujiwara, *et al.*, “Simple method of generating and distributing frequency-entangled qudits,” *Quantum Science and Technology*, vol. 1, no. 1, p. 015004, 2016.
- [52] D. Zhang, Y. Zhang, X. Li, *et al.*, “Generation of high-dimensional energy-time-entangled photon pairs,” *Phys. Rev. A*, vol. 96, p. 053849, 5 Nov. 2017. DOI: [10.1103/PhysRevA.96.053849](https://doi.org/10.1103/PhysRevA.96.053849). [Online]. Available: <https://link.aps.org/doi/10.1103/PhysRevA.96.053849>.
- [53] J. Daboul, X. Wang, and B. C. Sanders, “Quantum gates on hybrid qudits,” *Journal of Physics A: Mathematical and General*, vol. 36, no. 10, pp. 2525–2536, Feb. 2003. DOI: [10.1088/0305-4470/36/10/312](https://doi.org/10.1088/0305-4470/36/10/312). [Online]. Available: <https://doi.org/10.1088/0305-4470/36/10/312>.
- [54] A. Babazadeh, M. Erhard, F. Wang, *et al.*, “High-dimensional single-photon quantum gates: Concepts and experiments,” *Phys. Rev. Lett.*, vol. 119, p. 180510, 18 Nov. 2017. DOI: [10.1103/PhysRevLett.119.180510](https://doi.org/10.1103/PhysRevLett.119.180510). [Online]. Available: <https://link.aps.org/doi/10.1103/PhysRevLett.119.180510>.
- [55] N. T. Islam, C. C. W. Lim, C. Cahall, J. Kim, and D. J. Gauthier, “Provably secure and high-rate quantum key distribution with time-bin qudits,” *Sci. Adv.*, vol. 3, no. 11, e1701491, 2017.

- [56] M. Kues, C. Reimer, P. Roztock, *et al.*, “On-chip generation of high-dimensional entangled quantum states and their coherent control,” *Nature*, vol. 546, no. 7660, p. 622, 2017.
- [57] H.-H. Lu, J. M. Lukens, N. A. Peters, *et al.*, “Electro-optic frequency beam splitters and tritters for high-fidelity photonic quantum information processing,” *Phys. Rev. Lett.*, vol. 120, p. 030 502, 3 Jan. 2018. DOI: [10.1103/PhysRevLett.120.030502](https://doi.org/10.1103/PhysRevLett.120.030502). [Online]. Available: <https://link.aps.org/doi/10.1103/PhysRevLett.120.030502>.
- [58] P. Imany, J. A. Jaramillo-Villegas, O. D. Odele, *et al.*, “50-ghz-spaced comb of high-dimensional frequency-bin entangled photons from an on-chip silicon nitride microresonator,” *Opt. Express*, vol. 26, no. 2, pp. 1825–1840, 2018.
- [59] P. Imany, J. A. Jaramillo-Villegas, M. S. Alshaykh, *et al.*, “High-dimensional optical quantum logic in large operational spaces,” *npj Quantum Inf.*, vol. 5, no. 1, pp. 1–10, Jul. 2019.
- [60] C. Reimer, S. Sciara, P. Roztock, *et al.*, “High-dimensional one-way quantum processing implemented on d-level cluster states,” *Nat. Phys.*, vol. 15, no. 2, p. 148, 2019.
- [61] B. P. Lanyon, M. Barbieri, M. P. Almeida, *et al.*, “Simplifying quantum logic using higher-dimensional Hilbert spaces,” *Nature Physics*, vol. 5, no. 2, pp. 134–140, 2009, ISSN: 1745-2481. DOI: [10.1038/nphys1150](https://doi.org/10.1038/nphys1150). [Online]. Available: <https://doi.org/10.1038/nphys1150>.
- [62] M. Neeley, M. Ansmann, R. C. Bialczak, *et al.*, “Emulation of a quantum spin with a superconducting phase qubit,” *Science*, vol. 325, no. 5941, pp. 722–725, 2009.
- [63] M. Fiorentino and F. N. Wong, “Deterministic controlled-not gate for single-photon two-qubit quantum logic,” *Phys. Rev. Lett.*, vol. 93, no. 7, p. 070 502, 2004.
- [64] K. H. Kagalwala, G. Di Giuseppe, A. F. Abouraddy, and B. E. Saleh, “Single-photon three-qubit quantum logic using spatial light modulators,” *Nat. Commun.*, vol. 8, no. 1, p. 739, 2017.
- [65] A. J. Moore, Y. Wang, Z. Hu, S. Kais, and A. M. Weiner, “Statistical approach to quantum phase estimation,” *New Journal of Physics*, vol. 23, no. 11, p. 113 027, Nov. 2021. DOI: [10.1088/1367-2630/ac320d](https://doi.org/10.1088/1367-2630/ac320d). [Online]. Available: <https://doi.org/10.1088/1367-2630/ac320d>.

- [66] E. Liberty, F. Woolfe, P.-G. Martinsson, V. Rokhlin, and M. Tygert, “Randomized algorithms for the low-rank approximation of matrices,” *Proceedings of the National Academy of Sciences*, vol. 104, no. 51, pp. 20 167–20 172, 2007, ISSN: 0027-8424. DOI: [10.1073/pnas.0709640104](https://doi.org/10.1073/pnas.0709640104). eprint: <https://www.pnas.org/content/104/51/20167.full.pdf>. [Online]. Available: <https://www.pnas.org/content/104/51/20167>.
- [67] A. Daskin and S. Kais, “Decomposition of unitary matrices for finding quantum circuits: Application to molecular hamiltonians,” *J. Chem. Phys.*, vol. 134, no. 14, p. 144 112, 2011.
- [68] M. A. Nielsen and I. Chuang, *Quantum computation and quantum information*, 2002.
- [69] P. W. Shor, “Algorithms for quantum computation: Discrete logarithms and factoring,” in *Proceedings 35th annual symposium on foundations of computer science*, Ieee, 1994, pp. 124–134.
- [70] S. Lloyd, M. Mohseni, and P. Rebentrost, “Quantum principal component analysis,” *Nature Physics*, vol. 10, no. 9, pp. 631–633, 2014.
- [71] T. Byrnes, G. Forster, and L. Tessler, “Generalized grover’s algorithm for multiple phase inversion states,” *Phys. Rev. Lett.*, vol. 120, p. 060 501, 6 Feb. 2018. DOI: [10.1103/PhysRevLett.120.060501](https://doi.org/10.1103/PhysRevLett.120.060501). [Online]. Available: <https://link.aps.org/doi/10.1103/PhysRevLett.120.060501>.
- [72] A. Aspuru-Guzik, A. D. Dutoi, P. J. Love, and M. Head-Gordon, “Simulated quantum computation of molecular energies,” *Science*, vol. 309, no. 5741, pp. 1704–1707, 2005.
- [73] A. Daskin and S. Kais, “Direct application of the phase estimation algorithm to find the eigenvalues of the hamiltonians,” *Chemical Physics*, vol. 514, pp. 87–94, 2018.
- [74] J. Preskill, “Quantum computing in the nisq era and beyond,” *Quantum*, vol. 2, p. 79, 2018.
- [75] M. Dob š í ček, G. Johansson, V. Shumeiko, and G. Wendin, “Arbitrary accuracy iterative quantum phase estimation algorithm using a single ancillary qubit: A two-qubit benchmark,” *Phys. Rev. A*, vol. 76, 030306(R), 3 Sep. 2007. DOI: [10.1103/PhysRevA.76.030306](https://doi.org/10.1103/PhysRevA.76.030306). [Online]. Available: <https://link.aps.org/doi/10.1103/PhysRevA.76.030306>.
- [76] D. Wang, O. Higgott, and S. Brierley, “Accelerated variational quantum eigensolver,” *Physical review letters*, vol. 122, no. 14, p. 140 504, 2019.
- [77] A. Peruzzo, J. McClean, P. Shadbolt, *et al.*, “A variational eigenvalue solver on a photonic quantum processor,” *Nature communications*, vol. 5, no. 1, pp. 1–7, 2014.

- [78] G. Aleksandrowicz, T. Alexander, P. Barkoutsos, *et al.*, *Qiskit: An Open-source Framework for Quantum Computing*, version 0.7.2, Jan. 2019. DOI: [10.5281/zenodo.2562111](https://doi.org/10.5281/zenodo.2562111). [Online]. Available: <https://doi.org/10.5281/zenodo.2562111>.
- [79] R. LaRose, A. Tikku, É. O’Neel-Judy, L. Cincio, and P. J. Coles, “Variational quantum state diagonalization,” *npj Quantum Information*, vol. 5, no. 1, pp. 1–10, 2019.
- [80] M. Cerezo, K. Sharma, A. Arrasmith, and P. J. Coles, “Variational quantum state eigensolver,” arXiv:2004.01372, Apr. 2020.
- [81] P. J. J. O’Malley, R. Babbush, I. D. Kivlichan, *et al.*, “Scalable quantum simulation of molecular energies,” *Phys. Rev. X*, vol. 6, p. 031007, 3 Jul. 2016. DOI: [10.1103/PhysRevX.6.031007](https://doi.org/10.1103/PhysRevX.6.031007). [Online]. Available: <https://link.aps.org/doi/10.1103/PhysRevX.6.031007>.
- [82] R. K. Wangsness and F. Bloch, “The dynamical theory of nuclear induction,” *Phys. Rev.*, vol. 89, p. 728, 1953.
- [83] H. Grabert, *Projection Operator Techniques in Nonequilibrium Statistical Mechanics*. Berlin: Springer-Verlag, 1982.
- [84] R. Kubo, M. Toda, and N. Hashitsume, *Statistical Physics II - Nonequilibrium Statistical Mechanics*. Berlin: Springer-Verlag, 1983.
- [85] B. B. Laird, J. Budimir, and J. L. Skinner, “Quantum-mechanical derivation of the Bloch equations: Beyond the weak coupling limit,” *J. Chem. Phys.*, vol. 94, p. 4391, 1991.
- [86] N. G. V. Kampen, *Stochastic Processes in Physics and Chemistry*. Amsterdam: Elsevier, 1992.
- [87] W. T. Pollard, A. K. Felts, and R. A. Friesner, “The Redfield equation in condensed-phase quantum dynamics,” *Adv. Chem. Phys.*, vol. XCIII, p. 77, 1996.
- [88] D. Kohen, C. C. Marston, and D. J. Tannor, “Phase space approach to theories of quantum dissipation,” *J. Chem. Phys.*, vol. 107, p. 5236, 1997.
- [89] R. Kosloff, M. A. Ratner, and W. B. Davis, “Dynamics and relaxation in interacting systems: Semigroup approach,” *J. Chem. Phys.*, vol. 106, p. 7036, 1997.
- [90] J. Cao, “Phase space study of Bloch-Redfield theory,” *J. Chem. Phys.*, vol. 107, p. 3204, 1997.

- [91] Q. Shi and E. Geva, “Stimulated Raman Adiabatic Passage in The Presence of Dephasing,” *J. Chem. Phys.*, vol. 119, pp. 11 773–11 787, 2003.
- [92] C. Baiz, K. Kubarych, and E. Geva, “Molecular theory and simulation of coherence transfer in metal carbonyls and its signature on multidimensional infrared spectra,” *J. Phys. Chem. B*, vol. 115, pp. 5322–5339, 2011.
- [93] A. G. Redfield, “On the theory of relaxation processes,” *IBM Jr.*, vol. 1, p. 19, 1957.
- [94] R. Zwanzig, *Nonequilibrium Statistical Mechanics*. New York: Oxford University Press, 2001.
- [95] V. May and O. Kühn, *Charge and Energy Transfer Dynamics in Molecular Systems*. Berlin: Willey-VCH, 2000.
- [96] A. Nitzan, *Chemical Dynamics in Condensed Phases*. New York: Oxford University Press, 2006.
- [97] H.-P. Breuer and F. Petruccione, *The Theory of Open Quantum Systems*. Oxford: Oxford Press, 2002.
- [98] S. J. Jang, *DYNAMICS OF MOLECULAR EXCITONS*. Amsterdam: Elsevier, 2021.
- [99] Y. Lai and E. Geva, “On simulating the dynamics of electronic populations and coherences via quantum master equations based on treating off-diagonal electronic coupling terms as a small perturbation,” *J. Chem. Phys.*, vol. 155, pp. 204 101–19, 2021.
- [100] H. Chen and D. A. Lidar, “Hamiltonian open quantum system toolkit,” *Communications Physics*, vol. 5, p. 112, 2022. DOI: [10.1038/s42005-022-00887-2](https://doi.org/10.1038/s42005-022-00887-2).
- [101] E. Mulvihill, A. Schubert, X. Sun, B. D. Dunietz, and E. Geva, “A modified approach for simulating electronically nonadiabatic dynamics via the generalized quantum master equation,” *J. Chem. Phys.*, vol. 150, no. 3, p. 034 101, 2019.
- [102] E. Mulvihill, K. M. Lenn, X. Gao, A. Schubert, B. D. Dunietz, and E. Geva, “Simulating energy transfer dynamics in the fenna-matthews-olson complex via the modified generalized quantum master equation,” *J. Chem. Phys.*, vol. 154, no. 20, p. 204 109, 2021.
- [103] E. Mulvihill and E. Geva, “A Road Map to Various Pathways for Calculating the Memory Kernel of the Generalized Quantum Master Equation,” *J. Phys. Chem. B*, vol. 125, no. 34, pp. 9834–9852, 2021.
- [104] F. Bloch, “Generalized theory of relaxation,” *Phys. Rev.*, vol. 105, p. 1206, 1957.

- [105] E. Mulvihill and E. Geva, “Simulating the dynamics of electronic observables via reduced-dimensionality generalized quantum master equations,” *J. Chem. Phys.*, vol. 156, no. 4, p. 044119, 2022.
- [106] F. Haake, “Statistical treatment of open systems by generalized master equations,” *Springer Tracts Mod. Phys.*, vol. 66, p. 98, 1973.
- [107] B. Yoon, J. M. Deutch, and J. H. Freed, “A comparison of generalized cumulant and projection operator methods in spin-relaxation theory,” *J. Chem. Phys.*, vol. 62, pp. 4687–4696, 1975.
- [108] G. Lindblad, “On the generators of quantum dynamical semigroups,” *Commun. Math. Phys.*, vol. 48, p. 119, 1976.
- [109] V. Gorini, A. Kossokowski, and E. C. G. Sudarshan, “Completely positive dynamical semigroups of n-level systems,” *J. Math. Phys.*, vol. 17, p. 821, 1976.
- [110] I. Oppenheim, K. E. Shuler, and G. H. Weiss, *Stochastic Processes in Chemical Physics: The Master Equation*. Cambridge MA: MIT Press, 1977.
- [111] R. Alicki and K. Lendi, *Quantum Dynamical Semigroups and Applications*. Berlin: Springer-Verlag, 1987.
- [112] D. Xu and K. Schulten, “Coupling of protein motion to electron transfer in a photosynthetic reaction center: investigating the low temperature behavior in the framework of the spin–boson model,” *Chem. Phys.*, vol. 182, pp. 91–117, 1994.
- [113] Y. Zhao and W. Liang, “Charge transfer in organic molecules for solar cells: Theoretical perspective,” *Chem. Soc. Rev.*, vol. 41, pp. 1075–1087, 2012. DOI: [10.1039/C1CS15207F](https://doi.org/10.1039/C1CS15207F). [Online]. Available: <http://pubs.rsc.org/en/content/articlelanding/2012/cs/c1cs15207f>.
- [114] M. H. Lee, B. D. Dunietz, and E. Geva, “Calculation from first principles of intramolecular golden-rule rate constants for photo-induced electron transfer in molecular donor-acceptor systems,” *J. Phys. Chem. C*, vol. 117, pp. 23391–23401, 2013.
- [115] M. H. Lee, B. D. Dunietz, and E. Geva, “Donor-to-donor vs. donor-to-acceptor interfacial charge transfer states in the phthalocyanine-fullerene organic photovoltaic system,” *J. Phys. Chem. Lett.*, vol. 5, pp. 3810–3816, 2014.
- [116] Z. Hu, G. S. Engel, F. H. Alharbi, and S. Kais, “Dark states and delocalization: Competing effects of quantum coherence on the efficiency of light harvesting systems,” *J. Chem. Phys.*, vol. 148, no. 6, p. 064304, 2018.

- [117] Z. Hu, G. S. Engel, and S. Kais, “Double-excitation manifold’s effect on exciton transfer dynamics and the efficiency of coherent light harvesting,” *Phys. Chem. Chem. Phys.*, vol. 20, no. 47, pp. 30 032–30 040, 2018.
- [118] A. J. Daley, “Quantum trajectories and open many-body quantum systems,” *Adv. Phys.*, vol. 63, no. 2, pp. 77–149, 2014.
- [119] H. M. Wiseman and G. J. Milburn, *Quantum Measurement and Control*. Cambridge University Press, 2009. DOI: [10.1017/CBO9780511813948](https://doi.org/10.1017/CBO9780511813948).
- [120] A. Ishizaki and G. R. Fleming, “Quantum Coherence in Photosynthetic Light Harvesting,” *Annu. Rev. Condens. Matter Phys.*, vol. 3, no. 1, pp. 333–361, Mar. 2012.
- [121] D. Brian and X. Sun, “Generalized quantum master equation: A tutorial review and recent advances,” *Chin. J. Chem. Phys.*, vol. 34, no. 5, pp. 497–524, 2021.
- [122] X. Dan, M. Xu, Y. Yan, and Q. Shi, “Generalized master equation for charge transport in a molecular junction: Exact memory kernels and their high order expansion,” *J. Chem. Phys.*, vol. 156, no. 13, p. 134 114, 2022.
- [123] P. A. Liddell, D. Kuciauskas, J. P. Sumida, *et al.*, “Photoinduced charge separation and charge recombination to a triplet state in a carotene-porphyrin-fullerene triad,” *J. Am. Chem. Soc.*, vol. 119, no. 6, pp. 1400–1405, 1997. DOI: [10.1021/ja9631054](https://doi.org/10.1021/ja9631054). [Online]. Available: <http://pubs.acs.org/doi/abs/10.1021/ja9631054>.
- [124] P. A. Liddell, G. Kodis, A. L. Moore, T. A. Moore, and D. Gust, “Photo switching of photoinduced electron transfer in a dithienylethene-porphyrin-fullerene triad molecule,” *J. Am. Chem. Soc.*, vol. 124, no. 26, pp. 7668–7669, 2002. DOI: [10.1021/ja026327c](https://doi.org/10.1021/ja026327c). [Online]. Available: <http://pubs.acs.org/doi/abs/10.1021/ja026327c>.
- [125] J.-L. Brédas, D. Beljonne, V. Coropceanu, and J. Cornil, “Charge-transfer and energy-transfer processes in π -conjugated oligomers and polymers: a molecular picture,” *Chem. Rev.*, vol. 104, no. 11, pp. 4971–5004, Nov. 2004.
- [126] A. C. Rizzi, M. van Gastel, P. A. Liddell, *et al.*, “Entropic changes control the charge separation process in triads mimicking photosynthetic charge separation,” *J. Phys. Chem. A*, vol. 112, no. 18, pp. 4215–4223, 2008. DOI: [10.1021/jp712008b](https://doi.org/10.1021/jp712008b). [Online]. Available: <http://pubs.acs.org/doi/abs/10.1021/jp712008b>.
- [127] H. Tian, Z. Yu, A. Hagfeldt, L. Kloo, and L. Sun, “Organic redox couples and organic counter electrode for efficient organic dye-sensitized solar cells,” *J. Am. Chem. Soc.*, vol. 133, no. 24, pp. 9413–9422, 2011. DOI: [10.1021/ja2030933](https://doi.org/10.1021/ja2030933). [Online]. Available: <http://pubs.acs.org/doi/abs/10.1021/ja2030933>.

- [128] A. Mishra, M. K. R. Fischer, and P. Bäuerle, “Metal-free organic dyes for dye-sensitized solar cells: From structure: Property relationships to design rules,” *Angew. Chem. Int. Ed.*, vol. 48, no. 14, pp. 2474–2499, 2009. DOI: [10.1021/anie.200804709](https://doi.org/10.1021/anie.200804709).
- [129] S. M. Feldt, E. A. Gibson, E. Gabrielsson, L. Sun, G. Boschloo, and A. Hagfeldt, “Design of organic dyes and cobalt polypyridine redox mediators for high-efficiency dye-sensitized solar cells,” *J. Am. Chem. Soc.*, vol. 132, no. 46, pp. 16 714–16 724, 2010. DOI: [10.1021/ja1088869](https://doi.org/10.1021/ja1088869). [Online]. Available: <http://pubs.acs.org/doi/abs/10.1021/ja1088869>.
- [130] R. Xia, T. Bian, and S. Kais, “Electronic structure calculations and the ising hamiltonian,” *J. Phys. Chem. B*, vol. 122, no. 13, pp. 3384–3395, 2017.
- [131] R. Xia and S. Kais, “Quantum machine learning for electronic structure calculations,” *Nat. Commun.*, vol. 9, no. 1, pp. 1–6, 2018.
- [132] N. Wiebe, D. W. Berry, P. Høyer, and B. C. Sanders, “Simulating quantum dynamics on a quantum computer,” *J. Phys. A Math. Theor.*, vol. 44, no. 44, p. 445 308, 2011.
- [133] P. J. Ollitrault, A. Miessen, and I. Tavernelli, “Molecular quantum dynamics: A quantum computing perspective,” *Acc. Chem. Res.*, vol. 54, no. 23, pp. 4229–4238, 2021.
- [134] Y.-X. Yao, N. Gomes, F. Zhang, *et al.*, “Adaptive variational quantum dynamics simulations,” *PRX Quantum*, vol. 2, no. 3, p. 030 307, 2021.
- [135] L. Tagliacozzo, “Optimal simulation of quantum dynamics,” *Nature Physics*, vol. 18, no. 9, pp. 970–971, 2022.
- [136] H. Wang, S. Ashhab, and F. Nori, “Quantum algorithm for simulating the dynamics of an open quantum system,” *Phys. Rev. A*, vol. 83, no. 6, p. 062 317, 2011.
- [137] D.-S. Wang, D. W. Berry, M. C. De Oliveira, and B. C. Sanders, “Solovay-kitaev decomposition strategy for single-qubit channels,” *Phys. Rev. Lett.*, vol. 111, no. 13, p. 130 504, 2013.
- [138] S.-J. Wei, D. Ruan, and G.-L. Long, “Duality quantum algorithm efficiently simulates open quantum systems,” *Sci. Rep.*, vol. 6, no. 1, pp. 1–9, 2016.
- [139] M. Kliesch, T. Barthel, C. Gogolin, M. Kastoryano, and J. Eisert, “Dissipative quantum church-turing theorem,” *Phys. Rev. Lett.*, vol. 107, no. 12, p. 120 501, 2011.
- [140] R. Sweke, I. Sinayskiy, D. Bernard, and F. Petruccione, “Universal simulation of markovian open quantum systems,” *Phys. Rev. A*, vol. 91, no. 6, p. 062 308, 2015.

- [141] A. W. Schlimgen, K. Head-Marsden, L. M. Sager, P. Narang, and D. A. Mazziotti, “Quantum simulation of open quantum systems using a unitary decomposition of operators,” *Phys. Rev. Lett.*, vol. 127, no. 27, p. 270 503, 2021.
- [142] Y. Zhang, Z. Hu, Y. Wang, and S. Kais, “Quantum simulation of the radical pair dynamics of the avian compass,” *The Journal of Physical Chemistry Letters*, vol. 14, no. 3, pp. 832–837, 2023.
- [143] Z. Hu, R. Xia, and S. Kais, “A quantum algorithm for evolving open quantum dynamics on quantum computing devices,” *Scientific reports*, vol. 10, no. 1, pp. 1–9, 2020.
- [144] K. Head-Marsden, S. Krastanov, D. A. Mazziotti, and P. Narang, “Capturing non-markovian dynamics on near-term quantum computers,” *Phys. Rev. Res.*, vol. 3, no. 1, p. 013 182, 2021.
- [145] Z. Hu, K. Head-Marsden, D. A. Mazziotti, P. Narang, and S. Kais, “A general quantum algorithm for open quantum dynamics demonstrated with the fenna-matthews-olson complex,” *Quantum*, vol. 6, p. 726, 2022.
- [146] J. A. Pauls, Y. Zhang, G. P. Berman, and S. Kais, “Quantum coherence and entanglement in the avian compass,” *Phys. Rev. E*, vol. 87, p. 062 704, 6 2013.
- [147] Y. Zhang, G. P. Berman, and S. Kais, “Sensitivity and entanglement in the avian chemical compass,” *Phys. Rev. E*, vol. 90, p. 042 707, 4 2014.
- [148] Y. Zhang, G. P. Berman, and S. Kais, “The radical pair mechanism and the avian chemical compass: Quantum coherence and entanglement,” *Int. J. Quantum Chem.*, vol. 115, pp. 1327–1341, 19 2014.
- [149] C. A. Dodson, P. J. Hore, and M. I. Wallace, “A radical sense of direction: Signalling and mechanism in cryptochrome magnetoreception,” *Trends Biochem. Sci.*, vol. 38, 9 2013.
- [150] W. Wiltschko and R. Wiltschko, “Magnetic orientation and magnetoreception in birds and other animals,” *J. Comp. Physiol. A*, vol. 191, p. 675, 2005.
- [151] W. Wiltschko and R. Wiltschko, “Magnetic compass of european robins,” *Science*, vol. 176, p. 62, 1972.
- [152] R. Wiltschko and W. Wiltschko, “Avian magnetic compass: Its functional properties and physical basis,” *Curr. Zool.*, vol. 56, p. 265, 2010.

- [153] A. F. Davila, G. Fleissner, M. Winklhofer, and N. Petersen, “A new model for a magnetoreceptor in homing pigeons based on interacting clusters of super-paramagnetic magnetite,” *Phys Chem Earth*, vol. 28, p. 647, 2003.
- [154] W. Wiltschko, U. Munro, H. Ford, and R. Wiltschko, “Red light disrupts magnetic orientation of migratory birds,” *Nature*, vol. 364, p. 525, 1993.
- [155] W. Wiltschko and R. Wiltschko, “Migratory orientation of european robins is affected by the wavelength of light as well as by a magnetic pulse,” *J. Comp. Physiol. A*, vol. 177, p. 363, 1995.
- [156] W. Wiltschko and R. Wiltschko, “Pigeon homing: Effect of various wavelengths of light during displacement,” *Naturwissenschaften*, vol. 85, p. 164, 1998.
- [157] W. Wiltschko and R. Wiltschko, “The effect of yellow and blue light on magnetic compass orientation in european robins, *Erithacus rubecula*,” *J. Comp. Physiol. A*, vol. 184, p. 295, 1999.
- [158] R. Wiltschko, T. Ritz, K. Stapput, P. Thalau, and W. Wiltschko, “Two different types of light-dependent responses to magnetic fields in birds,” *Curr. Biol.*, vol. 15, p. 1518, 2005.
- [159] K. Stapput, P. Thalau, R. Wiltschko, and W. Wiltschko, “Orientation of birds in total darkness,” *Curr. Biol.*, vol. 18, p. 602, 2008.
- [160] R. Wiltschko, S. Denzau, D. Gehring, P. Thalau, and W. Wiltschko, “Magnetic orientation of migratory robins, *Erithacus rubecula*, under long-wavelength light,” *J. Exp. Biol.*, vol. 214, p. 3096, 2011.
- [161] R. Wiltschko and W. Wiltschko, “Evidence for the use of magnetic outward-journey information in homing pigeons,” *Naturwissenschaften*, vol. 65, p. 112, 1978.
- [162] E. M. Gauger, E. Rieper, J. J. L. Morton, S. C. Benjamin, and V. Vedral, “Sustained quantum coherence and entanglement in the avian compass,” *Phys. Rev. Lett.*, vol. 106, p. 040503, 4 Jan. 2011. DOI: [10.1103/PhysRevLett.106.040503](https://doi.org/10.1103/PhysRevLett.106.040503). [Online]. Available: <https://link.aps.org/doi/10.1103/PhysRevLett.106.040503>.
- [163] Y. Wang, E. Mulvihill, Z. Hu, *et al.*, “Simulation of open quantum system dynamics based on the generalized quantum master equation on quantum computing devices,” *arXiv preprint arXiv:2209.04956*, 2022.
- [164] S. Nakajima, “On the quantum theory of transport phenomena,” *Prog. Theor. Phys.*, vol. 20, pp. 948–959, 1958.

- [165] R. Zwanzig, “Ensemble method in the theory of irreversibility,” *J. Chem. Phys.*, vol. 33, pp. 1338–1341, 1960.
- [166] W. Pfalzgraff, A. Montoya-Castillo, A. Kelly, and T. Markland, “Efficient construction of generalized master equation memory kernels for multi-state systems from nonadiabatic quantum-classical dynamics,” *J. Chem. Phys.*, vol. 150, pp. 244 109–16, 2019.
- [167] J. H. Fetherolf and T. C. Berkelbach, “Linear and nonlinear spectroscopy from quantum master equations,” *J. Chem. Phys.*, vol. 147, no. 24, p. 244 109, 2017.
- [168] T. P. Fay, L. P. Lindoy, and D. E. Manolopoulos, “Electron spin relaxation in radical pairs: Beyond the redfield approximation,” *J. Chem. Phys.*, vol. 151, no. 15, p. 154 117, 2019.
- [169] A. J. Schile and D. T. Limmer, “Simulating conical intersection dynamics in the condensed phase with hybrid quantum master equations,” *J. Chem. Phys.*, vol. 151, no. 1, p. 014 106, 2019.
- [170] A. Y. Vlasov, “Noncommutative tori and universal sets of nonbinary quantum gates,” *J. Math. Phys.*, vol. 43, no. 6, pp. 2959–2964, 2002.
- [171] D. P. DiVincenzo, “Two-bit gates are universal for quantum computation,” *Phys. Rev. A*, vol. 51, no. 2, p. 1015, 1995.
- [172] D. Gottesman, “Fault-tolerant computation with higher-dimensional systems,” in *Lecture Notes in Computer Science*, ser. NASA International Conference on Quantum Computing and Quantum Communications, W. C.P., Ed., vol. 1509, Berlin: Springer, 1999, pp. 302–313.
- [173] D. L. Zhou, B. Zeng, Z. Xu, and C. P. Sun, “Quantum computation based on d-level cluster state,” *Phys. Rev. A*, vol. 68, p. 062 303, 6 Dec. 2003. DOI: [10.1103/PhysRevA.68.062303](https://doi.org/10.1103/PhysRevA.68.062303). [Online]. Available: <https://link.aps.org/doi/10.1103/PhysRevA.68.062303>.
- [174] S. S. Bullock, D. P. O’Leary, and G. K. Brennen, “Asymptotically optimal quantum circuits for d -level systems,” *Phys. Rev. Lett.*, vol. 94, p. 230 502, 23 Jun. 2005. DOI: [10.1103/PhysRevLett.94.230502](https://doi.org/10.1103/PhysRevLett.94.230502). [Online]. Available: <https://link.aps.org/doi/10.1103/PhysRevLett.94.230502>.
- [175] W.-D. Li, Y.-J. Gu, K. Liu, Y.-H. Lee, and Y.-Z. Zhang, “Efficient universal quantum computation with auxiliary Hilbert space,” *Phys. Rev. A*, vol. 88, p. 034 303, 3 Sep. 2013. DOI: [10.1103/PhysRevA.88.034303](https://doi.org/10.1103/PhysRevA.88.034303). [Online]. Available: <https://link.aps.org/doi/10.1103/PhysRevA.88.034303>.

- [176] B. Mischuck and K. Mølmer, “Qudit quantum computation in the Jaynes-Cummings model,” *Phys. Rev. A*, vol. 87, p. 022341, 2 Feb. 2013. DOI: [10.1103/PhysRevA.87.022341](https://doi.org/10.1103/PhysRevA.87.022341). [Online]. Available: <https://link.aps.org/doi/10.1103/PhysRevA.87.022341>.
- [177] M. Reck, A. Zeilinger, H. J. Bernstein, and P. Bertani, “Experimental realization of any discrete unitary operator,” *Phys. Rev. Lett.*, vol. 73, pp. 58–61, 1 Jul. 1994. DOI: [10.1103/PhysRevLett.73.58](https://doi.org/10.1103/PhysRevLett.73.58). [Online]. Available: <https://link.aps.org/doi/10.1103/PhysRevLett.73.58>.
- [178] D. J. Rowe, B. C. Sanders, and H. de Guise, “Representations of the Weyl group and Wigner functions for SU(3),” *J. Math. Phys.*, vol. 40, no. 7, pp. 3604–3615, 1999. DOI: [10.1063/1.532911](https://doi.org/10.1063/1.532911). [Online]. Available: <https://doi.org/10.1063/1.532911>.
- [179] A. Muthukrishnan and C. R. Stroud, “Multivalued logic gates for quantum computation,” *Phys. Rev. A*, vol. 62, p. 052309, 5 Oct. 2000. DOI: [10.1103/PhysRevA.62.052309](https://doi.org/10.1103/PhysRevA.62.052309). [Online]. Available: <https://link.aps.org/doi/10.1103/PhysRevA.62.052309>.
- [180] G. K. Brennen, D. P. O’Leary, and S. S. Bullock, “Criteria for exact qudit universality,” *Phys. Rev. A*, vol. 71, p. 052318, 5 May 2005. DOI: [10.1103/PhysRevA.71.052318](https://doi.org/10.1103/PhysRevA.71.052318). [Online]. Available: <https://link.aps.org/doi/10.1103/PhysRevA.71.052318>.
- [181] D. Gottesman, “Theory of fault-tolerant quantum computation,” *Phys. Rev. A*, vol. 57, pp. 127–137, 1 Jan. 1998. DOI: [10.1103/PhysRevA.57.127](https://doi.org/10.1103/PhysRevA.57.127). [Online]. Available: <https://link.aps.org/doi/10.1103/PhysRevA.57.127>.
- [182] P. Boykin, T. Mor, M. Pulver, V. Roychowdhury, and F. Vatan, “A new universal and fault-tolerant quantum basis,” *Inf. Process. Lett.*, vol. 75, no. 3, pp. 101–107, 2000, ISSN: 0020-0190. DOI: [https://doi.org/10.1016/S0020-0190\(00\)00084-3](https://doi.org/10.1016/S0020-0190(00)00084-3). [Online]. Available: <http://www.sciencedirect.com/science/article/pii/S0020019000000843>.
- [183] J. Patera and H. Zassenhaus, “The Pauli matrices in n dimensions and finest gradings of simple lie algebras of type A_{n-1} ,” *J. Math. Phys.*, vol. 29, no. 3, pp. 665–673, 1988.
- [184] D. Gottesman, A. Kitaev, and J. Preskill, “Encoding a qubit in an oscillator,” *Phys. Rev. A*, vol. 64, no. 1, p. 012310, 2001.
- [185] M. A. Nielsen, M. J. Bremner, J. L. Dodd, A. M. Childs, and C. M. Dawson, “Universal simulation of hamiltonian dynamics for quantum systems with finite-dimensional state spaces,” *Phys. Rev. A*, vol. 66, p. 022317, 2 Aug. 2002. DOI: [10.1103/PhysRevA.66.022317](https://doi.org/10.1103/PhysRevA.66.022317). [Online]. Available: <https://link.aps.org/doi/10.1103/PhysRevA.66.022317>.
- [186] Z. Webb, “The Clifford group forms a unitary 3-design,” *Quantum Inf. Comput.*, vol. 16, no. 15&16, pp. 1379–1400, 2016. [Online]. Available: <http://www.rintonpress.com/xxqic16/qic-16-1516/1379-1400.pdf>.

- [187] D. Gottesman and I. L. Chuang, “Demonstrating the viability of universal quantum computation using teleportation and single-qubit operations,” *Nature*, vol. 402, no. 6760, pp. 390–393, 1999, ISSN: 1476-4687. DOI: [10.1038/46503](https://doi.org/10.1038/46503). [Online]. Available: <https://doi.org/10.1038/46503>.
- [188] B. Eastin and E. Knill, “Restrictions on transversal encoded quantum gate sets,” *Phys. Rev. Lett.*, vol. 102, p. 110502, 11 Mar. 2009. DOI: [10.1103/PhysRevLett.102.110502](https://doi.org/10.1103/PhysRevLett.102.110502). [Online]. Available: <https://link.aps.org/doi/10.1103/PhysRevLett.102.110502>.
- [189] B. Zeng, H. Chung, A. W. Cross, and I. L. Chuang, “Local unitary versus local Clifford equivalence of stabilizer and graph states,” *Phys. Rev. A*, vol. 75, p. 032325, 3 Mar. 2007. DOI: [10.1103/PhysRevA.75.032325](https://doi.org/10.1103/PhysRevA.75.032325). [Online]. Available: <https://link.aps.org/doi/10.1103/PhysRevA.75.032325>.
- [190] R. A. Low, “Learning and testing algorithms for the Clifford group,” *Phys. Rev. A*, vol. 80, p. 052314, 5 Nov. 2009. DOI: [10.1103/PhysRevA.80.052314](https://doi.org/10.1103/PhysRevA.80.052314). [Online]. Available: <https://link.aps.org/doi/10.1103/PhysRevA.80.052314>.
- [191] A. M. Childs, “Secure assisted quantum computation,” *arXiv:quant-ph/0111046*, 2001.
- [192] W. van Dam and M. Howard, “Noise thresholds for higher-dimensional systems using the discrete wigner function,” *Phys. Rev. A*, vol. 83, p. 032310, 3 Mar. 2011. DOI: [10.1103/PhysRevA.83.032310](https://doi.org/10.1103/PhysRevA.83.032310). [Online]. Available: <https://link.aps.org/doi/10.1103/PhysRevA.83.032310>.
- [193] H. Anwar, E. T. Campbell, and D. E. Browne, “Qutrit magic state distillation,” *New J. Phys.*, vol. 14, no. 6, p. 063006, Jun. 2012. DOI: [10.1088/1367-2630/14/6/063006](https://doi.org/10.1088/1367-2630/14/6/063006). [Online]. Available: <https://doi.org/10.1088/1367-2630/14/6/063006>.
- [194] E. T. Campbell, H. Anwar, and D. E. Browne, “Magic-state distillation in all prime dimensions using quantum Reed-Muller codes,” *Phys. Rev. X*, vol. 2, p. 041021, 4 Dec. 2012. DOI: [10.1103/PhysRevX.2.041021](https://doi.org/10.1103/PhysRevX.2.041021). [Online]. Available: <https://link.aps.org/doi/10.1103/PhysRevX.2.041021>.
- [195] C. M. Wilmott, “On swapping the states of two qudits,” *Int. J. Quantum Inf.*, vol. 09, no. 06, pp. 1511–1517, 2011. DOI: [10.1142/S0219749911008143](https://doi.org/10.1142/S0219749911008143). eprint: <https://doi.org/10.1142/S0219749911008143>. [Online]. Available: <https://doi.org/10.1142/S0219749911008143>.
- [196] C. M. Wilmott and P. R. Wild, “On a generalized quantum swap gate,” *Int. J. Quantum Inf.*, vol. 10, no. 03, p. 1250034, 2012. DOI: [10.1142/S0219749912500347](https://doi.org/10.1142/S0219749912500347). eprint: <https://doi.org/10.1142/S0219749912500347>. [Online]. Available: <https://doi.org/10.1142/S0219749912500347>.

- [197] N. D. Mermin, “From classical state swapping to quantum teleportation,” *Phys. Rev. A*, vol. 65, p. 012320, 1 Dec. 2001. DOI: [10.1103/PhysRevA.65.012320](https://doi.org/10.1103/PhysRevA.65.012320). [Online]. Available: <https://link.aps.org/doi/10.1103/PhysRevA.65.012320>.
- [198] K. Fujii, “Exchange gate on the qudit space and fock space,” *J. Opt. B*, vol. 5, no. 6, S613–S618, Oct. 2003. DOI: [10.1088/1464-4266/5/6/011](https://doi.org/10.1088/1464-4266/5/6/011). [Online]. Available: <https://doi.org/10.1088/1464-4266/5/6/011>.
- [199] G. A. Paz-Silva, S. Rebić, J. Twamley, and T. Duty, “Perfect mirror transport protocol with higher dimensional quantum chains,” *Phys. Rev. Lett.*, vol. 102, p. 020503, 2 Jan. 2009. DOI: [10.1103/PhysRevLett.102.020503](https://doi.org/10.1103/PhysRevLett.102.020503). [Online]. Available: <https://link.aps.org/doi/10.1103/PhysRevLett.102.020503>.
- [200] X. Wang, “Continuous-variable and hybrid quantum gates,” *J. Phys. A*, vol. 34, no. 44, pp. 9577–9584, Oct. 2001. DOI: [10.1088/0305-4470/34/44/316](https://doi.org/10.1088/0305-4470/34/44/316). [Online]. Available: <https://doi.org/10.1088/0305-4470/34/44/316>.
- [201] G. Alber, A. Delgado, N. Gisin, and I. Jex, “Efficient bipartite quantum state purification in arbitrary dimensional Hilbert spaces,” *J. Phys. A*, vol. 34, no. 42, pp. 8821–8833, Oct. 2001. DOI: [10.1088/0305-4470/34/42/307](https://doi.org/10.1088/0305-4470/34/42/307). [Online]. Available: <https://doi.org/10.1088/0305-4470/34/42/307>.
- [202] A. M. C. R. Stroud, “Quantum fast fourier transform using multilevel atoms,” *J. Mod. Opt.*, vol. 49, no. 13, pp. 2115–2127, 2002. DOI: [10.1080/09500340210123947](https://doi.org/10.1080/09500340210123947). eprint: <https://doi.org/10.1080/09500340210123947>. [Online]. Available: <https://doi.org/10.1080/09500340210123947>.
- [203] D. G. Cory, M. D. Price, W. Maas, *et al.*, “Experimental quantum error correction,” *Phys. Rev. Lett.*, vol. 81, pp. 2152–2155, 10 Sep. 1998. DOI: [10.1103/PhysRevLett.81.2152](https://doi.org/10.1103/PhysRevLett.81.2152). [Online]. Available: <https://link.aps.org/doi/10.1103/PhysRevLett.81.2152>.
- [204] E. Dennis, “Toward fault-tolerant quantum computation without concatenation,” *Phys. Rev. A*, vol. 63, p. 052314, 5 Apr. 2001. DOI: [10.1103/PhysRevA.63.052314](https://doi.org/10.1103/PhysRevA.63.052314). [Online]. Available: <https://link.aps.org/doi/10.1103/PhysRevA.63.052314>.
- [205] Y. Shi, “Both Toffoli and controlled-NOT need little help to do universal quantum computation,” *arXiv preprint quant-ph/0205115*, 2002.
- [206] M. A. Nielsen and I. L. Chuang, *Quantum Computation and Quantum Information: 10th Anniversary Edition*, 10th. New York, NY, USA: Cambridge University Press, 2011, ISBN: 1107002176, 9781107002173.

- [207] A. Aspuru-Guzik, A. D. Dutoi, P. J. Love, and M. Head-Gordon, “Simulated quantum computation of molecular energies,” *Science*, vol. 309, no. 5741, pp. 1704–1707, 2005, ISSN: 0036-8075. DOI: [10.1126/science.1113479](https://doi.org/10.1126/science.1113479). eprint: <https://science.sciencemag.org/content/309/5741/1704.full.pdf>. [Online]. Available: <https://science.sciencemag.org/content/309/5741/1704>.
- [208] P. W. Shor, “Algorithms for quantum computation: Discrete logarithms and factoring,” in *Proceedings 35th Annual Symposium on Foundations of Computer Science*, Nov. 1994, pp. 124–134. DOI: [10.1109/SFCS.1994.365700](https://doi.org/10.1109/SFCS.1994.365700).
- [209] R. Cleve, A. Ekert, C. Macchiavello, and M. Mosca, “Quantum algorithms revisited,” *Proceedings of the Royal Society of London. Series A: Mathematical, Physical and Engineering Sciences*, vol. 454, no. 1969, pp. 339–354, 1998.
- [210] Y.-M. Di and H.-R. Wei, “Synthesis of multivalued quantum logic circuits by elementary gates,” *Phys. Rev. A*, vol. 87, p. 012325, 1 Jan. 2013. DOI: [10.1103/PhysRevA.87.012325](https://doi.org/10.1103/PhysRevA.87.012325). [Online]. Available: <https://link.aps.org/doi/10.1103/PhysRevA.87.012325>.
- [211] F. S. Khan and M. Perkowski, “Synthesis of multi-qudit hybrid and d-valued quantum logic circuits by decomposition,” *Theor. Comput. Sci.*, vol. 367, no. 3, pp. 336–346, 2006, ISSN: 0304-3975. DOI: <https://doi.org/10.1016/j.tcs.2006.09.006>. [Online]. Available: <http://www.sciencedirect.com/science/article/pii/S0304397506006049>.
- [212] M. A. Nielsen, M. R. Dowling, M. Gu, and A. C. Doherty, “Quantum computation as geometry,” *Science*, vol. 311, no. 5764, pp. 1133–1135, 2006.
- [213] M. A. Nielsen, “A geometric approach to quantum circuit lower bounds,” *arXiv preprint quant-ph/0502070*, 2005.
- [214] D. Deutsch, “Quantum theory, the Church–Turing principle and the universal quantum computer,” *J. Phys. A*, vol. 400, no. 1818, pp. 97–117, 1985. DOI: [10.1098/rspa.1985.0070](https://doi.org/10.1098/rspa.1985.0070). [Online]. Available: <https://royalsocietypublishing.org/doi/abs/10.1098/rspa.1985.0070>.
- [215] D. P. Deutsch and R. Jozsa, “Rapid solution of problems by quantum computation,” *Proc. Royal Soc. Lond. A*, vol. 439, pp. 553–558, 1992. DOI: [10.1098/rspa.1992.0167](https://doi.org/10.1098/rspa.1992.0167).
- [216] M. Van den Nest, “Universal quantum computation with little entanglement,” *Phys. Rev. Lett.*, vol. 110, p. 060504, 6 Feb. 2013. DOI: [10.1103/PhysRevLett.110.060504](https://doi.org/10.1103/PhysRevLett.110.060504). [Online]. Available: <https://link.aps.org/doi/10.1103/PhysRevLett.110.060504>.
- [217] M. Howard, J. Wallman, V. Veitch, and J. Emerson, “Contextuality supplies the ‘magic’ for quantum computation,” *Nature*, vol. 510, p. 351, Jun. 2014, Article. [Online]. Available: <https://doi.org/10.1038/nature13460>.

- [218] S. Kochen and E. P. Specker, “The problem of hidden variables in quantum mechanics,” in *The Logico-Algebraic Approach to Quantum Mechanics: Volume I: Historical Evolution*. Dordrecht: Springer Netherlands, 1975, pp. 293–328, ISBN: 978-94-010-1795-4. DOI: . [Online]. Available:
- [219] A. A. Klyachko, M. A. Can, S. Binicio ğlu, and A. S. Shumovsky, “Simple test for hidden variables in spin-1 systems,” *Phys. Rev. Lett.*, vol. 101, p. 020403, 2 Jul. 2008. DOI: [10.1103/PhysRevLett.101.020403](https://doi.org/10.1103/PhysRevLett.101.020403). [Online]. Available: <https://link.aps.org/doi/10.1103/PhysRevLett.101.020403>.
- [220] X. Zhan, J. Li, H. Qin, Z.-h. Bian, and P. Xue, “Linear optical demonstration of quantum speed-up with a single qudit,” *Opt. Express*, vol. 23, no. 14, pp. 18422–18427, Jul. 2015. DOI: [10.1364/OE.23.018422](https://doi.org/10.1364/OE.23.018422). [Online]. Available: <http://www.opticsexpress.org/abstract.cfm?URI=oe-23-14-18422>.
- [221] Y. Fan, “A generalization of the Deutsch-Jozsa algorithm to multi-valued quantum logic,” in *37th International Symposium on Multiple-Valued Logic (ISMVL’07)*, May 2007, pp. 12–12. DOI: [10.1109/ISMVL.2007.3](https://doi.org/10.1109/ISMVL.2007.3).
- [222] E. Kiktenko, A. Fedorov, A. Strakhov, and V. Man’ko, “Single qudit realization of the Deutsch algorithm using superconducting many-level quantum circuits,” *Phys. Lett. A*, vol. 379, no. 22, pp. 1409–1413, 2015, ISSN: 0375-9601. DOI: <https://doi.org/10.1016/j.physleta.2015.03.023>. [Online]. Available: <http://www.sciencedirect.com/science/article/pii/S0375960115002753>.
- [223] A. R. Kessel and N. M. Yakovleva, “Implementation schemes in NMR of quantum processors and the Deutsch-Jozsa algorithm by using virtual spin representation,” *Phys. Rev. A*, vol. 66, p. 062322, 6 Dec. 2002. DOI: [10.1103/PhysRevA.66.062322](https://doi.org/10.1103/PhysRevA.66.062322). [Online]. Available: <https://link.aps.org/doi/10.1103/PhysRevA.66.062322>.
- [224] E. Bernstein and U. Vazirani, “Quantum complexity theory,” *SIAM Journal on Computing*, vol. 26, no. 5, pp. 1411–1473, 1997. DOI: [10.1137/S0097539796300921](https://doi.org/10.1137/S0097539796300921). eprint: <https://doi.org/10.1137/S0097539796300921>. [Online]. Available: <https://doi.org/10.1137/S0097539796300921>.
- [225] R. Krishna, V. Makwana, and A. P. Suresh, “A generalization of Bernstein-Vazirani algorithm to qudit systems,” *arXiv preprint arXiv:1609.03185*, 2016.
- [226] Z. Zilic and K. Radecka, “Scaling and better approximating quantum Fourier transform by higher radices,” *IEEE Transactions on Computers*, vol. 56, no. 2, pp. 202–207, Feb. 2007. DOI: [10.1109/TC.2007.35](https://doi.org/10.1109/TC.2007.35).

- [227] D. Coppersmith, “An approximate Fourier transform useful in quantum factoring,” *arXiv preprint quant-ph/0201067*, 2002.
- [228] V. V. Shende, S. S. Bullock, and I. L. Markov, “Synthesis of quantum-logic circuits,” *IEEE Transactions on Computer-Aided Design of Integrated Circuits and Systems*, vol. 25, no. 6, pp. 1000–1010, Jun. 2006. DOI: [10.1109/TCAD.2005.855930](https://doi.org/10.1109/TCAD.2005.855930).
- [229] V. Parasa and M. Perkowski, “Quantum phase estimation using multivalued logic,” in *2011 41st IEEE International Symposium on Multiple-Valued Logic*, May 2011, pp. 224–229. DOI: [10.1109/ISMVL.2011.47](https://doi.org/10.1109/ISMVL.2011.47).
- [230] D. S. Abrams and S. Lloyd, “Quantum algorithm providing exponential speed increase for finding eigenvalues and eigenvectors,” *Phys. Rev. Lett.*, vol. 83, pp. 5162–5165, 24 Dec. 1999. DOI: [10.1103/PhysRevLett.83.5162](https://doi.org/10.1103/PhysRevLett.83.5162). [Online]. Available: <https://link.aps.org/doi/10.1103/PhysRevLett.83.5162>.
- [231] J. Pan, Y. Cao, X. Yao, *et al.*, “Experimental realization of quantum algorithm for solving linear systems of equations,” *Phys. Rev. A*, vol. 89, no. 2, p. 022313, 2014.
- [232] H. S. Tonchev and N. V. Vitanov, “Quantum phase estimation and quantum counting with qudits,” *Phys. Rev. A*, vol. 94, p. 042307, 4 Oct. 2016. DOI: [10.1103/PhysRevA.94.042307](https://doi.org/10.1103/PhysRevA.94.042307). [Online]. Available: <https://link.aps.org/doi/10.1103/PhysRevA.94.042307>.
- [233] H. Wang, S. Kais, A. Aspuru-Guzik, and M. R. Hoffmann, “Quantum algorithm for obtaining the energy spectrum of molecular systems,” *Phys. Chem. Chem. Phys.*, vol. 10, pp. 5388–5393, 35 2008. DOI: [10.1039/B804804E](https://doi.org/10.1039/B804804E). [Online]. Available: <http://dx.doi.org/10.1039/B804804E>.
- [234] A. Daskin, A. Grama, G. Kollias, and S. Kais, “Universal programmable quantum circuit schemes to emulate an operator,” *J. Chem. Phys.*, vol. 137, no. 23, p. 234112, 2012.
- [235] S. Kais, “Introduction to quantum information and computation for chemistry,” *Quantum Inf. Comput. Chem.*, vol. 154, pp. 1–38, 2014.
- [236] T. Bian, D. Murphy, R. Xia, A. Daskin, and S. Kais, “Quantum computing methods for electronic states of the water molecule,” *Mol. Phys.*, vol. 117, no. 15-16, pp. 2069–2082, 2019.
- [237] M. Sawerwain and W. Leoński, “Quantum circuits based on qutrits as a tool for solving systems of linear equations,” *arXiv:1309.0800*, 2013.
- [238] Y. Fan, “Applications of multi-valued quantum algorithms,” *arXiv:0809.0932*, 2008. DOI: [10.1109/ISMVL.2007.3](https://doi.org/10.1109/ISMVL.2007.3).

- [239] H. Li, C. Wu, W. Liu, P. Chen, and C. Li, “Fast quantum search algorithm for databases of arbitrary size and its implementation in a cavity QED system,” *Phys. Lett. A*, vol. 375, no. 48, pp. 4249–4254, 2011, ISSN: 0375-9601. DOI: <https://doi.org/10.1016/j.physleta.2011.10.016>. [Online]. Available: <http://www.sciencedirect.com/science/article/pii/S0375960111012369>.
- [240] E. S. Kyoseva and N. V. Vitanov, “Coherent pulsed excitation of degenerate multistate systems: Exact analytic solutions,” *Phys. Rev. A*, vol. 73, p. 023 420, 2 Feb. 2006. DOI: [10.1103/PhysRevA.73.023420](https://link.aps.org/doi/10.1103/PhysRevA.73.023420). [Online]. Available: <https://link.aps.org/doi/10.1103/PhysRevA.73.023420>.
- [241] R. Raussendorf and H. J. Briegel, “A one-way quantum computer,” *Phys. Rev. Lett.*, vol. 86, pp. 5188–5191, 22 May 2001. DOI: [10.1103/PhysRevLett.86.5188](https://link.aps.org/doi/10.1103/PhysRevLett.86.5188). [Online]. Available: <https://link.aps.org/doi/10.1103/PhysRevLett.86.5188>.
- [242] E. Farhi, J. Goldstone, S. Gutmann, and M. Sipser, “Quantum computation by adiabatic evolution,” *arXiv:quant-ph/0001106*, 2000.
- [243] D. Aharonov, W. van Dam, J. Kempe, Z. Landau, S. Lloyd, and O. Regev, “Adiabatic quantum computation is equivalent to standard quantum computation,” *SIAM J. Comput.*, vol. 37, no. 1, pp. 166–194, 2007. DOI: [10.1137/S0097539705447323](https://doi.org/10.1137/S0097539705447323).
- [244] M. H. Freedman, M. Larsen, and Z. Wang, “A modular functor which is universal for quantum computation,” *Commun. Math. Phys.*, vol. 227, no. 3, pp. 605–622, Jun. 2002. DOI: [10.1007/s002200200645](https://doi.org/10.1007/s002200200645).
- [245] H. J. Briegel and R. Raussendorf, “Persistent entanglement in arrays of interacting particles,” *Phys. Rev. Lett.*, vol. 86, pp. 910–913, 5 Jan. 2001. DOI: [10.1103/PhysRevLett.86.910](https://doi.org/10.1103/PhysRevLett.86.910).
- [246] M. Hein, J. Eisert, and H. J. Briegel, “Multipartite entanglement in graph states,” *Phys. Rev. A*, vol. 69, p. 062 311, 6 Jun. 2004. DOI: [10.1103/PhysRevA.69.062311](https://doi.org/10.1103/PhysRevA.69.062311).
- [247] M. A. Nielsen, “Cluster-state quantum computation,” *Rep. Math. Phys.*, vol. 57, no. 1, pp. 147–161, Feb. 2006. DOI: [10.1016/S0034-4877\(06\)80014-5](https://doi.org/10.1016/S0034-4877(06)80014-5).
- [248] A. Keet, B. Fortescue, D. Markham, and B. C. Sanders, “Quantum secret sharing with qudit graph states,” *Phys. Rev. A*, vol. 82, p. 062 315, 6 Dec. 2010. DOI: [10.1103/PhysRevA.82.062315](https://link.aps.org/doi/10.1103/PhysRevA.82.062315). [Online]. Available: <https://link.aps.org/doi/10.1103/PhysRevA.82.062315>.
- [249] J. Joo, C.-W. Lee, S. Kono, and J. Kim, “Logical measurement-based quantum computation in circuit-qed,” *Sci. Rep.*, vol. 9, no. 1, p. 16 592, Nov. 2019. DOI: [10.1038/s41598-019-52866-3](https://doi.org/10.1038/s41598-019-52866-3).

- [250] A. B. Finnila, M. A. Gomez, C. Sebenik, C. Stenson, and J. D. Doll, “Quantum annealing: A new method for minimizing multidimensional functions,” *Chem. Phys. Lett.*, vol. 219, no. 5, pp. 343–348, 1994, ISSN: 0009-2614. DOI: [https://doi.org/10.1016/0009-2614\(94\)00117-0](https://doi.org/10.1016/0009-2614(94)00117-0). [Online]. Available: <http://www.sciencedirect.com/science/article/pii/0009261494001170>.
- [251] T. Kadowaki and H. Nishimori, “Quantum annealing in the transverse ising model,” *Phys. Rev. E*, vol. 58, pp. 5355–5363, 5 Nov. 1998. DOI: [10.1103/PhysRevE.58.5355](https://doi.org/10.1103/PhysRevE.58.5355). [Online]. Available: <https://link.aps.org/doi/10.1103/PhysRevE.58.5355>.
- [252] A. Das and B. K. Chakrabarti, “Colloquium: Quantum annealing and analog quantum computation,” *Rev. Mod. Phys.*, vol. 80, pp. 1061–1081, 3 Sep. 2008. DOI: [10.1103/RevModPhys.80.1061](https://doi.org/10.1103/RevModPhys.80.1061). [Online]. Available: <https://link.aps.org/doi/10.1103/RevModPhys.80.1061>.
- [253] R. Barends, J. Kelly, A. Megrant, *et al.*, “Superconducting quantum circuits at the surface code threshold for fault tolerance,” *Nature*, vol. 508, no. 7497, pp. 500–503, Apr. 2014. DOI: [10.1038/nature13171](https://doi.org/10.1038/nature13171).
- [254] J. M. Martinis and M. R. Geller, “Fast adiabatic qubit gates using only σ_z control,” *Phys. Rev. A*, vol. 90, p. 022307, 2 Aug. 2014. DOI: [10.1103/PhysRevA.90.022307](https://doi.org/10.1103/PhysRevA.90.022307). [Online]. Available: <https://link.aps.org/doi/10.1103/PhysRevA.90.022307>.
- [255] E. Zahedinejad, J. Ghosh, and B. C. Sanders, “High-fidelity single-shot Toffoli gate via quantum control,” *Phys. Rev. Lett.*, vol. 114, p. 200502, 20 May 2015. DOI: [10.1103/PhysRevLett.114.200502](https://doi.org/10.1103/PhysRevLett.114.200502). [Online]. Available: <https://link.aps.org/doi/10.1103/PhysRevLett.114.200502>.
- [256] E. Zahedinejad, J. Ghosh, and B. C. Sanders, “Designing high-fidelity single-shot three-qubit gates: A machine-learning approach,” *Phys. Rev. Applied*, vol. 6, p. 054005, 5 Nov. 2016. DOI: [10.1103/PhysRevApplied.6.054005](https://doi.org/10.1103/PhysRevApplied.6.054005). [Online]. Available: <https://link.aps.org/doi/10.1103/PhysRevApplied.6.054005>.
- [257] S. Watabe, Y. Seki, and S. Kawabata, “Enhancing quantum annealing performance by a degenerate two-level system,” *Sci. Rep.*, vol. 10, p. 146, Dec. 2020. DOI: [10.1038/s41598-019-56758-4](https://doi.org/10.1038/s41598-019-56758-4).
- [258] A. Hutter and D. Loss, “Quantum computing with parafermions,” *Phys. Rev. B*, vol. 93, p. 125105, 12 Mar. 2016. DOI: [10.1103/PhysRevB.93.125105](https://doi.org/10.1103/PhysRevB.93.125105). [Online]. Available: <https://link.aps.org/doi/10.1103/PhysRevB.93.125105>.

- [259] A. Dua, B. Malomed, M. Cheng, and L. Jiang, “Universal quantum computing with parafermions assisted by a half-fluxon,” *Phys. Rev. B*, vol. 100, p. 144508, 14 Oct. 2019. DOI: [10.1103/PhysRevB.100.144508](https://doi.org/10.1103/PhysRevB.100.144508). [Online]. Available: <https://link.aps.org/doi/10.1103/PhysRevB.100.144508>.
- [260] A. Kitaev, “Fault-tolerant quantum computation by anyons,” *Ann. Phys. (N. Y.)*, vol. 303, no. 1, pp. 2–30, 2003, ISSN: 0003-4916. DOI: [https://doi.org/10.1016/S0003-4916\(02\)00018-0](https://doi.org/10.1016/S0003-4916(02)00018-0). [Online]. Available: <http://www.sciencedirect.com/science/article/pii/S0003491602000180>.
- [261] F. Jelezko, T. Gaebel, I. Popa, M. Domhan, A. Gruber, and J. Wrachtrup, “Observation of coherent oscillation of a single nuclear spin and realization of a two-qubit conditional quantum gate,” *Phys. Rev. Lett.*, vol. 93, p. 130501, 13 Sep. 2004. DOI: [10.1103/PhysRevLett.93.130501](https://doi.org/10.1103/PhysRevLett.93.130501). [Online]. Available: <https://link.aps.org/doi/10.1103/PhysRevLett.93.130501>.
- [262] L. Childress, M. V. Gurudev Dutt, J. M. Taylor, *et al.*, “Coherent dynamics of coupled electron and nuclear spin qubits in diamond,” *Science*, vol. 314, no. 5797, pp. 281–285, 2006, ISSN: 0036-8075. DOI: [10.1126/science.1131871](https://doi.org/10.1126/science.1131871). eprint: <https://science.sciencemag.org/content/314/5797/281.full.pdf>. [Online]. Available: <https://science.sciencemag.org/content/314/5797/281>.
- [263] P. Neumann, J. Beck, M. Steiner, *et al.*, “Single-shot readout of a single nuclear spin,” *Science*, vol. 329, no. 5991, pp. 542–544, 2010, ISSN: 0036-8075. DOI: [10.1126/science.1189075](https://doi.org/10.1126/science.1189075). eprint: <https://science.sciencemag.org/content/329/5991/542.full.pdf>. [Online]. Available: <https://science.sciencemag.org/content/329/5991/542>.
- [264] D. Loss and D. P. DiVincenzo, “Quantum computation with quantum dots,” *Phys. Rev. A*, vol. 57, pp. 120–126, 1 Jan. 1998. DOI: [10.1103/PhysRevA.57.120](https://doi.org/10.1103/PhysRevA.57.120). [Online]. Available: <https://link.aps.org/doi/10.1103/PhysRevA.57.120>.
- [265] K. C. Nowack, F. H. L. Koppens, Y. V. Nazarov, and L. M. K. Vandersypen, “Coherent control of a single electron spin with electric fields,” *Science*, vol. 318, no. 5855, pp. 1430–1433, 2007, ISSN: 0036-8075. DOI: [10.1126/science.1148092](https://doi.org/10.1126/science.1148092). eprint: <https://science.sciencemag.org/content/318/5855/1430.full.pdf>. [Online]. Available: <https://science.sciencemag.org/content/318/5855/1430>.
- [266] G. J. Milburn, “Photons as qubits,” *Physica Scripta*, vol. T137, p. 014003, Dec. 2009. DOI: [10.1088/0031-8949/2009/t137/014003](https://doi.org/10.1088/0031-8949/2009/t137/014003). [Online]. Available: <https://doi.org/10.1088/0031-8949/2009/t137/014003>.

- [267] R. Prevedel, P. Walther, F. Tiefenbacher, *et al.*, “High-speed linear optics quantum computing using active feed-forward,” *Nature*, vol. 445, no. 7123, pp. 65–69, 2007, ISSN: 1476-4687. DOI: [10.1038/nature05346](https://doi.org/10.1038/nature05346). [Online]. Available: <https://doi.org/10.1038/nature05346>.
- [268] I. Chiorescu, Y. Nakamura, C. J. P. M. Harmans, and J. E. Mooij, “Coherent quantum dynamics of a superconducting flux qubit,” *Science*, vol. 299, no. 5614, pp. 1869–1871, 2003, ISSN: 0036-8075. DOI: [10.1126/science.1081045](https://doi.org/10.1126/science.1081045). eprint: <https://science.sciencemag.org/content/299/5614/1869.full.pdf>. [Online]. Available: <https://science.sciencemag.org/content/299/5614/1869>.
- [269] J. Clarke and F. K. Wilhelm, “Superconducting quantum bits,” *Nature*, vol. 453, no. 7198, pp. 1031–1042, 2008, ISSN: 1476-4687. DOI: [10.1038/nature07128](https://doi.org/10.1038/nature07128). [Online]. Available: <https://doi.org/10.1038/nature07128>.
- [270] R. Blatt and D. Wineland, “Entangled states of trapped atomic ions,” *Nature*, vol. 453, no. 7198, pp. 1008–1015, 2008, ISSN: 1476-4687. DOI: [10.1038/nature07125](https://doi.org/10.1038/nature07125). [Online]. Available: <https://doi.org/10.1038/nature07125>.
- [271] I. Bloch, “Quantum coherence and entanglement with ultracold atoms in optical lattices,” *Nature*, vol. 453, no. 7198, pp. 1016–1022, 2008, ISSN: 1476-4687. DOI: [10.1038/nature07126](https://doi.org/10.1038/nature07126). [Online]. Available: <https://doi.org/10.1038/nature07126>.
- [272] F. Troiani and M. Affronte, “Molecular spins for quantum information technologies,” *Chem. Soc. Rev.*, vol. 40, no. 6, pp. 3119–3129, 2011.
- [273] L. Bogani and W. Wernsdorfer, “Molecular spintronics using single-molecule magnets,” in *Nanoscience And Technology: A Collection of Reviews from Nature Journals*, World Scientific, 2010, pp. 194–201.
- [274] J. M. Clemente-Juan, E. Coronado, and A. Gaita-Ariño, “Magnetic polyoxometalates: From molecular magnetism to molecular spintronics and quantum computing,” *Chem. Soc. Rev.*, vol. 41, no. 22, pp. 7464–7478, 2012.
- [275] G. Aromí, D. Aguila, P. Gamez, F. Luis, and O. Roubeau, “Design of magnetic coordination complexes for quantum computing,” *Chem. Soc. Rev.*, vol. 41, no. 2, pp. 537–546, 2012.
- [276] I. L. Chuang, L. M. Vandersypen, X. Zhou, D. W. Leung, and S. Lloyd, “Experimental realization of a quantum algorithm,” *Nature*, vol. 393, no. 6681, p. 143, 1998.
- [277] L. M. Vandersypen, M. Steffen, G. Breyta, C. S. Yannoni, M. H. Sherwood, and I. L. Chuang, “Experimental realization of Shor’s quantum factoring algorithm using nuclear magnetic resonance,” *Nature*, vol. 414, no. 6866, p. 883, 2001.

- [278] E. Moreno-Pineda, C. Godfrin, F. Balestro, W. Wernsdorfer, and M. Ruben, “Molecular spin qubits for quantum algorithms,” *Chem. Soc. Rev.*, vol. 47, pp. 501–513, 2018. DOI: [10.1039/C5CS00933B](https://doi.org/10.1039/C5CS00933B). [Online]. Available: <http://dx.doi.org/10.1039/C5CS00933B>.
- [279] M. Erhard, R. Fickler, M. Krenn, and A. Zeilinger, “Twisted photons: New quantum perspectives in high dimensions,” *Light Sci. Appl.*, vol. 7, p. 17146, 2018. DOI: [10.1038/lsa.2017.146](https://doi.org/10.1038/lsa.2017.146).
- [280] M. Kues, C. Reimer, P. Roztocki, *et al.*, “On-chip generation of high-dimensional entangled quantum states and their coherent control,” *Nature*, vol. 546, no. 6760, pp. 622–626, 2017. DOI: [10.1038/46503](https://doi.org/10.1038/46503).
- [281] H.-H. Lu, J. M. Lukens, N. A. Peters, *et al.*, “Electro-optic frequency beam splitters and tritters for high-fidelity photonic quantum inf. process.,” *Phys. Rev. Lett.*, vol. 120, no. 3, p. 030502, 2018.
- [282] P. Imany, J. A. Jaramillo-Villegas, O. D. Odele, *et al.*, “50-ghz-spaced comb of high-dimensional frequency-bin entangled photons from an on-chip silicon nitride microresonator,” *Opt. Express*, vol. 26, no. 2, pp. 1825–1840, 2018.
- [283] P. Imany, J. A. Jaramillo-Villegas, M. S. Alshaykh, *et al.*, “High-dimensional optical quantum logic in large operational spaces,” *npj Quantum Inf.*, vol. 5, no. 1, Jul. 2019, ISSN: 2056–6387. DOI: [10.1038/s41534-019-0173-8](https://doi.org/10.1038/s41534-019-0173-8).
- [284] P. C. Humphreys, B. J. Metcalf, J. B. Spring, *et al.*, “Linear optical quantum computing in a single spatial mode,” *Phys. Rev. Lett.*, vol. 111, p. 150501, 15 Oct. 2013. DOI: [10.1103/PhysRevLett.111.150501](https://doi.org/10.1103/PhysRevLett.111.150501). [Online]. Available: <https://link.aps.org/doi/10.1103/PhysRevLett.111.150501>.
- [285] D. Mc Hugh and J. Twamley, “Trapped-ion qutrit spin molecule quantum computer,” *New J. Phys.*, vol. 7, no. 1, p. 174, 2005.
- [286] F. A. Bovey, P. A. Mirau, and H. Gutowsky, *Nuclear magnetic resonance spectroscopy*. Elsevier, 1988.
- [287] C. P. Slichter, *Principles of magnetic resonance*. Springer Science & Business Media, 2013, vol. 1.
- [288] J.-S. Lee and A. K. Khitrin, “Projective measurement in nuclear magnetic resonance,” *Appl. Phys. Lett.*, vol. 89, no. 7, p. 074105, 2006.

- [289] E. Moreno Pineda, T. Komeda, K. Katoh, M. Yamashita, and M. Ruben, “Surface confinement of TbPc2-SMMs: Structural, electronic and magnetic properties,” *Dalton Trans.*, vol. 45, pp. 18 417–18 433, 46 2016. DOI: [10.1039/C6DT03298B](https://doi.org/10.1039/C6DT03298B). [Online]. Available: <http://dx.doi.org/10.1039/C6DT03298B>.
- [290] M. Ganzhorn, S. Klyatskaya, M. Ruben, and W. Wernsdorfer, “Strong spin–phonon coupling between a single-molecule magnet and a carbon nanotube nanoelectromechanical system,” *Nat. Nanotechnol.*, vol. 8, no. 3, p. 165, 2013.
- [291] M. Urdampilleta, S. Klyatskaya, J.-P. Cleuziou, M. Ruben, and W. Wernsdorfer, “Supramolecular spin valves,” *Nat. Mater.*, vol. 10, no. 7, p. 502, 2011.
- [292] S. Thiele, F. Balestro, R. Ballou, S. Klyatskaya, M. Ruben, and W. Wernsdorfer, “Electrically driven nuclear spin resonance in single-molecule magnets,” *Science*, vol. 344, no. 6188, pp. 1135–1138, 2014.
- [293] N. Ishikawa, M. Sugita, T. Okubo, N. Tanaka, T. Iino, and Y. Kaizu, “Determination of ligand-field parameters and f-electronic structures of double-decker bis (phthalocyaninato) lanthanide complexes,” *Inorganic chemistry*, vol. 42, no. 7, pp. 2440–2446, 2003.
- [294] C. Godfrin, A. Ferhat, R. Ballou, *et al.*, “Operating quantum states in single magnetic molecules: Implementation of grover’s quantum algorithm,” *Phys. Rev. Lett.*, vol. 119, no. 18, p. 187 702, 2017.
- [295] D. Cozzolino, B. Da Lio, D. Bacco, and L. K. Oxenløwe, “High-dimensional quantum communication: Benefits, progress, and future challenges,” *Adv. Quantum Technol.*, vol. 2, no. 12, p. 1 900 038, 2019.
- [296] L. Sheridan and V. Scarani, “Security proof for quantum key distribution using qudit systems,” *Phys. Rev. A*, vol. 82, no. 3, p. 030 301, 2010.
- [297] Z. Liu and H. Fan, “Decay of multiqubit entanglement,” *Phys. Rev. A*, vol. 79, no. 6, p. 064 305, 2009.
- [298] S. Ecker, F. Bouchard, L. Bulla, *et al.*, “Overcoming noise in entanglement distribution,” *Phys. Rev. X*, vol. 9, no. 4, p. 041 042, 2019.
- [299] M. Jafarzadeh, Y.-D. Wu, Y. R. Sanders, and B. C. Sanders, “Randomized benchmarking for qudit Clifford gates,” *New J. Phys.*, vol. 22, no. 06, p. 063 014, Jun. 2020. DOI: [10.1088/1367-2630/ab8ab1](https://doi.org/10.1088/1367-2630/ab8ab1).
- [300] A. Morvan, V. Ramasesh, M. Blok, *et al.*, “Qutrit randomized benchmarking,” *arXiv preprint arXiv:2008.09134*, 2020.

- [301] M. Kononenko, M. Yurtalan, J. Shi, and A. Lupascu, “Characterization of control in a superconducting qutrit using randomized benchmarking,” *arXiv preprint arXiv:2009.00599*, 2020.
- [302] D. M. Reich, G. Gualdi, and C. P. Koch, “Optimal qudit operator bases for efficient characterization of quantum gates,” *J. Phys. A-Math Theor*, vol. 47, no. 38, p. 385 305, 2014.
- [303] G. Gualdi, D. Licht, D. M. Reich, and C. P. Koch, “Efficient monte carlo characterization of quantum operations for qudits,” *Phys. Rev. A*, vol. 90, no. 3, p. 032 317, 2014.
- [304] M. M. Wilde, *Quantum Information Theory*. Cambridge University Press, 2013.
- [305] H.-H. Lu, J. M. Lukens, N. A. Peters, B. P. Williams, A. M. Weiner, and P. Lougovski, “Quantum interference and correlation control of frequency-bin qubits,” *Optica*, vol. 5, no. 11, pp. 1455–1460, Nov. 2018.
- [306] P. Imany, O. D. Odele, M. S. Alshaykh, H.-H. Lu, D. E. Leaird, and A. M. Weiner, “Frequency-domain hong–ou–mandel interference with linear optics,” *Opt. Lett.*, vol. 43, no. 12, pp. 2760–2763, 2018.
- [307] J. M. Lukens, N. T. Islam, C. C. W. Lim, and D. J. Gauthier, “Reconfigurable generation and measurement of mutually unbiased bases for time-bin qudits,” *Appl. Phys. Lett.*, vol. 112, no. 11, p. 111 102, 2018.
- [308] T. Ikuta and H. Takesue, “Implementation of quantum state tomography for time-bin qudits,” *New J. Phys.*, vol. 19, no. 1, p. 013 039, 2017.
- [309] J. M. Lukens, H.-H. Lu, B. Qi, P. Lougovski, A. M. Weiner, and B. P. Williams, “All-optical frequency processor for networking applications,” *Journal of Lightwave Technology*, vol. 38, no. 7, pp. 1678–1687, 2019.
- [310] J. T. Seeley, M. J. Richard, and P. J. Love, “The bravyi-kitaev transformation for quantum computation of electronic structure,” *The Journal of chemical physics*, vol. 137, no. 22, p. 224 109, 2012.
- [311] Q. Sun, T. C. Berkelbach, N. S. Blunt, *et al.*, “Pyscf: The python-based simulations of chemistry framework,” *WIREs Computational Molecular Science*, vol. 8, no. 1, e1340, 2018. DOI: <https://doi.org/10.1002/wcms.1340>. eprint: <https://onlinelibrary.wiley.com/doi/pdf/10.1002/wcms.1340>. [Online]. Available: <https://onlinelibrary.wiley.com/doi/abs/10.1002/wcms.1340>.

- [312] J. R. McClean, N. C. Rubin, K. J. Sung, *et al.*, “OpenFermion: The electronic structure package for quantum computers,” *Quantum Science and Technology*, vol. 5, no. 3, p. 034014, Jun. 2020. DOI: [10.1088/2058-9565/ab8ebc](https://doi.org/10.1088/2058-9565/ab8ebc). [Online]. Available: <https://doi.org/10.1088/2058-9565/ab8ebc>.
- [313] L. H. Pedersen, N. M. Møller, and K. Mølmer, “Fidelity of quantum operations,” *Physics Letters A*, vol. 367, no. 1-2, pp. 47–51, 2007.
- [314] J. R. McClean, J. Romero, R. Babbush, and A. Aspuru-Guzik, “The theory of variational hybrid quantum-classical algorithms,” *New Journal of Physics*, vol. 18, no. 2, p. 023023, Feb. 2016. DOI: [10.1088/1367-2630/18/2/023023](https://doi.org/10.1088/1367-2630/18/2/023023). [Online]. Available: <https://doi.org/10.1088/1367-2630/18/2/023023>.
- [315] C. Kokail, C. Maier, R. van Bijnen, *et al.*, “Self-verifying variational quantum simulation of lattice models,” *Nature*, vol. 569, no. 7756, pp. 355–360, 2019.
- [316] Z. Hu, R. Xia, and S. Kais, “A quantum algorithm for evolving open quantum dynamics on quantum computing devices,” *Sci. Rep.*, vol. 10, p. 3301, 2020.
- [317] Z. Hu, K. Head-Marsden, D. A. Mazziotti, P. Narang, and S. Kais, “A general quantum algorithm for open quantum dynamics demonstrated with the fenna-matthews-olson complex,” *Quantum*, vol. 6, p. 726, 2022.
- [318] E. Levy and O. M. Shalit, “Dilation theory in finite dimensions: The possible, the impossible and the unknown,” *Rocky Mt. J. Math.*, vol. 44, no. 1, pp. 203–221, 2014.
- [319] I. K. Kominis, “The radical-pair mechanism as a paradigm for the emerging science of quantum biology,” *Mod. Phys. Lett. B*, vol. 29, no. Supplement 1, p. 1530013, 2015.
- [320] H. Zadeh-Haghighi and C. Simon, “Magnetic field effects in biology from the perspective of the radical pair mechanism,” *J. R. Soc. Interface*, vol. 19, no. 193, p. 20220325, 2022.
- [321] N. Lyu, E. Mulvihill, M. B. Soley, E. Geva, and V. S. Batista, “Tensor-train thermo-field memory kernels for generalized quantum master equations,” *arXiv preprint arXiv:2208.14273*, 2022.
- [322] A. Gilyén, Y. Su, G. H. Low, and N. Wiebe, “Quantum singular value transformation and beyond: Exponential improvements for quantum matrix arithmetics,” in *Proceedings of the 51st Annual ACM SIGACT Symposium on Theory of Computing*, 2019, pp. 193–204.
- [323] D. Camps, L. Lin, R. Van Beeumen, and C. Yang, “Explicit quantum circuits for block encodings of certain sparse matrices,” *arXiv preprint arXiv:2203.10236*, 2022.

- [324] A. J. Leggett, S. Chakravarty, A. T. Dorsey, M. P. A. Fisher, A. Garg, and W. Zwerger, “Dynamics of the dissipative two-state system,” *Rev. Mod. Phys.*, vol. 59, pp. 1–85, 1 Jan. 1987. DOI: [10.1103/RevModPhys.59.1](https://doi.org/10.1103/RevModPhys.59.1). [Online]. Available: <https://link.aps.org/doi/10.1103/RevModPhys.59.1>.
- [325] U. Weiss, *Quantum Dissipative Systems*, 4th. WORLD SCIENTIFIC, 2012. DOI: [10.1142/8334](https://doi.org/10.1142/8334). eprint: <https://www.worldscientific.com/doi/pdf/10.1142/8334>. [Online]. Available: <https://www.worldscientific.com/doi/abs/10.1142/8334>.
- [326] Q. Shi and E. Geva, “A new approach to calculating the memory kernel of the generalized quantum master equation for an arbitrary system-bath coupling,” *J. Chem. Phys.*, vol. 119, pp. 12 063–12 076, 2003.
- [327] S. Chatterjee and N. Makri, “Real-Time Path Integral Methods, Quantum Master Equations, and Classical vs Quantum Memory,” *J. Phys. Chem. B*, vol. 123, pp. 10 470–10 482, 2019.
- [328] J. J. Vartiainen, M. Möttönen, and M. M. Salomaa, “Efficient decomposition of quantum gates,” *Phys. Rev. Lett.*, vol. 92, no. 17, p. 177 902, 2004.
- [329] L. Gyongyosi, “Quantum state optimization and computational pathway evaluation for gate-model quantum computers,” *Sci. Rep.*, vol. 10, no. 1, pp. 1–12, 2020.
- [330] N. Lacroix, C. Hellings, C. K. Andersen, *et al.*, “Improving the performance of deep quantum optimization algorithms with continuous gate sets,” *PRX Quantum*, vol. 1, no. 2, p. 110 304, 2020.
- [331] R. Iten, R. Moyard, T. Metger, D. Sutter, and S. Woerner, “Exact and practical pattern matching for quantum circuit optimization,” *ACM Trans. Quantum Comput.*, vol. 3, no. 1, pp. 1–41, 2022.
- [332] N. Abdessaied, R. Wille, M. Soeken, and R. Drechsler, “Reducing the depth of quantum circuits using additional circuit lines,” in *International Conference on Reversible Computation*, Springer, 2013, pp. 221–233.
- [333] L. Viola and S. Lloyd, “Dynamical suppression of decoherence in two-state quantum systems,” *Phys. Rev. A*, vol. 58, no. 4, p. 2733, 1998.
- [334] G. S. Uhrig, “Keeping a quantum bit alive by optimized π -pulse sequences,” *Phys. Rev. Lett.*, vol. 98, no. 10, p. 100 504, 2007.
- [335] K. Khodjasteh and D. A. Lidar, “Fault-tolerant quantum dynamical decoupling,” *Phys. Rev. Lett.*, vol. 95, no. 18, p. 180 501, 2005.

- [336] K. Khodjasteh and D. A. Lidar, “Performance of deterministic dynamical decoupling schemes: Concatenated and periodic pulse sequences,” *Phys. Rev. A*, vol. 75, no. 6, p. 062310, 2007.
- [337] J. R. West, B. H. Fong, and D. A. Lidar, “Near-optimal dynamical decoupling of a qubit,” *Phys. Rev. Lett.*, vol. 104, no. 13, p. 130501, 2010.
- [338] B. Pokharel, N. Anand, B. Fortman, and D. A. Lidar, “Demonstration of fidelity improvement using dynamical decoupling with superconducting qubits,” *Phys. Rev. Lett.*, vol. 121, no. 22, p. 220502, 2018.
- [339] P. Das, S. Tannu, S. Dangwal, and M. Qureshi, “Adapt: Mitigating idling errors in qubits via adaptive dynamical decoupling,” in *MICRO-54: 54th Annual IEEE/ACM International Symposium on Microarchitecture*, 2021, pp. 950–962.
- [340] P. Jurcevic, A. Javadi-Abhari, L. S. Bishop, *et al.*, “Demonstration of quantum volume 64 on a superconducting quantum computing system,” *Quantum Sci. Technol.*, vol. 6, no. 2, p. 025020, 2021.
- [341] N. Ofek, A. Petrenko, R. Heeres, *et al.*, “Extending the lifetime of a quantum bit with error correction in superconducting circuits,” *Nature*, vol. 536, no. 7617, pp. 441–445, 2016.
- [342] L. Hu, Y. Ma, W. Cai, *et al.*, “Quantum error correction and universal gate set operation on a binomial bosonic logical qubit,” *Nat. Phys.*, vol. 15, no. 5, pp. 503–508, 2019.
- [343] P. Campagne-Ibarcq, A. Eickbusch, S. Touzard, *et al.*, “Quantum error correction of a qubit encoded in grid states of an oscillator,” *Nature*, vol. 584, no. 7821, pp. 368–372, 2020.
- [344] H. Paik, D. I. Schuster, L. S. Bishop, *et al.*, “Observation of high coherence in josephson junction qubits measured in a three-dimensional circuit qed architecture,” *Phys. Rev. Lett.*, vol. 107, no. 24, p. 240501, 2011.
- [345] M. Reagor, W. Pfaff, C. Axline, *et al.*, “Quantum memory with millisecond coherence in circuit qed,” *Phys. Rev. B*, vol. 94, no. 1, p. 014506, 2016.
- [346] C. S. Wang, J. C. Curtis, B. J. Lester, *et al.*, “Efficient multiphoton sampling of molecular vibronic spectra on a superconducting bosonic processor,” *Phys. Rev. X*, vol. 10, no. 2, p. 021060, 2020.
- [347] C. S. Wang, N. E. Frattini, B. J. Chapman, *et al.*, “Observation of wave-packet branching through an engineered conical intersection,” *arXiv preprint arXiv:2202.02364*, 2022.

- [348] P. Virtanen, R. Gommers, T. E. Oliphant, *et al.*, “SciPy 1.0: Fundamental Algorithms for Scientific Computing in Python,” *Nature Methods*, vol. 17, pp. 261–272, 2020. DOI: [10.1038/s41592-019-0686-2](https://doi.org/10.1038/s41592-019-0686-2).